EFFECT OF PROCESS VARIABLES AND SINTERING METHOD ON THE MICROSTRUCTURE AND PROPERTIES OF ITO-BOROSILICATE GLASS COMPOSITES

A Dissertation
Presented to
The Academic Faculty

by

Thomas Rudzik

In Partial Fulfillment
of the Requirements for the Degree
Doctor of Philosophy in the
School of Materials Science and Engineering

Georgia Institute of Technology
[August 2019]

EFFECT OF PROCESS VARIABLES AND SINTERING METHOD ON THE MICROSTRUCTURE AND PROPERTIES OF ITO-BOROSILICATE GLASS COMPOSITES

Approved by:

Dr. Rosario Gerhardt, Advisor
School of Materials Science and Engineering
Georgia Institute of Technology

Dr. Kyriaki Kalaitzidou
School of Mechanical Engineering
Georgia Institute of Technology

Dr. Faisal Alamgir
School of Materials Science and Engineering
Georgia Institute of Technology

Dr. Robert Speyer
School of Materials Science and Engineering
Georgia Institute of Technology

Dr. Chaitanya Deo
School of Mechanical Engineering
Georgia Institute of Technology

Dr. Jan Ilavsky
X-ray Science Division
Argonne National Lab

Date Approved: [April 26, 2019]

I would like to dedicate this work to my parents, John and Lynne Rudzik, my grandparents, John and Vera Rudzik, and my advisor, Dr. Rosario Gerhardt. In this culmination of many years of work, I must thank each of you for your support and guidance. This work would never have happened without you and I will always be grateful for what you have done for me.

ACKNOWLEDGEMENTS

I acknowledge Dr. Chaitanya Deo, Dr. Luke Walker, and Dr. Erica Corral for assistance with SPS processing equipment and Dr. Tom Quantrille for assistance with HP equipment. I acknowledge Dr. Ken Littrell, Jeff Bunn, and Paris Cornwell for assistance with the CG2-SANS setup at ORNL, Dr. Ken Littrell and Luke Heroux for running the USANS equipment at the BL-A1 beamline at ORNL, Dr. Ke An and Matt Frost for assistance with the neutron diffraction equipment at the BL-7 beamline at ORNL, and Dr. Jan Ilavsky for operating the USAXS/SAXS/WAXS equipment at the 9ID-C beamline at ANL and providing exceptional feedback and support in our experiments. Funding support from the National Science Foundation is also acknowledged. I acknowledge and thank Dr. Tim Pruyn, Dr. Joungho Jin, Dr. Ning Xia, and Morgan Watt for equipment training and for always providing help when I needed it. Finally, I would like to acknowledge and thank Dr. Deo, Dr. Kalaitzidou, Dr. Alamgir, Dr. Speyer, and Dr. Ilavsky for their time and effort in participating in my proposal and defense. I especially acknowledge Dr. Gerhardt, whose guidance and support have been indispensable. I cannot thank you enough.

TABLE OF CONTENTS

:

LIST OF TABLES

LIST OF FIGURES

LIST OF SYMBOLS AND ABBREVIATIONS

ITO	Tin-doped indium oxide, commonly known as indium tin oxide
ATO	Antimony-doped tin oxide, commonly known as antimony tin oxide
HP	Hot pressing
SPS	Spark plasma sintering
IS	Ac impedance spectroscopy
SAS	Small-angle scattering
SANS	Small-angle neutron scattering
USANS	Ultra-small-angle neutron scattering
SAXS	Small-angle x-ray scattering
USAXS	Ultra-small-angle x-ray scattering
WAXS	Wide-angle x-ray scattering
XRD	X-ray diffraction
SEM	Secondary electron microscopy
EDS	Energy-dispersive x-ray spectroscopy
UV-Vis	Ultraviolet-visible spectrophotometry
BSE	Backscattered electrons
A.U.	Arbitrary units
phr	The mass of filler material per 100g of matrix material
RD	Relative density

SUMMARY

The most prevalent fabrication method for ceramics is powder processing, in which ceramic powders are consolidated at elevated temperatures below their melting point in a process known as sintering. Through densification mechanisms such as solid-state diffusion and viscous flow, sintering can produce large bulk ceramic pieces with densities very close to the theoretical values using temperatures far below the melting temperature. While sintering has long been used to fabricate crystalline ceramics, new avenues of research have emerged more recently. For example, recent research has also shown that sintering can be useful in processing materials such as ceramic glasses, metals, and polymers. These materials have traditionally been made using other processing techniques such as melt processing, but sintering has been found to enable the formation of unique microstructures which have not been achievable using other fabrication methods. Additionally, new sintering methods have been developed which can impose novel process environments and show great potential in optimizing material properties.

Composites consisting of indium tin oxide, the predominant transparent conducting oxide, as a filler within a borosilicate glass matrix have been fabricated via hot pressing (HP) and spark plasma sintering (SPS). HP simply combines elevated temperatures and pressures and has been in use for far longer than SPS but is limited by slow heating rates. SPS is newer and more specialized, combining elevated temperatures and pressures with the application of an electric current through the sintering die and/or powder, which subjects the powder to an electric field and allows for far higher heating rates. Both sintering methods are shown to allow a grain-like glass matrix structure to form without

incorporating the ITO into the glass particles, leading to the formation of segregated ITO networks and an accompanying drop in impedance of up to 12 orders of magnitude. In doing so, these networks imparted electrical conductivity to the composites while requiring far less filler material (under 1 vol% ITO under all studied conditions) to achieve percolation than other fabrication methods.

It was found that the HP process achieved consolidation of the powder mixes at a temperature 70°C lower than that required by the SPS process, despite many previous reports in the literature that SPS generally imparts superior properties and requires lower temperatures. While investigating the reasons behind this apparent contradiction, it was found that the mechanisms at play in the SPS process were more numerous and complicated than those in HP, thus requiring a more detailed study.

Since the driving force for consolidation in sintering is dependent on the instantaneous state of the microstructure, which evolves throughout the sintering process, it varies between locations in the powder bed and is constantly changing with time at each location. Due to the complexity in the sintering mechanisms, it has not yet been possible to accurately predict the sintering processing parameters necessary to achieve a specific microstructure or properties for a given material, and development of sintering processes has primarily been achieved through a brute-force trial and error approach. The SPS process introduces additional complications due to the application of an applied current. A systematic investigation found that interactions between the temperature, pressure, applied current and resulting voltage, hold time, heating rate, and material variables make it difficult to isolate the effects of changing a single variable. Furthermore, there is a widespread lack of understanding regarding the significance of the applied current and

resultant electric field on the densification process, as well as the codependence between these parameters and other processing variables.

Throughout this study, many conventional characterization methods such as SEM and XRD were employed to characterize the fabricated composites. Additionally, a detailed ac impedance spectroscopy study on both powder compacts and sintered samples was undertaken. Results showed how the SPS applied current and voltage are related to other variables such as the heating rate, applied pressure, maximum temperature, and equipment/tooling geometry. By enabling separation of the electrical responses of the different microstructural features present in the sample via equivalent circuit fitting, the impedance data provided extensive insight on the effects of changing sintering process variables and showed strong potential for facilitating further understanding and advancement in this field.

CHAPTER 1. BACKGROUND AND MOTIVATION

This thesis presents data concerning the fabrication of tin-doped indium oxide (ITO)-borosilicate glass composites which make use of the sintered microstructure to form segregated, percolated ITO networks. The background section introduces the core concepts involved in the project, including the thermodynamic basis for the sintering process, electrical percolation, and ac impedance spectroscopy, and establishes the motivation for this work. Different aspects of the formation and characterization of the composite samples are discussed in separate chapters, including characterization of the initial powder mixtures, a comparison of the hot pressing (HP) and spark plasma sintering (SPS) processes, analysis of the effects of different processing variables of the SPS process on the resulting microstructures, and detailed characterization of impedance spectroscopy data for the various sample sets via equivalent circuit fitting.

1.1 Background

1.1.1 Thermodynamics and stages of the sintering process

When starting with a powder, assuming the particles are roughly monosize and spherical, it is well known that packing efficiency is limited to a maximum of 74%. To achieve high density bulk pieces via sintering, the particles must deform to fill the gaps. The elimination of these gaps also eliminates the associated particle-air surface area and reduces the surface free energy. The combination of reduced interfacial energy and area provides the driving force for consolidation as shown in equation 1.1, where γ is the specific interfacial energy, A is the total interfacial area, γA is the total interfacial energy

of the powder compact, $\Delta\gamma$ is the change in interfacial energy due to densification, and ΔA is the change in total interfacial area due to grain coarsening.[1]

Although there is a driving force for densification, at ambient temperatures, the kinetics of the mechanisms by which the consolidation occurs tend to be far slower than any practical fabrication timescale, so elevated temperatures are employed to accelerate the kinetics exponentially. The consolidation process is often described as three distinct stages, defined by the dominant microstructural feature in each, as shown in Figure 1.1.[1] In the initial stage (Figure 1.1(a)), material in contacting particles migrates to the contact point, resulting in neck formation and growth. In the intermediate stage (Figure 1.1(b)), the particles have deformed into polyhedral shapes better suited to fill the available space and the remaining pore volume has segregated to the edges of the polyhedra, forming

$$\Delta(\gamma A) = \Delta\gamma A + \gamma\Delta A \tag{1.1}$$

interconnected channels. These channels then close, leaving isolated pores within the microstructure, which are the dominant feature of the final stage of sintering (Figure 1.1(c)).

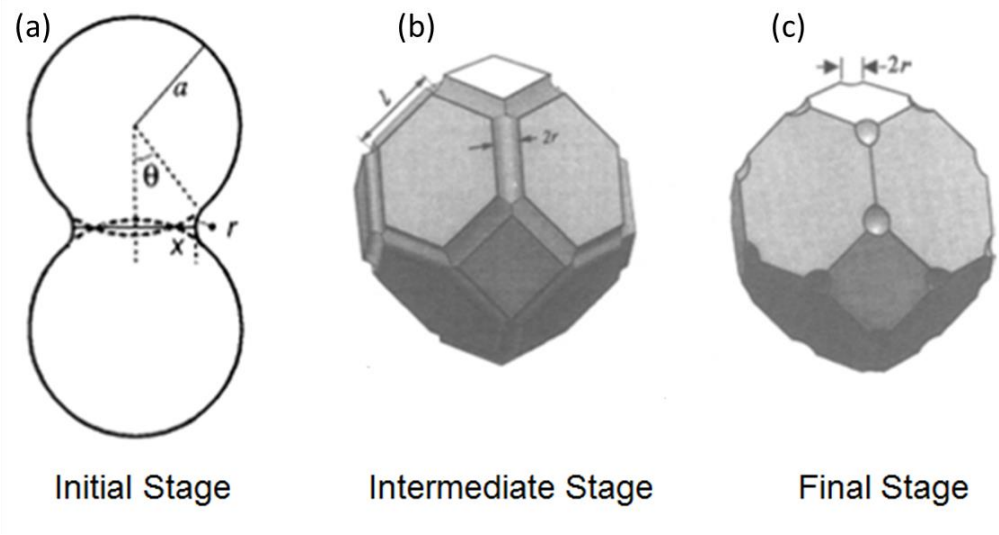

Figure 1.1. Schematics of the microstructural features defining each of the three distinct stages of sintering, adapted from [1]. The (a) initial stage features neck formation and growth, the (b) intermediate stage is defined by particle deformation to polyhedra and segregation of pores to their edges, forming interconnected channels, and the (c) final stage exhibits closure of the pore channels, resulting in isolated pores at the corners of the polyhedra.

Although each stage features distinct microstructural differences, the interfaces between powder particles and the geometry, volume, and distribution of the pores define the microstructure throughout the sintering process.

The properties of a material are strongly dependent on its microstructure. Therefore, establishment of the processing-microstructure-property relationships for a given material enables starting with the desired material properties and arriving at a set of processing conditions which will achieve those properties, rather than trying many different processing conditions until those which achieve the desired properties are found. Since the needs-driven approach made possible with knowledge of the key relationships is generally far less costly and time consuming, it is very much preferred over the alternative of iterative guesswork. In the case of processing via sintering, relating the final microstructure to the

processing parameters has proven to be a considerable challenge; since the particle-pore interfacial area is the driving force for densification and the pore characteristics constantly evolve throughout the sintering process, the progression of densification is directly dependent on the instantaneous state of the microstructure at any given point in the process. Therefore, the processing-microstructure relationships in sintered materials can only be established if all aspects of the microstructure can be determined continuously throughout sintering which has yet to be accomplished.

1.1.2 Enhanced Sintering Methods: HP and SPS

In addition to elevated temperatures, externally applied pressure can be applied to powders, either unidirectionally or isotropically, which enhances both the driving force for densification and the kinetics of the densification mechanisms.[1] Sintering involving simultaneous heating via external resistive heating coils and applied uniaxial pressure is called hot pressing (HP) (Figure 1.2). Moderate applied pressures, usually in the range of 20-50 MPa, increase the driving force for densification and can activate additional densification mechanisms, such as plastic deformation and creep, which have a significant impact.[1] These factors can decrease the temperature required to eliminate the pores by hundreds of degrees compared to that without applied pressure[2], resulting in faster and cheaper processing, which has spurred its widespread use.

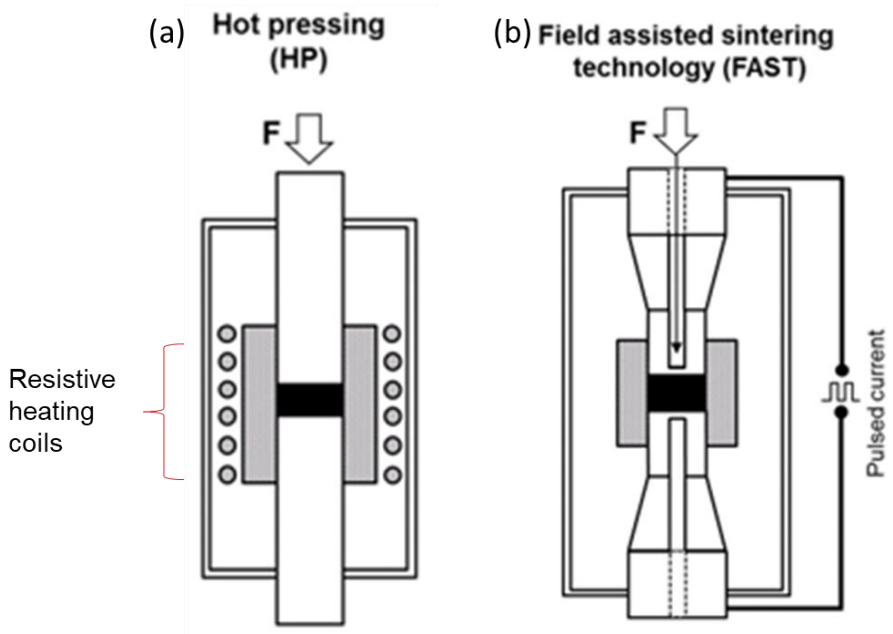

Figure 1.2. Schematics of different pressure-assisted sintering techniques, adapted from [1]. In (a) hot pressing, pressure is applied to the powder uniaxially and heat is applied via resistive heating coils. In (b) spark plasma sintering (SPS), also referred to as FAST, pressure is applied uniaxially, but heating is accomplished by a strong pulsed current sent through the graphite punches which travels through either the die or the powder itself inducing Joule heating.

Spark plasma sintering (SPS), which is also known by many other names including field assisted sintering technique (FAST) and pulsed electric current sintering (PECS), applies uniaxial pressure just like hot pressing, but the heat applied to the powders is generated by applying a pulsed dc current directly through either the powder itself or through the surrounding die, resulting in Joule heating (Figure 1.2(b)). The currents used often range from hundreds to thousands of amps, and as a result, heating rates of hundreds of degrees Celsius per minute are standard, and rates exceeding 1000 °C/min are possible. In contrast, HP equipment generally cannot achieve heating rates exceeding 20 °C/min, and heating rates of under 10 °C/min are the most common.[3]

1.1.3 Ac impedance spectroscopy

Alternating current electrical signals are strongly affected by interfaces since they influence the current, phase angle, and the input/output voltage.[4,5] As a result, ac impedance spectroscopy (IS) is a useful technique for characterizing all types of interfaces, including pores[6,7], multi-phase interfaces[8,9], and grain boundaries,[10] all of which may be present in powder compacts before and during sintering and in the final sintered samples.[5-7] Each material phase and type of interface has its own electrical response which is induced at a specific frequency range. Therefore, measuring the impedance over a frequency range of many orders of magnitude characterizes the electrical response of each unique microstructural feature in a material.[8,11] Furthermore, IS data can be fit to a theoretical model in which an equivalent circuit is found which reproduces the experimental data and through this method, enables the responses to be separated and assigned to microstructural features which are expected to, or have been observed to be, present in the material.

The wide applicability and high sensitivity of IS has proven invaluable in the characterization of sintered samples and of insulating matrix – conducting filler composites similar to those studied in this work[5,12,13], and was thus employed extensively as a crucial primary characterization tool.

1.1.3.1 Polarization phenomena

Dielectric spectroscopy measures charge density fluctuations in a material with a time-dependent electric field.[14] These fluctuations are generally caused due to polarization mechanisms, which can be separated into different classes including electronic polarization, ionic polarization, orientation polarization, and interfacial polarization.[14] In

every case, polarization does not occur instantly, and thus each process occurs over a characteristic time scale.[8,14] Therefore, if subjected to an alternating electric field, any mechanism will only show a strong response when the frequency of the field is such that the mechanism will be complete over the time period that the field stays oriented in one direction. This period is called the relaxation time of the process, and the frequency range over which the dominant polarization mechanism changes is known as dielectric relaxation.[8] Any dielectric relaxation process can be described by the Debye equation:

$$\varepsilon^* = \varepsilon_\infty + \frac{(\varepsilon_s - \varepsilon_\infty)}{1 + j\omega\tau} \tag{1.2}$$

where ε* is the complex dielectric permittivity, ε_∞ is the high-frequency dielectric permittivity, ε_s is the lowest-frequency dielectric permittivity, ω is the angular frequency, ω = 2πf, where f is the frequency, j is the constant $\sqrt{-1}$, and τ is the relaxation time.[8] Thus, the responses from different relaxation processes can be separated and identified based on the frequencies at which they respond, allowing for a far more detailed characterization than is possible with standard dc electrical measurements.[5]

Electronic polarization involves separation of the centers of positive and negative charge of an atom, which occurs when an electric field distorts the geometry of the electron cloud, as is shown schematically in Figure 1.3 (a).[14] In the plot, the responses of the different mechanisms are shown in terms of the dielectric constant, k, and the dielectric loss, tan δ. The dielectric constant is equivalent to the real part of the complex permittivity, ε', and the dielectric loss is defined as

$$\tan \delta = \frac{\varepsilon'}{\varepsilon''} \quad (2)$$

where ε'' is the imaginary part of the complex permittivity.[8] electronic polarization dominates the high ac frequency electrical response of a typical material, as shown in Figure 1.4.[14] The strength of the electronic polarization is related to the number of electrons involved and the separation distance between the charge centers through the equation

$$P = Zqd \quad (1.3)$$

where Z is the atomic number of the atom, which is equal to the number of electrons for an atom with no charge, d is the distance between the charge centers, and q is the elementary charge constant, equal to $1.609\times 10^{-19}\ \frac{Coulombs}{m}$.[8]

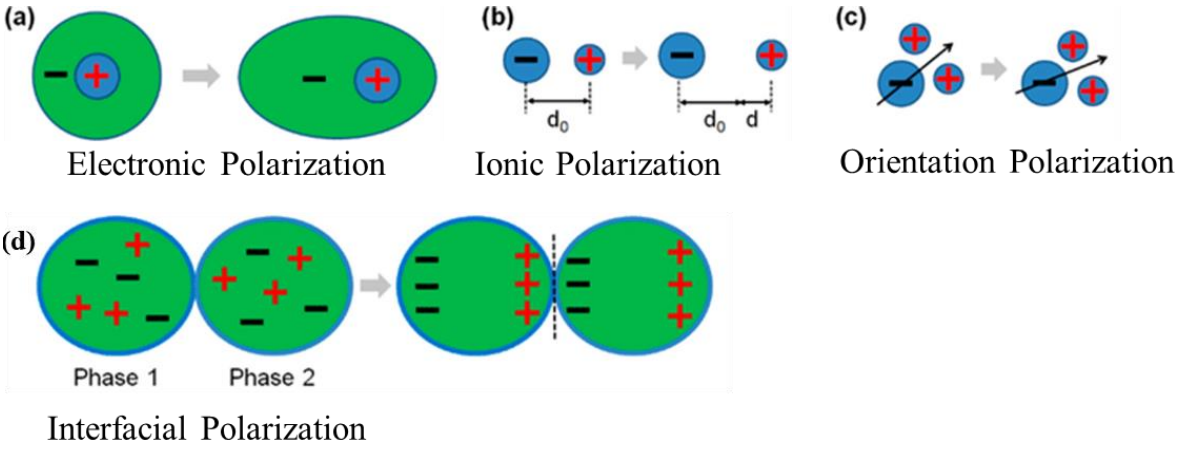

Figure 1.3. Diagrams of four polarization mechanisms, (a) electronic, (b) ionic, (c) orientation, and (d) interfacial polarization, which can all be present in ceramic materials. Adapted from [14].

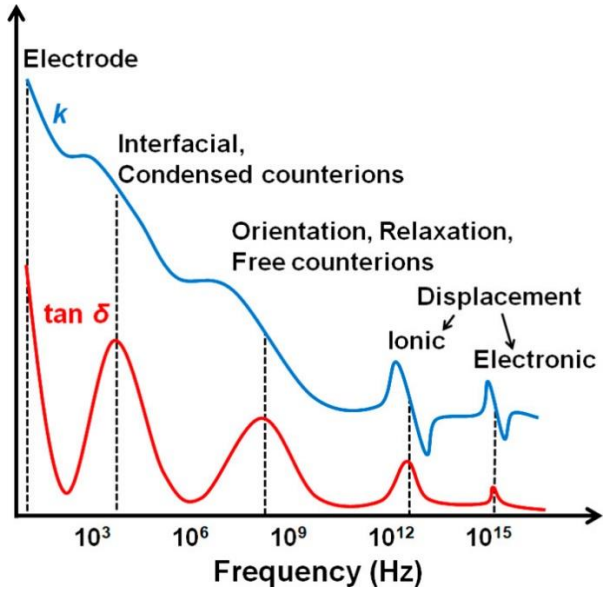

Figure 1.4. Plot showing general frequency ranges for the different types of polarization mechanisms and the expected electrical responses in terms of the dielectric constant, k, and the dielectric loss, tan δ. Adapted from [14].

Ionic polarization occurs when cations and anions are displaced in opposing directions upon being subjected to an external electric field (Figure 1.3 (b)).[14] This comes about due to temporary dipoles, which can occur in any ionically bonded material.[8] This process

responds at high field frequencies, though not as high as electronic polarization mechanisms (Figure 1.4).[14]

Orientational polarization describes the reorientation of permanent dipoles upon the application of an electric field (Figure 1.3(c)).[14] Permanent dipoles are present in materials such as ferroelectrics below their Curie temperature and polar liquids including water.[8] This process manifests at intermediate field frequencies, as indicated in Figure 1.4.[14]

Interfacial polarization, also known as space charge polarization, occurs when charge carriers pile up at an interface (Figure 1.3(d)).[8,14] This interface could be that between grains of phases with substantially different electrical properties or between grains of the same phase if there is a concentrated or depleted region of defects or impurities at that boundary.[8] The interface can also be that between the sample under test and the contacting electrode required to conduct the electrical testing, which requires consideration when identifying the individual components of the electrical response.[8] The space-charge polarization process responds at low frequencies, as shown in Figure 1.4.[14] When studying the responses over the entire frequency range, a pattern is apparent in which polarization mechanisms involving larger length scales, and thus larger distances over which the charge carriers travel, respond at lower frequencies compared to shorter-range mechanisms. This is not coincidental; it comes about because the frequency is inversely related to time, and it is logical that charge carriers require more time to move larger distances, so the larger the length scale, the smaller the response frequency.

1.1.3.2 Impedance spectroscopy fundamental concepts

Ac impedance spectroscopy (IS) is an electrical characterization method in which an ac current is applied through a sample and the resulting current, I, voltage, V, and phase angle, θ, are measured.[8] The electric field produced by the applied current will cause the different polarization mechanisms possible in the test material to occur depending on the ac frequency, so by testing at many different frequencies over a range of many orders of magnitude, all of the individual responses can be characterized. The impedance vector, Z*, is defined as

$$Z^*(\omega) = \frac{V(\omega)}{I(\omega)} \tag{1.4}$$

where $V(\omega) = V_m \sin(\omega t)$, $I(\omega) = I_m \sin(\omega t + \theta)$, ω is the phase angle as defined earlier, and θ is the phase difference between the current and voltage.[12] As with the permittivity, the impedance vector is a complex value with both a real part, Z', and an imaginary part, Z''.

Analysis of the data from ac impedance testing is accomplished through a fitting process called equivalent circuit fitting, whereby the complex impedance is fit to a circuit composed of individual resistive, capacitive, and inductive elements. Each of these elements has a characteristic relationship between the applied field frequency and the resulting impedance which is easy to idenfity in plots of the impedance magnitude, |Z| and the impedance phase angle, θ. The impedance magnitude is calculated from the equation

$$|Z| = \sqrt{(Z')^2 + (Z'')^2} \tag{1.5}$$

and the impedance phase angle is expressed as:

$$\theta = tan^{-1}(\frac{Z''}{Z'}) \tag{1.6}$$

The characteristic responses of the ideal circuit elements in terms of |Z| and θ are shown in Figure 1.5. The ideal resistor has zero slope in |Z| and a θ of 0°, the ideal capacitor has a negative slope in |Z| and a θ of -90°, and the ideal inductor has a positive slope in |Z| and a θ of 90°.

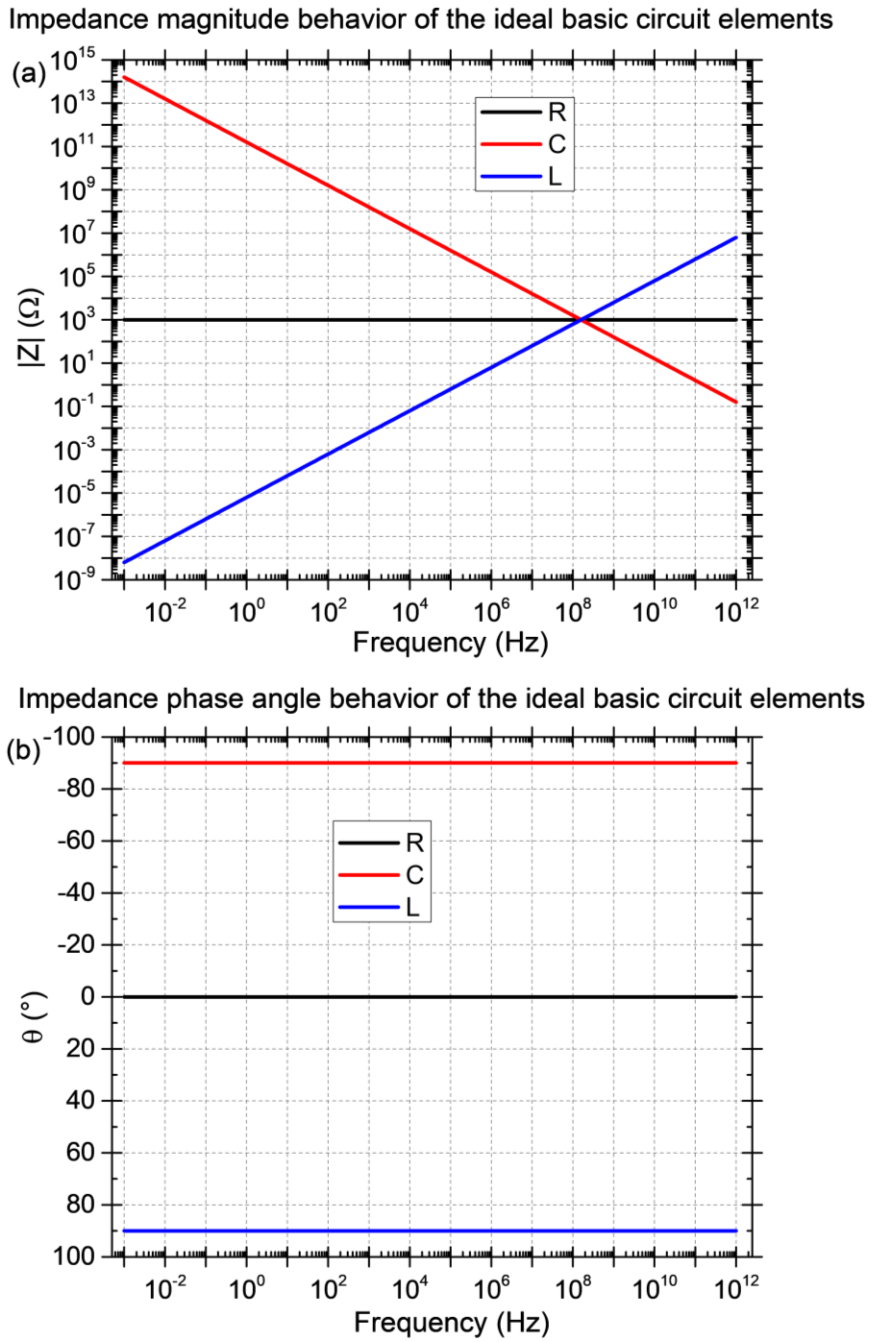

Figure 1.5. The characteristic impedance responses of ideal resistor (R), capacitor (C), and inductor (L) circuit elements in terms of (a) the impedance magnitude and (b) the impedance phase angle.

Ideal resistors exhibit only real impedance and ideal capacitors and inductors exhibit only imaginary impedance, but in practice, the appropriate model to fit a material's impedance

response will usually require multiple elements connected together in either series or parallel configurations. Therefore, when attempting to determine what circuit elements are present in the impedance response of a sample, the slopes of the curve in |Z| and the values in θ will be a combination of those from the ideal element constituents. For example, a combined resistor and capacitor will show a |Z| trend with both a zero slope region and a negative slope region, while the θ trend will show linear regions with values of zero and -90, if the frequency range is large enough, with a transitional region between them.

The most common combinations of circuit elements which can fit impedance responses for a wide variety of of materials are a resistor and inductor in series (series RL) and a resistor and capacitor in parallel (parallel RC), which often provide good fits for conducting and insulatting samples, respectively (Figure 1.6).

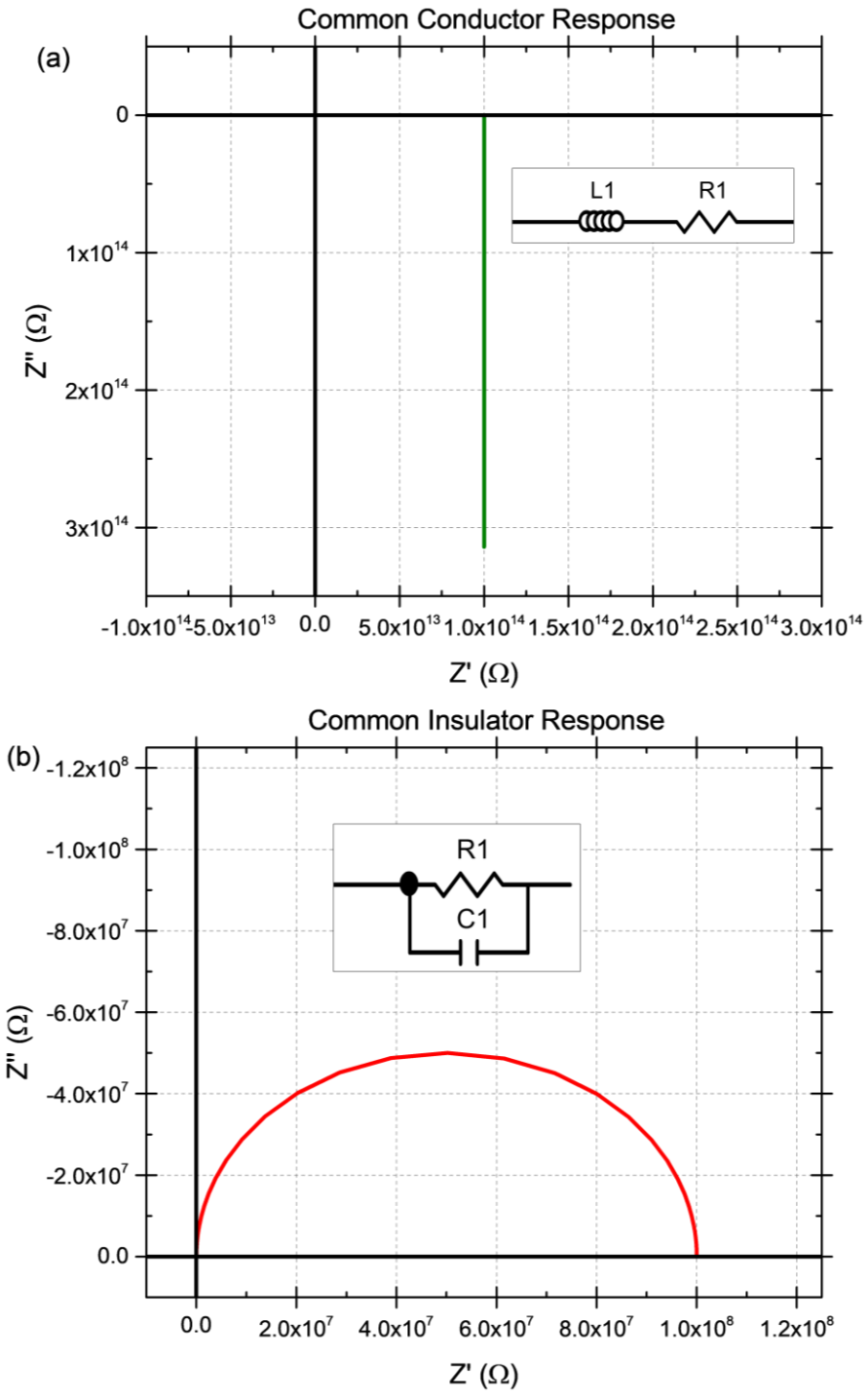

Figure 1.6. Plots showing the responses of (a) a series RL circuit and (b) a parallel RC circuit in the complex impedance plane. Insets in each plot show the circuit which gives the respective response.

Impedance data can also be interpreted using the other three dielectric functions, namely the admittance, Y*, permittivity, ε*, and electric modulus, M*. The impedance is related to the dielectric permittivity through the expression

$$Z^* = \frac{1}{j\omega C_0 \varepsilon^*} \tag{1.7}$$

where $j = \sqrt{-1}$ and C_0 is the geometric capacitance of the sample.[4] Admittance is the inverse of impedance and electric modulus is the inverse of permittivity, so as long as the geometric capacitance of the sample is known, it is possible to analyze the same measured data in each of these functions without the use of any adjustable parameters. Doing so can be very advantageous because some processes that may not be detectible using one of the functions can be easily detected using one of the others.[4,5]

1.2 Motivation

1.2.1 Motivation for the Fabrication of ITO-glass Composites

There is currently a large and growing market for display technology, from the ubiquitous smart phones, to the push toward making every appliance and surface come with a display and internet connection. Nearly all flat panel display technologies, such as LCDs and OLEDs, require the incorporation of a material which is both transparent and a good electrical conductor, and for such applications, the predominant material is tin-doped indium oxide, more commonly known as indium tin oxide, or ITO. Transparent conducting oxides, including ITO, possess this uncommon combination of properties owing to a band gap too large to absorb visible light in conjunction with shallow doping levels which

provide an abundance of electric charge carriers. Although many other transparent conducting oxides have been developed, ITO has been found to have the best combination of transparency and conductivity, but not without other drawbacks. Indium is quite expensive, and its cost will only increase with its increasing demand and it is unknown how much more can be mined economically. Thus, there is ever-growing pressure to move away from ITO. However, abandoning ITO is not the only option for alleviating the burden of its cost.

Composites are at the forefront of modern advanced materials, due to their ability to possess properties which exceed those of the constituent phases. Conductivity can be achieved in composites consisting of an insulating matrix material and a conducting filler material if there is a continuous network of the filler spanning the thickness of the composite. Generally, higher concentrations of functional filler materials degrade the mechanical properties of composites, and if the filler material is expensive, as in the case of ITO, it is especially advantageous to minimize the concentration required. Therefore, optimum properties will be achieved using the filler concentration at which the first continuous network forms, which is called the percolation threshold. However, the percolation threshold is not a fixed concentration, and the factors which affect the percolation threshold, such as the ratio of the sizes of the filler and matrix phases[15,16] and the way in which the filler is distributed within the matrix[13], can be manipulated to minimize the percolation threshold, thereby further optimizing the conducting composite.

One means by which the percolation threshold can be dramatically reduced is segregation of the filler by heavily restricting the volume which it can occupy within the microstructure[16], which has been demonstrated in powder mixes in which the particle size

ratio of the filler to the matrix is very small.[13] These powder mixes can then be consolidated to form dense percolated composites, as long as the filler network is not disrupted in the consolidation process. Many publications, including many in the Gerhardt group, have shown that for viscous matrix materials such as thermoplastic polymers[17,18] and ceramic glasses[5,12,13], the consolidation process causes the matrix particles to deform from spheres to polyhedra, giving a "grain-like" microstructure resembling that of a polycrystalline material.[6,10,13,19] Under specific temperature and pressure conditions, the matrix phase viscosity can be both low enough to deform to create a dense microstructure and high enough that the filler will not enter the matrix particles, instead being segregated into the interparticle boundaries (Figure 1.7), thus severely restricting the volume which the filler can occupy and correspondingly decreasing the percolation threshold. Previous work demonstrated successful segregated network formation and percolation thresholds of less than 1 vol% filler in sintered samples of antimony-doped tin oxide (ATO) nanoparticle filler-borosilicate glass microsphere matrix composites.[10] Given the superior optical and electrical properties of ITO compared to those of ATO, it was hypothesized that substituting the ATO for ITO should give better properties at a similarly low percolation threshold, which could result in composites with sufficient transparency and conductivity to be useful in electronic applications while vastly reducing the required amount of expensive ITO.

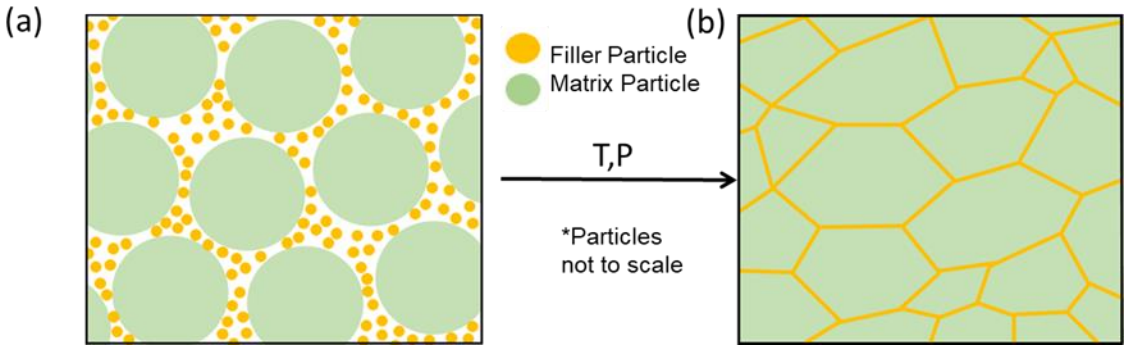

Figure 1.7. A diagram showing how segregated network composites can be fabricated using a sintering process. (a) A mixture of large matrix particles and small filler particles is subjected to a specific range of temperature and pressure conditions which allow the matrix particles to deform to eliminate the pore volume but do not allow the filler to incorporate into the matrix particles. The result is (b) a dense microstructure in which continuous networks of filler can form at very low filler concentrations.

1.2.2 Motivation for comparing the properties of composites made via HP and SPS

The HP method was initially used to fabricate the composites since it had proven successful in the previous work with ATO-borosilicate composites.[13] However, with access to far higher heating rates than HP, SPS can reach the target temperature in minutes or even seconds rather than hours, which has proven very useful for minimizing grain growth during sintering. Many publications comparing samples of the same material made using HP and SPS have reported a variety of additional advantages for SPS[2], including cleaner grain boundaries[20], increased superplasticity in ceramics[21,22], higher permittivity in ferroelectrics[23], higher chemical stability[24], higher hydrogen storage capacity in BCC solid metallic solutions[25], and improved thermoelectric[26,27], magnetic[28], and mechanical properties.[29] Additionally, SPS presents the promise of improvement in the optical properties[30,31] through the enhanced reduction in porosity and a reduction of impurities introduced during the sintering process, both of which have been identified as strongly affecting the optical properties of sintered materials.[32] Furthermore, many reports have

found that SPS not only reduces the required sintering time, but also the required temperature.[2] Therefore, a comparison between the results of the two methods was warranted to determine whether SPS would impart superior properties to the ITO-borosilicate composites.

1.2.3 Motivation for investigating the effects of changing sintering process parameters

Despite the substantial increase in the interest in field-assisted sintering methods over the past three decades[2], there are still many conflicting reports throughout the literature as to the nature and mechanisms of the effect of the SPS heating method on the densification of dielectric ceramic powders. Many research groups have found that SPS processing reduced the sintering time and/or temperature required to complete densification compared to hot pressing. These phenomena have been attributed to inaccurate measurement of the temperature[33,34], unintended overheating in the initial sintering stage[35], and the elevated heating rates available in SPS.[36] Others have claimed that the effects stem from combinations of high heating rates, adsorbed water, applied electric field, or current density.[37-39] In light of the confusion and mystery surrounding densification behavior in SPS, definitive proof of the dominant mechanisms would allow increased comparability between results obtained from different SPS equipment and enable the development of more accurate models to predict SPS sintering behavior.

1.3 Goals

The initial goal of this project was to create ITO-borosilicate composites with low resistivity and high optical transmittance while minimizing the required ITO concentration. The starting hypothesis was that by using ITO as the conducting filler material, the same

grain-like microstructure with a percolated filler network could be achieved and result in a superior combination of conductivity and optical properties under the same HP fabrication conditions in comparison to ATO-borosilicate composites which were made previously.[13] Based on the many reports of superior properties achieved via SPS compared to HP[2], it was hypothesized that use of the SPS process would result in improved optical properties and higher density[30,31], and could possibly even improve the electrical properties by removing undesirable impurities segregated to interparticle boundaries.[20]

The findings of tests on different SPS equipment using the same powder composition, ramp rate, hold temperature, hold time, and applied pressure led to the additional hypothesis that besides these variables, there must be other factors which strongly affect sintering behavior in these composites, despite finding that only the stated variables are commonly reported in the SPS literature. As a result, finding the additional factors which led to the observed differences between the samples made using the different SPS equipment became an additional goal, since an understanding of the effects of these factors would be necessary to be able to optimize the SPS process for the ITO-borosilicate composites.

Due to the complexity of sintering mechanisms, it was posited that the properties of the sintered composites could be further optimized if the sintering process could be thoroughly characterized in-situ. It was proposed that by combining the ac impedance spectroscopy (IS) and small angle scattering (SAS) methods during the sintering of powders the resulting data would be sufficiently comprehensive to allow for the development of sintering process models, thereby enabling the prediction of processing conditions necessary to achieve a desired microstructure and/or desired material properties. Based on this hypothesis, another

goal was to develop and demonstrate an in-situ characterization technique combining IS and SAS methods during sintering via the application of both pressure and elevated temperatures to a powder and, in doing so, prove that a process model could be developed from analysis of the resulting data. This work is presented in the appendix.

CHAPTER 2. EXPERIMENTAL METHODS

2.1 Materials and Powder Preparation

The filler material used for the majority of sintered samples was ITO nanoparticles from Inframat Advanced Materials (Manchester, CT) made up of 10 wt% SnO_2 in In_2O_3 with a size range 20-40 nm per the manufacturer (Figure 2.1(a)). The matrix material was solid borosilicate glass microspheres (GL-1079) obtained from Mo-Sci Corporation (Rolla, MO) with a size range of 45-53 μm (Figure 2.1(b)).

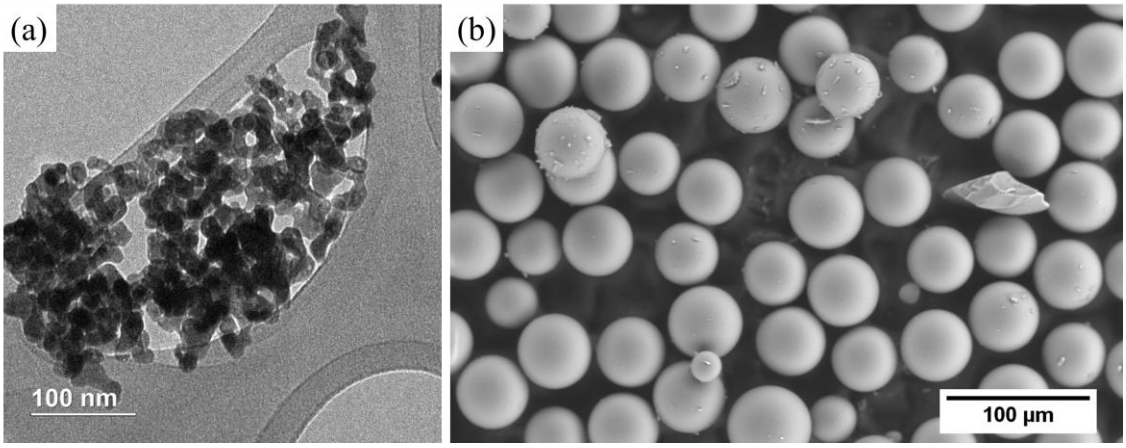

Figure 2.1. (a) TEM image of the ITO nanopowder and (b) SEM image of the borosilicate glass microspheres used for producing most of the sintered samples over the course of this thesis.

A set of powder mixes was made with a range of ITO concentrations, given in Table 2.1, in terms of phr, which stands for "per hundred resin" and is more commonly used in the field of polymer composites. For the present materials, this means the grams of ITO per hundred grams of glass and is roughly equal to the weight percent for dilute mixtures. Each powder composition was made by dry-mixing the two powders at room temperature using a ball mill with 5 mm spherical alumina media (99.5%) at a speed of 120 rpm. Each

composition was mixed in a separate mill with its own milling media to prevent cross-contamination. The compositions listed in Table 2.1 are given in phr, wt% and vol% because phr was used to determine the ratios to make the composites and this is how results are reported.

Table 2.1. The compositions of the powder mixtures sintered into glass composites

Powder Composition (ITO phr)	Powder Composition (ITO Wt %)	Powder Composition (ITO Vol %)
0.0	0.000	0
0.001	0.001	0
0.01	0.010	0.003
0.1	0.100	0.031
0.5	0.498	0.154
1.0	0.990	0.307
1.8	1.720	0.536
2.5	2.439	0.764
5.0	4.762	1.517
7.5	6.977	2.259
10.0	9.091	2.989

*Theoretical densities determined by a rule of mixtures calculation from the theoretical density of ITO (7.14 g/cm^2) and that of borosilicate glass (2.2 g/cm^2) given by the manufacturer.

2.2 Hot Pressing Procedure

A set of mixed powders encompassing all the compositions given in Table 2.1 was hot pressed using equipment (Astro Industries, Santa Barbara, CA) located at Advanced Composite Materials L.L.C (Greer, SC) to make three sintered samples of each composition. Each powder mix was pressed with a uniaxial pressure of 11.1 MPa in flowing N_2. A graphite foil-lined graphite die with 30-mm inner diameter was used to make three specimens with the same composition simultaneously, with graphite foil-lined graphite spacers used to separate the samples in the die (Figure 2.2). Ten grams of powder were used for each of the three samples in the die. The temperature was measured using a

thermocouple fully inserted into a radial hole in the die wall located at the center in the axial dimension. The powders were subjected to a heating rate of 17.5°C/min to 550°C, at which the temperature was held for 10 minutes, followed by a temperature ramp of 6°C/min to the maximum pressing temperature of 610°C, at which the temperature was held for another 10 minutes. This is shown graphically in Figure 2.3 along with the pressure profile. The pressure was ramped gradually to 11.1 MPa over the course of the temperature ramp to 550°C, and was fully released when the die had cooled to 300°C. The resulting samples were disks with a diameter of 30 mm and thickness of 4-6 mm.

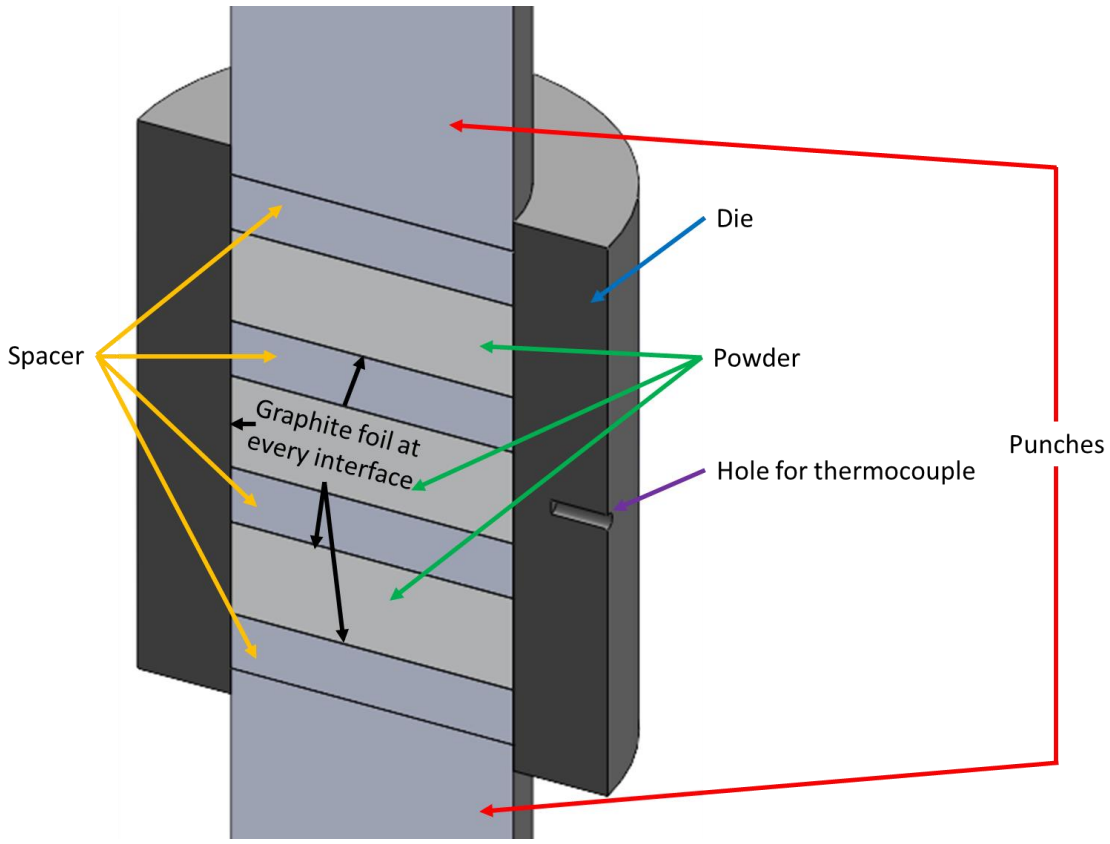

Figure 2.2. Schematic of the die assembly used when making the hot-pressed samples. Three samples were made simultaneously in the same die by using graphite spacer disks to separate the powder beds. Graphite foil was placed at all interfaces, so the graphite tooling was never in direct contact with other tooling pieces or with the powder. Temperature was measured with a thermocouple inserted into a radial hole in the die wall.

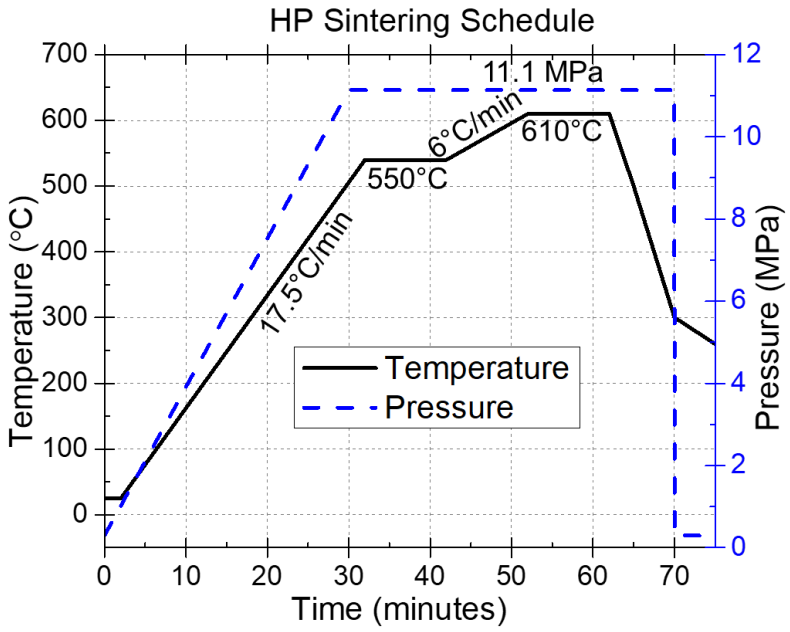

Figure 2.3. Standard temperature and pressure profiles used for most of the hot-pressed samples.

2.3 SPS Procedure

Spark plasma sintering was carried out using 3 different SPS equipment: A Thermal Technologies L.L.C model SPS 10-4, a Thermal Technologies L.L.C model SPS 25-10 and a Fuji Electronic Industrial Co., LTD Dr. Sinter model SPS-211Lx. These different equipment were designated as UA, TT, and GT, respectively. Common processing parameters among all samples were automatic temperature control mode, a hold time of 5 min at the hold temperature, a single ramp period with a constant programmed heating rate, constant pressure from the start of the ramp to the end of the hold, vacuum atmosphere, graphite tooling with graphite foil at every interface, and 20 mm sample diameter. For all samples made on all SPS equipment in this study, temperature was measured via a thermocouple fully inserted into a radial hole in the outer wall of the die. As each series of SPS samples had a different processing parameter changed, the conditions used to fabricate

each sample set are presented in in their respective sections in chapters 3-5. Powder mixes of each composition were placed in graphite foil-lined graphite dies (Figure 2.4). The most common set of processing parameters, used for all SPS samples in chapter 3, were a uniaxial pressure of 23.4 MPa and a heating rate of 50°C/min to a maximum temperature of 610°C (Figure 2.5) under vacuum to consolidate the powders into discs with diameters of 20 mm and thicknesses ranging from 2 to 3 mm. The full pressure was applied at the start of the temperature ramp and reduced to 5 MPa at the end of the temperature hold.

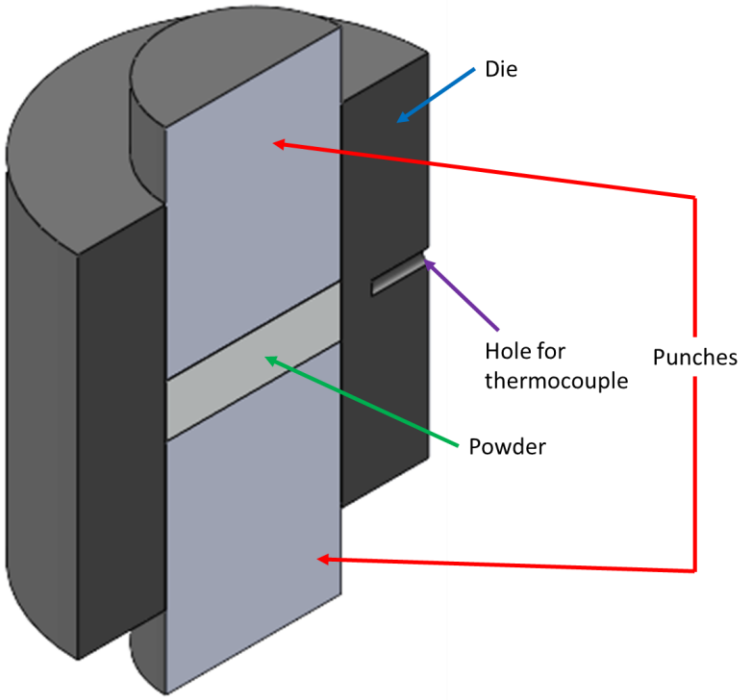

Figure 2.4. Schematic of the die setup used for all SPS samples. Only one sample was made in each SPS run. Like in the HP procedure, graphite foil was placed at all interfaces and the temperature was measured by a thermocouple fully inserted into a radial hole in the die wall.

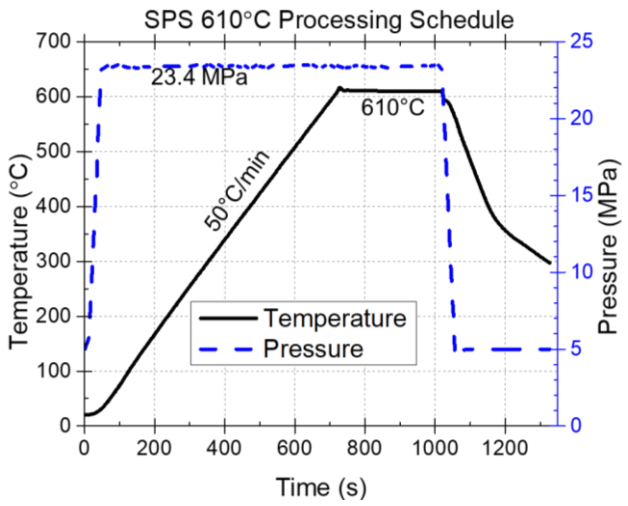

Figure 2.5. Standard temperature and pressure profiles for the SPS samples with hold temperatures of 610°C.

2.4 Sample Preparation for Characterization

2.4.1 Polishing

Samples were polished using silicon carbide grit paper (180-1200 grit) and alumina slurries (1 µm-0.05 µm) to prepare them for microscopy analysis. In cases where samples had cracks or chips before electrical testing had been conducted, such samples were sectioned using an Isomet 1000 precision saw (Buehler, Lake Bluff, IL) such that the remaining section's area could be easily calculated. Thus, the geometric capacitance of the sample could be determined more accurately, and issues in the electrical data due to internal breaks in the microstructure could be avoided.

2.4.2 Electrode Deposition

Before electrical characterization, electrodes had to be deposited on the sample surfaces perpendicular to the direction of intended current flow. For dense sample sets, silver (99.9% nominal purity) was sputtered onto the samples using a Denton Vacuum Desk II Turbo Sputter Coater (Denton Vacuum, Moorestown, NJ) to act as the contact electrodes. In the case of sample sets with porous samples, silver paint (Structure Probe Inc., West Chester, PA) was applied to each face, allowing the paint on each side to dry overnight. The samples were tested shortly after applying the electrodes to avoid any aging effects on the electrical data. It was necessary to use the same electrode deposition method for all samples within a set because sputtering produced a high purity, dense electrode, whereas the paint contains only 43% silver solids, and thus results in higher measured resistivity for the same sample.

2.5 Characterization Methods

2.5.1 Density

The densities of the sample sets showing no residual porosity were determined using the Archimedes method with distilled water. This method involves making two mass measurements for each sample using the same balance; one is conducted with the dry sample on top of the balance and one is conducted with the sample suspended below the balance and submerged in water. The temperature of the water is determined using a thermometer or thermocouple submerged in the water. With this data, the experimental density can be calculated through the formula

$$\rho = T\frac{M_d}{M_d - M_w} \tag{2.1}$$

where ρ is the experimental density in grams per cubic centimeter, T is the density of water at the measured temperature, M_d is the dry mass of the sample, and M_w is the mass measured when the sample was submerged in the water. For the hot-pressed samples and the UA SPS samples, Archimedes testing was conducted on-site, whereas for the TT and GT SPS samples, testing was conducted using equipment at the MILL facility at Georgia Tech. For sample sets with porous samples, the Archimedes method could not be used effectively due to the displacement of the air within the pores when submerged in water, so densities were calculated geometrically by measuring the dimensions and mass of each sample. The thickness and diameter of each sample was determined by averaging 4 measurements of each parameter on different areas of the sample, where each measurement was made using Etalon digital calipers (Etalon AG, Switzerland) with accuracy to 1 µm. The sample masses were measured using a Mettler AE 200 balance (Mettler-Toledo LLC, Columbus, OH) with accuracy to 100 µg.

2.5.2 Optical Microscopy

Low-magnification optical images were taken using the camera on an Iphone 5S to compare samples based on appearance and a background with a Georgia Tech logo was used to provide qualitative information on the translucency of each sample. Higher-magnification optical images were captured using a Celestron Pentaview LCD digital microscope, particularly for the more translucent SPS samples and for the as-received glass powder.

2.5.3 TGA/DSC

Thermogravimetric analysis (TGA) and differential scanning calorimetry (DSC) were conducted simultaneously on select powders and small sintered pieces using a Q600 SDT Simultaneous Thermal Analyzer (TA Instruments, New Castle, DE) (Figure 2.6).[40] A powder or solid sample with a mass between 10 and 20 mg is placed in a 90 μl alumina crucible at the end of a beam within a furnace. As the temperature is changed, the mass is continually measured with a balance mechanism and the temperature of the powder is continuously measured by a thermocouple which runs through the beam and ends just under the sample crucible. Data is compared with that of an empty sample crucible tested at the same time so temperature and weight change effects from the crucible can be removed. The temperature profile for a typical test consisted of a temperature ramp at a constant rate from room temperature to the desired maximum temperature, followed by a hold at the maximum temperature then a cooldown period. During the entire procedure, a purge gas, which could be compressed air, N_2, or argon, is passed through the furnace chamber at a constant rate of 100 ml/min.

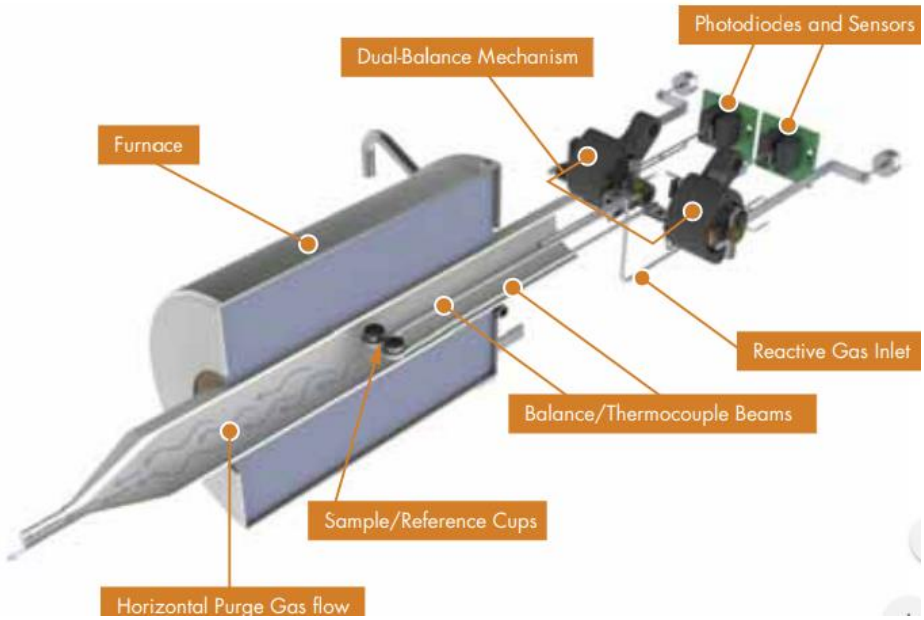

Figure 2.6.[40] Diagram of the TGA/DSC equipment used in this work. The sample and reference crucibles sit at the end of beams within the furnace. As the temperature is changed, a balance mechanism and thermocouples measure mass and temperature changes in the powder, thus providing TGA and DSC data, respectively.

The TGA data, which compares the mass vs the temperature, shows evidence of any chemical reactions in the sample material and the temperature at which they occur. These reactions will most commonly be decomposition of the sample material with the evolution of some gas, oxidation or reduction of the sample material, and evolution of gases from decomposition of impurities or evaporation of liquids such as adsorbed water.

The DSC data indicates heat flow into or out of the sample at each temperature. Changes in heat flow are often caused by phase changes or transitions in the sample material, such as the melting of a solid or a glass transition. For ceramic glass such as that used in the present study, DSC data should be able to show the glass transition temperature, the softening point, the crystallization temperature, and the melting temperature.

2.5.4 SEM

The microstructures of the ITO/glass composites were examined using a Hitachi S-3700N VP-SEM (Hitachi High Technologies America Inc., Dallas, TX). This equipment, a schematic of which is presented in Figure 2.7[41], has detectors for both secondary and backscattered electrons, and when detecting the backscattered electrons, can be run with a low pressure of N_2 gas flowing through the chamber. This gas flow is very helpful to reduce the detrimental effects of the buildup of surface charge on insulating samples because it enables some degree of discharging. This allowed for imaging of insulating samples without coating the surface with a conducting material, which would make the characterization less informative. Backscattered electrons result from elastic scattering of the incident electrons, which is stronger for phases with higher density, thereby giving phase-contrast, which can be very useful for composites characterization. Therefore, using the SEM equipment in backscatter mode with 30 Pa of flowing N_2 allowed for effective imaging of the topology of the uncoated samples while clearly distinguishing between ITO and glass regions. Other operating parameters used for this equipment were voltages ranging from 15 kV for conducting samples to 8 kV for some insulating samples, a probe current of 90 μA for optimal image resolution, and a sample-to-detector distance in the range of 4-10 mm, where samples experiencing more charging benefited from being further from the detector.

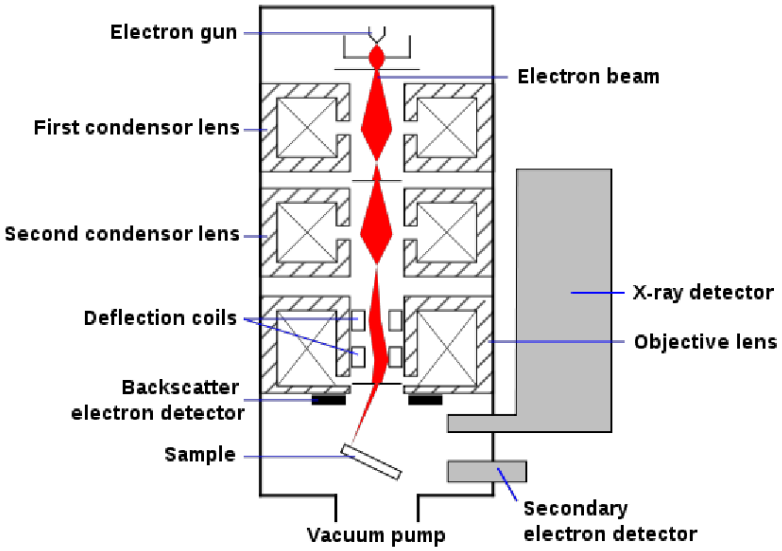

Figure 2.7.[41] Schematic of a typical SEM setup, showing the production and focusing of electrons, the interaction of electrons with the sample, and the detection of the scattered secondary electrons and backscattered electrons.

2.5.5 EDS

Using the same equipment, energy dispersive spectroscopy (EDS), in both 2D mapping and point identification modes, was employed to determine the compositions of various regions of each composite. EDS provides the relative concentrations of all elements detected within the current window of the detector and is based on the concept that the incident electrons excite atoms in the sample, which then emit a specific spectrum which is specific to each element (Figure 2.8).[42] Intensity data from the detector corresponding to different electromagnetic energies produce a set of peaks, which can then be compared to reference data for each element to find which element matches the observed peaks. All EDS data was acquired using an accelerating voltage of 15 kV and a sample-to-detector distance of 10 mm, which is required for proper functioning of the EDS detector.

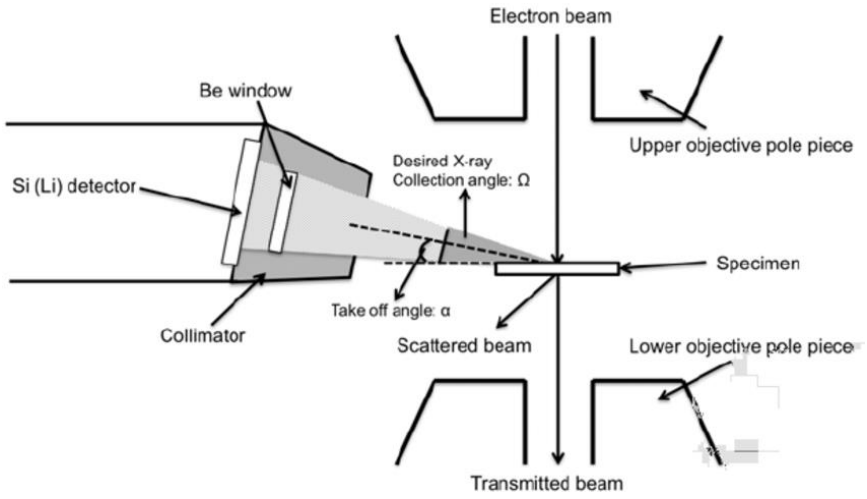

Figure 2.8.[42] Schematic of an EDS setup inside an SEM, where characteristic x-ray spectra specific to each element are measured by the detector. These x-ray signals are generated by the excitation of the electrons in the sample upon interaction with the incident electrons, which results in a subsequent relaxation of the excited electrons. The energy lost in the relaxation process, which is specific to each element and the type of relaxation, is emitted as the x-rays, which are then collected by the detector.

2.5.6 XRD

The composition data were supported with XRD data gathered using an X'Pert PRO Alpha-1 (PANalytical B. V.). In XRD, incident x-rays strike the surface of the sample using a range of different incident angles. The intensity of diffracted x-rays at each incident angle are then measured by a detector. A signal stronger than the background will only be detected at angles for which the x-rays scatter coherently. The condition for coherent scattering is given by Bragg's Law,

$$n\lambda = 2d * sin\theta \tag{2.2}$$

where λ is the wavelength of the incident x-rays, θ is the incident angle, and d is the distance between crystallographic planes in the sample material. From the schematic in Figure 2.9[43],

the basis for this relationship can be more clearly understood. Due to the dependence of the detected signal on this distance, which is specific to every material phase, the acquired spectrum can then be matched to a database of reference measurements to determine the phase(s) present in the sample.

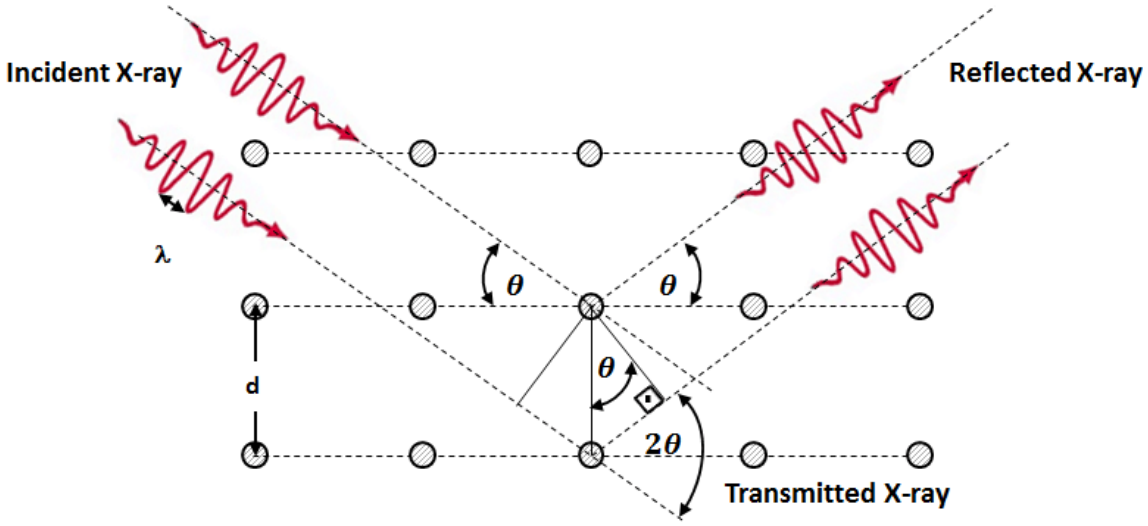

Figure 2.9.[43] Schematic showing how Bragg's Law defines the condition for coherent scattering of x-rays. The horizontal rows of dots represent the crystallographic planes of the sample material. The symbols in this schematic represent the same variables as in equation (2.2).

Typical equipment conditions used for XRD testing were a Cu Kα incident beam, a 0.04 radian Soller slit on the incident side, a 10 mm by 10 mm mask on the incident side, a divergence slit of 0.25 mm, an incident slit of 1 mm, and a 5-mm slit on the diffracted side.

2.5.7 UV-Vis

Measurement of the optical transmittance of the HP samples was conducted using a Cary 60 UV-Vis spectrophotometer (Agilent Technologies, Santa Clara, CA) over a

wavelength range 300- 800 nm. The basis of this test is to measure the transmittance of the incident light over a wavelength range encompassing the entire visible spectrum. The general test setup is shown in Figure 2.10[44], with the only difference in this work being the use of a solid sample holder which fixed the sample in place without obstructing the path of the light. Each wavelength is tested concurrently, and from this data, the light transmittance of different samples can be quantitatively compared. Furthermore, this test can be used to determine the effects of processing changes on the transmittance, such as the addition of an annealing step, by testing the same sample before and after the change. To facilitate a useful comparison between the samples, the clearest 0.0 phr sample in a given sample set was used as a baseline. Doing so set the absolute transmittance of the baseline sample at each wavelength as 100%, so all other samples' percent transmittances are relative to those of the baseline.

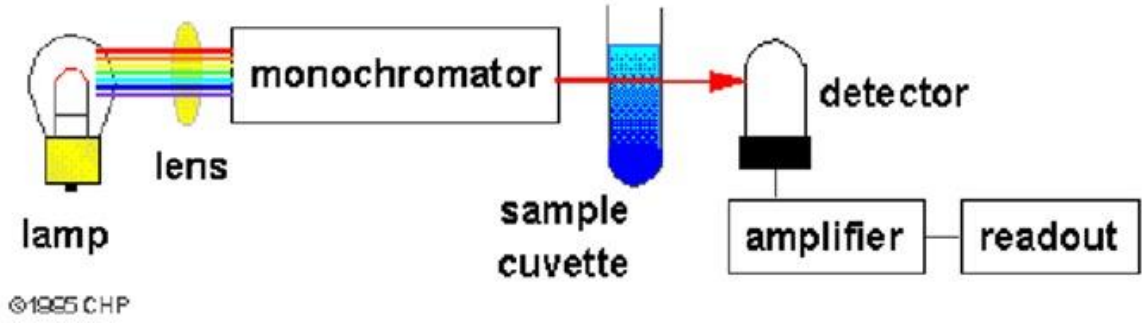

Figure 2.10.[44] Schematic of the UV-Vis process. In this work, the only difference is that solid samples are being tested, so a sample holder is used to position the sample within the equipment such that the signal can pass through it.

2.5.8 Ac Impedance Spectroscopy

Electrical characterization was performed using multiple equipment setups. The most commonly used setup was a Solartron 1260 analyzer in conjunction with a Solartron 1296

Dielectric Interface (Solartron Analytical,Farnborough, Hampshire, UK). Each frequency sweep covered a range 10 MHz-0.1 Hz under a constant ac voltage of 500 mV or 2V. To get more accurate data for conducting samples, such samples were also tested using the 1260 in standalone mode and/or with a Gamry Reference 5000e potentiostat (Gamry Instruments, Warminster, PA). Sintered samples were tested in a "parallel plate" arrangement test fixture, and for most tests, the electric field was applied parallel to the direction in which pressure had been applied during sintering (Figure 2.11). The resistivity of each sample was calculated from the impedance magnitude at the lowest measured frequency and geometric measurements of the sample, as done in previous work.[13] This entailed using the formula

$$\rho = R(\frac{A}{t}) \tag{2.3}$$

where ρ is the resistivity of the sample in Ω·cm, R is the resistance in Ω derived from the impedance magnitude data, A is the cross-sectional area of the sample perpendicular to the direction of the applied current, and t is the thickness sample parallel to the direction of applied current.

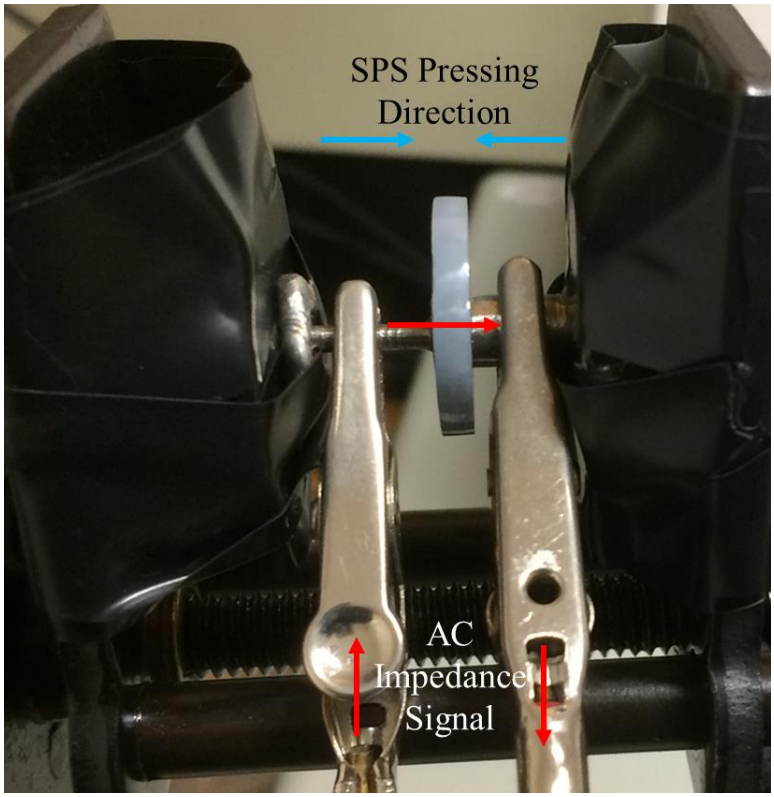

Figure 2.11. Test fixture for impedance measurements on the sintered samples in a parallel plate arrangement. The impedance signal passes through the alligator clips and the pins holding the sample on either side. The pins are electrically isolated from the rest of the test stand. Most testing was carried out on the samples in the pressing direction as indicated.

The testing process was similar for powders, where the only major differences were the addition of an electrically insulating die to contain the powder and the use of conductive punches to make electrical contact with the powder. The specific setup used for in-situ IS testing during powder compaction in Dr. Rosario Gerhardt's lab is shown in Figure 2.12. The thickness of the powder was determined from measurement of the displacement of the load frame or press which applied pressure to the powder.

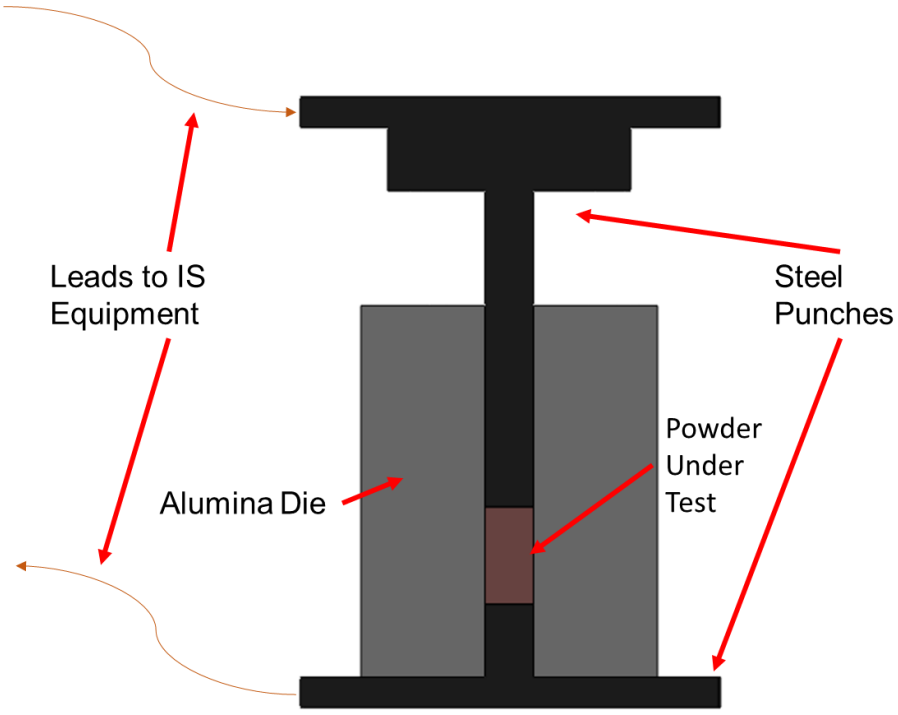

Figure 2.12. Schematic of the die assembly used to conduct in-situ IS testing during powder compaction.

In the case of the hot-pressed composite data, where multiple samples were produced at each composition, resistivity data is presented as an average, with error bars representing the range of 95% confidence as calculated through a bootstrapping process described and used by other authors.[45,46] For the present data, the confidence range was determined from the statistical analysis of 10000 simulated data sets.

Equivalent circuit fitting was carried out using the Z-View (Scribner Associates Inc.) software. A circuit model developed by a previous student[12] was used as a starting point for modeling all pre-percolation samples, as this model was proven to be effective for modeling similar conducting-filler composite samples. A model with fewer elements was used for fitting the percolated samples. Details of the various models will be presented in Chapter 6.

CHAPTER 3. CHARACTERIZATION OF POWDER COMPACTS AS A FUNCTION OF APPLIED PRESSURE AND GLASS-ITO COMPOSITION

3.1 In-situ IS procedure and setup

Mixed powders of each of the compositions given in Table 2.1, as well as the pure ITO nanopowder, were poured into a 10 mm ID polycrystalline alumina die, and stainless steel punches were inserted into either side of the die (Figure 2.12). This assembly was then placed into a Carver 3851 hydraulic press (Carver Inc., Wabash, IN), and leads from a Solartron 1296 dielectric interface connected to a Solartron 1260 impedance analyzer (Solartron Analytical, Farnborough, Hampshire, UK) were attached to the bases of the punches using alligator clips (Figure 3.1). This setup and testing procedure were initially developed through previous work in the Gerhardt group.[47] An initial 0 MPa test was carried out after manually raising the bottom platen of the press until the top punch made contact with the top platen, then running an impedance test. The impedance testing procedure was a frequency sweep from 10 MHz to 100 mHz, sampling at 10 points per decade under a constant ac voltage of 500 mV. Upon completion of each IS test, the load applied by the press was increased such that the applied pressure on the powder increased by 5 MPa, at which point the powder was given a couple of minutes to settle then the next IS test was conducted. This process was repeated up to a maximum applied pressure of 50 MPa.

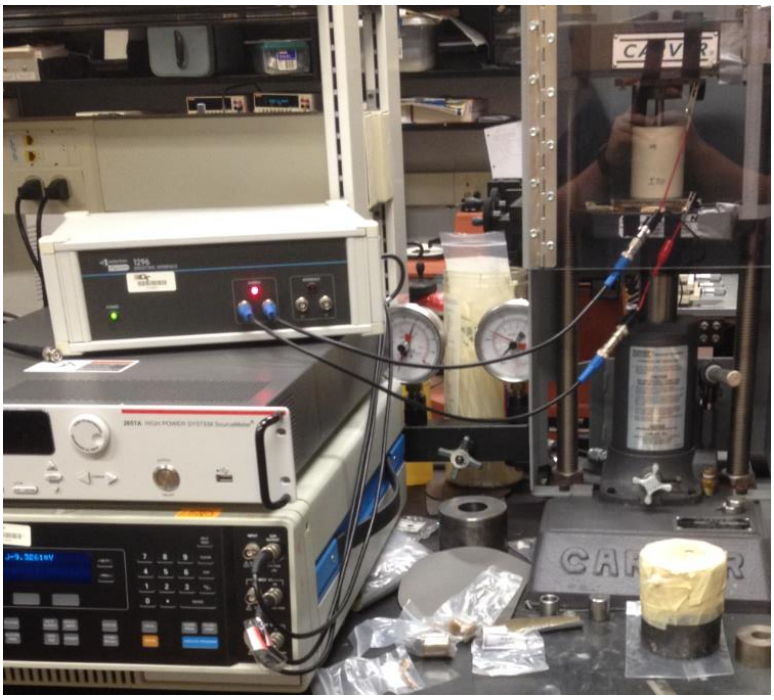

Figure 3.1. Test setup for in-situ IS during the compaction of borosilicate glass microsphere-ITO nanoparticle powder mixes. The Solartron 1260 and 1296 can be seen on the left, with wires extending from the 1296 to the stainless-steel punches within the Carver press on the right side of the image.

3.2 Effects of changing ITO concentration on electrical properties

Ac impedance testing was conducted on borosilicate-ITO powder mixes with a range of concentrations from 0.0 phr to 10.0 phr and a range of pressures from 0 MPa to 50 MPa. Figure 3.2 (a-c) shows complex impedance data over the range of powder compositions at a constant applied pressure of 50 MPa, with each plot showing a different scale on the same plot. The trend seen here, which was characteristic for all plots of all compositions under constant pressure, shows a gradual, sequential decrease in impedance with increasing ITO concentration, with a total decrease of over 5 orders of magnitude between the 0.0 and 10.0 phr powders. Since the ITO is electrically conductive while the glass is not, the decrease in impedance with increasing ITO concentration was expected. The conductivity of the

ITO itself can be seen in Figure 3.2 (d), where the positive Z'' values indicate a combination of inductive and resistive behavior typical of electrical conductors.[8] This is also evident in the impedance magnitude (Figure 3.2 (e)), which shows a value of approximately 2 Ω. Although the complex impedance data cannot all be seen in the same plot window, the complex plots preserve finer details in the data which the impedance magnitude and phase angle (Figure 3.2(f)) lose, so making observations based on all of these plots was important.

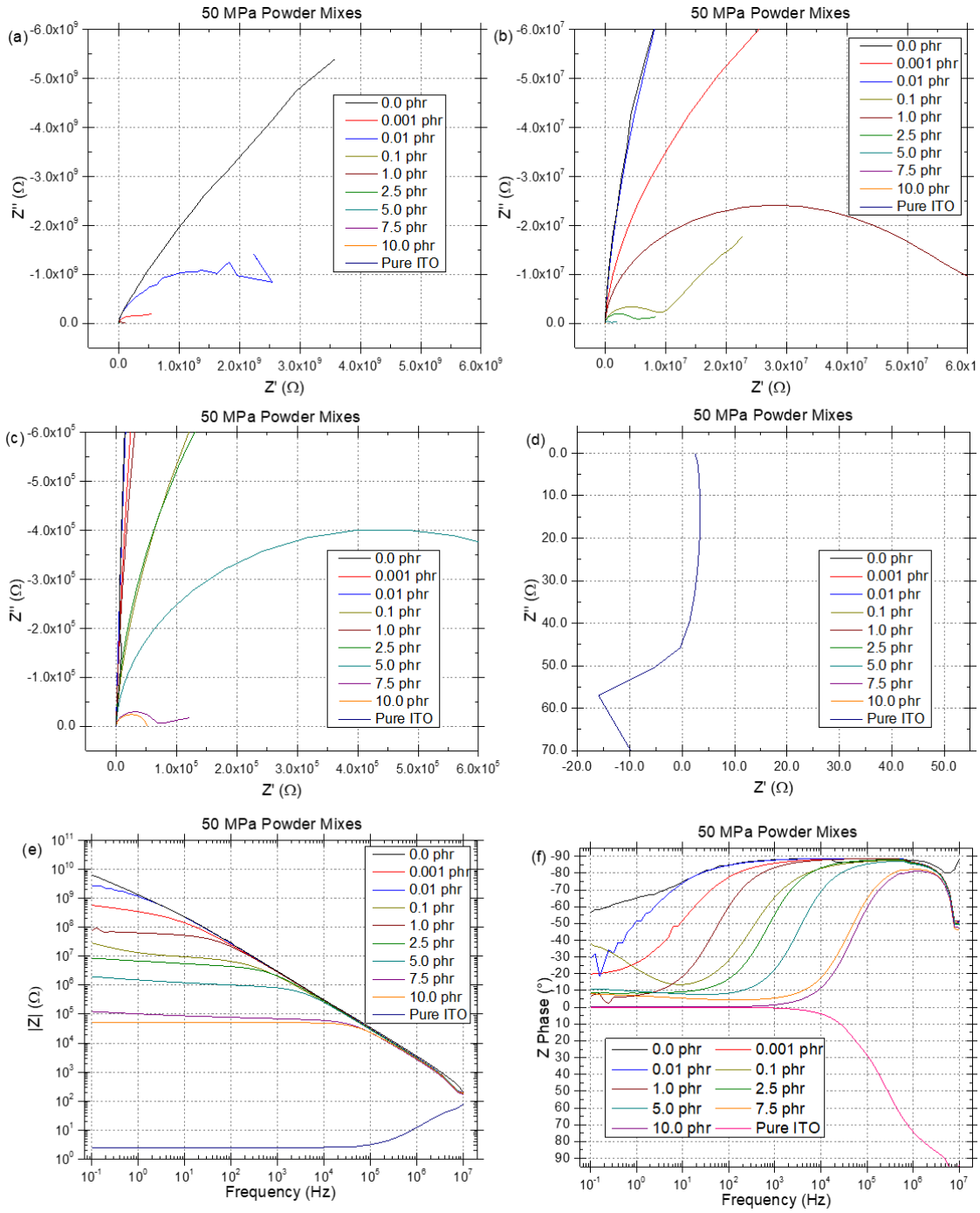

Figure 3.2. Plots of the (a-d) complex impedance, (e) impedance magnitude, and (f) impedance phase angle data from borosilicate-ITO powders made with a range of ITO concentrations under a consistent uniaxial pressure of 50 MPa. To be able to see all of the data, (a) shows the largest curves, (b) is a zoomed in window of (a), (c) is a zoomed in window of (b), and (d) shows the small curve of the pure ITO.

Resistivity values for each powder were derived as explained in the experimental methods chapter, section 2.5.8, and are presented in Figure 3.3. Like the impedance magnitude trend, the resistivity data show a general trend of decreasing resistivity with increasing ITO concentration. The pure glass resistivity value of just under 10^{10} Ω·cm was significantly less than the expected value for the glass of around 10^{12} Ω·cm. However, this was not unexpected since silica-based glasses are well known to be hydrophilic[48], and adsorbed water strongly affects electrical behavior[49], particularly in insulating samples. Furthermore, since these materials are in powder form, the surface area available for adsorption is large, especially for the ITO nanopowder, allowing more water to incorporate into the powder compact.

The resistivities at high ITO concentrations, except for the pure ITO, remained relatively large compared to the values from samples of the same composition subjected to different sintering procedures, as will be discussed in CHAPTER 4. Additionally, a dramatic drop, indicative of percolation, is not seen until reaching the pure ITO. Both of these behaviors come about due to the low relative densities of the powder in comparison to the sintered samples, which makes the formation of complete ITO particle networks far more difficult.

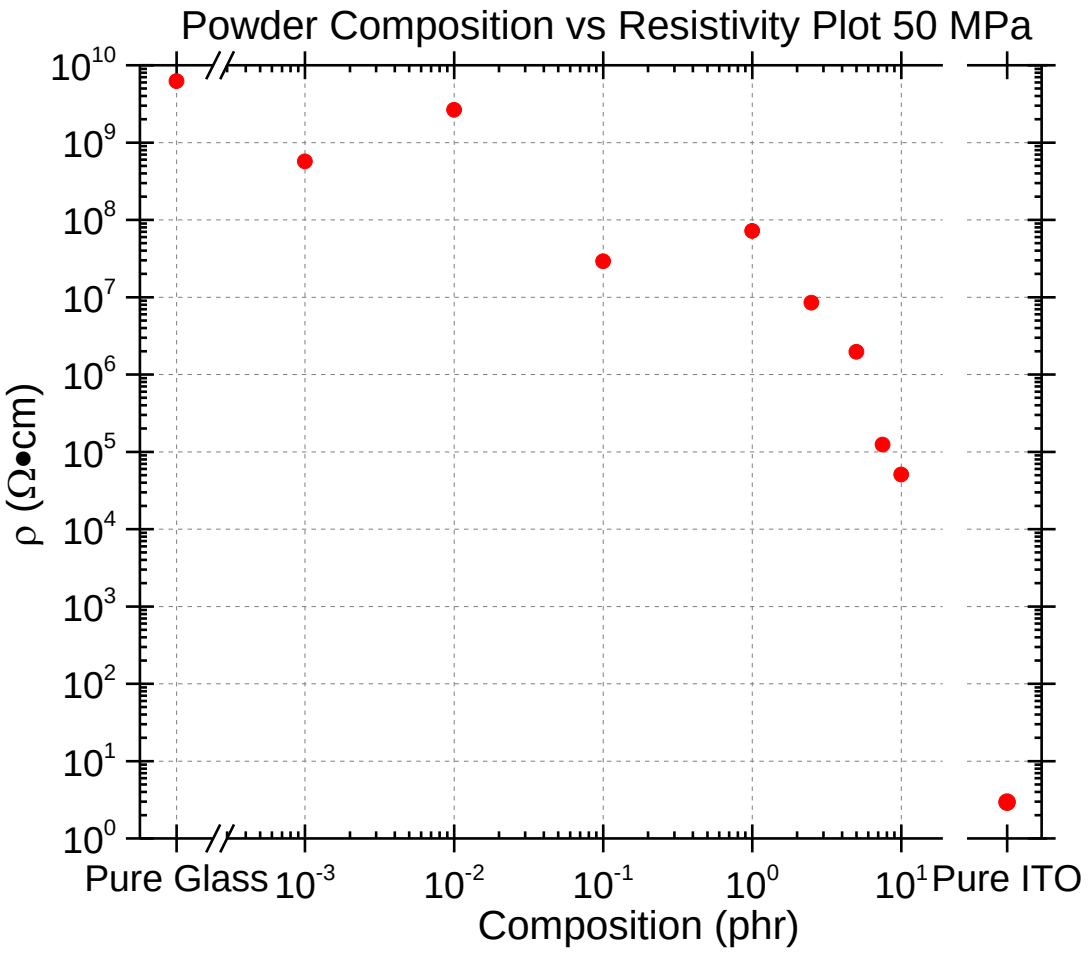

Figure 3.3. The resistivities of all powder compositions, including the pure constituent powders, as a function of composition.

Equivalent circuit fitting parameter values are presented in Figure 3.4. The appropriate model was found to be the same as had been found previously for ATO-borosilicate glass powder mixtures.[12] Detailed explanation of the development of the model, the determination of what parameters to hold constant, justification for changes in the model over the studied ITO concentration range, assignment of the parts equivalent circuit to microstructural phenomena in the samples, and analysis of the trends in the element values will be addressed in CHAPTER 6.

Composition (phr)	L-ITO (H)	R-ITO (Ω)	$R_{ITO\text{-}Grain1}$ (Ω)	$CPE_{T\text{-}Grain1}$ (F)	$CPE_{P\text{-}Grain1}$	$R_{ITO\text{-}Grain2}$ (Ω)	$CPE_{T\text{-}Grain2}$ (F)	$CPE_{P\text{-}Grain2}$	R_{Glass} (Ω)	$CPE_{T\text{-}Glass}$ (F)	$CPE_{P\text{-}Glass}$
Pure Glass	N.A.	N.A.	2.72E+08	2.91E-11	1.00	2.87E+10	1.55E-10	0.69	4.21E+14	4.50E-11	1.00
0.001	4.75E-07	6.07	5.86E+07	7.78E-11	1.00	1.02E+09	1.19E-09	0.38	4.21E+14	5.18E-11	1.00
0.01	4.75E-07	6.07	1.88E+08	5.16E-11	1.00	3.96E+09	1.97E-10	0.56	4.21E+14	5.03E-11	1.00
0.1	4.75E-07	6.07	3.39E+07	5.39E-08	1.00	1.44E+07	8.58E-09	0.34	4.21E+14	5.57E-11	1.00
1	4.75E-07	6.07	1.80E+07	2.59E-11	1.00	5.85E+07	2.41E-09	0.37	4.21E+14	5.07E-11	1.00
2.5	4.75E-07	6.07	1.47E+06	2.86E-11	1.00	2.05E+07	1.01E-07	0.16	4.21E+14	5.22E-11	1.00
5	4.75E-07	6.07	5.17E+05	1.30E-11	1.00	9.23E+06	6.39E-07	0.17	4.21E+14	5.03E-11	1.00
7.5	4.75E-07	6.07	4.31E+04	1.83E-11	1.00	5.56E+06	1.32E-05	0.12	4.21E+14	5.16E-11	1.00
10	4.75E-07	6.07	3.84E+04	7.62E-11	1.00	1.27E+04	3.61E-09	0.81			

Figure 3.4. Equivalent circuit fitting model and corresponding element values of the impedance data for the different powder compositions subjected to 50 MPa applied pressure.

3.3 Effects of changing applied pressure on electrical properties

Figure 3.5 shows the complex impedance, impedance magnitude, and impedance phase angle for the same sample of 2.5 phr powder over the range of applied pressures. Although the changes are not nearly as large as those resulting from changing the ITO concentration, increasing the applied pressure resulted in a sequential decrease in impedance. Increasing the pressure on the powder was expected to improve the quality of the contacts between the powder particles, which would, therefore, allow an electric current to more easily traverse the powder bed. The data confirms the expected trend. Since the total change in impedance was far smaller than in the case of changing the ITO concentration, the complex plot (Figure 3.5 (a)) is able to show the changes elegantly, whereas the differences are far harder to see upon examination of the less-sensitive impedance magnitude (Figure 3.5 (b)) and phase angle (Figure 3.5 (c)) data.

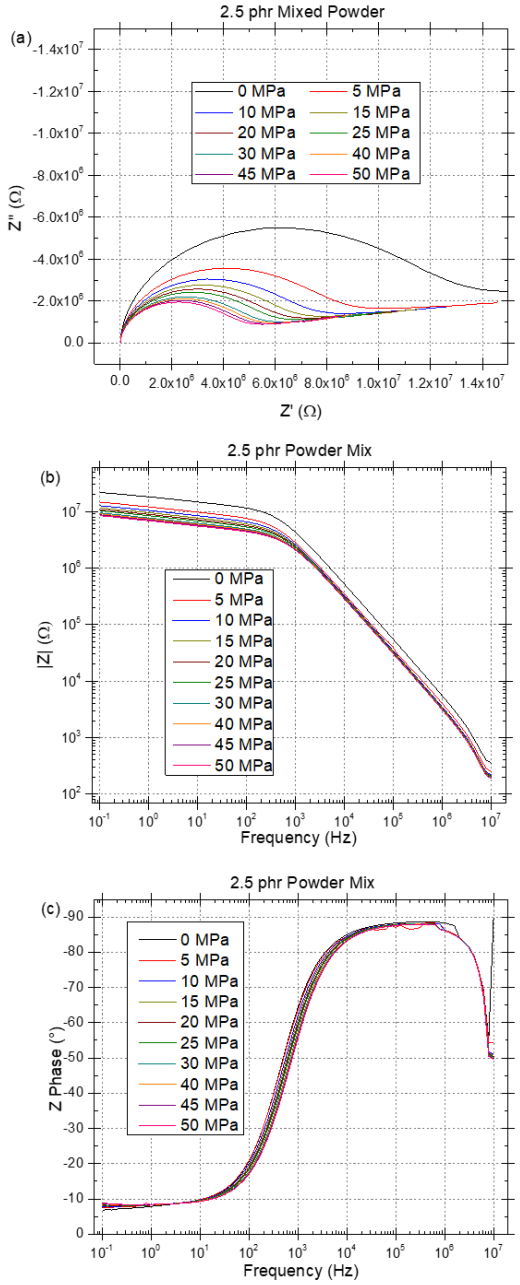

Figure 3.5. Plots of the (a) complex impedance, (b) impedance magnitude, and (c) impedance phase angle of the same sample of 2.5 phr mixed powder under different applied pressures.

The change in resistivity with changing applied pressure is shown in Figure 3.6. In this case, the resistivity does not change much over the range of applied pressures. However,

there is a consistent trend of decreasing resistivity with increasing pressure, as was also seen in the impedance magnitude data. This series of tests, among others measuring impedance during in-situ powder compaction, would lead to a similar setup and testing procedure becoming a core component in the development of a novel in-situ characterization technique combining ac impedance spectroscopy and small angle scattering methods during powder compaction. Details of this work are presented in Appendix A.

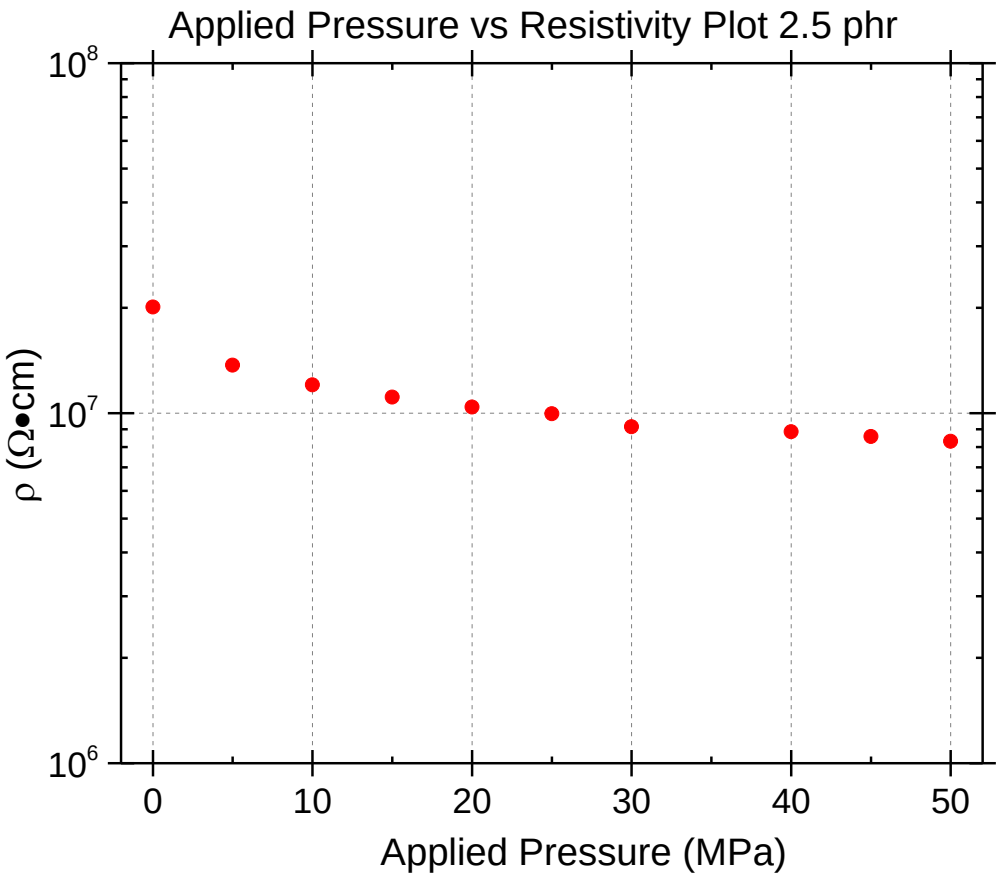

Figure 3.6. The calculated resistivity with respect to applied pressure for the 2.5 phr powder sample.

The impedance data from this series of tests was best fit to the same equivalent circuit model shown for the changing composition test series.[12] This is shown along with the corresponding circuit element values in Figure 3.7. The trends in the table will prove to be very similar to those of sintered samples made using different applied pressures, details of which are presented in CHAPTER 6, section 6.7. However, the effect of pressure changes on the electrical properties will prove to be more dramatic in those samples since the applied pressure increased the density of the sintered sample in addition to improving the

quality of the particle-particle contacts. A detailed analysis of the circuit fitting results and their relation to the sample microstructural features is provided in CHAPTER 6.

Pressure (MPa)	L-ITO (H)	R-ITO (Ω)	$R_{ITO\text{-}Grain1}$ (Ω)	$CPE_{T\text{-}Grain1}$ (F)	$CPE_{P\text{-}Grain1}$	$R_{ITO\text{-}Grain2}$ (Ω)	$CPE_{T\text{-}Grain2}$ (F)	$CPE_{P\text{-}Grain2}$	R_{Glass} (Ω)	$CPE_{T\text{-}Glass}$ (F)	$CPE_{P\text{-}Glass}$
0	4.75E-07	6.07	4.26E+06	1.16E-11	1.00	3.59E+07	3.19E-08	0.18	4.21E+14	2.89E-11	1.00
5	4.75E-07	6.07	1.78E+06	3.91E-11	1.00	3.59E+07	5.30E-08	0.14	4.21E+14	4.41E-11	1.00
10	4.75E-07	6.07	1.37E+06	5.01E-11	1.00	3.70E+07	6.49E-08	0.14	4.21E+14	4.71E-11	1.00
15	4.75E-07	6.07	1.96E+06	2.60E-11	1.00	2.39E+07	6.66E-08	0.16	4.21E+14	4.76E-11	1.00
20	4.75E-07	6.07	1.81E+06	2.72E-11	1.00	2.33E+07	7.27E-08	0.16	4.21E+14	4.87E-11	1.00
25	4.75E-07	6.07	1.71E+06	2.82E-11	1.00	2.29E+07	7.82E-08	0.16	4.21E+14	4.95E-11	1.00
30	4.75E-07	6.07	1.55E+06	2.99E-11	1.00	2.28E+07	8.91E-08	0.16	4.21E+14	5.08E-11	1.00
40	4.75E-07	6.07	1.48E+06	3.03E-11	1.00	2.23E+07	9.32E-08	0.15	4.21E+14	5.14E-11	1.00
45	4.75E-07	6.07	1.42E+06	3.14E-11	1.00	2.25E+07	9.87E-08	0.15	4.21E+14	5.20E-11	1.00
50	4.75E-07	6.07	1.37E+06	3.17E-11	1.00	2.25E+07	1.04E-07	0.15	4.21E+14	5.24E-11	1.00

Figure 3.7. Equivalent circuit fitting model and corresponding element values of the impedance data for the 2.5 phr powder over the pressure range of 0 - 50 MPa.

CHAPTER 4. COMPARISON OF THE HP AND SPS SINTERING METHODS

This chapter details the results of an investigation into the differences between ITO-borosilicate composites made using SPS to those made using HP. Data from the HP samples will be presented first, followed by SPS data, each in its own section. Then, the results are compared, leading to the conclusions of this investigation. The majority of the work presented in this chapter was published as a paper in the Journal of the American Ceramic Society[50].

4.1 Hot-pressed Sample Results

4.1.1 Optical and microstructural characterization

The original goal of this work was to compare the electrical and optical properties of hot-pressed ITO-borosilicate glass composites to those of hot-pressed ATO-borosilicate glass composites made by a previous student.[51,52] Toward this end, the processing parameters used for the HP samples were chosen based on those used previously; three 30 mm diameter samples were made at a time using 10g of powder in graphite foil–lined graphite dies in an atmosphere of flowing N_2. The uniaxial pressure ramped gradually to a maximum of 11.1 MPa over the course of the initial temperature ramp at 17.5 °C/min to 550°C. After a hold of 10 min, the temperature was ramped at 6°C/min to the final hold temperature of 610°C, followed by another 10 min hold at that temperature. The 11.1 MPa applied pressure was released after the equipment had cooled to 300°C/min after the final hold.

SEM characterization of the HP samples showed no visible residual porosity (Figure 4.1). It is also apparent that the glass formed a grain-like microstructure regardless of the ITO concentration, which is critical for segregated network formation. As expected, the microstructure is easier to see at the higher ITO concentrations due to the density contrast of BSE microscopy since the density of ITO is more than 3 times that of the borosilicate glass. Since the ITO shows up as white in the images, it is also clear that the ITO successfully segregated to the interparticle boundaries.

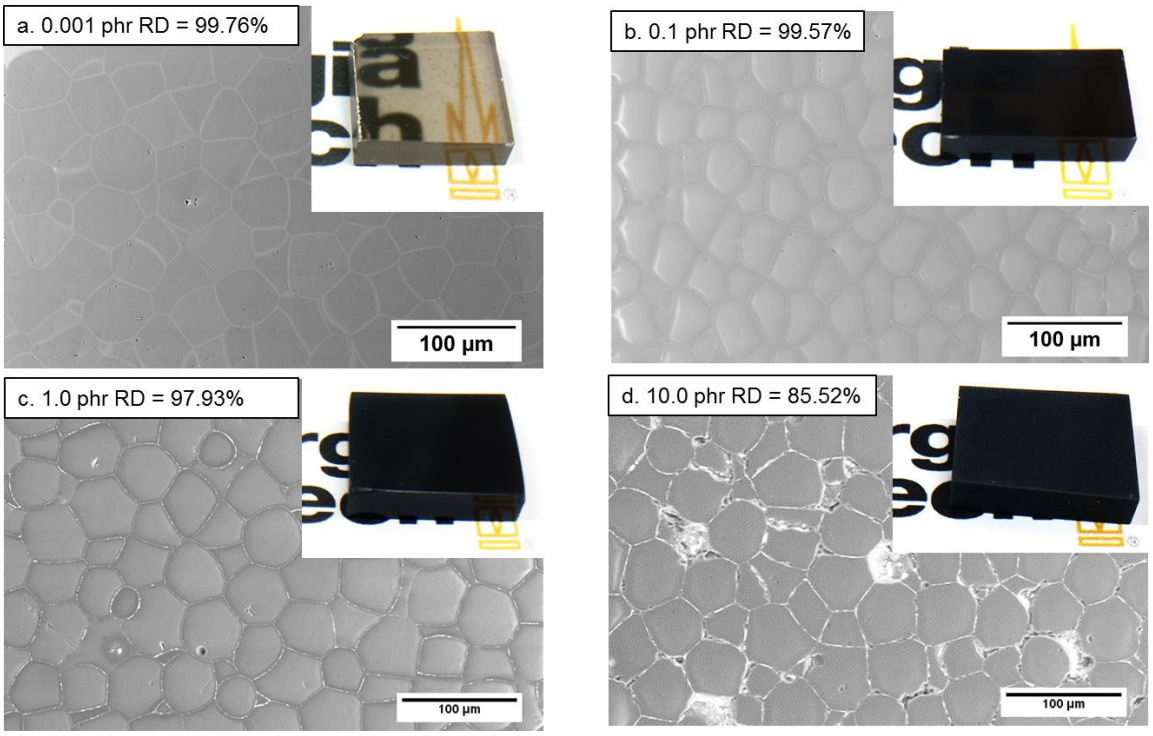

Figure 4.1.[50] SEM images of (a) 0.001 phr, (b) 0.1 phr, (c) 1.0 phr, and (d) 10.0 phr hot-pressed samples. No porosity can be seen in the interparticle boundaries, indicating the achievement of high relative density. The ITO, seen exclusively in the interparticle boundaries, appears white due to the density contrast of BSE microscopy. Insets show optical images of the respective samples, which show a rapid loss of translucency with increasing ITO concentration.

At the highest ITO concentrations, the microstructures show agglomerates of ITO and an uneven ITO distribution. This behavior is common for nanopowders and hinders the

formation of complete networks in the composites, resulting in a higher percolation threshold. An additional feature of many of the high-phr samples is pull-out of the ITO regions at the surface during the polishing process. This is responsible for the apparent porosity in some areas in Figure 4. (d) and indicates that the ITO regions are structurally weak.

Relative densities of the HP samples are given in the labels of Figure 4.1 (a-d) and in Table 4.1, which shows consistent, high density at low ITO concentrations. This high density began to deteriorate at 0.5 phr, at which point the relative density decreased with increasing ITO concentration. The decreasing relative density was accompanied by a loss of translucency, which is addressed in the following paragraphs.

Table 4.1.[50] Calculated Archimedes density data and relative densities for the HP samples

ITO Concentration (phr)	Theoretical Density (g/cm^3)	Average Experimental Density (g/cm^3)	Average Relative Density	Standard Deviation
0.0	2.20	2.19	99.68	0.10
0.001	2.20	2.20	99.75	0.01
0.01	2.20	2.20	99.75	0.01
0.1	2.21	2.20	99.59	0.01
0.5	2.23	2.20	98.86	0.02
1.0	2.25	2.20	97.99	0.08
1.75	2.29	2.21	96.70	0.02
2.5	2.32	2.21	95.41	0.04
5.0	2.44	2.23	91.45	0.10
7.5	2.55	2.25	88.51	0.09
10.0	2.65	2.27	85.55	0.06

The insets in Figure 4.1 show optical images of the same sample as the corresponding SEM images. These show a relatively high optical transmission at the lowest phr values, although a dark haziness is also present, as evidenced by the color change of the background. Since this darkness was also present in sintered glass samples containing no ITO (0 phr), and since graphite surrounded the sample from all sides, and since there are reports on carbon contamination during sintering in the literature[53], it was proposed that carbon contamination was the cause. The darkness was consistently more pronounced at the edge of the sample, forming a dark ring around the clearer center. This suggested that carbon diffused into the glass during the sintering process, rather than being inadvertently introduced into the powder before sintering.

The translucency dropped rapidly with increasing ITO concentration, and by 1.0 phr all samples were opaque. After this point, the color of the samples gradually became a lighter blue (Figure 4.1(d)). These patterns were observed in all sample sets, regardless of processing conditions, and are both related to the behavior of the ITO nanopowder under the conditions used for sintering. High-magnification SEM images of the ITO regions (Figure 4.2)[54] revealed that the nanopowder particles did not sinter to a noticeable degree, so the ITO regions were essentially still powder after the glass had sintered. This is not necessarily unexpected, considering that the few existing reports of ITO sintering in the literature generally used temperatures between 950 and 1200°C to achieve some degree of densification and in all cases, it has been found that ITO is difficult to sinter due to the propensity for decomposition and subsequent sublimation of In_2O_3 at elevated temperatures.[55,56]

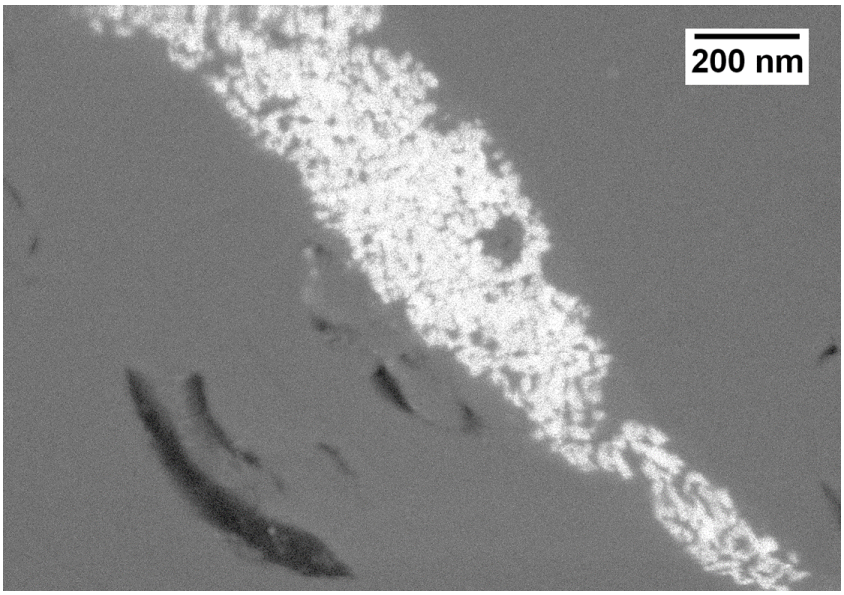

Figure 4.2.[54] SEM image at a high magnification, focused on one of the ITO regions between sintered glass particles. Clearly, the ITO does not consolidate within the glass under the sintering conditions used in this work, as individual powder particles can be distinguished all along these boundaries.

Since the ITO phase in the sintered samples has not densified, it causes a high degree of scattering due to frequent changes in refractive index and high curvature of the particle-pore interfaces due to the small particle size.[32] Therefore, it is evident that the loss in translucency with increasing ITO concentration is partially due to having a higher volume percent of highly scattering ITO phase within the microstructure. This would be expected since the density of the powder-like ITO regions are far less than the theoretical density of ITO, so the larger the volume percent of the ITO regions, the lower the density of the composite should be relative to the theoretical density. The color change with increasing ITO concentration is caused by reduction of the ITO. For all sintering techniques and equipment used in this work, graphite was used for the tooling and the foil at the interfaces, thereby requiring that all sintering be done in reducing atmospheres so as not to oxidize the graphite. The color of ITO is sensitive to oxidation and ranges from bright yellow when

fully oxidized to dark blue when reduced[57], so the blue seen in samples with high ITO concentration is from the reduced ITO. Some attempts were made to anneal samples in air after sintering to revert the color under the assumption that the lighter yellow of the oxidized ITO would be more conducive to improved translucency and that any carbon contamination could be removed via oxidation, forming CO or CO_2.[58] These were mostly unsuccessful, but the potential further research in this area is discussed in the future work section.

Closer optical inspection of the low-phr samples revealed a uniform distribution of small dark spots which were also found to be present in the as-received glass (Figure 4.3), and were ultimately attributed to impurity species including Ca, Mg, Na, Cl, Fe, and Zr. Attempts to remove impurities were not successful, and possible solutions are discussed in the future work section. The effects of this issue, along with the dark rings at the sample edges and the rapid decrease in translucency with increasing ITO concentration, were quantified using UV-Vis testing (Figure 4.4). In this data, the strong effect of the ITO concentration on the transmittance can be seen, with values approaching 0 at 0.1 phr and no transmittance at any wavelength by 1.0 phr. The effect of the glass impurities, ITO distribution in the test location, and/or carbon contamination manifest in the UV-Vis data as the large standard deviations in the 0.001 phr and 0.01 phr data. It is presumed that the higher phr samples would continue to show these large deviations if not for the transmittance becoming too small for the data to show these variations, as the features seen in the translucent samples which reduced the transmittance remain present in the higher-phr samples.

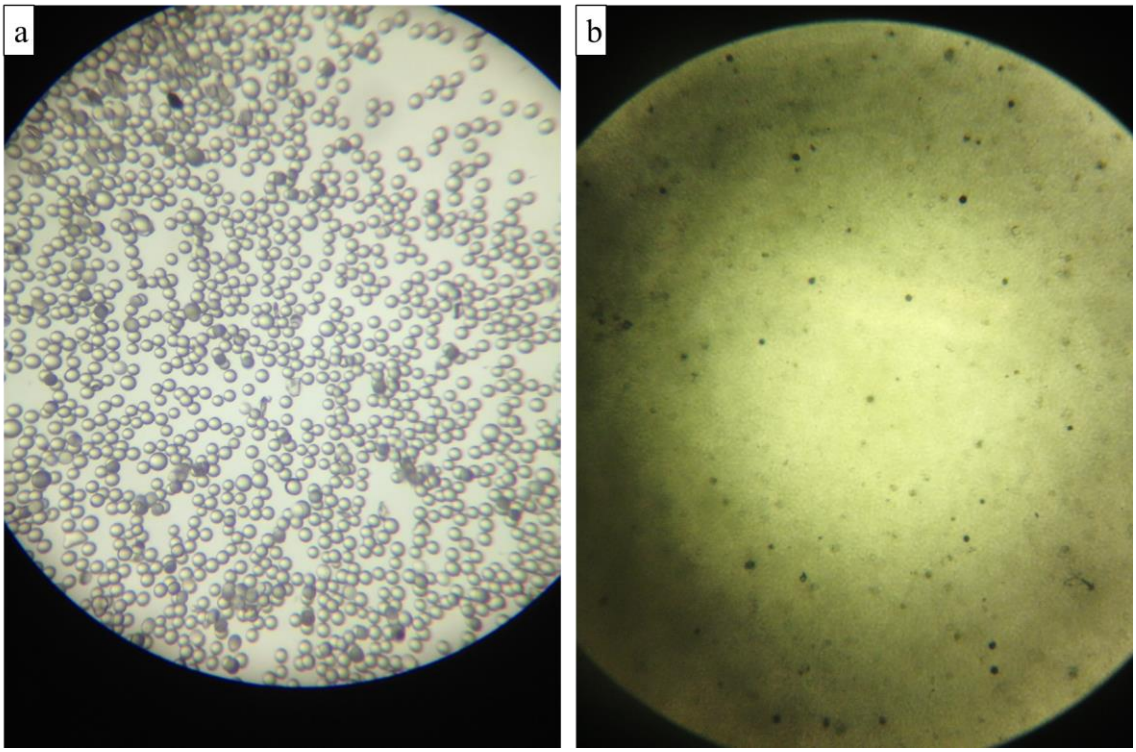

Figure 4.3. Optical images of (a) the as-received glass microspheres and (b) a 0.01 phr HP sample, both showing the presence of darker particles spread throughout. Based on this evidence, impurities and uniformity issues were identified as a significant factor contributing to light transmission loss in the samples with low ITO concentrations.

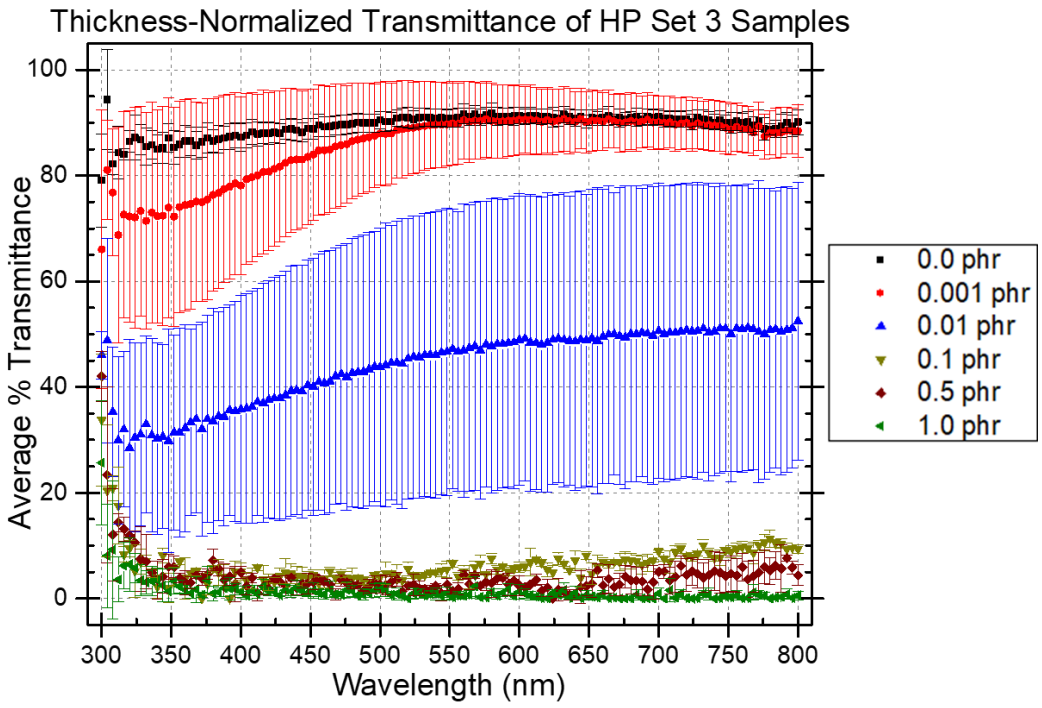

Figure 4.4.[54] UV-Vis data for HP samples over a range of compositions. Data points represent the average transmittance of the three samples made at each composition and error bars indicate the standard deviation between the data for the three samples. The transmittance dropped rapidly with increasing ITO concentration and became almost negligible at 0.1 phr, as observed in the earlier optical images (Figure 4.1). The combination of potential carbon contamination and impurities in the glass are responsible for the large standard deviations both between samples of the same composition and even for tests on different locations on the same sample.

To achieve the goal of a low percolation threshold, an additional requirement on the microstructure was to not develop anisotropy in the glass particles due to the uniaxial applied pressure, which would tend to break the ITO networks. Therefore, further microscopy was carried out on sample surfaces parallel to the direction of the applied pressure to determine the extent to which the pressure was inducing anisotropy in the glass under the chosen sintering conditions. The microstructures showed a low degree of anisotropy regardless of the ITO concentration (Figure 4.5) and the high phr samples

showed no elevated concentration of breaks in the networks even around the more isotropic particles.

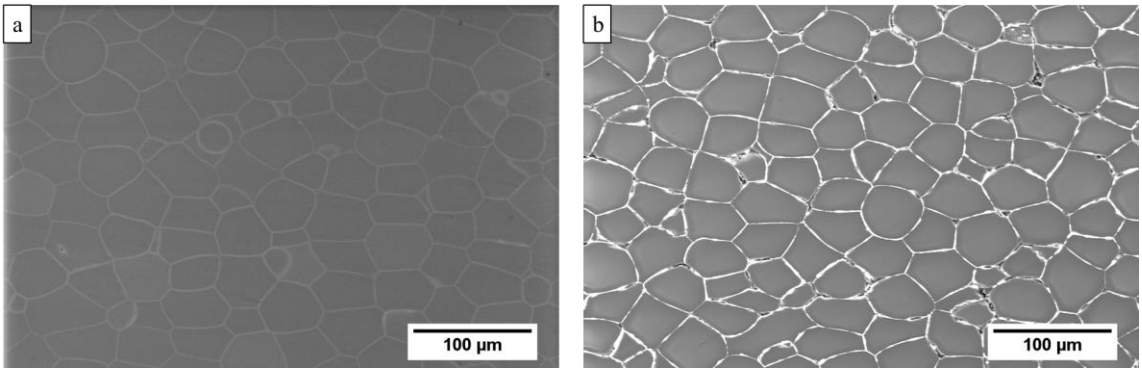

Figure 4.5. BSE images of the surfaces parallel to the direction of applied pressure for (a) 0.001 phr and (b) 10.0 phr samples. In each, the pressing direction is up and down, so any anisotropy in the glass particles resulting from sintering should manifest as preferential elongation along the left-right axis. In each case, a small preference is observed, but this does not seem to have disrupted the ITO network in the 10.0 phr sample.

4.1.2 Chemical and phase characterization

XRD data, presented in Figure 4.6, showed the emergence of ITO peaks beginning at around 0.5 phr, with peaks increasing in intensity relative to the background as the ITO concentration increased. Similar behaviour was observed in all sample sets, but only the HP data is presented in the figure. This trend is exactly as expected and indicates that the ITO did not experience any significant reactions, phase changes, or decomposition resulting from the sintering process. The borosilicate glass peak is at around 22° (2θ) for all samples, and such a single, broad peak is characteristic of amorphous phases. Since this peak was maintained in these samples, it was determined that the glass did not undergo devitrification under the implemented sintering conditions. No peaks were seen which could not be attributed to either the borosilicate glass or the ITO, so there were no

impurities or unintended phases presenting at high enough concentrations to emerge from the noise. However, the XRD equipment is not capable of detecting trace impurities or identifying where different phases are present in the sample since the data collection takes place over the entirety of the sample rather than localized regions of the sample.

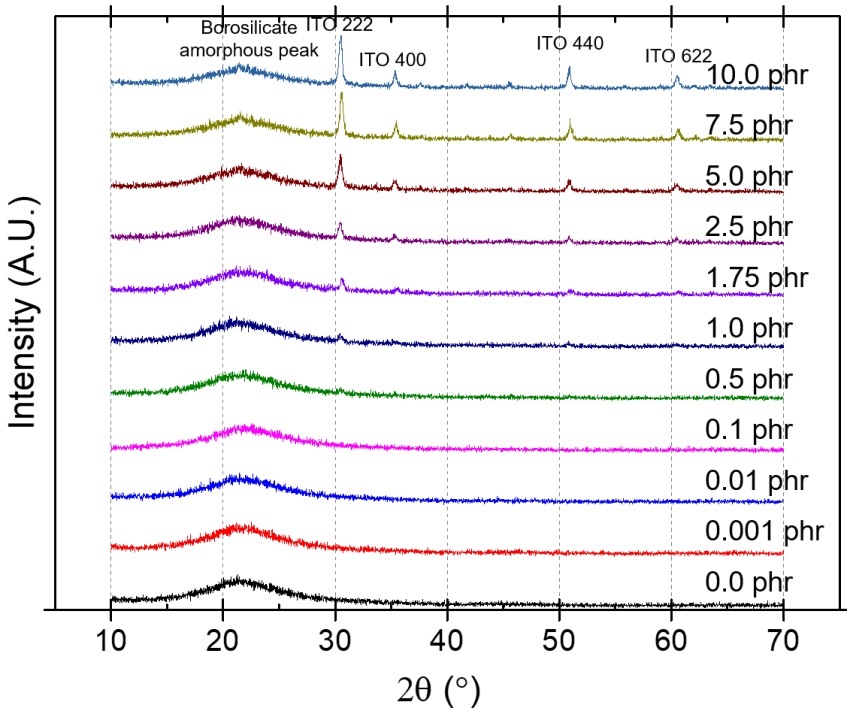

Figure 4.6.[50] XRD data for the hot-pressed samples. The broad borosilicate peak remains consistent for all ITO concentrations, whereas the ITO peaks begin to show at 0.5 phr and grow in relative intensity with increasing ITO concentration. All these trends are exactly as expected for the composites.

To get chemical information on local inhomogeneities in the microstructure and more sensitive detection of impurity species, EDS testing was conducted on a selection of samples with different ITO concentrations. In support of the BSE data, EDS verified that the vast majority of the ITO segregated to the boundaries between the sintered glass particles, as shown in Figure 4.7 (a,b) for a 1.75 phr sample.

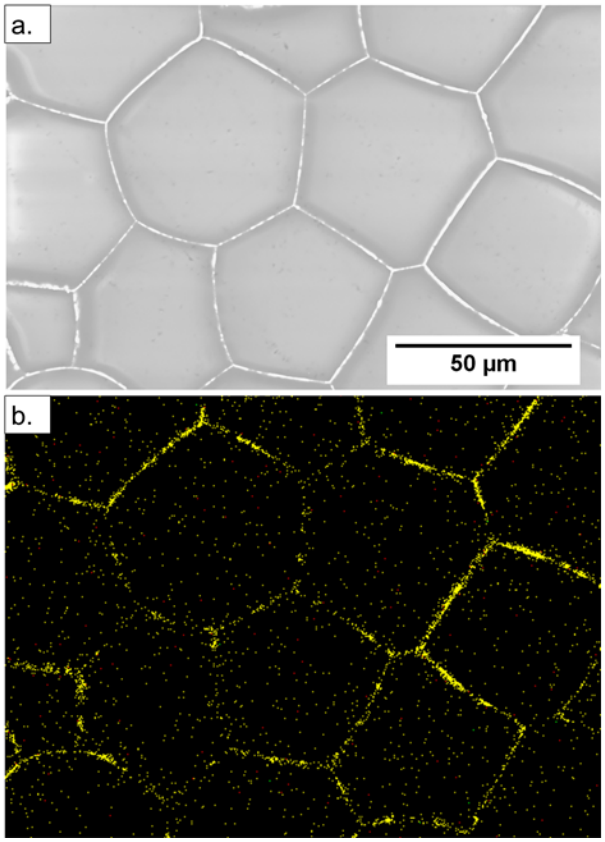

c.

Element	Weight%	Atomic%
O	60.32	72.75
Na	1.93	1.62
Al	1.16	0.83
Si	35.95	24.70
In	0.63	0.11

Figure 4.7.[50] (a) BSE image and (b) indium EDS map of the same area of a 1.75 phr HP sample. The ITO has clearly segregated to the boundaries between the glass regions, as almost all of the indium is found in these regions. Relative concentrations of each element detected within this sample window are shown in (c).

From the corresponding chemical composition data (Figure 4.7 (c)), only O, Si, Na, Al, and In were identified, despite a measurement range as low as 0.01% by either weight or atomic percent. It is important to note here that boron cannot be detected by EDS due to its very low atomic number, although other EDS tests proved that the equipment could detect carbon. This explains the absence of boron in the data, and the detectability of carbon means that the sample area did not contain any significant carbon concentration.

4.1.3 Electrical Characterization

Ac impedance data of the HP samples indicated a percolation threshold between 0.5 and 1.0 phr, which is seen in the impedance magnitude data (Figure 4.8 (a)) as a decrease in the low-frequency magnitude of approximately 7 orders of magnitude and in the phase angle data (Figure 4.8 (b)) as a shift from negative to positive values. After reaching percolation, further addition of ITO mildly decreased the impedance by improving the number and quality of contacts between ITO particles, thus improving the quality of the percolated network.[2] Close inspection of the pre-percolation curves reveals an inconsistent relationship between the ITO concentration and the low-frequency impedance data, whereas the post-percolation data show a consistent trend of decreasing impedance with increasing ITO concentration. This pre-percolation phenomenon was present in all sample sets regardless of the sintering conditions or sintering method. Since the pre-percolation data show similar impedance values over the entire frequency range, the non-sequential order of the curves is likely a result of the sensitivity of the impedance measurements to a multitude of factors which could have differed over the course of fabricating the samples. Such factors include small differences in the processing parameters experienced by the samples arising from the accuracy limits of the various equipment, variation in the distribution of filler or electrically conductive contaminant particles between samples and/or within samples,[52,59] and changes in humidity between measurements.[49] The impedance responses of highly insulating samples are particularly sensitive to humidity and electrically-conducting contaminant effects, whereas composites near the percolation threshold are more sensitive to small variations in filler distribution, which can be the difference between a complete or broken ITO network. In addition to the

disordering of the impedance data with respect to ITO concentration, these factors also resulted in high variation in the data for different samples with the same powder composition, especially near the percolation threshold.[59,60]

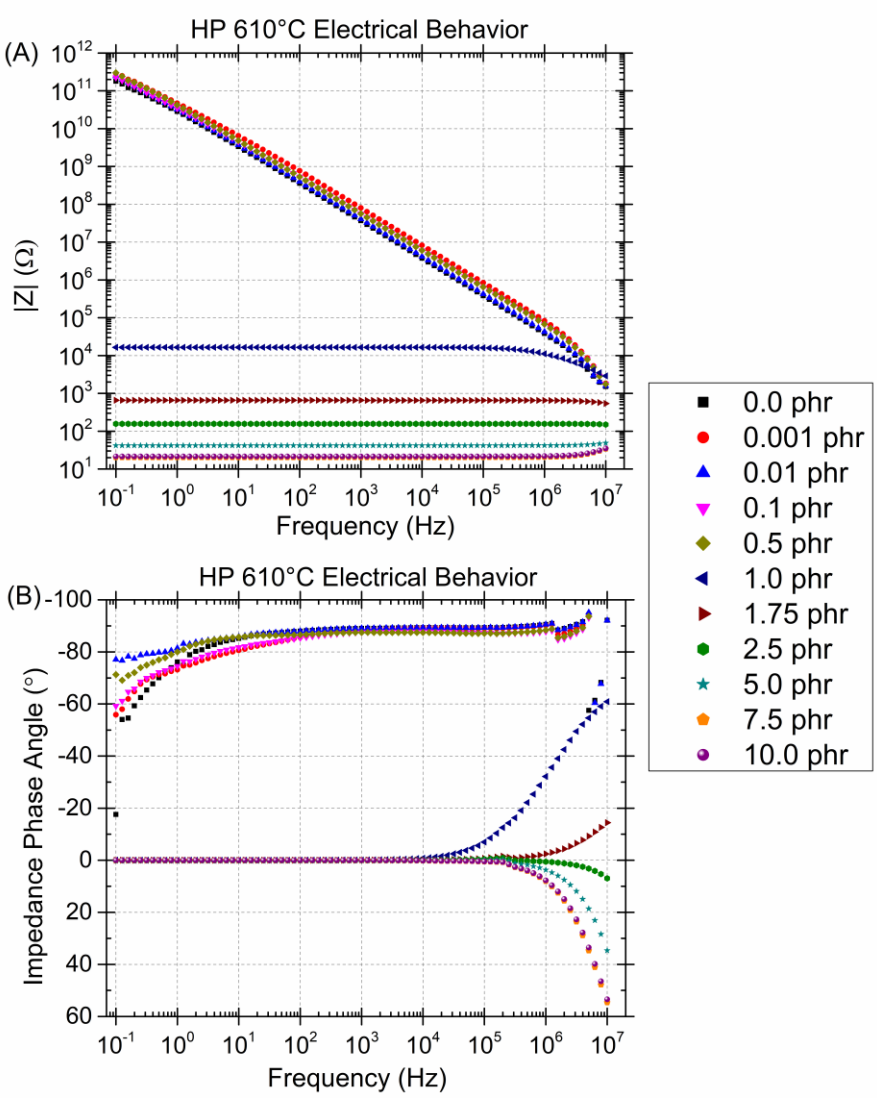

Figure 4.8.[50] (a) Impedance magnitude and (b) impedance phase angle data for the HP samples.5 The impedance magnitude data shows crossing of the percolation threshold between the 0.5 phr and 1.0 phr compositions as the dramatic difference of around 7 orders of magnitude between the respective data at low frequencies. This corresponds to a shift in the phase angle from negative to positive values, which indicates a shift from capacitive to inductive behavior, as would be expected upon achieving percolation.

The minimum impedance values of the HP sample set, on the order of 10^1 Ω, were achieved in the 10.0 ITO phr samples. These values indicated that the composites can attain good conductivity despite their small ITO concentrations, as 10 phr is equivalent to

approximately 3 volume percent ITO (Table 4.1). All the discussed trends in the electrical response mirror those seen in the previous work with ATO nanopowder-borosilicate microsphere composites,[51] indicating very similar densification behaviour in the two composite systems when produced via hot pressing.

4.2 SPS Results

4.2.1 Microstructural, optical, and density characterization

The first SPS sample set was made using the same powder mixes as the HP samples and processed under the conditions given in Section 2.3 using the UA equipment and a hold temperature of 610°C. The microstructures, presented in Figure 4.9, show significant porosity regardless of ITO concentration. Optical images showed no translucency in any samples except the 0.001 phr sample, and even that sample shows significant light scattering. This is unsurprising, since residual porosity scatters light very strongly.[32] The relative densities corroborate these observations (Table 4.2), with lower relative densities at every powder composition than the HP samples of the same composition, excepting the 5.0 phr sample density. Both this anomaly and the lack of a composition vs density trend in the samples until 2.5 phr were not anticipated, given the relatively sequential trend in the HP sample data. Since both the open porosity and the low-relative-density ITO phase both contribute to the overall relative density, the change in behaviour at high ITO concentrations may simply be due to a shift in the dominant contributing factor from open pores to the ITO phase, given that the effect of the ITO phase increases with increasing ITO concentration.

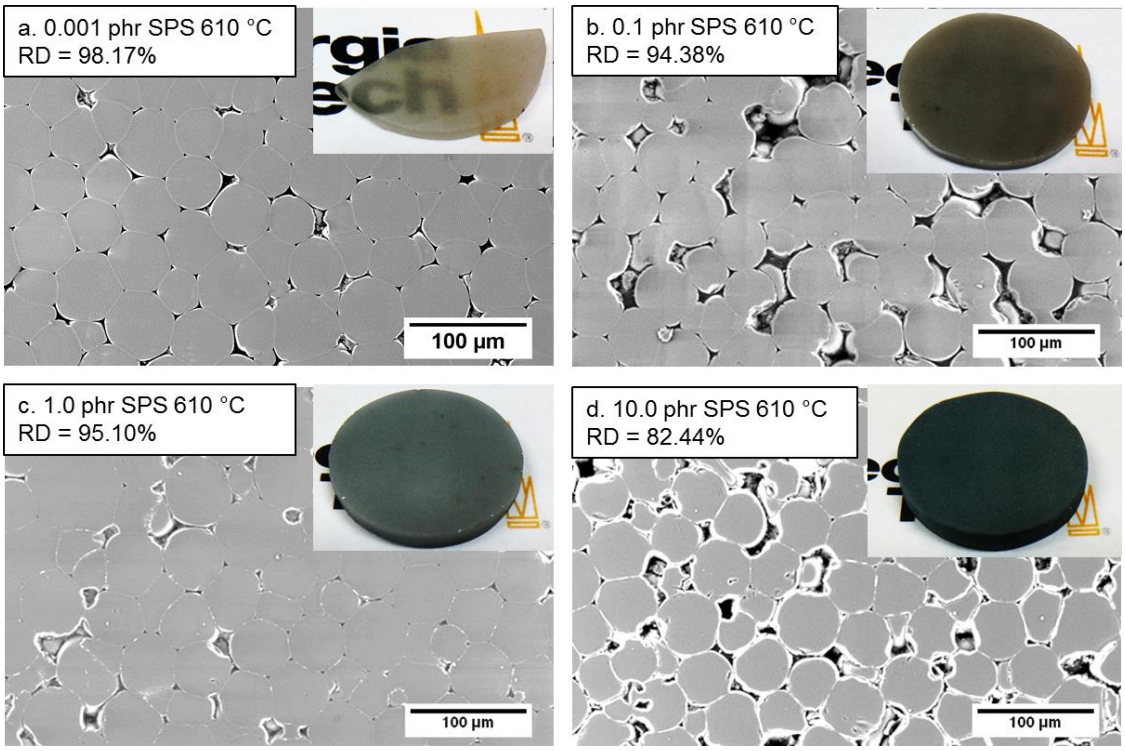

Figure 4.9.[50] BSE images of (a) 0.001 phr, (b) 0.1 phr, (c) 1.0 phr, and (d) 10.0 phr samples, all showing porosity throughout the microstructures. This is reflected quantitatively in the relative densities given in the labels of the respective samples.

Table 4.2.[50] Experimental and relative densities of the SPS 610°C samples

ITO Concentration (phr)	Theoretical Density (g/cm^3)	Experimental Density (g/cm^3)	Relative Density
0.001	2.20	2.16	98.17
0.01	2.20	2.04	92.68
0.1	2.21	2.08	94.38
0.5	2.23	2.08	93.48
1.0	2.25	2.14	95.10
2.5	2.32	2.24	96.41
5.0	2.44	2.17	88.98
7.5	2.55	2.18	85.55
10.0	2.65	2.18	82.44

Unfortunately, the nature of the SPS process complicates the matter, since it is plausible that the formation of a conducting network through the powder at percolation could affect the SPS process by providing an additional path for the current as it passes through the die. If some fraction of the current were to use such a path, the distribution of current around the powder compact would be altered, and it is not known how the sintering behaviour would be affected.[61,62] The effect of current flowing through the ITO network could be even more impactful; since Joule heating is the mechanism of heat generation in SPS, current through the ITO should generate strong localized Joule heating along the conducting network which, depending on the severity of the heating, could result in sintering or decomposition of the ITO, or to melting of the glass adjacent to the network.[61,62] However, the degree to which the ITO concentration affected the sintering behaviour itself could not be determined from the microstructural and density data alone, so analysis of the electrical behaviour of the composites was crucial to understanding how the nature of the SPS process affected the powder mixes to bring about the substantial microstructural differences.

4.2.2 Ac impedance spectroscopy characterization

The impedance magnitude and phase angle results (Figure 4.10 (a,b)) indicate a percolation threshold between 1.0 and 2.5 phr and a normal pattern of decreasing impedance with increasing ITO concentration for the post-percolation samples. Given the amount of residual porosity seen in the samples, it was somewhat surprising that the percolation threshold was not affected drastically, indicating that the ITO networks were able to remain intact despite the free space into which the ITO could fall and the permeability of the microstructure to air and water vapor which could thereby access the

ITO. Despite the similar percolation thresholds between these and the HP samples, the pre-percolation curves exhibit strange behaviour which was not observed in the data for the HP samples. The most noticeable differing feature is the phase angle beginning to move toward 0° at far higher frequencies and corresponding changes in the slopes of the magnitudes from negative to 0 at 1 Hz or even larger frequencies. The slope change occurred at different frequencies for the different samples, resulting in the lack of a pattern in the low-frequency impedances with respect to the compositions. An additional unexpected behaviour was a sudden increase in the slopes of the magnitudes in the 0.1 and 0.5 phr data with corresponding increases in the phase angles. In both of these phase angle curves there is an initial change towards 0° at intermediate frequencies followed by a plateau or even a small movement back towards -90°, and finally moving back toward 0° at the low frequencies. Such behaviour was not observed in any of the HP data and, notably, is seen in all pre-percolation SPS curves except for those of the 0.001 phr and 1.0 phr samples.

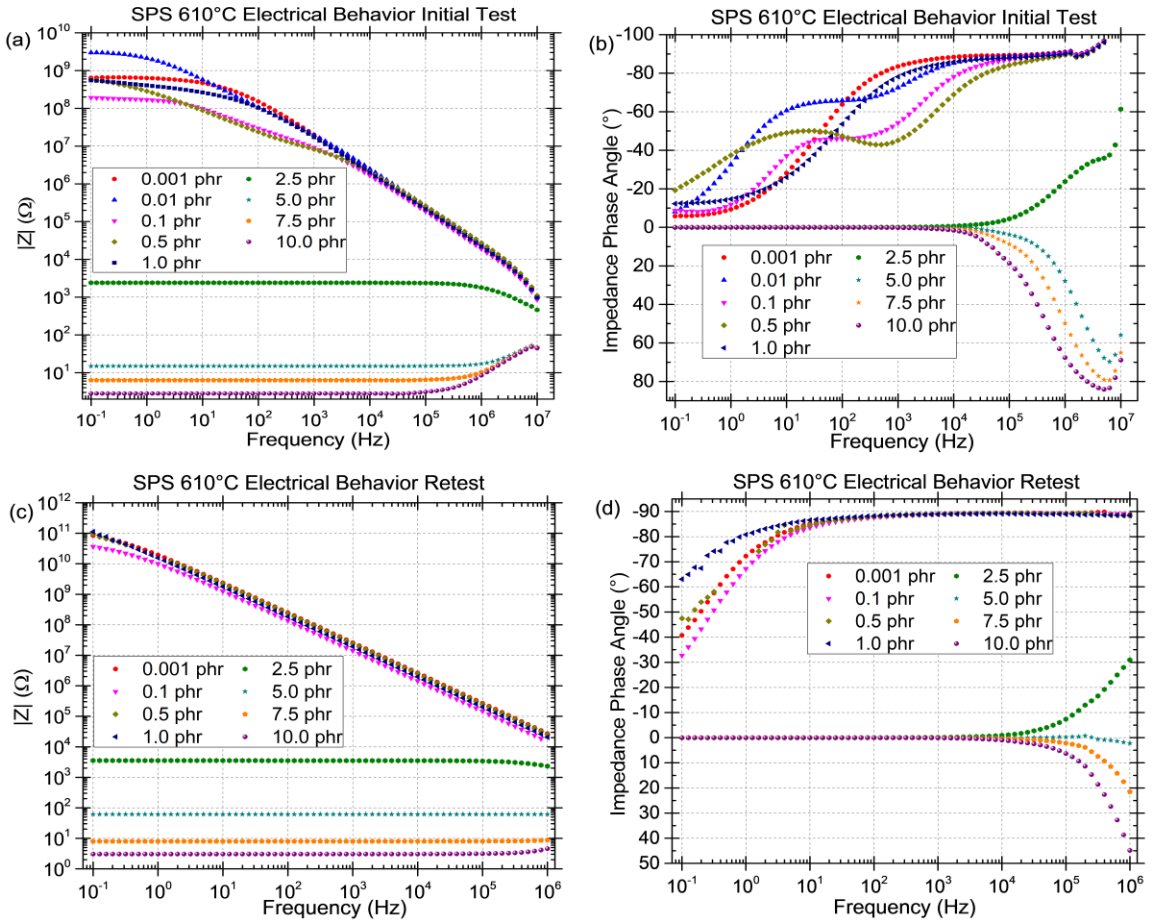

Figure 4.10.[50] Impedance magnitude and (b) phase angle plots for the SPS samples with a hold temperature of 610°C. The pre-percolation curves show a strange behavior not seen in other sample sets. However, a follow-up test conducted later gave similar (c) magnitude and (d) phase angle trends to the HP data. Percolation occurred between 1.0 and 2.5 phr.

The electrical testing of these samples was carried out soon after they were fabricated, whereas other sample sets were generally tested weeks to months after fabrication because other characterization methods had to be carried out before application of the silver electrodes. Therefore, the samples were retested at a later time to determine whether the difference in testing procedure was behind the difference in electrical data trends. Note that the 0.01 phr sample was damaged between the tests so there is no data for it in the retest. The retest results, shown in Figure 4.10 (c, d), were far more similar to those

of the HP samples (Figure 4.8) and the only major difference remaining between the data sets is the higher percolation threshold in the SPS set. The most logical explanations for the change in behaviour are either slow re-oxidation of the ITO or impurities in the glass, or elevated humidity during the initial testing. The retests were conducted at a low relative humidity of 16%. Since the behaviour did not become more pronounced as the ITO concentration increased, glass impurity oxidation and adsorbed water seem more likely to have caused the differences. The presence of the residual porosity observed in the microstructures (Figure 4.9) makes these samples more susceptible to humidity-related effects due to the increased surface area available to water adsorption, and the retests were carried out in a low-humidity environment, so this may be the most likely explanation.

A final set of impedance tests was conducted at 50% and 73% relative humidity conditions to try to differentiate between humidity and oxidation effects. The results, shown in Figure 4.11, shows that the behavior seen in the original tests most closely matches the 73% relative humidity behavior, but the impedance magnitudes are still smaller in the original tests. Therefore, it is concluded that either a very high relative humidity during testing or a high humidity in combination with oxidation of the ITO over time was responsible for the behavioural difference between the initial tests and the retests.

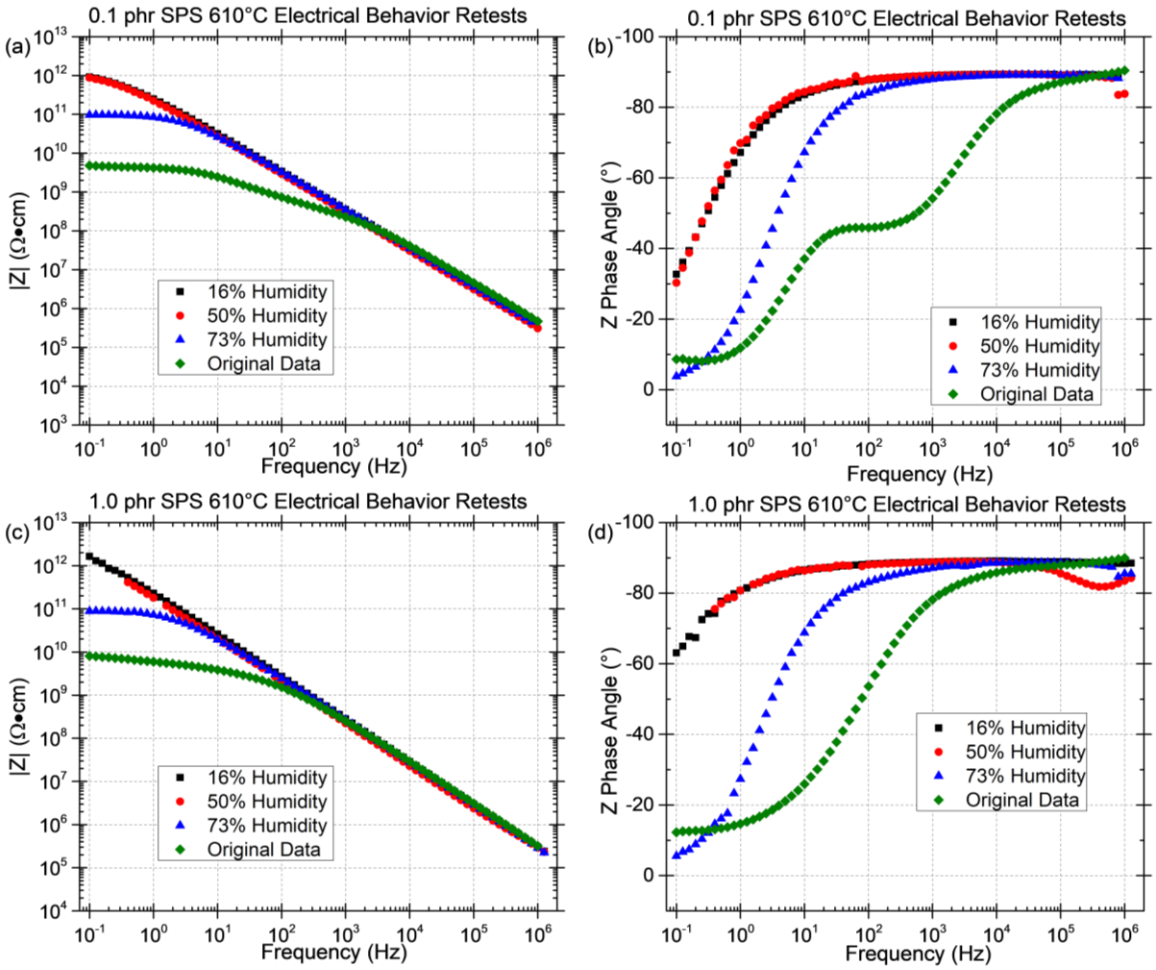

Figure 4.11. Ac impedance data for the SPS 610°C samples tested at relative humidities of 50% and 73%, along with the data from the initial tests and the retests (16% humidity). Results for the 0.1 phr impedance magnitude and phase angle as well as the 1.0 phr impedance magnitude and phase angle are shown in (a-d), respectively.

Further analysis of the impedance trends required equivalent circuit fitting, which will be addressed in CHAPTER 6.

4.3 Comparing the HP and SPS results

Although the HP and SPS samples with the same compositions showed clear differences in densification behaviour, the previous results could not definitively prove that

the differences were due solely to the differences between the HP and SPS processes since multiple process parameters differed between the two sample sets. In an attempt to isolate the effects of the differences between the two sintering methods, a 1.75 phr sample was made on the TT SPS equipment using conditions as close as possible to those used for the HP samples (see Section 2.2), with the same powder mixture, powder mass, sample diameter, hold temperatures, hold times, heating rates, applied pressure, and sintering atmosphere. As opposed to the relatively dense 1.75 phr HP samples (Figure 4.12 (a)), the SPS sample (Figure 4.12 (b)) was shockingly porous, with no visible evidence of deformation of the glass particles and a relative density far lower than any other sample made thus far. As shown in the insets, comparison of the appearances of the HP and SPS samples was equally dramatic, with the dense HP sample appearing dark and thin and the SPS sample appearing nearly white and very thick. Based on these observations, the effects of the two sintering methods on the sintering behaviour was revealed to be far greater than was originally thought based on the first SPS sample set.

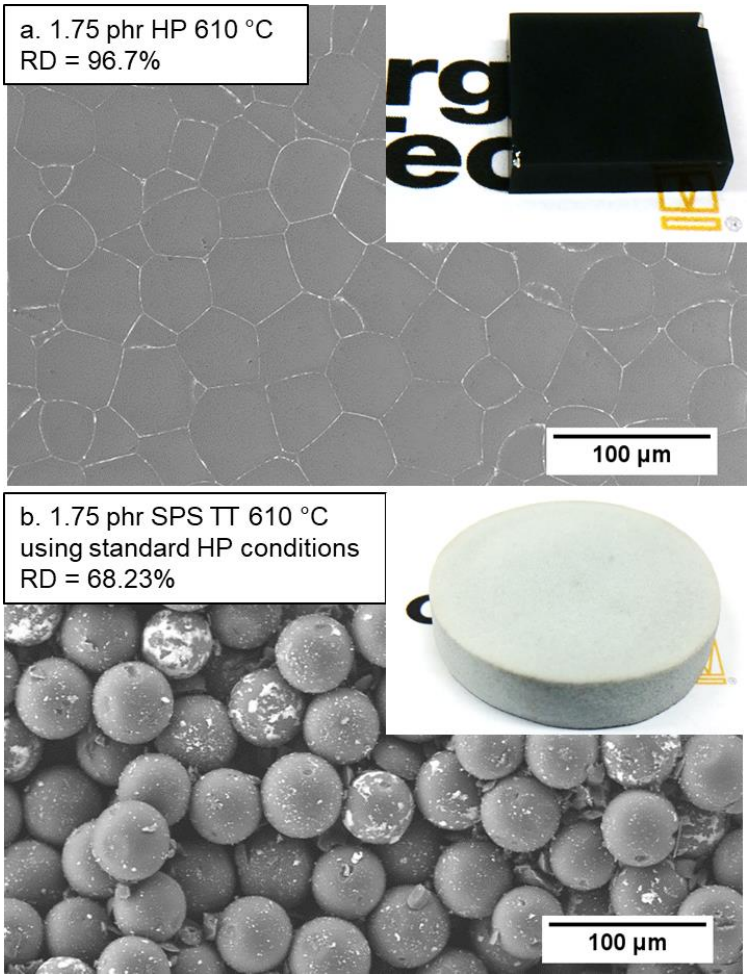

Figure 4.12.[54] BSE (a) HP and (b) SPS samples made using the same powder composition, hold temperature, hold time, ramp rate, and applied pressure. There is clearly a massive difference in densification behavior, with the HP sample showing little residual porosity and the SPS sample showing no microstructural deformation of the glass particles and maintaining a similar appearance to the loose powder. The relative density data confirmed the observed microstructural difference, and optical images, given in the insets, show a very dark and thin HP sample and a light, thick SPS sample.

Additional samples were fabricated to determine what sintering conditions would be required for SPS samples to achieve dense microstructures like those of the HP samples. These were made on the TT SPS equipment with the 1.75 phr powder composition and the processing conditions of the previous SPS samples but with hold temperatures of 610, 620, 655, and 680°C. The microstructures (Figure 4.13(a-d)) showed little densification in the

610 and 620°C samples, an interesting behavior in the 655°C sample with one side appearing porous and the other dense, and high density throughout the 680°C sample. A sample set made with all powder compositions under the same conditions as detailed in section 2.3, except with a hold temperature of 680°C, and using the same SPS equipment verified that this temperature was sufficient to make the glass particles deform to fill the available space. For additional details and analysis of these samples, refer to Section 6.6. Although some porosity is seen on one side of the 655°C sample, the glass is significantly deformed, and the relative density, compared to that of the other samples, suggests that densification in this sample was very near to reaching completion. The difference in microstructure on either side of this sample, while surprising, was observed in multiple other samples under different sintering conditions and made with different SPS equipment. It was postulated that this phenomenon may result from a directional densification process, in which a densification interface, in the same manner as a reaction front, moves along the direction of applied pressure, and that samples exhibiting the part porous – part dense behavior happened to stop densifying while the densification front was between the outer faces of the sample. However, this phenomenon was not explored further.

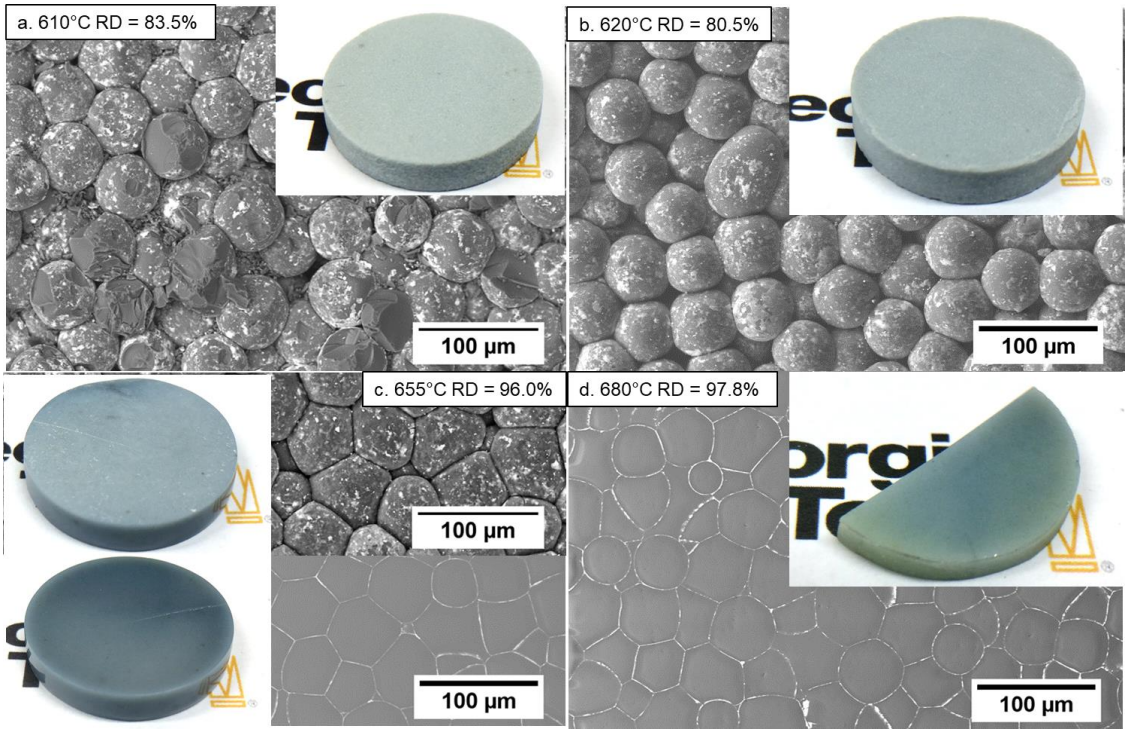

Figure 4.13.[50] BSE images of 1.75 phr SPS TT samples with hold temperatures of (a) 610°C, (b) 620°C, (c) 655°C, and (d) 680°C. Set values for the ramp rate, hold time, and applied pressure were held constant, as well as a vacuum atmosphere. The lower two temperatures were not sufficient to densify the samples, as indicated by very little particle deformation, relative densities in the low 80's, and thick, light-blue appearances (insets). The 655°C sample had one porous side and one dense side, although the porous side shows more deformation than the lower-temperature samples. The depth of the porous region is likely small based on the high relative density value. The 680°C sample showed low residual porosity in the microstructure and possessed a relative density close to that of the 1.75 phr HP samples.

Another interesting microstructural observation is that the 610 and 620°C SPS samples show noticeably less densification than the samples of similar composition made previously on the UA equipment (Figure 4.9 (c) and Table 4.2). This and other observations comparing samples made using different SPS equipment was explored in more detail and will be presented in CHAPTER 5.

Comparing the resistivity values for the HP and SPS sample sets (Figure 4.14) summarizes the trends seen in the impedance data; Resistivities remain relatively constant

before percolation and the HP and SPS retest values were close, although the initial SPS values were consistently lower due to the wavy phase angle phenomenon described earlier (Figure 4.10 (b)), The percolation threshold was higher for the SPS samples, possibly due to the open porosity disrupting the networks to some extent. For both sample sets, percolation decreased the resistivity by many orders of magnitude and the resistivities continued to decrease as the ITO concentration increased. The HP data showed a higher variance near the percolation threshold, but such information could not be gathered for the SPS samples because only 1 sample was made at each composition. Finally, the resistivity of the SPS samples is seen to drop below that of the HP samples for compositions above 5.0 phr, although it is not obvious why this would occur.

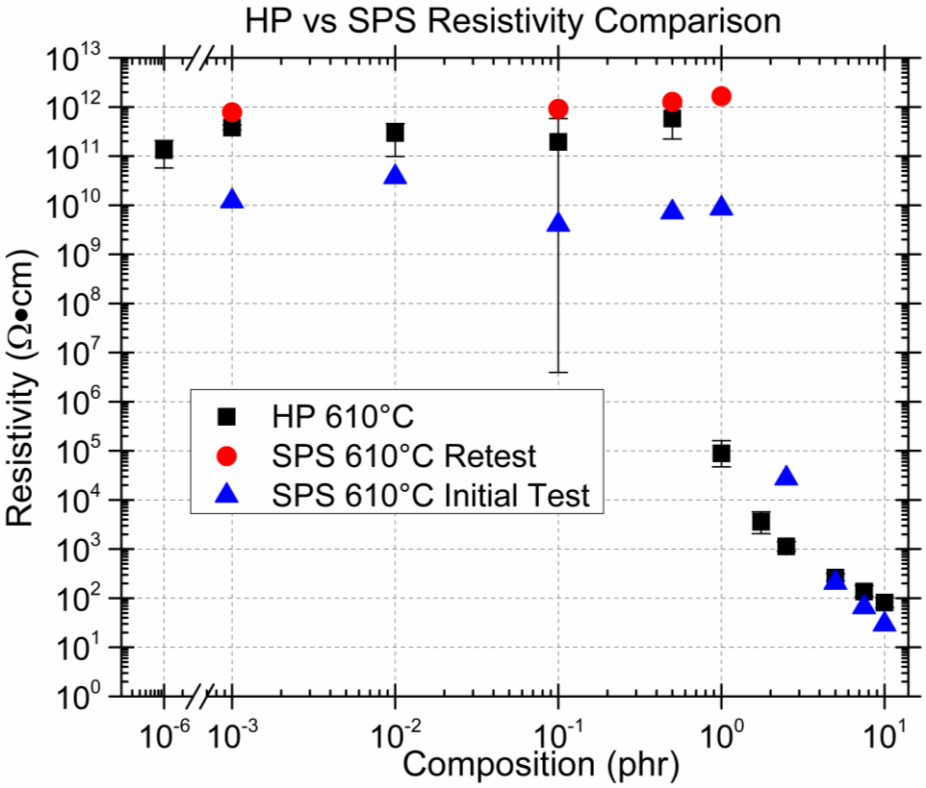

Figure 4.14.[50] Resistivity data for the HP and SPS samples made with a hold temperature of 610°C and other conditions as given in sections 2.2-2.3. HP samples consistently exhibited higher pre-percolation resistivity compared to the initial SPS 610°C data, but slightly lower values than those of the retested SPS samples. The HP samples reached the percolation threshold at a lower ITO concentration but after percolation, the resistivity values became similar for the two sintering methods, with a crossover point at 5.0 phr after which the SPS samples had the lower resistivities.

Most of the mechanisms reported to explain the differences in microstructure and properties between HP and SPS, which were listed in section 1.2.3, cannot explain the lower relative densities in the SPS samples compared to the HP samples obtained in the current study, especially considering that the SPS samples were made at more than double the heating rate and more than double the pressure of the HP samples. Reports on the facilitation of densification by the applied electric field via a mechanism specific to ceramic glasses[63,64] would also seem to only ever result in assisting densification, rather than hindering it. The only proposed mechanism that was found which could account for the

observed behavior was a publication by Holland et al.[36], in which the combined effects of heating rate and applied field interact with the space charge regions at the grain boundaries of the dielectric particles. In that work, sintering hydroxyapatite nanopowders with an applied electric field resulted in lower density than the same sintering procedure without an electric field at the lowest heating rate to be tested, which was 50 °C[36], the same heating rate used for SPS processing in the present study. This mechanism would also explain why the SPS sample made using the low heating rates of the HP processing conditions (Figure 4.12 (b)) resulted in a far lower relative density than the standard SPS samples produced with a heating rate of 50 °C/min.

4.4 Conclusions

Borosilicate glass matrix-ITO filler composites were successfully fabricated using hot pressing and SPS under processing conditions which formed segregated ITO networks. The formation of the segregated networks resulted in low percolation thresholds between 0.154 and 0.764 vol% ITO and resistivities as low as 29 (Ω·cm) at 2.99 vol% ITO under all of the studied processing conditions. The hot-pressed samples, which were processed at a maximum temperature of 610°C, densified completely, whereas the SPS samples processed to the same maximum temperature possessed lower relative densities. Comparison of punch position data from samples made with maximum temperatures of 610°C, 620°C, 655°C, and 680°C showed a large shift in final density between 620°C and 655°C, indicative of crossing the pressure-dependent ductile-to-brittle transition of the glass during SPS sintering. Only the samples brought to 680°C showed no observable porosity, indicating that the composite powders had to be subjected to much higher temperatures to achieve complete densification when SPS was used rather than HP. This

result contradicts the findings of many reports in the literature, which have reported full densification at lower times and temperatures when using SPS. While most of the proposed mechanisms to explain the effect of the SPS sintering process would not be able to explain the lower densities seen in the SPS samples, one possible explanation which does support these results is that proposed by Holland et al[36] involving a synergistic effect between the heating rate and the electric field, which leads to enhanced densification only when the heating rate is above a threshold value but can hinder densification at lower heating rates.

CHAPTER 5. SPS PARAMETRIC STUDY

In this chapter, data from multiple series of SPS samples will be presented. In each, a single independent, user-controlled processing parameter is varied, while all others are held constant. Each sample set is discussed in its own section and analyzed to identify relevant trends and reveal underlying behaviors. It will be shown that many of the parameters such as temperature and applied pressure are interdependent on one another and that errors associated with overshoots can result in misleading conclusions regarding the effect of ramp rate, applied pressure, hold temperature or hold time.

Spark plasma sintering was carried out using 3 different SPS equipment: A Thermal Technologies L.L.C model SPS 10-4, a Thermal Technologies L.L.C model SPS 25-10 and a Fuji Electronic Industrial Co., LTD Dr. Sinter model SPS-211Lx. The different equipment were designated as UA, TT, and GT, respectively. Common processing parameters among all samples were automatic temperature control mode, a hold time of 5 min at the hold temperature, a single ramp period with a constant programmed heating rate, constant pressure from the start of the ramp to the end of the hold, vacuum atmosphere, graphite tooling with graphite foil at every interface, and 20 mm sample diameter. As each series of investigated runs changed a different processing parameter, the conditions used to fabricate each sample set are presented in Table 5.1.

Table 5.1. Processing Parameters for All Sample Sets Discussed in Chapter 5

SPS Process Parameter	Equipment comparison	GT 2.5 phr pressure comparison	GT 0.1 phr pressure comparison	TT 2.5 phr pressure comparison	GT 2.5 phr hold temperature comparison	TT 2.5 phr hold temperature comparison	GT 2.5 phr ramp rate comparison	GT 7.5 phr ramp rate comparison
SPS equipment	Thermal Technologies L.L.C model 10-4 (UA), Thermal Technologies L.L.C model SPS 25-10 (TT), Fuji Electronic Industrial Co. LTD Dr. Sinter model SPS-211Lx (GT)	Fuji Electronic Industrial Co. LTD Dr. Sinter model SPS-211Lx	Fuji Electronic Industrial Co. LTD Dr. Sinter model SPS-211Lx	Thermal Technologies L.L.C model SPS 25-10	Fuji Electronic Industrial Co. LTD Dr. Sinter model SPS-211Lx	Thermal Technologies L.L.C model SPS 25-10	Fuji Electronic Industrial Co. LTD Dr. Sinter model SPS-211Lx	Fuji Electronic Industrial Co. LTD Dr. Sinter model SPS-211Lx
Ramp rate (°C/min)	50	50	50	50	50	50	2, 20, 50, 100, 125, 150, 200	2, 20, 50, 200
Maximum temperature (°C)	610	610	610	610	610-680, 10°C interval	610, 620, 655, 680	610	610
Applied pressure (MPa)	23.4	5, 11.1, 23.4, 40	5, 11.1, 23.4, 40	5, 11.1, 23.4, 40	23.4	23.4	23.4	23.4
Sintering atmosphere	vacuum	vacuum	vacuum	vacuum	vacuum	vacuum	vacuum	vacuum
Vacuum pressure (Pa)	0.83 (TT), 12.59 (UA), 25.8 (GT)	~20	~20		~20		~20	~20
Tooling type	graphite with graphite foil	graphite with graphite foil	graphite with graphite foil	graphite with graphite foil	graphite with graphite foil	graphite with graphite foil	graphite with graphite foil	graphite with graphite foil
Tooling material	Isopressed graphite Mersen 2160 (TT), CalNano graphite (GT)	CalNano graphite	CalNano graphite	Isopressed graphite Mersen 2160	CalNano graphite	Isopressed graphite Mersen 2160	CalNano graphite	CalNano graphite
Die ID (mm)	20	20	20	20	20	20	20	20
Die OD (mm)	unknown (UA), 50 (TT), 40 (GT)	40	40	50	40	50	40	40
Distance between temperature measurement location and powder (mm)	3 (TT), 3.5 (GT)	3.5 (GT)	3.5 (GT)	3	3.5 (GT)	3	3.5 (GT)	3.5 (GT)
Temperature measurement method	TC K-type ungrounded Omega 1/16" diam (GT), TC K-type ungrounded (UA), TC C-type ungrounded 1.5mm diam(TT)	TC K-type ungrounded Omega 1/16" diam (GT)	TC K-type ungrounded Omega 1/16" diam (GT)	TC C-type ungrounded 1.5mm diam(TT)	TC K-type ungrounded Omega 1/16" diam (GT)	TC C-type ungrounded 1.5mm diam(TT)	TC K-type ungrounded Omega 1/16" diam (GT)	TC K-type ungrounded Omega 1/16" diam (GT)
Puke Pattern (ms)	40 on/10 off (GT), 25 on/5 off (TT)	40 on/10 off (GT)	40 on/10 off (GT)	25 on/5 off	40 on/10 off (GT)	25 on/5 off	40 on/10 off (GT)	40 on/10 off (GT)
PID Coefficients (%,s,s)	15/18/3 (GT)	15/18/3 (GT)	15/18/3 (GT)		15/18/3 (GT)		15/18/3 (GT)	15/18/3 (GT)

As a result of these investigations, it will also be shown that the experimental details most commonly reported in the SPS literature are insufficient to enable reproducibility, and that even the data which is reported, such as experimental temperature profiles, have low sensitivity to potentially major differences in sintering behavior. This is shown to be true for the temperature profiles of all sample sets, given in Figure 5.1.[65]

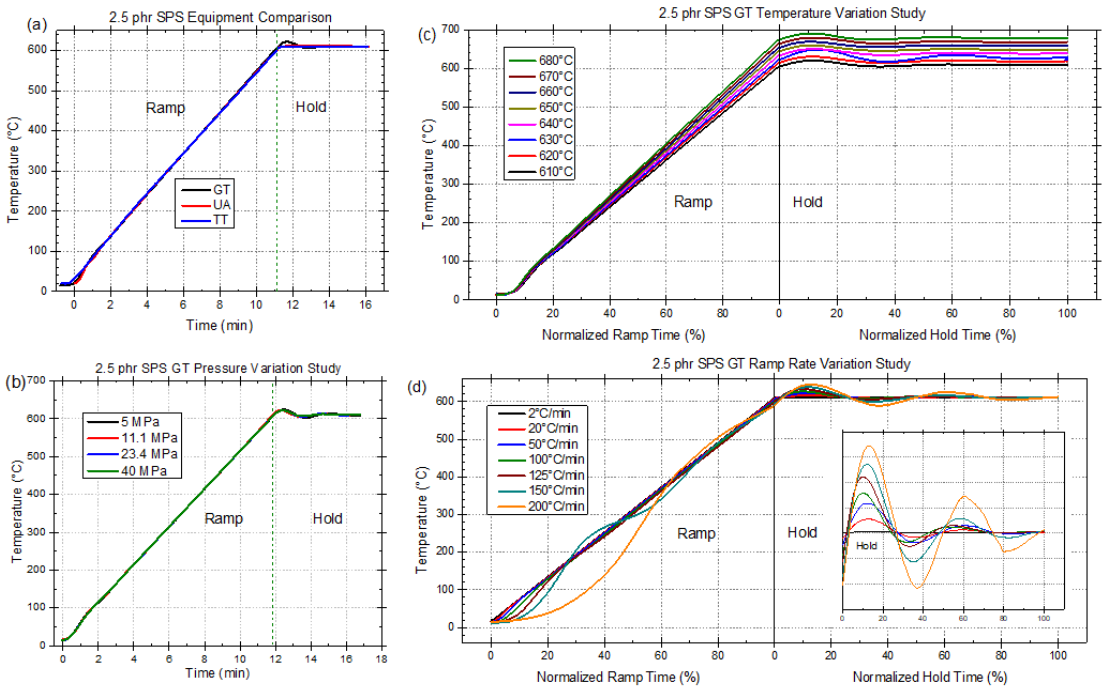

Figure 5.1.[65] Temperature profiles of the (a) equipment comparison, (b) pressure comparison, (c) maximum temperature comparison, and (d) ramp rate comparison sample sets. For the samples within each comparison, the other parameters were kept constant. The inset in (d) is a magnified view of the hold period, showing the clear sequential increase in maximum temperature overshoot and overall fluctuations with increasing heating rate. For heating rates below 125°C, this data seems relatively consistent within each sample set, contrary to the substantial differences observed in the microstructures and current and voltage profiles. This suggests that the temperature profiles were largely insensitive to the factors which were responsible for the differences in densification behavior within all the sample sets.

5.1 Analysis of SPS Metadata

All SPS equipment utilized over the course of this work recorded the measured temperature, the current and voltage through the complete circuit, the applied pressure and chamber pressure, and the displacement of the moving punch. For all SPS equipment used, the temperature was measured with an ungrounded thermocouple fully inserted into a radial hole in the center of the die wall. Therefore, the temperature measurement location was very near the powder, improving measurement accuracy and reducing response lag, yet

would not compromise the die's resistance to the internal pressure during sintering. The applied current travels through both the die assembly and the internal circuitry of the SPS system and can be represented by a set of resistors in series, as shown in Figure 5.2. The voltage measured by the equipment is that of the total circuit, so the actual voltage across the die assembly will be the total measured voltage minus the voltage of the electrodes and cables, whereas the measured current will be the same as the current through the die assembly. Although details of the internal circuitry of the various SPS equipment were not available, their effect on the data should be the same for all tests on the same equipment so the relative difference in values between samples still provided useful analysis.

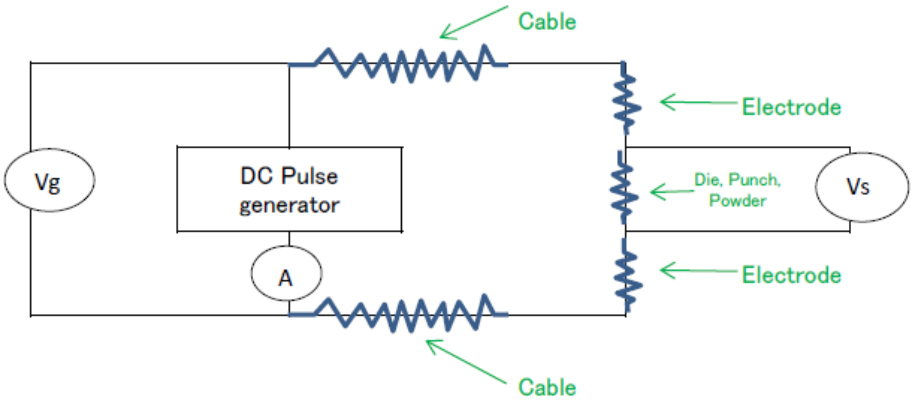

Figure 5.2. Schematic of the path of the applied SPS current. Vg is the voltage recorded by the data logging software, whereas Vs is the voltage across the graphite tooling. The current is consistent throughout the circuit whenever the resistive elements are in series, so the value measured at the generator, A, will be the same as the value into and out of the electrodes.

The sampling rate used in recording the data was 1 point/s for both Thermal Technologies equipment (UA and TT) and 2 points/s for the Dr. Sinter equipment (GT). The instantaneous heating rate was derived from the time and temperature data, where the heating rate at a given time was calculated as the slope of the line between two points, each

1.5 s on either side of that time, on the time-temperature plot so that local averaging reduced the effects of noise on the data.

The punch displacements were plotted using a convention that positive displacement corresponds to upward movement of the top punch. Therefore, positive displacement indicates expansion of the die assembly, which is primarily due to thermal expansion, and negative displacement indicates contraction of the die assembly, which is indicative of densification of the powder bed. In determining the densification of the powder from the punch displacement data, the thermal expansion of the tooling and powder as well as the changes in displacement when changing the applied pressure must be accounted for, as the measured displacement will be the sum of these factors and the change of powder thickness due to densification. The optimal method to remove these factors is to conduct a "dummy test"[66-68], in which an SPS run is conducted under the same conditions as used for sintering the powder, but with a fully dense sample of the same material as the powder taking the place of the powder. This run can then be used as a baseline so the effects of thermal expansion and changing applied pressure can be subtracted. With the correct data on the change in powder thickness due to powder densification, a relative density can then be derived easily since the diameter and mass of the powder is fixed, making the change in density directly proportional to the change in powder thickness.

However, a dummy test could not be performed in the present work due to a lack of further access to the University of Arizona SPS equipment. Therefore, the effect of changing applied pressure was removed by only plotting data taken while the applied pressure was constant. Then, as long as only the differences between samples rather than absolute values are considered, the thermal expansion can be ignored if it can be assumed

that the powder and die assembly experienced the same thermal expansion for every test. However, small variations in the mass of the powder bed and lag in the response of the temperature measurement can prevent accuracy of such an assumption. Therefore, in order to enable valid comparisons between samples, the punch displacements were normalized to a maximum positive value of 1, thereby normalizing the thermal expansion of all samples to the same value.

An additional consideration for comparison plots of the various processing parameters over time was that for samples made with different heating rates or different hold temperatures, with all other parameters held constant, the time spent in the ramp stage will be different for each sample. The resulting displacement of the curves makes comparison more difficult, so instead, each data set was separated into separate ramp and hold plots, and the time axes used for plotting were the percentage of the total ramp time and percentage of the total hold time, respectively. Through this means, the data for all samples starts and ends at the same position on the x-axis, which is especially valuable for comparisons at the transition between the ramp and hold periods.

For sample sets with the same ramp and hold periods (pressure variation, equipment variation), time was plotted on an absolute scale with the ramp and hold in one plot, and the starting times for all data curves in each comparison plot were shifted such that all samples reach the hold at the same time value, and no curve begins at a time exceeding t=0 s.

For the current and voltage data, the first data point with both current and voltage values greater than 0 was designated as time t=0, and the first data point with lower current than

the previous point, near the hold temperature, was designated as the first point of the hold period, as it is indicative that the set point has reached the hold temperature in the temperature control software.

5.2 SPS Equipment Comparison Study

Initially, three samples were made, each on a different SPS equipment, with the simple aim of showing that similar results could be attained when using the same starting powder and identical input conditions. The samples were made as indicated in Table 5.1 for the "equipment comparison" test series. Although the ramp rate, hold temperature, hold time, atmosphere, pressure, and powder were the same, there were clear, dramatic microstructural differences between the three samples, as exemplified by the back-scattered electron (BSE) images shown in Figure 5.3. The sample made using the Thermal Technologies SPS 25-10 (TT) equipment (Figure 5.3 (a)) shows very little deformation of the glass particles and high residual porosity, while the other samples show a far higher degree of densification. Even these two other samples (Figure 5.3 (b-c), however, exhibited distinct differences. The sample made using the Thermal Technologies SPS 10-4 equipment (UA) had a seemingly identical degree of porosity on both sides of the sample, whereas the sample made using the Fuji Electronic Industrial Co. Dr. Sinter model SPS-211Lx equipment (GT) appeared completely dense on one side but not dense on the other side. Initially, this behavior was baffling, considering that all processing parameters generally reported in the literature (hold temperature, atmosphere, sample size, pressure, hold time and heating rate) were the same between the samples.

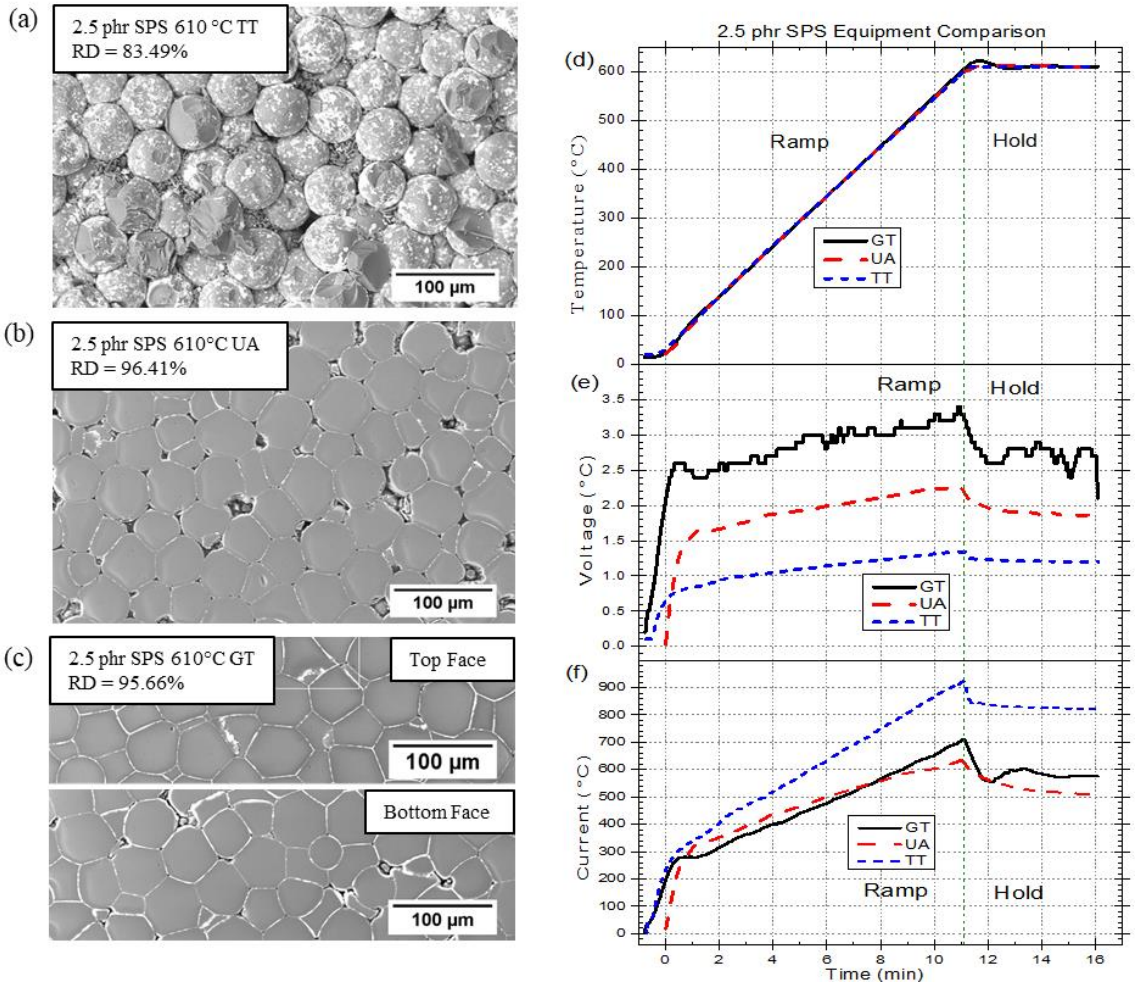

Figure 5.3.[65] SEM backscatter images of 2.5 phr SPS samples made using the (a) TT, (b) UA, and (c) GT SPS equipment, along with the corresponding (d) temperature vs time, (e) voltage and (f) current profiles. Despite fabricating these samples under identical temperature and pressure schedules and with the same atmosphere type, sample size, tooling material, and powder batch, the microstructures show dramatic differences in densification behavior, which are reflected in the voltage and current profiles.

When examining the recorded temperature profiles of the three samples made using the three different SPS equipment (Figure 5.3 (d), repeated from Figure 5.1(a)), they appear to have very similar behavior, with only small deviations at the start of the ramp and the start of the hold. The average ramp rate was at 50°C/min as programmed, and the temperature overshoot at the start of the hold was relatively mild, with respective overshoot values of

3.4°C, 1°C, and 12°C for the UA, TT, and GT samples. It is well known that electrical properties are very sensitive to many factors, so the voltage and current data, automatically recorded in all data collection software used on all equipment in this study, was plotted to try to find hidden processing differences which must have been present to cause the differences in densification behavior observed.

The voltage data in Figure 5.3 (e) shows clear differences between the three samples, with similar profile shapes, but maximum voltages of 2.3, 1.3, and 4.7 V for the UA, TT, and GT samples, respectively. These differences in voltage, and the resulting electric fields, across the powder certainly have the potential to be a significant contributing factor in the densification differences, as attested to by many reports of voltage and/or electric field effects in densification via SPS in the literature[36,63,64,69,70]. If some threshold value of electric field strength can activate additional sintering mechanisms, as has also been reported[36,63], the observed difference in field strength in these samples of up to nearly a factor of 4 could result in a difference in densification far greater than a linear relationship would predict. Therefore, it is important to determine the source of this difference in applied voltage.

Potential sources of the observed differences in applied voltage fall into three primary categories, discounting heating rate and hold temperature, as these were set to the same values for the samples displayed in Figure 5.3 (50°C/min and 610°C). The first is the tooling material properties, the second is the tooling geometry and the third is the SPS equipment itself and its controlling software. Table 5.2 presents the details of the properties of the tooling used in the equipment comparison samples. In the present study, the most obvious difference in tooling geometry was the die wall thickness, where the CalNano

tooling had a wall thickness of 10 mm and the Mersen tooling had a wall thickness of 15 mm. From a simple comparison of the change in area perpendicular to the direction of current flow for the unchanging 20 mm diameter circle of powder within the dies of different wall thicknesses, for a given applied voltage, the electric field strength would be expected to be 1.56 times greater when using the CalNano tooling relative to the field strength when using the Mersen tooling. Additionally, the temperature difference between the die and the punches will be larger when the die wall is thicker, resulting in increased lag in the response of the temperature control program[71], as is further discussed in the following paragraph. A direct relationship between die wall thickness and SPS voltage has already been established[72], so since the difference in die wall thicknesses was relatively large, it is likely a primary factor in the voltage discrepancies observed in the present study.

Table 5.2.[65] Selection of properties of the graphite tooling used for SPS

Properties	CalNano Graphite (GT)	Mersen 2160 Graphite (TT)
Bulk Density	1.85 g/cm3	1.84 g/cm3
Grain Size (Average)	1 µm	5 µm
Specific Resistance	1525 µ ohm-cm	1500 µ ohm-cm
Flexural Strength	86.5 Mpa	76 Mpa
Compressive Strength	160 Mpa	167 Mpa
Porosity	9.00%	7.00%
Thermal Conductivity	81.2 W/m°K	84 W/m°K
Ash Content	200 ppm	150 ppm
Coefficient of Thermal Expansion: 400 - 500°C	6.8 x 10E-6/°C	6.0 x 10E-6/°C

All three samples were made using automatic or programmed temperature schedules in which the temperature measured by the thermocouple in each SPS machine is compared with the set temperature each time the data is sampled. The difference in these values determines the controller's response to try to minimize this difference. Since the software

only cares about the set temperature, it will change applied current and voltage values to any values which will reduce the temperature difference. The means by which the controller determines changes to make in the current and voltage outputs is through the proportional-integral-derivative (PID) method. Since different SPS equipment will have different power output ranges and differences in the control software, including factors such as the rate of current change it will use in response to a given temperature difference, which are defined by the PID coefficients, it is very likely that different equipment will impose different current and voltage profiles to achieve identical temperature profiles. Furthermore, it has been demonstrated that the response of the PID control program is strongly influenced by both the heating response and lag in the heating response.[71,73-76] This lag arises from the distance between the primary location of heat generation and the location of temperature measurement, and is strongly dependent on the tooling geometry and on the thermal contact resistances of the parts between the two locations.[71,76] Therefore, the PID program is influenced by the tooling geometry and properties which, as discussed in the previous paragraphs, can easily differ between SPS setups. Evidence of differences in the responses of the PID controllers in the different SPS equipment, despite identical programmed temperature schedules, is shown by comparing Figure 5.3(e) to Figure 5.3(f). The difference in voltage between the samples stays approximately consistent, but the differences in current change throughout the sintering process, especially during the ramp stage. Therefore, these results suggest that merely listing the heating rate, applied pressure, hold time and hold temperature used to make samples is not enough to truly compare samples made in different SPS machines.

5.3 Pressure Variation Study

In this sample set, different pressures were applied to determine the effect of pressure on both the microstructures as well as the effect on the electrical behavior of the SPS system throughout a sintering procedure. The specific processing parameters used are given in Table 5.1. The voltage and current profiles, shown in Figure 5.4 (a) and Figure 5.4 (b) respectively,[65] show a decreasing voltage and increasing current with increasing applied pressure. As with the equipment comparison temperature profiles, the temperature profiles failed to show any differences (Figure 5.1(b)).

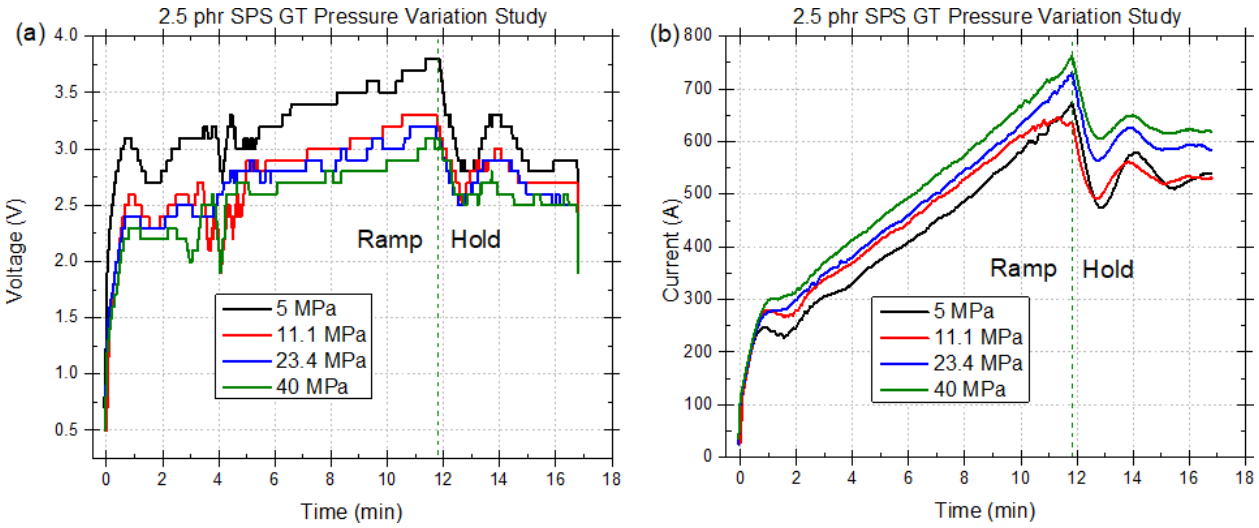

Figure 5.4.[65] Plots of the changes in (a) voltage and (b) the applied current over the course of the ramp and hold sintering stages for samples made using a range of applied pressures with no other parameters changed. Higher pressures required lower voltages while current is seen to increase with increasing applied pressure, likely by improving the quality of conducting interfaces between tooling parts.[78] This will affect many other aspects of the sintering process.

Since no specific current or voltage values are specified in the control program, it would seem that these sequential changes result from changes in the electrical properties of the SPS setup, which then necessitate different current and voltage values to achieve the

same temperature and ramp rate conditions. In fact, this would be expected, because the axial pressure applied through the punches will generate reactionary radial forces on the inner die wall according to the Poisson ratios of the punch and powder materials.[77] The radial force has been shown to improve the interfacial contacts between the die and punches[78], thereby reducing the electrical resistance of these interfaces. Therefore, it is logical that, for a constant power output from the SPS equipment, lower electrical resistance through the tooling assembly would result in lower voltage and higher current. Again, since relationships between voltage, electric field, and/or current density on densification behavior in SPS have been reported extensively in the literature[36,63,64,69,70], it is reasonable to conclude that changes in applied pressure will indirectly affect all factors dependent on the electrical parameters. Comparison of the microstructures (Figure 5.5(a-d))[65] and their respective relative densities appears to confirm the presence of pressure effects beyond driving force and kinetics, since if these were the only effects, density would be expected to consistently increase with increasing pressure, which was not the case here.

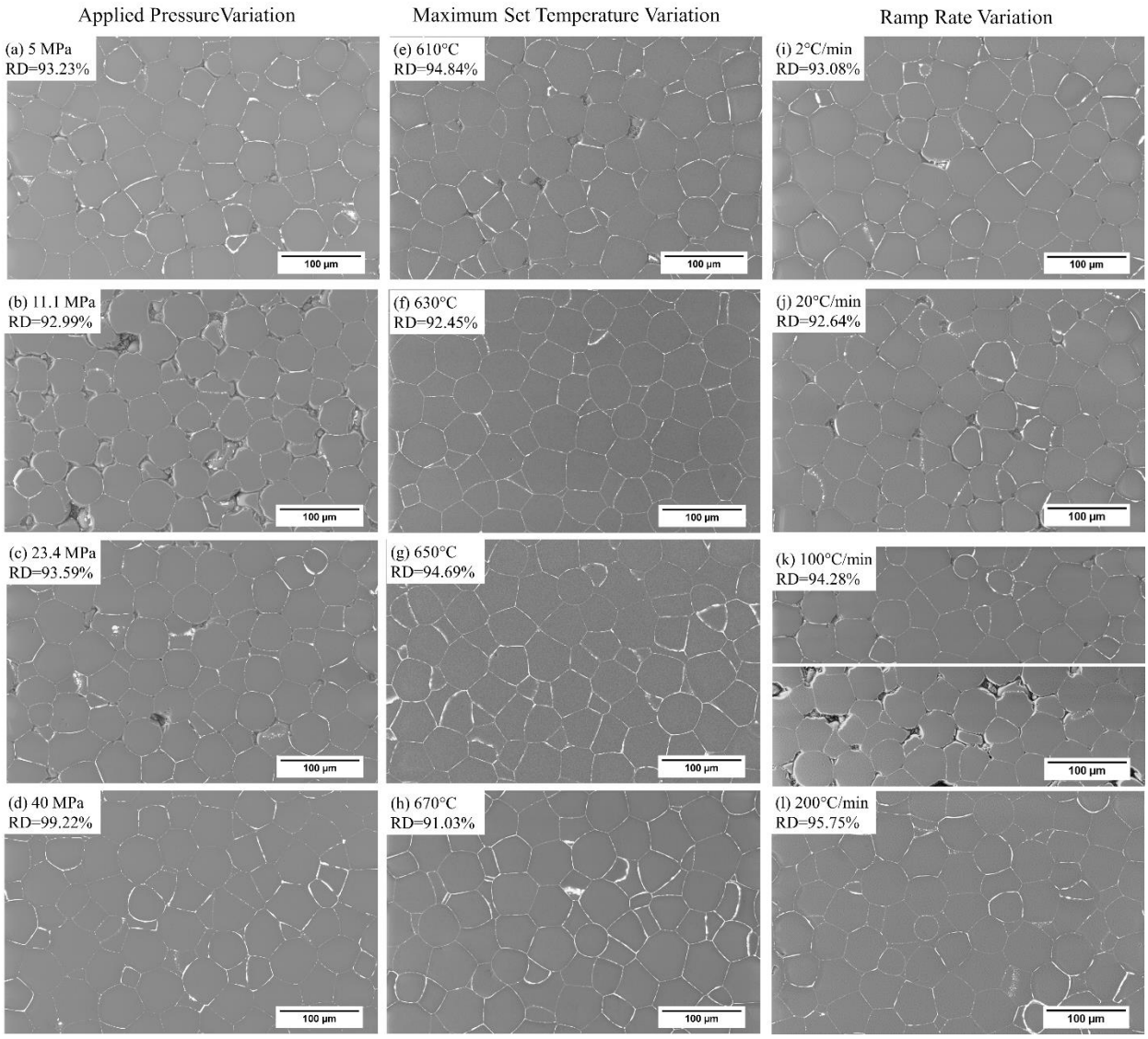

Figure 5.5.[65] SEM backscattered electron images of samples made with the GT SPS equipment for the applied pressure set (a-d) maximum set temperature set (e-h), and heating rate set (i-l) as discussed in sections 5.3, 5.4, and 5.5, respectively. The relative density (RD) for each sample is included in the legend for each micrograph.

5.4 Temperature Variation Study

These samples were processed to a range of hold temperatures, up to 680°C, as given in Table 5.1. The observed trend of increasing maximum current with increasing hold temperature is as expected according to the mechanism of Joule heating (Figure 5.6(a)).

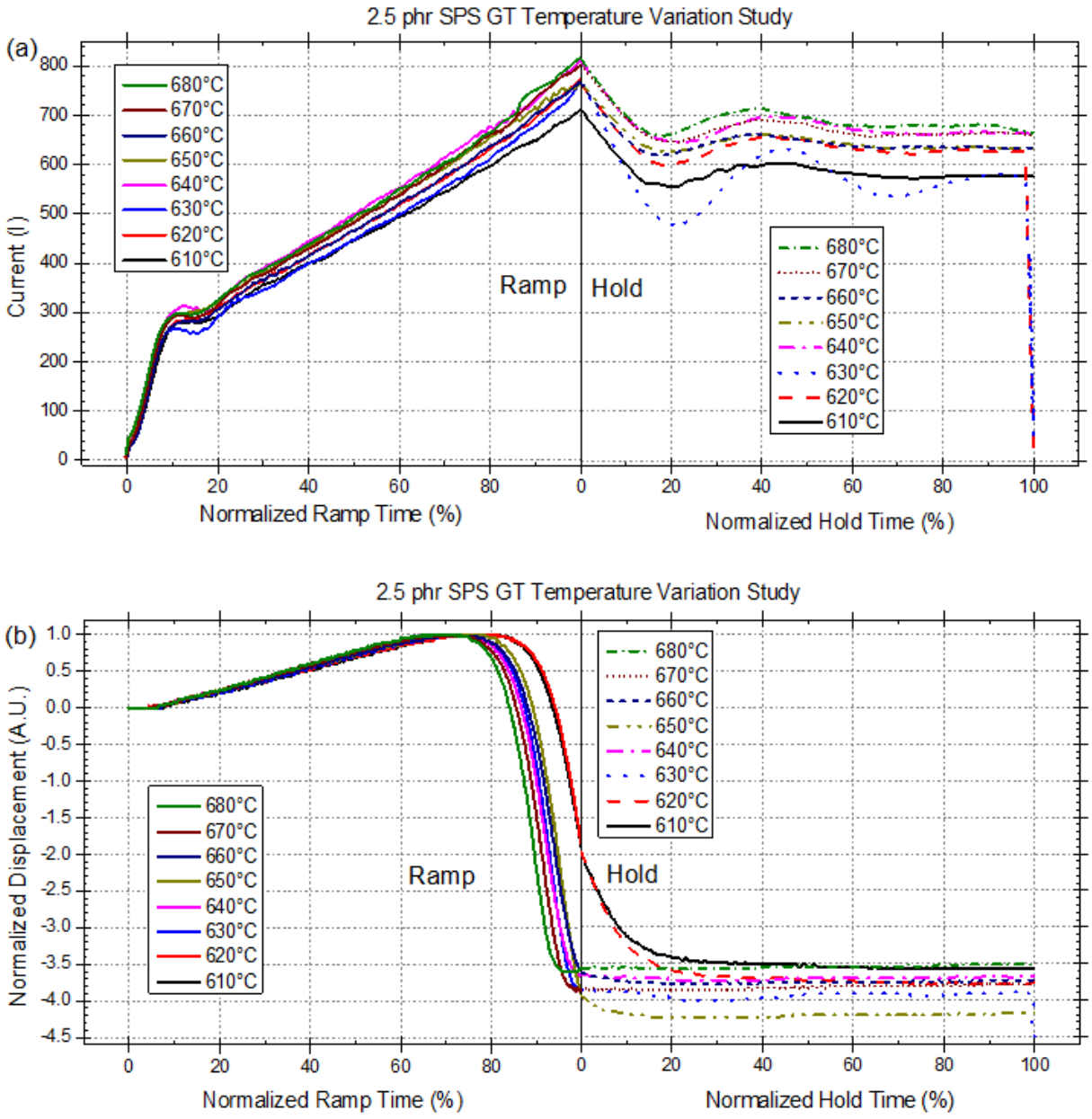

Figure 5.6. Data on the (a) current and (b) top punch displacement for 2.5 phr samples using different hold temperatures while maintaining a 50°C/min ramp, 5 min hold, and 23.4 MPa applied pressure in vacuum atmosphere with the GT equipment. The displacement data shows a very non-sequential trend in the final degree of densification, which may be due to activation of an additional densification mechanism[63,69] or crossing some transition temperature[66].

The temperature vs time profiles were also sequential (Figure 5.1(c)), but abnormally high instability was seen in the data for the 630°C sample and appeared to be quite repeatable between two different samples made with that hold temperature. This may be indicative of the crossing of some transition point, such as the glass transition[66] or a densification mechanism transition[36,63,69] under these processing conditions.

The generally-consistent order of the current curves (Figure 5.6 (a)) seems at first to be wholly unrelated to the normalized punch displacement data, shown in Figure 5.6(b). A plot of the minimum normalized displacement relative to the hold temperature (Figure 5.7), which constitutes a comparison of the displacements late in the hold period in Figure 5.6(b) when the values have stabilized, also fails to show a clear relationship between them; while there is a general trend of a greater displacement magnitude as the hold temperature approaches 650°C from both higher and lower temperatures, the 640°C and 660°C samples saw less displacement than the surrounding temperatures on either side. The microstructures also showed only subtle differences (Figure 5.5 (e-h)). However, two important trends were observed in the displacement data, the first being that the form of the curve in the area around the transition from the ramp to the hold period changes between the 620°C and 630°C samples. The 610°C and 620°C displacement data show that these samples were still only partially through the densification process at the start of the hold, densified more slowly than the higher-temperature samples, and, most notably, that the densification process continued well into the hold period. In the samples with maximum temperatures above 620°C, the samples showed more densification by the end of the ramp and a faster rate of densification, but densification halted abruptly around the start of the hold. As a result, the degree of densification of the low-temperature samples caught up to

that of the high-temperature samples, with the 620°C sample surpassing the 680°C sample. The behavioral shift between 620°C and 630°C supports the hypothesized crossing of some transition value in the applied voltage, electric field, or current, and a change in densification rate upon crossing a transition has also been reported by a different group, which attributed the change in behavior to crossing an electric field strength threshold.[76] It should be noted that a shift in behavior similar to that observed in the GT temperature variation sample set was also observed above 620°C in a different set of samples made using the TT SPS equipment (Figure 5.8).[50,65] However, in this figure, which shows the displacement, current, and voltage for samples made with 4 different hold temperatures, it can be seen that although the higher-temperature samples experienced far more displacement, all samples continued to densify at the start of the hold; this was possibly due to the lower voltages across the powders in the TT equipment which, as discussed in section 5.2, may not have been sufficient to activate an additional sintering mechanism.

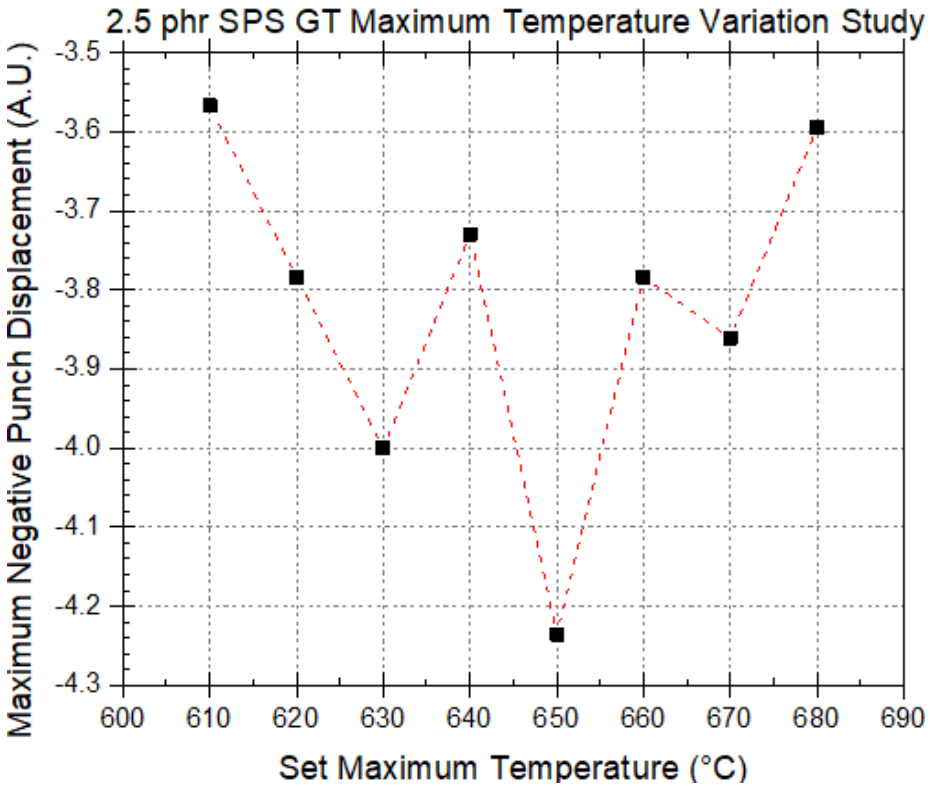

Figure 5.7.[65] Comparison of the maximum set temperature to the maximum negative (downward) displacement of the top punch of the SPS equipment. Although it may be predicted that a linear relationship should be present, this is clearly not the case here. The strange behavior may result from the presence of multiple active densification mechanisms which can either help or hinder total densification.

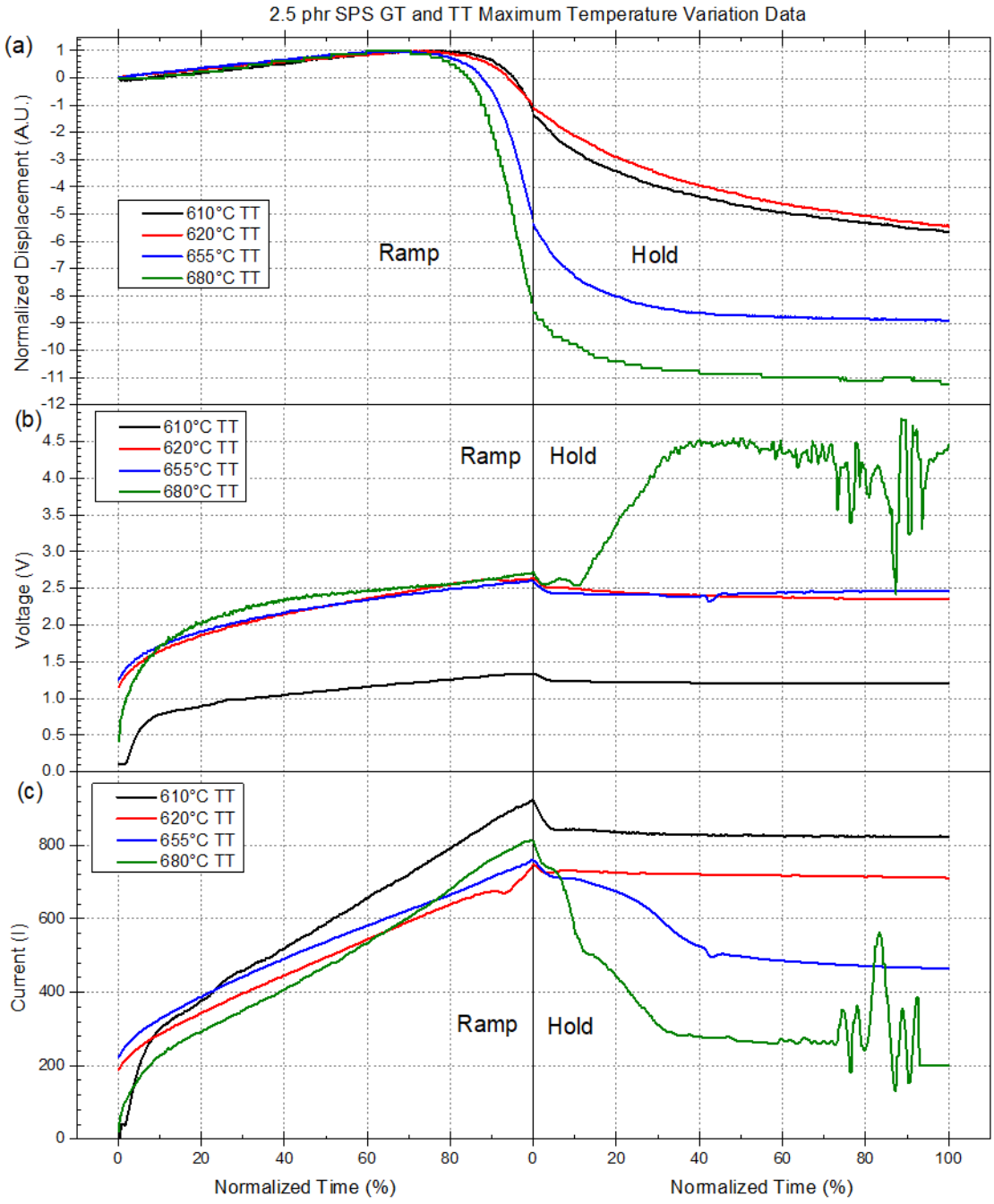
2.5 phr SPS GT and TT Maximum Temperature Variation Data
(a)
Normalized Displacement (A.U.)
610°C TT
620°C TT
655°C TT
680°C TT
Ramp
Hold
(b)
Voltage (V)
610°C TT
620°C TT
655°C TT
680°C TT
Ramp
Hold
(c)
Current (I)
610°C TT
620°C TT
655°C TT
680°C TT
Ramp
Hold
Normalized Time (%)
Normalized Time (%)

Figure 5.8.[50,65] (a) Normalized displacement, (b) voltage, and (c) current profiles for four TT samples made under the temperature variation study conditions but with maximum temperatures as given. There is a jump in the degree of densification above 620°C in the TT samples, like in the GT data, but a continuation of densification in all TT samples regardless of maximum temperature accompanied by increases in voltage and decreases in current, very unlike the GT data. This could be related to the higher voltages, and therefore electric fields, for the GT samples in the ramp stage, which may be activating an additional densification mechanism that can cause this densification arrest phenomenon.[71-73] As with the GT temperature variation data, the TT current profiles do not exhibit a clear relationship between the displacement and the current.

The other trend in the maximum temperature data displayed in Figure 5.6(a) involves the point at which the abrupt halt of densification occurs in the higher-temperature samples. The displacement plot shows densification stopping earlier with higher applied temperature, at least for the samples above 650°C, and the comparison of the temperature and displacement data confirmed that the temperature at which densification halted decreased with increasing hold temperature. This resulted in less densification in these samples, even though they reached higher temperatures and maintained those higher temperatures throughout the hold (Figure 5.1 (c)). Since sintering is a thermally-dependent process first and foremost, this result was very surprising. 650°C gave the largest displacement of all the hold temperatures investigated, and it seems that above this temperature, the negative impact of whatever is causing the arrest in densification overtakes the benefit of higher temperatures.

At the start of the hold, the biggest changes to the system are the rapid decreases of the heating rate and the current, making these the primary suspects related to the densification arrest or lack thereof. It has been reported that ramp rate[36] and electric field strength[63,69] can exhibit transition values, above which an additional sintering mechanism becomes active. The apparent transition between 620°C and 630°C in the present study is

consistent with the notion that the mechanism causing densification arrest is somehow related to either heating rate or applied current; if densification via the additional mechanism is allowed to finish it hinders further densification, whereas decreasing the heating rate and/or current before the additional mechanism is allowed to progress to completion will prevent the densification arrest phenomenon.

While the trends in the densification data are not yet fully understood, it seems undeniable that the electrical parameters influence the densification behavior, such that it can be drastically different even for small changes in the hold temperature, in a similar manner to the large differences seen in the voltage and current in the pressure variation study. Therefore, the electrical data for the SPS fabrication process is both meaningful and important for developing an understanding of the overall sintering behavior, and this data can provide unparalleled insight into the mechanisms of densification.

5.5 Ramp Rate Variation Study

A series of samples made using 7 different heating rates was fabricated under the conditions given in Table 5.1. Observing the temperature profiles (Figure 5.1 (d)), it is apparent that the temperature profiles seen by the powder for the heating rates above 50°C/min were different than the profile set in the program control software, becoming worse with increasing heating rates. This behavior was very consistent and was found to result from a combination of equipment response time delay and the manner in which the automatic mode program attempts to correct mismatch between the measured and set temperatures. These factors are addressed in more detail in the next section.

The 20°C/min and 50°C/min temperature profiles (Figure 5.1 (d)), while appearing similar to the 2°C/min data, are again hiding large differences in densification behavior, as seen in both the displacement data (Figure 5.9 (a)) and, to a lesser degree, in the microstructures (Figure 5.5 (i-l)). Here, there is a general trend of increasing downward punch travel (Figure 5.9 (a)) and decreasing apparent porosity (Figure 5.5 (i-l)) with increasing heating rate, except for the 2°C/min sample.

Attainment of higher heating rates in the SPS equipment requires higher current and higher voltage, and therefore higher electric field, compared to those needed at the lower heating rates, as shown in Figure 5.9. Working under the theory of an additional sintering mechanism which activates at some elevated voltage, current, electric field, or heating rate, the 2°C/min sample, densifying under only the initial, slower sintering mechanism may achieve a greater final degree of densification than the 20°C/min and 50°C/min samples simply due to the exponentially longer time spent at elevated temperature during the ramp stage, giving the lone mechanism enough time to outperform the intermediate heating rate samples. Additional trends with increasing ramp rate were an earlier start to densification in terms of the percentage ramp time (Figure 5.9 (a)), again excepting the 2°C/min sample, along with higher current (Figure 5.9 (b)) and voltage (Figure 5.9 (c)).

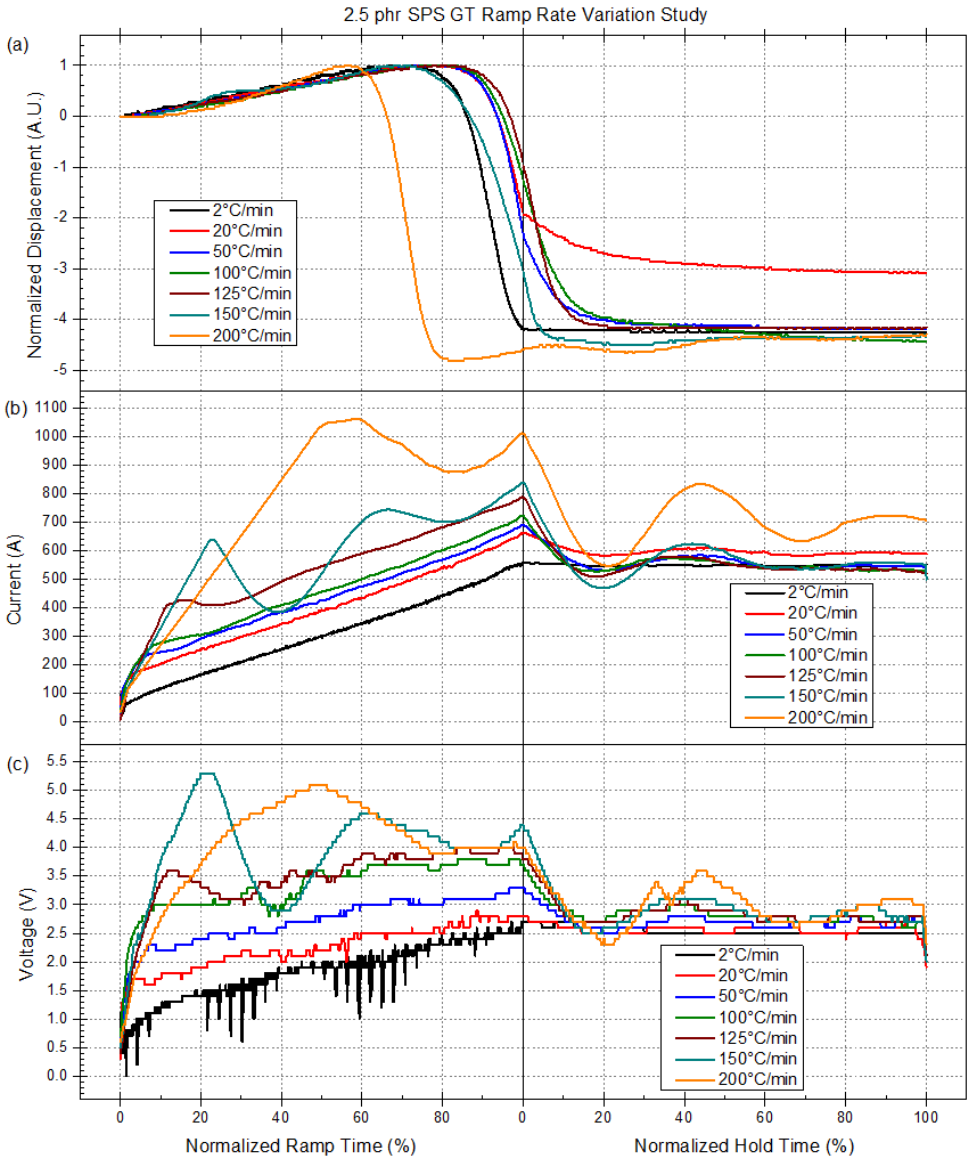

Figure 5.9.[65] (a) Punch displacement, (b) current, and (c) voltage profiles for samples made with a range of temperature ramp rates. The final displacements are not sequential with respect to the heating rate, which may indicate a change in the dominant densification mechanism at higher heating rates. Clearly, both current and voltage consistently increase with increasing heating rate, so any densification behavior sensitive to the current, voltage, or field strength is also dependent on the chosen heating rate. Additionally, strong fluctuations in the 150°C/min and 200°C/min data can be seen, which mirror those seen in the instantaneous heating rate and further prove that the fluctuations result in far harsher sintering conditions than would be anticipated.

However, despite the apparent heating rate trends, there are multiple issues preventing a legitimate comparison of the heating rate variation samples, and it is important to identify and quantify these factors if a true heating rate comparison is to be made.

5.6 Additional Complications Introduced with High Heating Rates

As shown in Figure 5.1 (d), ramp rates above 20°C/min show deviations from the programmed ramp rates and those above 100°C/min seem to be particularly problematic for the automatic temperature control software in the GT SPS equipment. The largest discrepancy between the measured and set temperatures results from the initial lag in heating rate at the start of the ramp. This primarily comes about due to thermal lag in the tooling, where the temperature increase via Joule heating takes time to reach the point at which the temperature is measured.[71] This effect has been shown to be significant due to high thermal contact resistance between the punches and the die, owing to both a low contact pressure and low thermal conductivity in the graphite foil in the thickness direction.[71] In attempting to correct the initial temperature lag, the equipment must substantially exceed the set heating rate to catch up to the set temperature, leading to a considerable overcorrection. This lag resulted in instability in both current (Figure 5.9(b)) and voltage (Figure 5.9(c)), especially in the 150°C/min and 200°C/min samples, as opposed to the gradual increases seen in the 2°C/min and 20°C/min samples.

The instantaneous heating rate over time (displayed in Figure 5.10 (a)) followed the trend in the current, with actual heating rates varying wildly over the course of the sintering program for the higher heating rates. The magnitude of heating rate overshoot during the ramp increased sharply above 100°C/min (Figure 5.10 (b)), reaching rates as high as

400°C/min for the 200°C/min sample and, for heating rates above 125°C/min, spending most of the ramp period nowhere near the programmed heating rate (Figure 5.10 (a)). The overcorrections continued but progressively died down over the ramp period. However, the instantaneous change in the set ramp rate at the start of the hold, which is larger for larger ramp rates, once again cannot be matched by the control program even for the 20°C/min ramp rate sample, resulting in a temperature overshoot and another series of overcorrections.

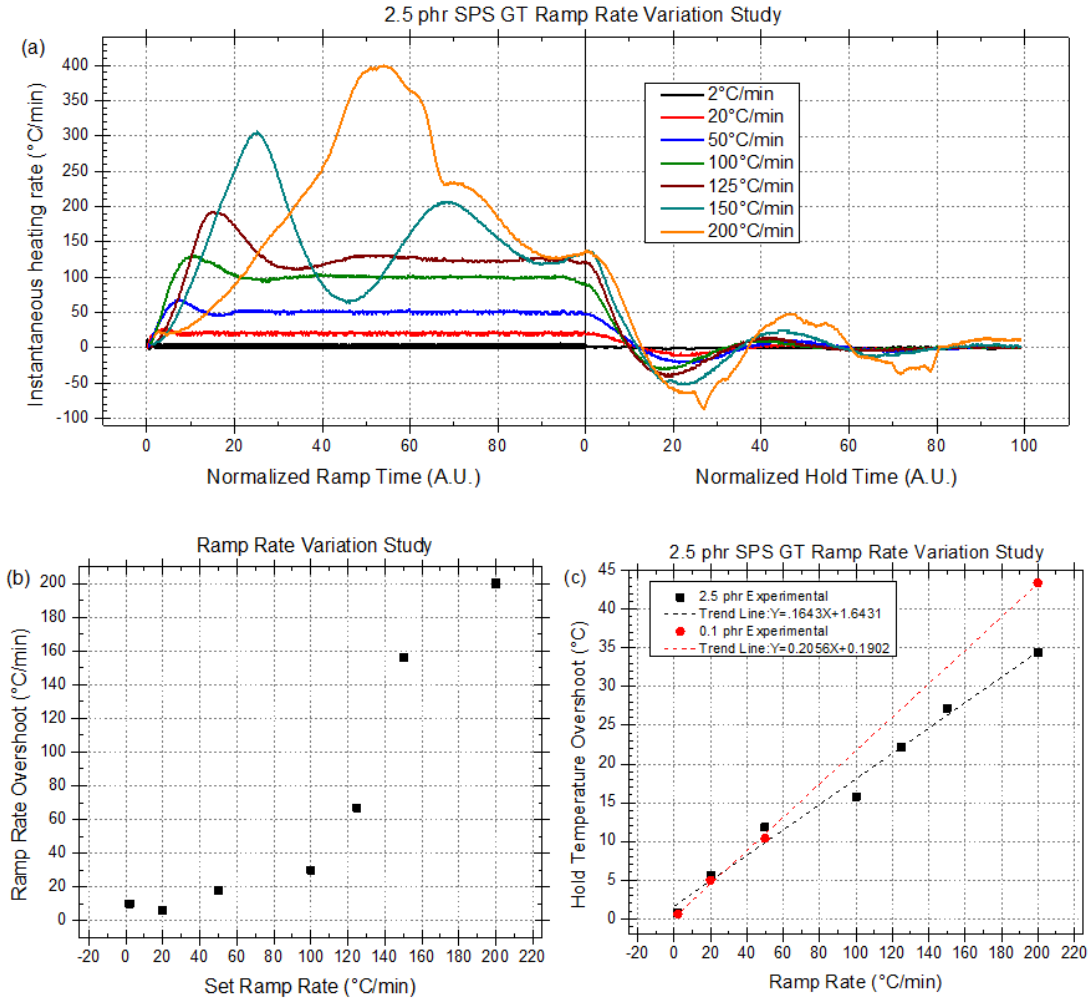

Figure 5.10.[65] Plots of (a) the instantaneous heating rate over time, (b) the maximum ramp rate overshoot during the ramp period, and (c) the maximum temperature overshoot at the start of the hold stage for the sample set made with different heating rates. The 200°C/min sample reached about 400°C/min at one point and almost never heated at 200°C/min. It also overshot the target temperature by more than 40°C. Thus, this sample cannot be properly compared to others, as it saw very dynamic processing conditions which at times significantly exceeded the intended conditions. The ramp rate overshoot trend was complicated, but the hold temperature overshoot showed a linear trend, and is therefore somewhat predictable. Data for samples made using powder with an ITO concentration of 0.1 phr, with an ITO to glass ratio of 0.001 by weight, are also included in (c) to show that a linear trend was also obtained for this different powder composition, although the slope was different.

The temperature overshoot exhibited a linear dependence with the set heating rate (Figure 5.10 (c)), with the best-fit trendline defined by the equation Y=0.1643X+1.6431, where Y is the overshoot in °C and X is the ramp rate in °C/min. A linear trend would make sense based on the nature of the thermal time lag since the temperature increase during the same period of the time lag will be larger for higher heating rates. Figure 5.10 (c) shows both the 2.5 phr samples described here as well as data from another set of samples of 0.1 phr composition (meaning an ITO to glass ratio of 0.001 by weight), which displayed a similar linear behavior with a best-fit trendline defined by the equation Y=0.2056X+0.1902, with variables as previously defined. The magnitudes of the maximum hold temperature overshoots, seen in Figure 5.10 (c), present perhaps the most obvious problem with drawing conclusions about the effect of ramp rate on densification. Since the temperature variation study showed that even a 10°C increase in temperature can substantially affect densification behavior, the overshoot of approximately 44°C in the 200°C/min test versus the less than 1°C overshoot in the 2°C/min sample prevents drawing any conclusions as to the effect of the heating rate on its own. Since the rapid heating rates also coincided with increased applied voltage and current, it is even more difficult to assign the observed behavior to specific parameters when comparing heating rate effects in SPS.

Beyond all the discussed factors which are inherent to generating fast heating rates in SPS, the very nature of rapid heating also presents problems which hinder accurate temperature measurement. Whereas temperature underestimation related to the location of temperature measurement has been explored both experimentally[79] and in simulations[33,71] for thermocouples and pyrometers, an additional complication which requires consideration is the response time, or time constant, of the temperature measurement

apparatus. This is a measure of the time required for the measurement device to change its measured temperature in response to an instantaneous change in the actual temperature, and it becomes considerably more important at high heating rates.

In the case of thermocouples used in SPS, the time constant can easily be larger than 5 seconds because only ungrounded thermocouples can be used, as otherwise the thermocouple and SPS tooling would be in direct electrical contact.[80] For example, a 1/16" diameter ungrounded thermocouple, such as that used in the GT equipment, will have a time constant of approximately 6 seconds. The maximum temperature lag for a given heating rate is calculated simply as the heating rate multiplied by the time constant[81], so the 200°C/min ramp sample should have created a temperature lag in the thermocouple of 20°C, and a 1000°C/min ramp, not unheard-of in the SPS community[2], should result in a temperature lag of 100°C. This will, therefore, add on top of the measured temperature overshoot and hinders the ability of the control equipment to respond to differences between the actual temperature and set temperature, which necessarily increases the severity of overcorrections throughout the SPS process. This is made worse in the case of a damaged thermocouple, as shown in Figure 5.11. In this figure, data for the temperature, voltage, current, displacement, and instantaneous heating rate are presented (Figure 5.11 (a-e)) for two samples made using the same materials, equipment, and set of processing conditions, but using two different thermocouples. The old, damaged thermocouple resulted in a far slower response time compared to a new thermocouple, resulting in far different microstructures (Figure 5.11 (f, g)).

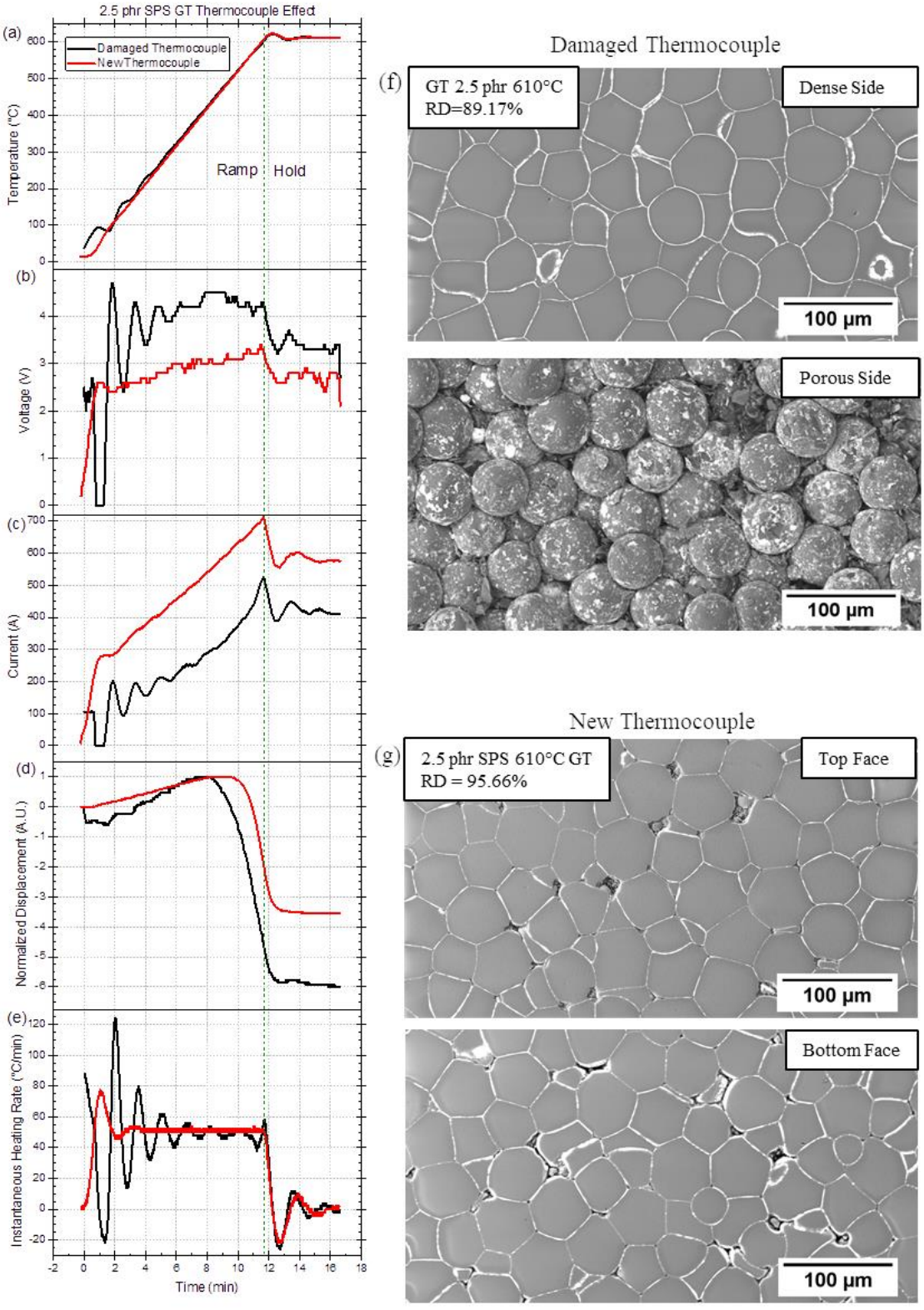
2.5 phr SPS GT Thermocouple Effect
(a)
Damaged Thermocouple
New Thermocouple
Temperature (°C)
Ramp
Hold
(b)
Voltage (V)
(c)
Current (A)
(d)
Normalized Displacement (A.U.)
(e)
Instantaneous Heating Rate (°C/min)
Time (min)
Damaged Thermocouple
(f)
GT 2.5 phr 610°C
RD=89.17%
Dense Side
100 µm
Porous Side
100 µm
New Thermocouple
(g)
2.5 phr SPS 610°C GT
RD = 95.66%
Top Face
100 µm
Bottom Face
100 µm

Figure 5.11.[65] (a) Temperature, (b) voltage, (c) current, (d) normalized displacement, and (e) instantaneous heating rate plots showing data from 2 samples of the same composition made with the same SPS equipment and with the same heating rate, maximum temperature, hold time, applied pressure, and under a vacuum atmosphere. It was found that the "damaged thermocouple" sample had a much higher response time compared to the "good thermocouple" sample and after the sample was made, it was found to be damaged and no longer usable. Although the temperature profiles seem quite similar, there was a clear difference in densification visible in the SEM images (e, f), as confirmed by the punch displacement profiles. The current and voltage profiles were far more sensitive to the difference in thermocouple behavior, as large fluctuations are evident, corresponding to the larger overcorrections made by the temperature control software. The result of the overcorrections is also seen in the instantaneous heating rate data, which shows both high fluctuations about the set heating rate of 50°C/min and a maximum heating rate greater than 120°C/min.

One final class of errors associated with high heating rates is the inability of the SPS hardware to keep up with changing conditions. It was demonstrated that, during the densification period, the punch displacement rate was fast enough that the equipment failed to maintain the programmed pressure at all but the lowest heating rates. This is shown in Figure 5.12 (a,b), in which periods of rapid displacement directly correlate with decreases in the measured applied pressure, with applied pressure decreasing from the set pressure by as much as 12.8% during densification of the 200°C/min sample. Additionally, it was generally observed that higher heating rates resulted in higher vacuum pressures in the SPS chamber, with the difference in pressure between the 2°C/min and 200°C/min samples becoming as large as 26 Pa, as shown in Figure 5.12 (c).

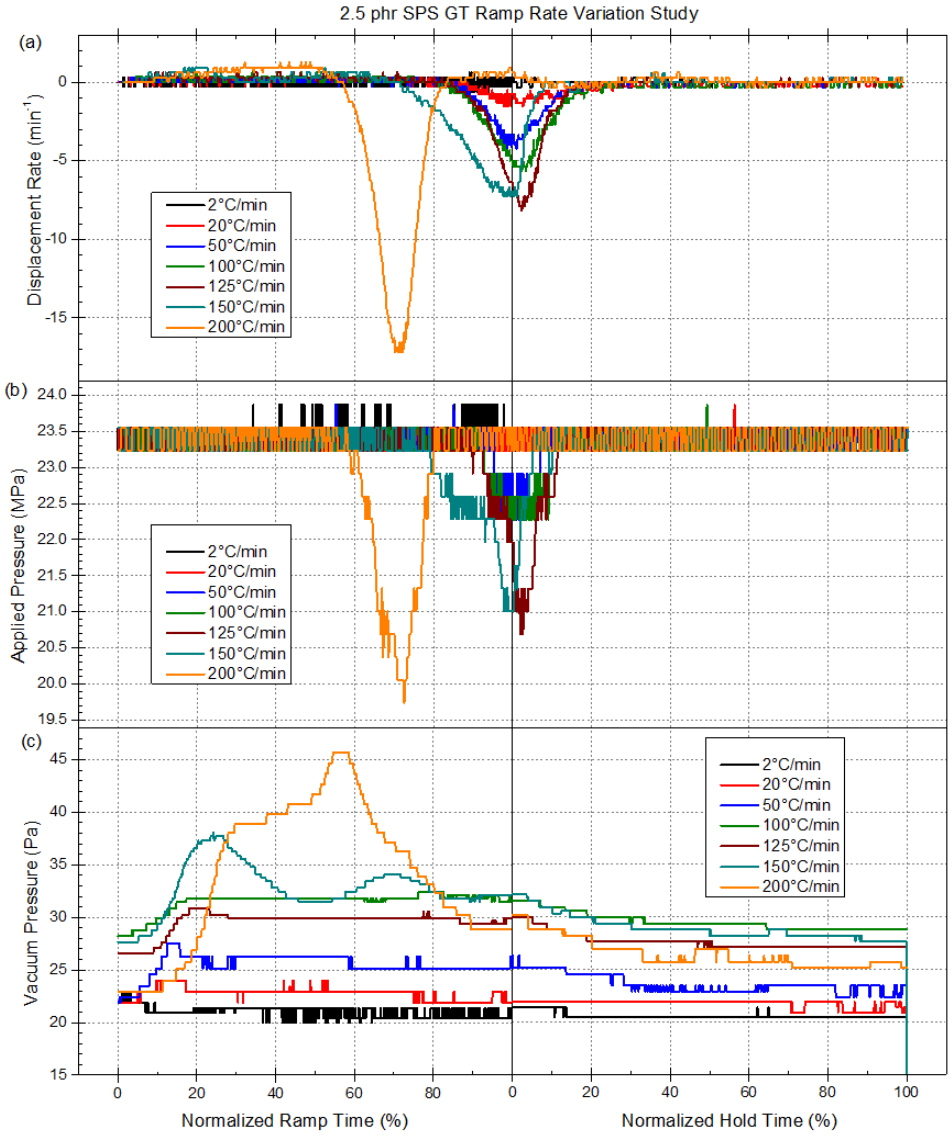

Figure 5.12. Plots of the (a) normalized displacement rate, (b) applied pressure, and (c) vacuum pressure over time for the ramp rate comparison samples. During the rapid densification periods for heating rates above 20°C/min and, especially, in the 200°C/min samples, the SPS equipment evidently cannot keep up with the shrinking powder bed, resulting in a noticeable dip in the applied pressure of as much as 12.8% or 3 MPa. Vacuum pressure seems consistently related to the ramp rate and can spike at high heating rates due to the massive overcorrections of the temperature control software. Greater heating rates resulted in larger chamber pressures, most likely owing to heat generation exceeding heat dissipation out of the chamber, thus raising the temperature of gas particles remaining in the chamber and resulting in higher chamber pressure since the chamber volume is constant.

5.7 Conclusions

In looking at the big picture of SPS processing, considering all the possible measurement errors, discrepancies between equipment hardware and software, and the sensitivity of the electrical behavior of the samples being sintered to the various experimental variables, it seems imperative that more attention be paid to the factors such as the current, voltage, instantaneous heating rate, temperature overshoot, thermal and temperature measurement lag, and differences in tooling properties and geometry. Ultimately, doing so could lead to a clearer understanding of SPS densification mechanisms and a far greater chance of demonstrating repeatability in densification behavior between labs, allowing for more rapid and cohesive progress in the field.

CHAPTER 6. ELECTRICAL CHARACTERIZATION BY MODELING OF IMPEDANCE DATA

In this chapter, impedance data from the samples presented in chapters 3-5, as well as some additional samples, will be analyzed in more depth using equivalent circuit fitting. The results of the fitting are then used to gain enhanced insight into the behavior of the materials systems, which in turn provide supporting information regarding the effects of different processing parameters on both the ITO-borosilicate powder mixes and sintered samples.

6.1 Initial equivalent circuit model

The starting point for the development of the equivalent circuit models which have been employed in the present work was a model developed by a previous student[12], which was applied to mixtures of borosilicate glass microspheres and ATO nanoparticles. This model, which has been reproduced in

Figure 6.1, provides representation of the electrical behavior within the individual ATO and glass phases, as well as accounting for the effects of ATO-glass interfaces and ATO-ATO particle contacts. The model was developed by first modelling the pure glass and pure ATO phases, which were fit to a parallel RC circuit and a series RL circuit, respectively.[12] These electrical responses were measured on the as-received pure powders under applied pressure, using the setup previously described in section 3.1. Impedance testing of a partially-sintered pure ATO sample gave a series RL in series with a parallel RC behavior.

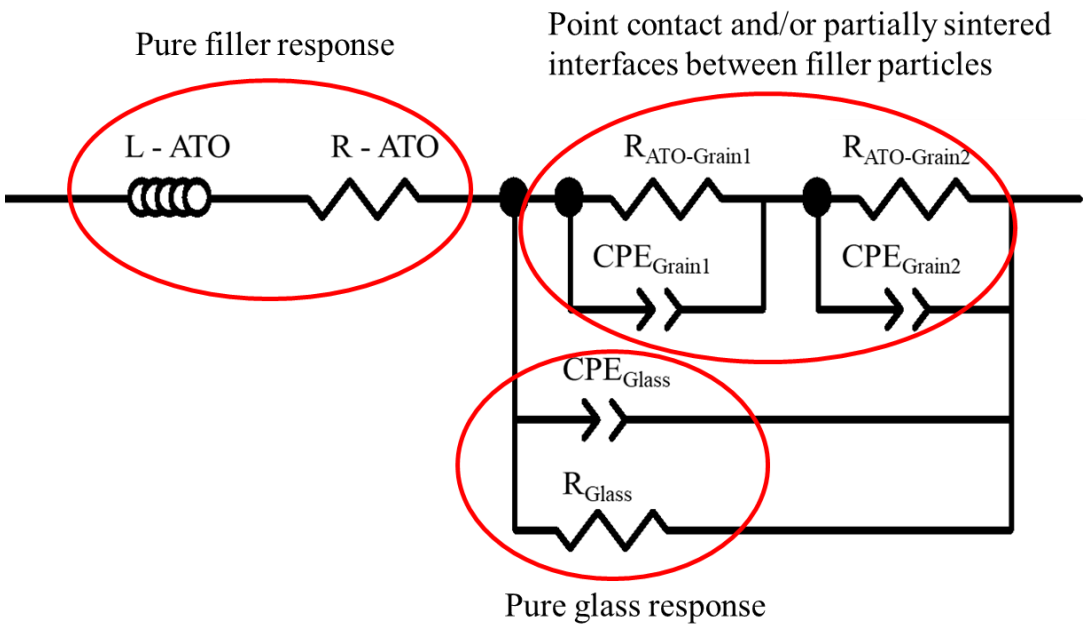

Figure 6.1. Equivalent circuit model developed in [12] to fit the impedance responses of sintered ATO-borosilicate composites fabricated using hot pressing. Subsections of the full model, circled in the diagram, were derived from fitting the responses of isolated phases and interfaces which comprise the actual composite microstructure. The individual elements were combined as shown to make the composite equivalent circuit, to which the impedance responses of the composite samples were successfully fitted. Adapted from [12].

This corresponded to an observed microstructure of a network of partially-connected ATO particles. Since this sample was fabricated under the same conditions as the glass composite samples, it was expected that this microstructure would be present in the ATO phase between the deformed glass particles, as was later confirmed. The last building block of the combined circuit came from a test of the pure ATO powder without any applied pressure, representing a structure of point contacts between ATO particles. This was fit to a series of two parallel RC elements. Through trials involving arranging each of the circuit components in different ways and attempting to fit impedance data from the sintered composite samples to the combined circuit, a configuration was found, shown in Figure

6.1, which consistently allowed accurate fitting of many samples over a range of filler concentrations.

6.2 ITO-borosilicate model

Due to the similarity in materials systems between the ATO-borosilicate system and the ITO-borosilicate system explored in the present work, it was expected that the same microstructural features upon which that model was developed would be present in the ITO composites and, therefore, the same equivalent circuit model would be applicable. The pure ITO response was measured on the dry-pressed ITO powder, giving the data shown in Figure 6.2(a). In the complex impedance plot of the data, the dominant trend in the data was a vertical line in the fourth quadrant, which corresponds to a series RL equivalent circuit (Figure 6.2 (b)). Regions of positive slope and zero slope in the frequency-explicit impedance magnitude, as well as both positive and near-zero values in the frequency-explicit impedance phase angle, corroborated the apparent series RL behavior (not shown). Upon fitting the data to a series RL model, a reasonable fit was achieved (Figure 6.2 (a, c)). However, it is also apparent that the observed response did not show ideal series RL behavior since the curve is not strictly vertical.

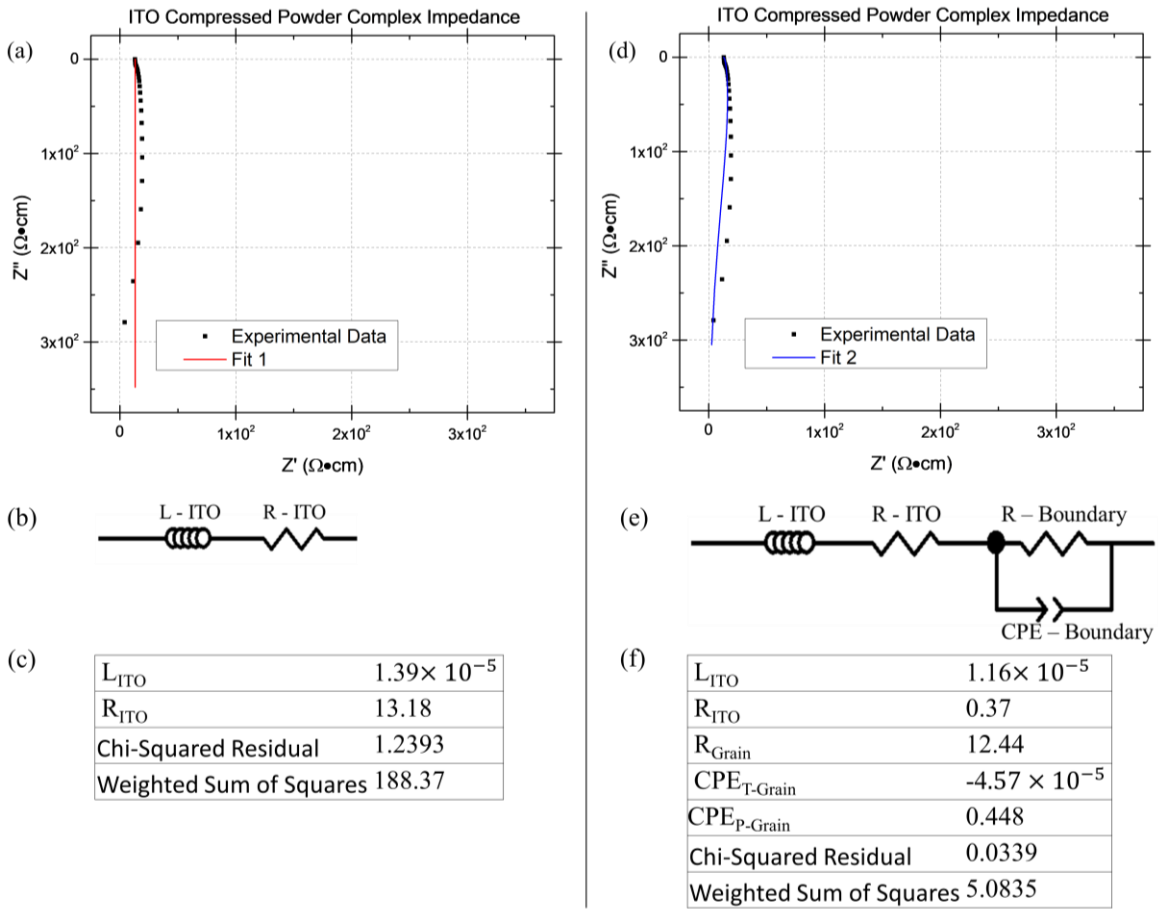

Figure 6.2. (a) A complex impedance plot showing the impedance response of compacted pure ITO powder (black squares) and an equivalent circuit fit (red line based on the circuit shown in (b). Element values and the resulting residuals are shown in (c). A second fit (blue line), more closely following the trend in the data, is shown in (d). This was based on a circuit model with additional elements, shown in (e). The element values (f) indicated that the added resistor and parallel CPE with a negative capacitance value was necessary to imitate the curvature in the experimental data. Lower values for the chi-squared and weighted sum of squares residuals confirmed that the fit was improved compared to the original series RL fit.

An improved fit was found, as shown in Figure 6.2 (d), by adding a parallel R-CPE circuit to the original series RL circuit (Figure 6.2 (e)). In doing so, the fit was able to curve in a similar manner to the experimental data, increasing the number of experimental features encapsulated in the fit. Additionally, this new model increased the accuracy of the fit as verified by higher values of the chi-squared and weighted sum of squares residuals

of the original model (Figure 6.2 (c)) compared to the new model (Figure 6.2 (f)). One noteworthy feature of the improved fit is the negative CTE-T value. Negative capacitance has been reported for a variety of materials systems[82-85], especially for multi-phase systems, and was found to be present in conducting filler – insulating matrix composites in multiple previous studies.[86,87] In the literature, negative capacitance has been attributed to space charge effects at interfaces or grain boundaries.[84,85] In the electrical data, evidence supporting a negative capacitance can be seen when the impedance data is converted to the permittivity.[86] In the frequency-dependent plot of the real permittivity, the data shows relatively small fluctuations around the $\epsilon' = 0$ line at high frequencies. However, below some threshold frequency, there is a rapid decrease in $\epsilon'$of several orders of magnitude greater than the fluctuations, with a consistent decreasing trend. Since the capacitance and permittivity only differ from scaling by the sample geometry, this negative ϵ' is indicative of negative real capacitance. Although deviation from a strictly vertical behavior in the fourth quadrant of the complex impedance could also be ascribed to a parallel RL circuit with a positive inductance, it was found to be more appropriate to use a negative capacitance for two reasons. Often negative capacitance and positive inductance are used interchangeably, and the preferred term for a given material system is just based on whether capacitive or inductive behavior is more expected for that material system.[84] In the present case, negative capacitance is preferred since the polarization response at grain/phase boundaries is commonly modelled with a separate parallel RC circuit.[8,12] Furthermore, negative capacitance is more appropriate here because a way to account for non-ideal behavior is not available for inductors, but is available for capacitors through the use of a constant phase element (CPE) in place of the capacitor in the model. Since a capacitor is

equivalent to a CPE with a CPE-P value of 1 and the value obtained in the fit was 0.448, the fit accounted for substantial deviation from ideal behavior, which an inductive element cannot do. Upon attempting to fit with an inductor in place of the CPE, the optimized fit had chi-squared and weighted sum of squares residual values of 0.0949 and 14.2, respectively, which are about 3 times the corresponding values for the optimized fit using a CPE. Therefore, a CPE with a negative capacitance was clearly the superior choice for the equivalent circuit.

A final point to be addressed regarding the impedance data for the compressed ITO nanopowder is that the need for the addition of the parallel R-CPE element did not follow the model for compressed ATO nanopowder found in previous work using the same testing apparatus.[1] In that case, it was found that only the series RL elements were necessary to accurately model the data. However, it was also found that the present model with the incorporation of the negative CPE in parallel with a resistor was the appropriate circuit model for a pure ATO sample made by sintering the nanopowder via hot-pressing.[12] For that sample, the need for the additional elements was attributed to changes in the interfaces between the nanoparticles as the sintering process deformed the particles to fill the available volume. This implies that the new interfaces are the source of the negative capacitance, leading to the question of why this behavior was seen in the ITO nanopowder that had not been sintered. This may be due to a few factors which gave the ITO powder similar interfacial features to the sintered ATO. The ITO nanopowder exhibited a high degree of aggregation and agglomeration in comparison to similar nanopowders and in TEM images the particles even appeared to be fused together, as seen in Figure 2.1(a). This could have resulted from the process used to synthesize this particular ITO nanopowder or

may have been induced after synthesis due to cyclic exposure to high and low humidities, which has been reported in the literature to induce an effect similar to cold sintering[88] for nanopowders.[89] In either case, it seems that the powder exhibited similar interfacial features in comparison with the partially sintered ATO and thus possessed a negative capacitance behavior as a result.

To determine how the sintering process would affect the impedance behavior of the ITO, impedance tests were conducted on pure ITO samples sintered via hot pressing (Figure 6.3) under the same conditions as the hot-pressed composite samples as discussed in Section 2.2. As expected based on reports of poor sinterability for ITO[55,56], the final densities of these samples were far below the theoretical values, and high porosity was confirmed through microscopy.

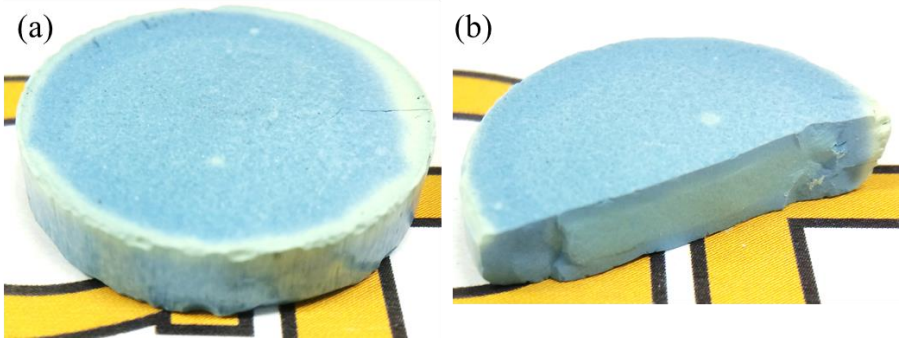

Figure 6.3. Optical images of two different hot-pressed pure ITO samples. Some notable features of these samples are the light-yellow rings at the outer edge, fairly low relative densities, and a yellow-green core, which can be seen in the second sample (b). The ITO starts yellow and the surface becomes blue due to reduction of the oxide so the core color results from the natural appearance of the oxide.

As with the data for the compacted ITO nanopowder, the data (Figure 6.4 (a)) showed primarily series LR behavior but with some deviation in Z' which could be fit by adding a parallel R-CPE circuit with a negative capacitance (Figure 6.4(b)). The circuit element

values (Figure 6.4(c)), in comparison to those of the compacted ITO nanopowder (Figure 6.2 (f)), show a smaller total resistance, smaller inductance and capacitance values, and a CPE-P value closer to that of ideal capacitive behavior. The reduced resistance was expected since the sintering process improves the quality of the interfaces between the particles and because the sintering was conducted in a reducing atmosphere, which has been demonstrated to increase the conductivity of ITO.[90] The apparent horizontal trend near the Z''=0 line could not be fit, nor could an explanation for its presence be found, but the trend was consistent among the sintered pure ITO samples as well as in the most conducting composite samples. This phenomenon was not explored further.

(a)

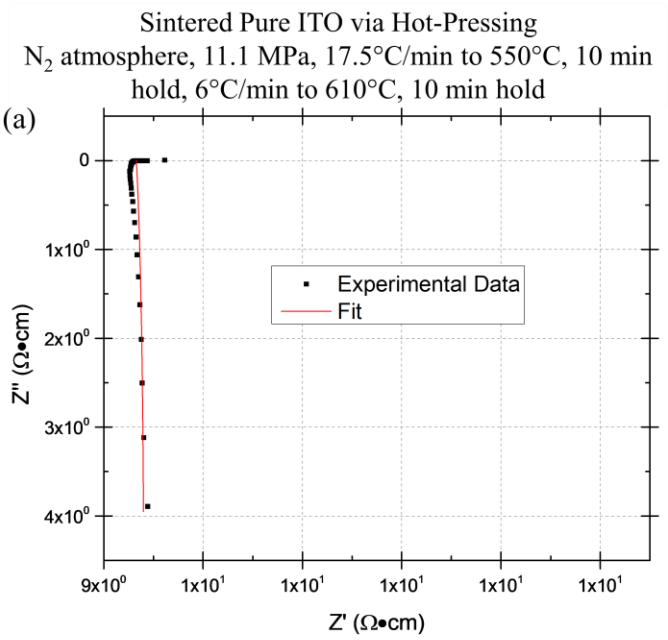

(b)

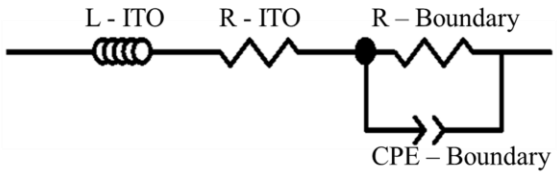

(c)

L_{ITO}	5.57×10^{-7}
R_{ITO}	6.07
R_{Grain}	3.258
$CPE_{T\text{-}Grain}$	-1.28×10^{-7}
$CPE_{P\text{-}Grain}$	0.813
Chi-Squared Residual	0.108
Weighted Sum of Squares	14.9

Figure 6.4. (a) Experimental complex impedance data (black squares) and equivalent circuit fit (red curve) for a pure ITO sample sintered via hot pressing. Like the data for the compacted ITO nanopowder, this data shows primarily series LR behavior with curvature that was fit by adding a parallel R-CPE circuit with a negative CPE-T value, with the complete circuit shown in (b). The element values and residuals for the fit are shown in (c).

Impedance testing on hot-pressed pure borosilicate glass samples gave a parallel R-CPE response, as indicated by the depressed semi-circular behavior in the first quadrant in the representative response shown in Figure 6.5(a). A fit using that circuit (Figure 6.5 (b))

gave a reasonable match to the trend in the experimental data as confirmed with the low residuals (Figure 6.5(c)). However, one issue to note with the fit resistance value is that the resistance of the pure glass should be at least $10^{12}\ \Omega$ rather than the fit value of 1.03×10^{11}. It is plausible that the discrepancy was caused by the carbon contamination observed in the hot-pressed samples, some of which may have remained even after isolating the center of each sample by sectioning off the edge regions. It is also possible that the testing environment influenced the impedance response since these particular measurements were conducted in late June and humidity has been proven to be able to significantly affect impedance data especially for insulating samples.[49]

Despite how close the fit was using the simple parallel R-CPE circuit, it was found that the fit could be greatly improved, as is clear in the complex impedance (Figure 6.5 (d)), if using a more complex circuit model based on that derived for ATO-glass composites.[12] This model, shown in Figure 6.5 (e), includes a series of 2 parallel R-CPE circuits, which is in parallel with the parallel R-CPE circuit of the glass. As indicated by the labels on the model, the additional elements represent impedance responses from the interfaces between the sintered glass particles. The need for these elements to optimize the fit is not surprising, since the sintering process was tailored to maintain boundaries between the glass particles and both the bulk glass phase and the interfaces should give separate impedance responses. With the addition of these elements to the model, the residuals were decreased by more than 1 order of magnitude (Figure 6.5(f)).

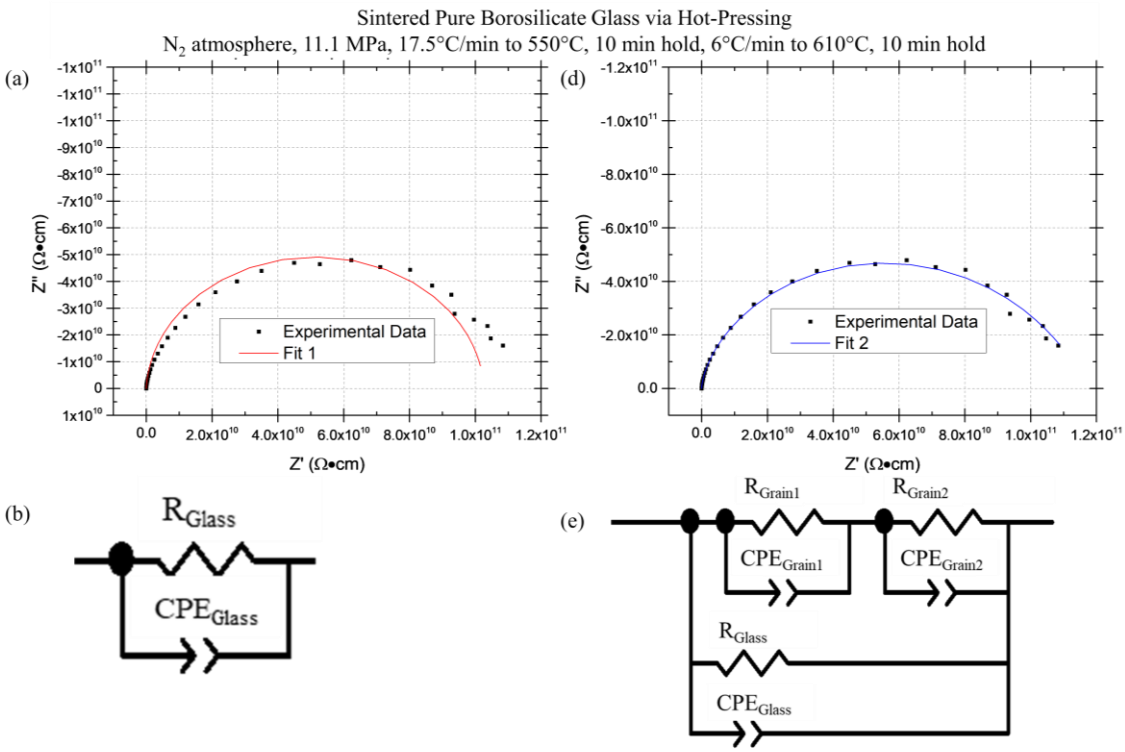

(c)

Chi-Squared Residual	0.038314
Weighted Sum of Squares	5.3256
R_{Glass}	1.03E+11
$CPE_{T\text{-}Glass}$	1.28E-12
$CPE_{P\text{-}Glass}$	0.97236

(f)

Chi-Squared Residual	0.001848
Weighted Sum of Squares	0.25133
R_{Grain1}	1.03E+11
$CPE_{T\text{-}Grain1}$	1.62E-12
$CPE_{P\text{-}Grain1}$	0.58463
R_{Grain2}	1.54E+10
$CPE_{T\text{-}Grain2}$	5.36E-12
$CPE_{P\text{-}Grain2}$	1
R_{Glass}	4.22E+14
$CPE_{T\text{-}Glass}$	9.07E-13
$CPE_{P\text{-}Glass}$	1

Figure 6.5. (a) Characteristic complex impedance response of hot-pressed pure glass samples, with the experimental data shown as black squares and a fit, shown as a red curve, using a simple parallel R-CPE circuit given in (b). The element values derived for this circuit, shown in (c), resulted in a reasonable fit, as the curve primarily exhibited the behavior expected from such a circuit. An improved fit (d) was achieved with a larger circuit (e), having far smaller residuals (f) and accounting for more of the microstructural features in the sintered samples.

Upon completion of finding equivalent circuits which fit each of the presented individual components of the actual composite microstructure, these elements could then

be combined to create a circuit which could fit the impedance data of the composite samples, as had been done with the ATO composites previously.[12]

6.3 Final composite equivalent circuits

Based on both the similar materials system compared to the previous ATO-borosilicate samples as well as the similar equivalent circuits found for the isolated components of the overall composite microstructure, the total equivalent circuit for the ATO-borosilicate composites[12] (Figure 6.1) was used to attempt to fit to the data for the present composites. In general, good fits were found for all pre-percolated samples using that equivalent circuit, an example of which is shown for a 0.01 phr sample in Figure 6.6. Here, it is shown that the data (black squares) and the fit (red curve) overlap in not only the complex impedance (Figure 6.6(a)) but also in the other three dielectric functions, namely the admittance (Figure 6.6(b)), the permittivity (Figure 6.6(c)), and the dielectric modulus (Figure 6.6(d)). Fitting to all of the dielectric functions has been proven to be very important for accurate characterization of the impedance response since the different functions emphasize or reveal different features of the impedance response which would be missed if only fitting to the impedance.[5,8,91,92] The quality of the fit across all functions indicates that the chosen circuit is appropriate for the composite samples in the present work.

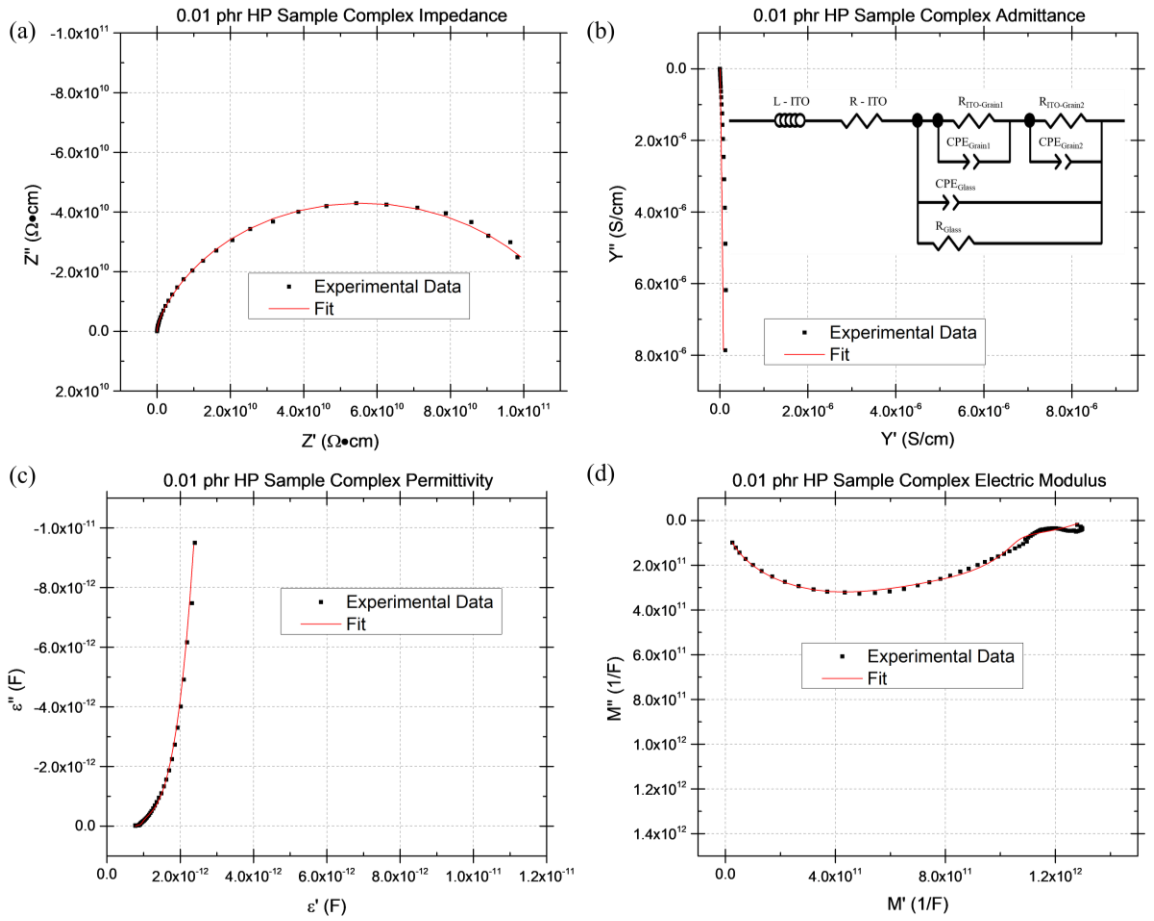

Figure 6.6. Impedance data (black) and equivalent circuit fit (red) in the (a) complex impedance, (b) complex admittance, (c) complex permittivity, and (d) complex dielectric modulus, for a 0.01 phr HP sample made under the standard HP conditions (see Section 2.2). Good fits were simultaneously achieved in all of the functions, indicating that the equivalent circuit was correct.

For the post-percolation composites, however, it was found that the complete model would give unstable fits. Instability in the fit values, indicated by large error values and failure to converge to a specific value, often serves as an indicator that the circuit model is incorrect.[93,94] For the post-percolation microstructure a different circuit would be expected since the availability of continuous conducting networks allows the current to avoid interacting with the glass matrix. The absence of these interactions would, logically, remove the parallel R-CPE elements pertaining to the glass from the overall equivalent

circuit. Good fits in all 4 dielectric functions based on the modified circuit were found for samples in the composition range just beyond the percolation threshold, an example of which is shown in Figure 6.7 (a-d).

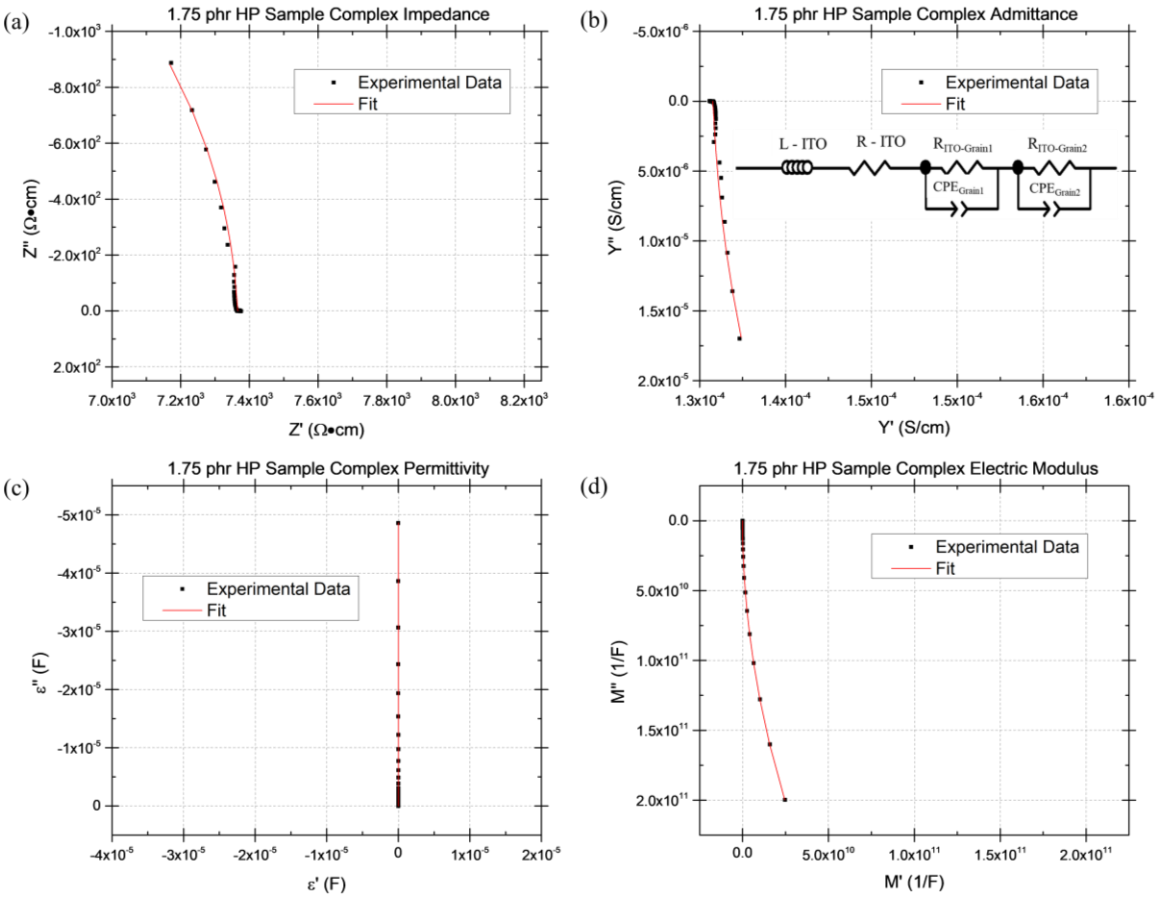

Figure 6.7. Plots of the (a) complex impedance, (b) complex admittance, (c) complex permittivity, and (d) complex dielectric modulus for testing results on a 1.75 phr HP sample (black squares) and the resulting fit (red curve) when using the circuit shown in the inset of (b).

For the samples well above percolation, one of the two parallel R-CPE circuits representing the grains was also unstable, and fitting was improved by removing the "grain 2" elements in addition to the "glass" elements. Such a change is plausible for the samples with filler concentrations well above the percolation threshold as the additional filler

creates additional potential pathways for the current, allowing it to avoid tenuous pathways or those with otherwise weak connections or poor interfaces. This modified circuit, with glass and grain 2 elements removed, was found to give good fits for the impedance data for samples with the highest ITO concentrations, as shown by the example in Figure 6.8 for a 7.5 phr HP sample. It should be noted that this model is identical to that which represented the partially-sintered pure ITO, which makes a lot of sense if there is enough ITO present.

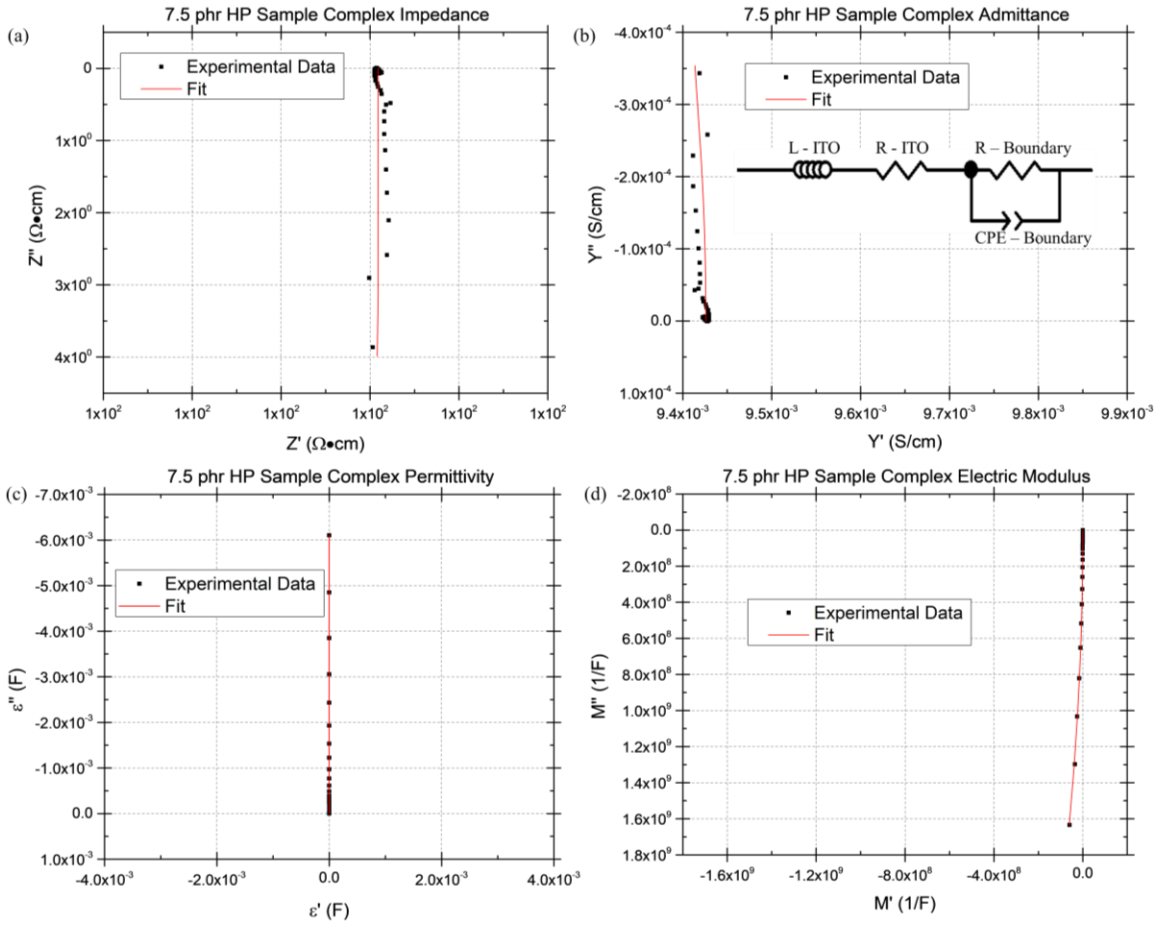

Figure 6.8. Plots of the (a) complex impedance, (b) complex admittance, (c) complex permittivity, and (d) complex dielectric modulus for testing results on a 7.5 phr HP sample (black squares) and the resulting fit (red curve) when using the circuit shown in the inset of (b).

The good fits in all four functions for the chosen equivalent circuits, seen over a wide number of the samples in this study, strongly indicate that these circuits are correct. Therefore, examination of how the individual elements change with changing processing parameters will reveal how the respective microstructural features changed, thus providing a more detailed characterization of the effects of changing processing parameters across and within the various sample sets.

6.4 HP composite changes with changing ITO concentration

Results of the fitting of all the hot-pressed composite sample data is given in Table 6.1. Fitting for all data followed one of the four applicable circuit models, summarized in Figure 6.9, and the table shows that the 0.0 phr samples were fit using the model in Figure 6.9(a), samples with compositions between 0.001 phr and 0.5 phr were fit using Figure 6.9 (b), 1.0 and 1.75 phr samples were fit to Figure 6.9 (c), and samples with compositions of 2.5 and greater were fit to Figure 6.9 (d).

Table 6.1. Circuit Element Values for HP Samples, 610°C Hold, 11.1 MPa Applied

Composition (phr)	Sample	L-ITO (H)	R-ITO (Ω)	$R_{TTO\text{-}Grain1}$ (Ω)	$CPE_{T\text{-}Grain1}$ (F)	$CPE_{P\text{-}Grain1}$	$R_{TTO\text{-}Grain2}$ (Ω)	$CPE_{T\text{-}Grain2}$ (F)	$CPE_{P\text{-}Grain2}$	R_{Glass} (Ω)	$CPE_{T\text{-}Glass}$ (F)	$CPE_{P\text{-}Glass}$
0	1	NA	NA	1.54E+10	5.36E-12	1.00	1.03E+11	1.62E-12	0.585	4.22E+14	9.07E-13	1.00
0	2	NA	NA	1.27E+10	5.63E-13	1.00	8.48E+12	6.77E-13	0.699	4.21E+14	7.52E-13	1.00
0	3	NA	NA	4.60E+09	2.49E-13	1.00	2.17E+11	1.20E-12	0.689	4.21E+14	9.00E-13	1.00
0.001	1	4.75E-07	6.069	1.41E+12	1.30E-12	1.00	3.98E+11	1.17E-12	0.627	4.21E+14	9.32E-13	1.00
0.001	2	4.75E-07	6.069	2.47E+10	1.10E-12	1.00	1.14E+11	2.12E-12	0.576	4.21E+14	1.03E-12	1.00
0.001	3	4.75E-07	6.069	2.73E+11	5.46E-12	1.00	1.30E+12	3.09E-12	0.562	4.21E+14	1.38E-12	1.00
0.01	1	4.75E-07	6.069	6.32E+09	8.19E-13	1.00	1.09E+11	2.82E-12	0.710	4.21E+14	1.22E-12	1.00
0.01	2	4.75E-07	6.069	4.41E+12	7.60E-13	1.00	3.07E+11	8.76E-13	0.659	4.21E+14	8.38E-13	1.00
0.01	3	4.75E-07	6.069	5.99E+10	6.09E-12	1.00	2.34E+11	2.60E-12	0.580	4.21E+14	1.18E-12	1.00
0.1	1	4.75E-07	6.069	7.13E+11	2.73E-12	1.00	1.00E+11	2.27E-12	0.788	4.21E+14	1.33E-12	1.00
0.1	2	4.75E-07	6.069	9.40E+09	2.38E-12	1.00	5.88E+12	2.25E-12	0.746	4.21E+14	1.52E-12	1.00
0.1	3	4.75E-07	6.069	8.98E+10	2.39E-12	1.00	2.89E+12	1.68E-12	0.882	4.21E+14	9.26E-13	1.00
0.5	1	4.75E-07	6.069	4.15E+04	6.10E-12	1.00	5.20E+05	1.95E-11	0.814	4.21E+14	1.76E-13	1.00
0.5	2	4.75E-07	6.069	5.99E+05	6.01E-11	1.00	3.34E+06	2.60E-10	0.614	4.21E+14	9.16E-13	1.00
0.5	3	4.75E-07	6.069	1.45E+09	7.11E-11	1.00	1.74E+10	1.43E-11	0.762	4.21E+14	6.51E-13	1.00
1	1	4.75E-07	6.069	1.39E+04	3.05E-11	1.00	3.22E+04	1.38E-11	0.949			
1	2	4.75E-07	6.069	1.15E+04	9.42E-12	1.00	4.58E+04	1.69E-11	0.941			
1	3	4.75E-07	6.069	2.02E+04	2.18E-11	1.00	1.36E+05	4.60E-11	0.892			
1.75	1	4.75E-07	6.069	5.19E+02	8.84E-11	1.00	1.51E+03	8.41E-11	0.759			
1.75	2	4.75E-07	6.069	4.24E+03	7.74E-12	1.00	3.13E+03	9.76E-11	0.700			
1.75	3	4.75E-07	6.069	4.21E+03	1.31E-11	1.00	1.47E+03	1.25E-12	1.00			
2.5	1	4.75E-07	6.069	1.40E+03	2.00E-11	0.948						
2.5	2	4.75E-07	6.069	1.06E+03	4.89E-09	0.596						
2.5	3	4.75E-07	6.069	2.94E+03	4.10E-12	0.933						
5	1	1.44E-05	6.069	7.99E+02	2.48E-11	1.00						
5	2	2.47E-06	6.069	2.17E+02	3.89E-11	1.00						
5	3	2.42E-06	6.069	2.37E+02	3.65E-11	1.00						
7.5	1	2.90E-06	6.069	1.72E+02	8.95E-11	1.00						
7.5	2	4.31E-06	6.069	3.27E+02	2.59E-11	1.00						
7.5	3	7.95E-07	6.069	1.00E+02	1.61E-11	1.00						
10	1	4.75E-07	6.069	5.64E+01	3.50E-11	1.00						
10	2	4.75E-07	6.069	1.34E+02	-1.33E-09	0.874						
10	3	4.75E-07	6.069	9.58E+01	-1.22E-09	0.913						

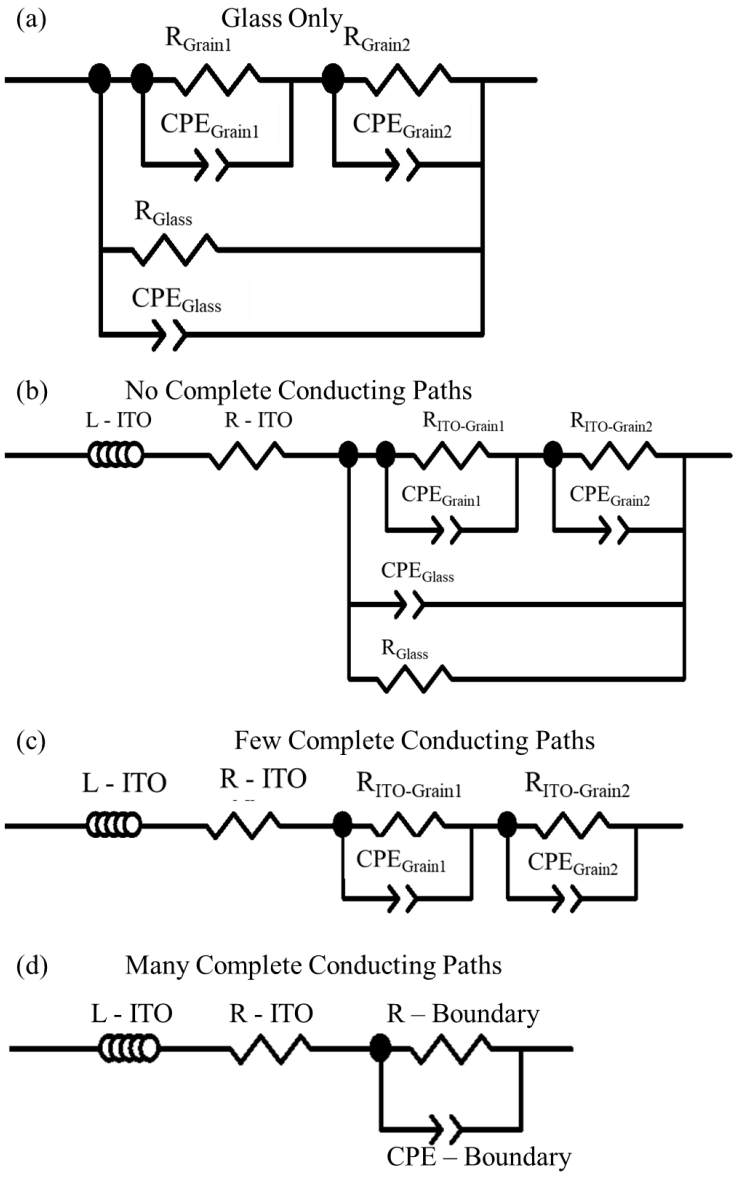

Figure 6.9. Derived equivalent circuits for (a) pure glass (0.0 phr) samples, (b) pre-percolation samples containing ITO, (c) Samples with compositions just above percolation, and (d) samples with compositions far above percolation. Changes in the circuit itself, rather than just the element values, indicate significant changes to the nature of current flow in the samples.

One feature seen in the table is a constant value for the ITO resistor and the glass resistor, when present, across all samples. Furthermore, the inductance value and CPE-P values for the glass and one of the two grains is constant across most of the samples. In all

cases where the circuit incorporated both grain 1 and grain 2 elements, the parallel R-CPE circuit possessing a CPE-P value of 1 was designated as grain 1 based on the reasoning that calling either set of elements grain 1 will result in the same fit. This being the case, establishing a convention that grain 1 is that with a CPE-P of 1 increases the likelihood that all grain 1 elements will represent similar microstructural characteristics and should therefore result in a more valid comparison in the grain 1 and grain 2 element values between various samples.

For circuit elements representing the pure ITO and glass phases, appropriate values were held constant based on the reasoning that these values should be very close across all tests since the same ITO and glass are used. Fixing these values was useful primarily because it prevents the fitting software from using unreasonable values for these elements. Due to the large number of elements in the model, close fits can be achieved by multiple combinations of element values, many of which use unreasonable values for multiple elements to achieve the same shape of the fit. In such cases, the starting values of the elements were far enough from the correct values that the software reached a local minimum in deviation from the experimental data. Since the fitting process works by iteratively changing element values to decrease this deviation, it will always settle in the local minimum closest to the starting values. This necessitates that the user of the fitting program can rule out unreasonable values based on knowledge of the properties of the sample. Whenever one of the element values can be safely assumed to be constant, it is advantageous to do so since it reduces the number of inappropriate element value combinations that the software can find to give a close fit to the data. This not only makes

it more likely that the final fit is physically meaningful, but also reduces fitting time and is therefore very useful.

In addition to improving the likelihood of physically meaningful element values in the fit, holding appropriate values constant allowed trends in the data to be more easily spotted, thus facilitating comparisons between impedance responses of samples made under different processing conditions. Differences are especially easy to see when presented as plots, which can be seen in Figure 6.10. Two common trends seen here, higher variance in pre-percolation samples and lower variance in post-percolation samples, mirror those seen in the resistivity (Figure 4.14). Furthermore, the general shape of the HP resistivity plot is also followed by the normalized resistances for both the grain 1 and grain 2 elements (Figure 6.10).

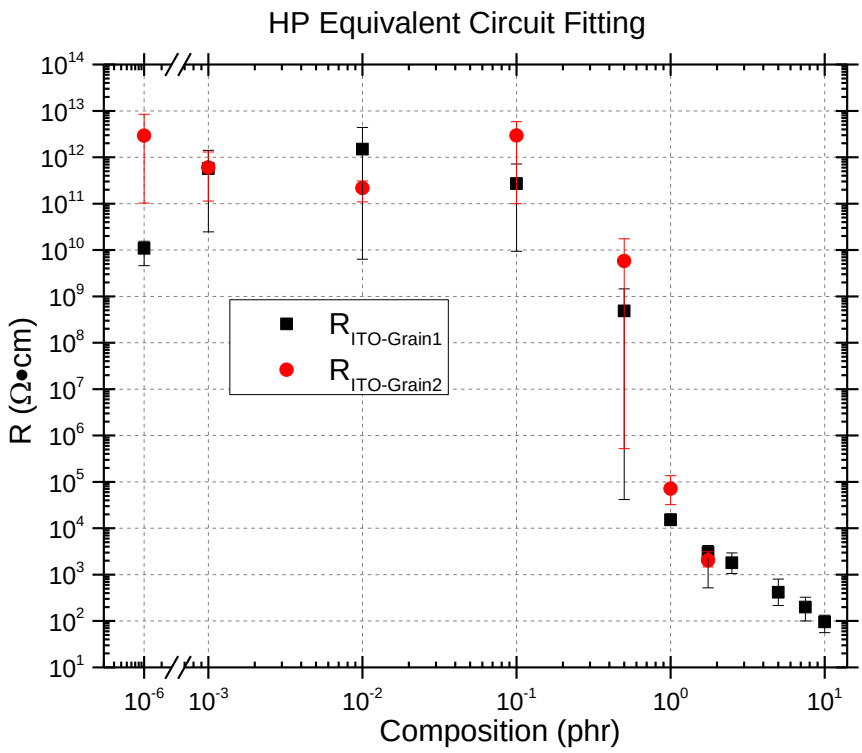

Figure 6.10. Geometry-normalized resistance values for the grain 1 and grain 2 resistors in the equivalent circuit fits for the hot-pressed samples. The general trends as a function of sample composition are similar between the two, and both are similar to the trend in the corresponding resistivity data for these samples, as would be expected. The similarities between the resistivity and grain resistance values seen here are representative of those seen for all other sample sets with changing composition.

Comparison of the CPE-T values of both grains as a function of ITO concentration in the HP fitting (Figure 6.11) again shows similar values and the same general trend between them. In the plot there seems to be two different regimes of relatively constant values with an abrupt jump of about one order of magnitude between them, which occurs between 0.5 phr and 1.0 phr. It would be reasonable to expect that such a shift would mirror the jump in resistivity (Figure 4.14) upon crossing the percolation threshold and, upon comparison of the two plots, this is indeed the case. What may not be expected is that the jump in

capacitance is to larger values upon reaching percolation, since capacitive behavior is usually associated with insulating behavior. Although there is certainly some microstructural feature responsible for this behavior, an explanation has not yet been found.

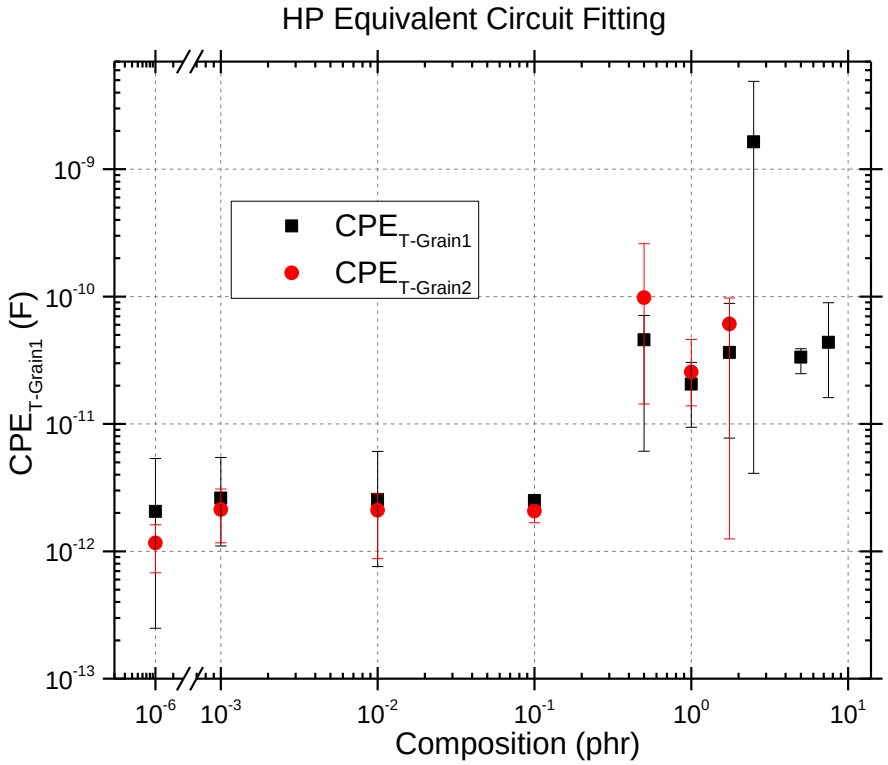

Figure 6.11. CPE-T values for the grain 1 and grain 2 constant phase elements in the HP equivalent circuit fits. The same general behavior is seen in both values as a function of composition, in which there are relatively consistent values with increasing ITO concentration up to 0.1 phr followed by a jump to larger values which again remain relatively constant.

6.5 SPS trends in comparison to the HP trends

Equivalent circuit fitting element values for the SPS UA 610°C samples are shown in Table 6.2. This fitting was carried out on both the initial and retested impedance data for these samples, as explained in section 4.2.2, so the 0.01 phr sample data is again absent in

the retest data. The data features the same progression between the different circuits given in Figure 6.9, but without the first circuit since no pure glass samples were made in this sample set. Since the percolation threshold was not seen until 2.5 phr for this sample set the corresponding circuit change occurs at this composition. No 1.75 phr sample was made, making the 2.5 phr sample the only one to exhibit the two-grain circuit without glass elements in both the initial tests and retests. However, the 5.0 phr sample seems to show behavior between this circuit and the 1-grain circuit, since its CPE-T was positive in both data sets.

Table 6.2. Equivalent Circuit Fit Values for SPS UA 610°C Samples

SPS UA 610°C Initial Tests

Composition (phr)	L-ITO (H)	R-ITO (Ω)	$R_{ITO\text{-}Grain1}$ (Ω)	$CPE_{T\text{-}Grain1}$ (F)	$CPE_{P\text{-}Grain1}$	$R_{ITO\text{-}Grain2}$ (Ω)	$CPE_{T\text{-}Grain2}$ (F)	$CPE_{P\text{-}Grain2}$	R_{Glass} (Ω)	$CPE_{T\text{-}Glass}$ (F)	$CPE_{P\text{-}Glass}$
0.001	4.75E-07	6.069	1.54E+08	5.62E-13	1.00	6.55E+09	1.21E-11	0.473	4.21E+14	7.85E-13	1
0.01	4.75E-07	6.069	1.91E+10	3.64E-12	1.00	3.65E+10	2.23E-11	0.480	4.21E+14	4.29E-13	1
0.1	4.75E-07	6.069	2.00E+09	8.58E-12	1.00	4.29E+09	1.35E-10	0.345	4.21E+14	3.32E-13	1
0.5	4.75E-07	6.069	5.45E+07	2.36E-13	1.00	1.08E+10	6.89E-11	0.598	4.21E+14	3.46E-13	1
1	4.75E-07	6.069	7.00E+08	1.30E-12	1.00	1.01E+10	4.86E-11	0.361	4.21E+14	5.12E-13	1
2.5	4.75E-07	6.069	1.14E+04	3.03E-11	1.00	3.03E+04	6.89E-11	0.810			
5	9.25E-06	6.069	6.75E+02	1.34E-11	1.00						
7.5	4.45E-06	6.069	8.07E+01	-1.24E-08	0.657						
10	4.21E-06	6.069	2.65E+01	-6.67E-08	0.716						

SPS UA 610°C Retests

Composition (phr)	L-ITO (H)	R-ITO (Ω)	$R_{ITO\text{-}Grain1}$ (Ω)	$CPE_{T\text{-}Grain1}$ (F)	$CPE_{P\text{-}Grain1}$	$R_{ITO\text{-}Grain2}$ (Ω)	$CPE_{T\text{-}Grain2}$ (F)	$CPE_{P\text{-}Grain2}$	R_{Glass} (Ω)	$CPE_{T\text{-}Glass}$ (F)	$CPE_{P\text{-}Glass}$
0.001	4.75E-07	6.069	1.35E+11	3.22E-13	1.00	1.41E+12	8.16E-13	0.601	4.21E+14	6.39E-13	1
0.1	4.75E-07	6.069	1.13E+11	2.27E-13	1.00	1.37E+12	6.03E-13	0.589	4.21E+14	4.32E-13	1
0.5	4.75E-07	6.069	1.45E+11	1.48E-13	1.00	2.14E+12	5.96E-11	0.635	4.21E+14	4.81E-13	1
1	4.75E-07	6.069	2.76E+11	1.30E-12	1.00	1.01E+10	4.86E-11	0.361	4.21E+14	5.12E-13	1
2.5	4.75E-07	6.069	1.14E+04	3.03E-11	1.00	3.03E+04	6.89E-11	0.810			
5	9.25E-06	6.069	6.75E+02	1.34E-11	1.00						
7.5	4.45E-06	6.069	8.07E+01	-1.24E-08	0.657						
10	4.21E-06	6.069	2.65E+01	-6.67E-08	0.716						

When comparing the grain 1 and 2 resistor values for the two sintering methods (Figure 6.12), additional distinct differences are apparent. An increase is seen at compositions in the middle of the pre-percolation region for the grain 1 HP and SPS initial test elements but not in the respective grain 2 elements. There is no clear explanation for this trend. The observation of this trend in the HP grain 1 data seems to contradict the consistency seen in the HP resistivity values for the pre-percolation compositions (Figure 4.14). However, this discrepancy was not seen when comparing the HP grain 1 and 2 resistances with each other, as was done in Figure 6.10. The grain 2 resistance data show the opposite trend relative to the grain 1 data for the pre-percolation samples so the average resistance of the two grains gives the same trend as the resistivity. A significant differentiating behavior between the two sintering methods is also observable when comparing the plots, wherein the pre-percolation regions in the HP data for the two grains show opposing trends but those of both of the SPS tests show the same trend between their two grains. Since the primary difference seen in the SEM images of the microstructures of the pre-percolation HP and SPS samples was porosity in the SPS samples but not in the HP samples, it can then be reasoned that the difference in trends in the resistance values is related to the difference in porosity between the two sample sets. However, to conclusively determine whether the porosity or differences in the two sintering processes themselves were the cause of the differences in the electrical behavior, high-density SPS samples had to also be tested and compared. These results are presented in the next section.

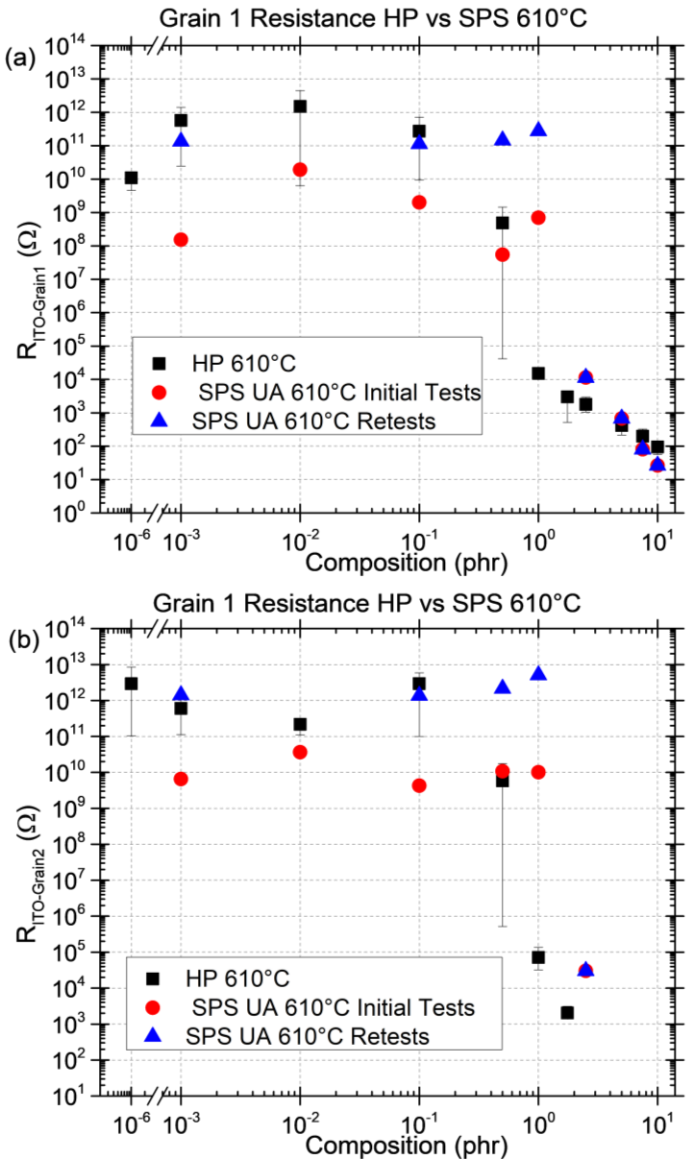

Figure 6.12. Comparison of the normalized resistance values in the equivalent circuit fits of the HP and SPS samples as a function of ITO concentration for the (a) grain 1 and (b) grain 2 resistance elements. For the SPS data, both the initial test and retest fit values are shown.

6.6 SPS composite changes with respect to changing hold temperature

Results of equivalent circuit fitting for the set of SPS UA samples made with a hold temperature of 680°C, ramp rate of 50°C/min, 5-minute hold, and 23.4 MPa applied pressure are given in Table 6.3. The appropriate circuit for each composition matches that of the same composition for the SPS UA 610°C samples, so there is at least a general consistency in the electrical behavior despite the difference in hold temperature. Since these SPS 680°C samples were approximately as dense as the HP 610°C samples, comparison of all three sample sets simultaneously should definitively show the effect of the porosity in the SPS 610°C samples as well as any differences between HP and SPS sample sets when both have high relative densities.

Table 6.3. Equivalent Circuit Fit Values for SPS UA 680°C Samples

Composition (phr)	L-ITO (H)	R-ITO (Ω)	$R_{ITO\text{-}Grain1}$ (Ω)	$CPE_{T\text{-}Grain1}$ (F)	$CPE_{P\text{-}Grain1}$	$R_{ITO\text{-}Grain2}$ (Ω)	$CPE_{T\text{-}Grain2}$ (F)	$CPE_{P\text{-}Grain2}$	R_{Glass} (Ω)	$CPE_{T\text{-}Glass}$ (F)	$CPE_{P\text{-}Glass}$
0.001	4.75E-07	6.069	5.93E+10	4.75E-13	1.00	3.43E+11	1.99E-13	0.722	4.21E+14	4.58E-13	1.00
0.01	4.75E-07	6.069	3.92E+12	8.85E-13	1.00	4.94E+12	1.22E-13	0.739	4.21E+14	3.88E-13	1.00
0.1	4.75E-07	6.069	4.85E+11	1.00E-11	1.00	7.80E+12	1.19E-13	0.738	4.21E+14	3.95E-13	1.00
0.5	4.75E-07	6.069	9.03E+12	1.99E-13	1.00	2.21E+12	1.59E-13	0.768	4.21E+14	3.97E-13	1.00
1	4.75E-07	6.069	1.06E+11	2.88E-13	1.00	1.19E+12	2.66E-13	0.834	4.21E+14	4.44E-13	1.00
2.5	4.75E-07	6.069	1.75E+03	5.21E-11	1.00	6.24E+03	3.51E-11	0.838			
5	4.75E-07	6.069	1.96E+02	6.30E-11	0.905						
7.5	1.65E-07	6.069	1.78E+01	-1.15E-08	0.836						
10	3.99E-07	6.069	1.84E+00	-5.95E-05	0.534						

Figure 6.13 shows the composition-dependent trends in all three sample sets for the grain 1 and grain 2 resistances, as well as the grain 2 CPE-T and the glass CPTE-T. All three sample sets show similar behavior in the grain 1 resistance and, therefore, grain 1 most likely represents the behavior of the typical ITO-glass interfaces since these should be similar in all sample sets. In the resistances of both grains, it is evident that both SPS sample sets show a percolation threshold between 1.0 and 2.5 phr. However, differences may have presented themselves if 1.75 phr samples had been made for these sample sets, so it cannot be stated with certainty that samples percolated at the same ITO concentration for both SPS hold temperatures.

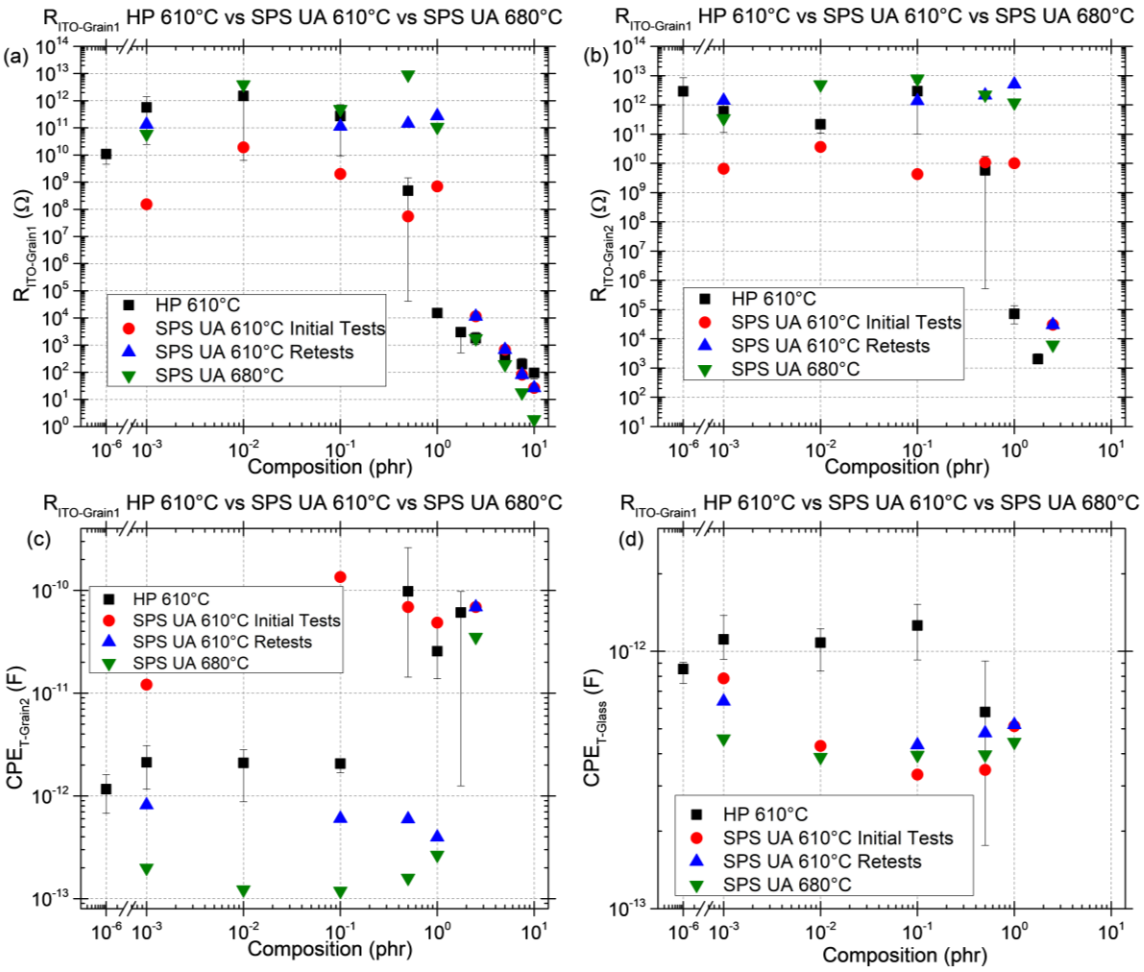

Figure 6.13. Equivalent circuit fitting element values of the (a) grain 1 and (b) grain 2 resistors and the (c) grain 2 and (d) glass CPEs for the respective sample sets. The associated values for the HP, SPS 610°C, and SPS 680°C samples are shown in the same plot to facilitate comparisons.

The grain 2 capacitance (CPE-T) data show clearer differences between the three sample sets at pre-percolation compositions. The data presents a consistent ordering of the curves, with the initial SPS 610°C samples possessing the largest capacitances, followed by the HP 610°C samples, the retested SPS 610°C samples, and the SPS 680°C samples which had the smallest capacitance values. All data sets except for that of the initial SPS 610°C tests show a jump to larger capacitance upon achieving percolation, further establishing that although the meaning of this behavior is unknown, it must be related to a

real microstructural feature in these samples which is common between all sample sets. The glass capacitance values show very similar trends in the SPS data at both temperatures but a different trend for the HP data. This indicates a difference in the behavior of the glass between the HP and SPS processes. Potential causes of this difference include different interactions of the different sintering atmospheres with the impurities in the glass, and changes in the compositions of the interfaces between glass particles which have been reported as a difference between the two sintering methods.[95]

Equivalent circuit fitting for a series of 2.5 phr SPS GT samples with hold temperatures over a range of values between 610°C and 680°C, shown in Table 6.4, provides finer detail on how hold temperature affects the electrical properties.

Table 6.4. SPS GT Hold Temperature Variation Equivalent Circuit Fitting

Hold Temperature (°C)	L-ITO (H)	R-ITO (Ω)	$R_{ITO-Grain1}$ (Ω)	$CPE_{T-Grain1}$ (F)	$CPE_{P-Grain1}$
610	4.75E-07	6.069	1.48E+03	1.55E-10	0.767
620	4.75E-07	6.069	1.20E+03	1.83E-11	0.872
630	4.75E-07	6.069	9.93E+02	9.00E-12	0.906
640	4.75E-07	6.069	1.07E+03	1.65E-10	0.772
650	4.75E-07	6.069	9.90E+02	1.03E-11	0.892
660	4.75E-07	6.069	1.11E+03	1.38E-11	0.877
670	4.75E-07	6.069	8.61E+02	1.16E-11	0.882
680	4.75E-07	6.069	8.70E+02	1.16E-09	0.673

Examination of the plotted grain 1 resistance values (Figure 6.14 (a)), which represent interfacial resistance between the ITO particles, shows that the resistance values for all samples are very similar, with only a small decrease as the hold temperature increases. This was to be expected since typical reported sintering temperatures for ITO are more than 300°C greater than those used to process the present samples and, as such, only a small

degree of deformation was achievable among the ITO grains to improve the interfacial contacts.[55,56,96] Comparison of the CPE-T and CPE-P values (Figure 6.14(b)) appears to show a perfect inverse relationship between the two. This behavior was seen in some of the other sample sets, but the cause is unknown.

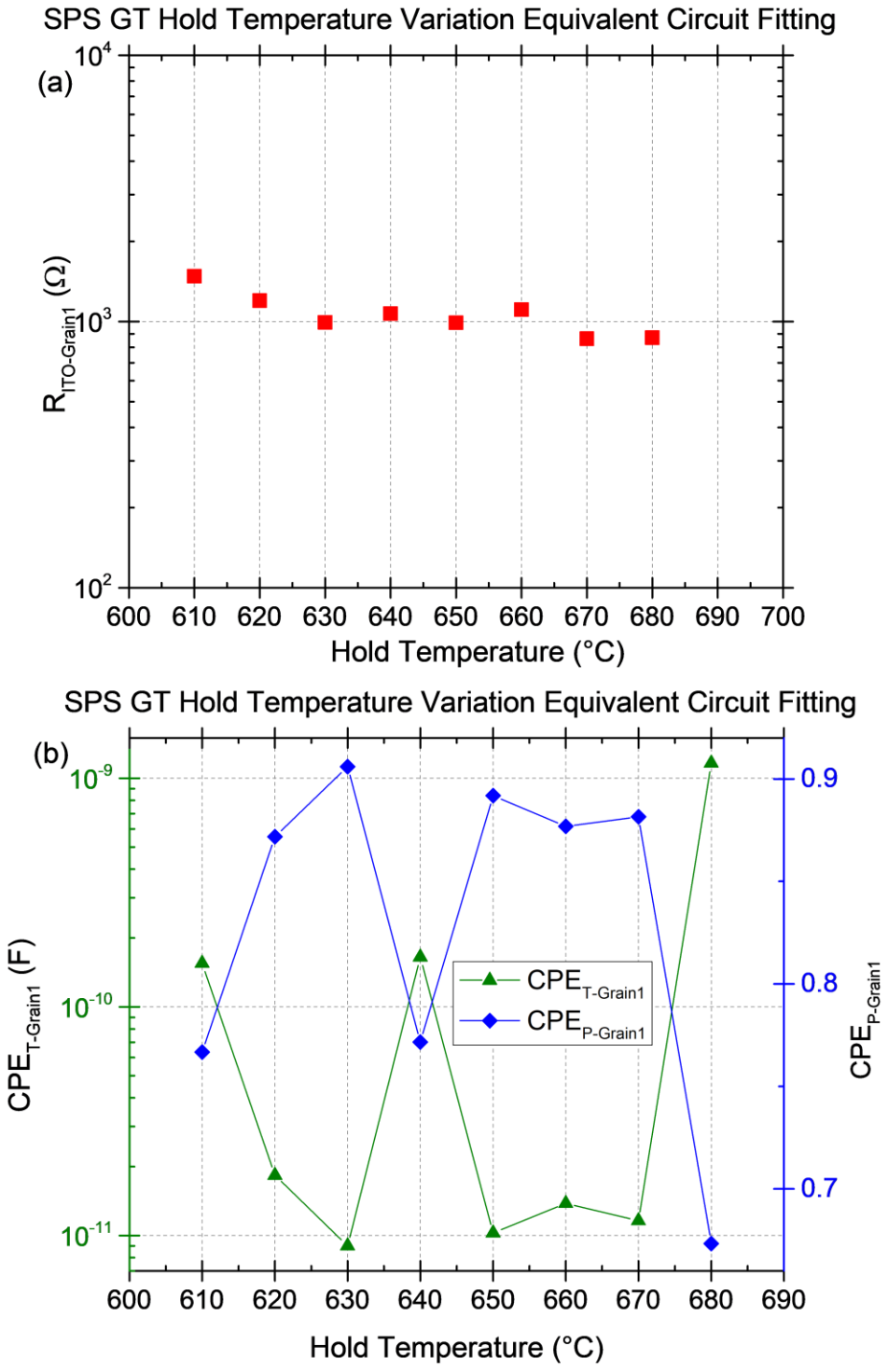

Figure 6.14. Equivalent circuit fitting values for (a) the intergranular resistors and for (b) the CPE-T and CPE-P as a function of hold temperature for SPS GT samples. The resistance values are quite consistent, with only a small decrease in resistance as the hold temperature increases. The CPE values show an interesting inverse relationship between the T and P values.

6.7 Changes as a function of applied pressure in SPS

The effects of changing the applied pressure for 2.5 phr SPS GT samples on the resulting equivalent circuit fits is shown in Table 6.5, and plots of the resistance values for grains 1 and 2 are shown in Figure 6.15. The table shows that all samples in this set had the same equivalent circuit. The plots show a consistent decrease in resistance with increasing pressure, as expected, and is the same trend as was seen in the SPS processing voltage and the inverse trend of the processing current (Figure 5.4), providing further evidence of the relationship between the electrical parameters used during SPS processing and the resulting electrical properties of the sintered sample.

Table 6.5. SPS GT 2.5 phr Pressure Variation Equivalent Circuit Fitting Values

Applied Pressure (MPa)	L-ITO (H)	R-ITO (Ω)	$R_{ITO\text{-}Grain1}$ (Ω)	$CPE_{T\text{-}Grain1}$ (F)	$CPE_{P\text{-}Grain1}$	$R_{ITO\text{-}Grain2}$ (Ω)	$CPE_{T\text{-}Grain2}$ (F)	$CPE_{P\text{-}Grain2}$
5.0	4.75E-07	6.069	2.02E+05	5.35E-11	1.00	7.08E+05	9.96E-11	0.756
11.1	4.75E-07	6.069	4.10E+04	2.23E-10	1.00	4.96E+05	1.41E-10	0.739
23.4	4.75E-07	6.069	1.65E+04	3.49E-12	1.00	5.39E+04	4.49E-11	0.875
40.0	4.75E-07	6.069	6.72E+03	2.59E-12	1.00	7.72E+03	2.94E-11	0.947

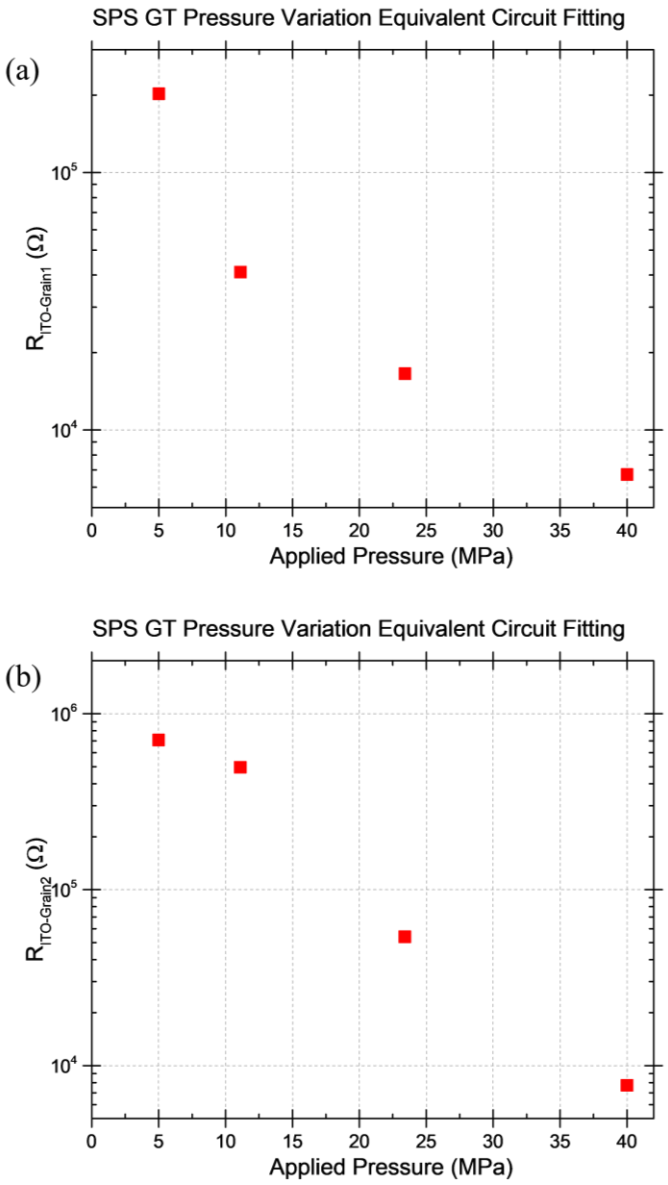

Figure 6.15. (a) Grain 1 and (b) grain 2 resistances in the equivalent circuit fits of GT SPS samples as a function of the applied pressure.

6.8 Changes as a function of heating rate in SPS

The 2.5 phr SPS GT samples made using different ramp rates gave equivalent circuit fits with values shown in Table 6.6. The primary difference here is that the 2°C/min sample

fit to the pre-percolation circuit, whereas the other samples fit to the two-grain post-percolation circuit.

Table 6.6. Equivalent Circuit Fit Values for SPS Samples with Changing Ramp Rate

Ramp Rate (°C/min)	L-ITO (H)	R-ITO (Ω)	$R_{ITO\text{-}Grain1}$ (Ω)	$CPE_{T\text{-}Grain1}$ (F)	$CPE_{P\text{-}Grain1}$	$R_{ITO\text{-}Grain2}$ (Ω)	$CPE_{T\text{-}Grain2}$ (F)	$CPE_{P\text{-}Grain2}$	R_{Glass} (Ω)	$CPE_{T\text{-}Glass}$ (F)	$CPE_{P\text{-}Glass}$
2	4.75E-07	6.069	2.38E+08	6.02E-10	1.00	1.08E+09	1.07E-11	0.758	4.21E+14	1.12E-12	1.00
20	4.75E-07	6.069	3.20E+04	2.89E-11	1.00	8.99E+04	1.06E-10	0.771			
50	4.75E-07	6.069	1.93E+04	2.65E-11	1.00	4.74E+04	7.41E-11	0.798			
200	4.75E-07	6.069	2.44E+04	3.80E-11	1.00	5.30E+04	1.56E-10	0.766			

Unsurprisingly, since the 2°C/min sample lacked a percolated conducting network, the element values for the 2°C/min sample all differed significantly from those of the other samples, as shown in Figure 6.16. For the other samples, however, all values remained fairly consistent.

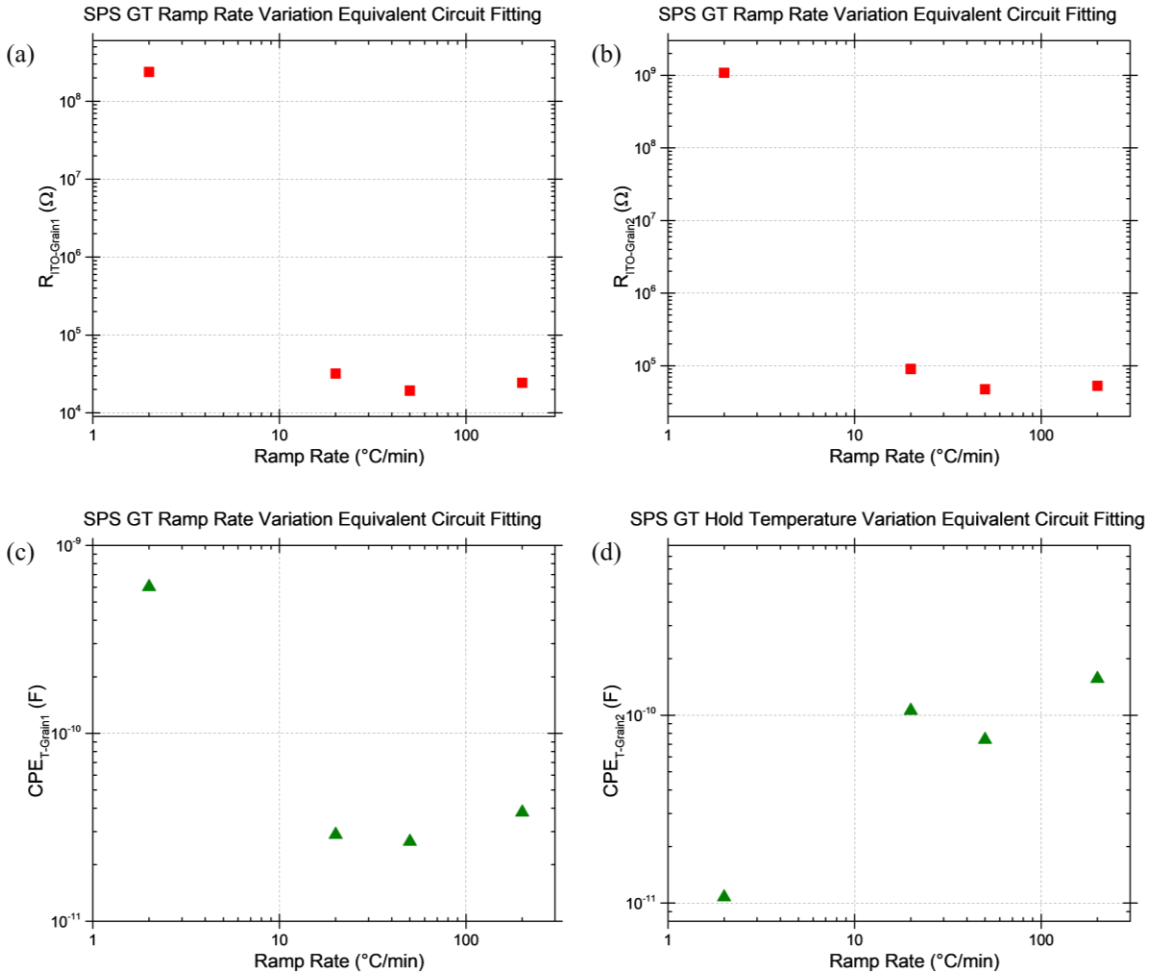

Figure 6.16. (a) Grain 1 and (b) grain 2 resistance values and (c) grain 1 and (d) grain 2 CPE-T values of the equivalent circuit fits for 2.5 phr GT SPS samples as a function of the ramp rate. For both elements in both grains, the values for the 2°C/min sample differ from those of the other heating rates by at least an order of magnitude, whereas the values for the other heating rates are quite close to each other.

6.9 Changes as a function of SPS equipment

Comparison of the equivalent circuit fitting results for SPS TT and SPS UA sample sets made using SPS with a hold temperature of 680°C, a ramp rate of 50°C/min, a hold time of 5 minutes, and an applied pressure of 23.4 MPa is presented here to show the high repeatability in the results between these sample sets. Fitting values for the grain 1 and 2 resistance values and the grain 2 and glass capacitance values are presented in Figure 6.17 and, in all cases, the two sets show the same trend and similar values. The specific fitting values for the SPS TT sample set are provided in Table 6.7. The only noticeable difference seen here compared to the SPS UA 680°C data is that the 5.0 phr samples were fit to a lone resistor, as there was not enough capacitive or inductive behavior in the response to fit such elements. However, since 5.0 phr lies at the transition between where capacitive or inductive behavior are more prevalent, the difference in the impedance response may be due simply to being so close to the transition point that no capacitive or inductive signal could overcome the noise in the measurement. Therefore, it is believed that this particular difference in the equivalent circuits does not indicate a massive difference in electrical behavior.

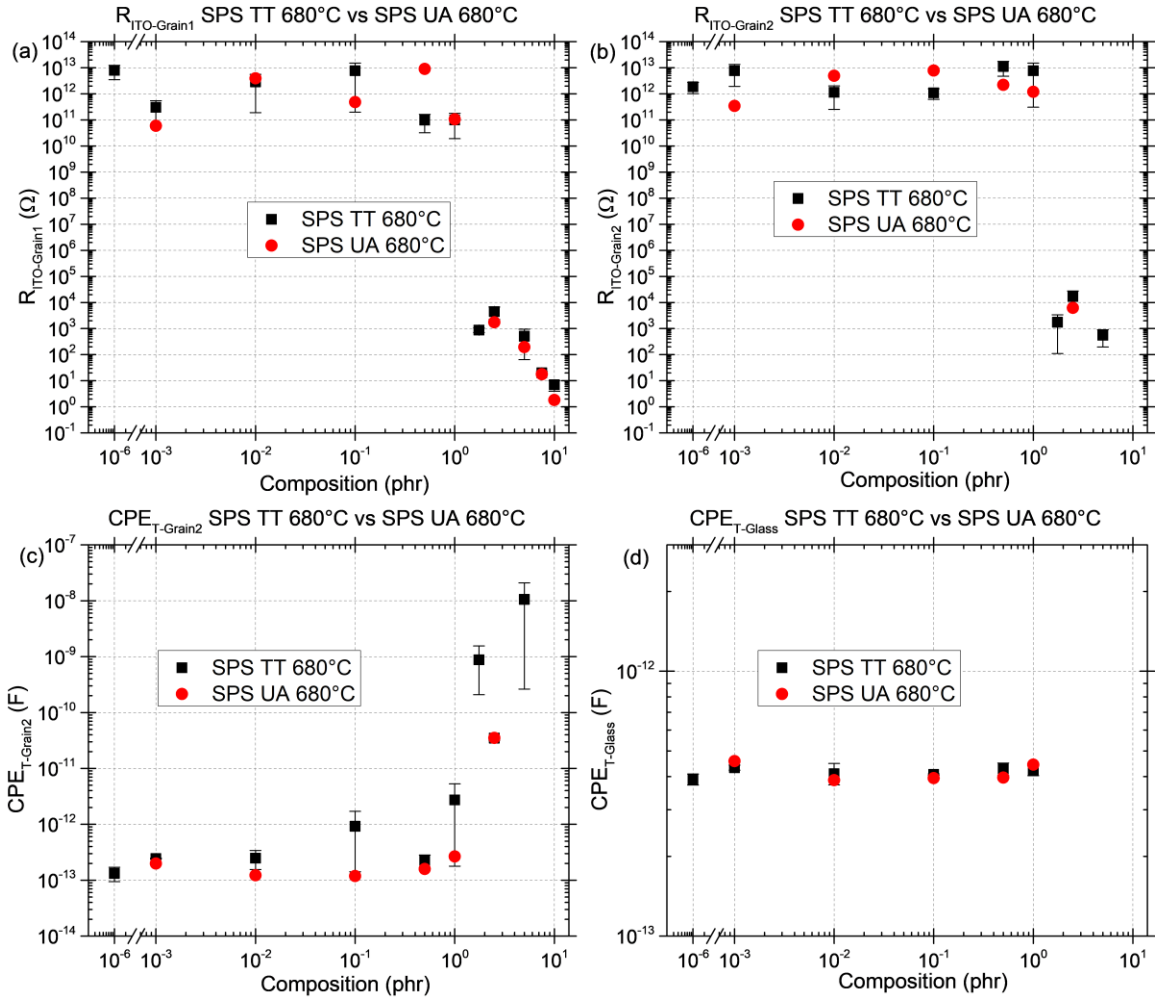

Figure 6.17. Circuit fitting element values for the (a) grain 1 and (b) grain 2 resistors and CPE-T values for (c) grain 2 and (d) the glass as a function of ITO concentration for the SPS TT and SPS UA samples made with a hold temperature of 680°C. The same trends and similar values are present in each case, indicating good repeatability between the two sample sets.

Table 6.7. Circuit Fitting Values for SPS TT 680°C Sample Set

Composition (phr)	Sample	L-ITO (H)	R-ITO (Ω)	$R_{ITO\text{-}Grain1}$ (Ω)	$CPE_{T\text{-}Grain1}$ (F)	$CPE_{P\text{-}Grain1}$	$R_{ITO\text{-}Grain2}$ (Ω)	$CPE_{T\text{-}Grain2}$ (F)	$CPE_{P\text{-}Grain2}$	R_{Glass} (Ω)	$CPE_{T\text{-}Glass}$ (F)	$CPE_{P\text{-}Glass}$
0	1	NA	NA	3.48E+12	3.46E-13	1.00	1.02E+12	1.70E-13	0.627	4.21E+14	3.72E-13	1.00
0	2	NA	NA	1.24E+13	1.52E-13	1.00	2.72E+12	9.39E-14	0.791	4.21E+14	4.09E-13	1.00
0.001	1	4.75E-07	6.069	5.43E+11	1.08E-12	1.00	1.94E+12	2.39E-13	0.640	4.21E+14	4.42E-13	1.00
0.001	2	4.75E-07	6.069	6.17E+10	2.58E-12	1.00	1.34E+13	2.48E-13	0.743	4.21E+14	4.23E-13	1.00
0.01	1	4.75E-07	6.069	1.90E+11	2.66E-12	1.00	2.02E+12	3.41E-13	0.595	4.21E+14	4.48E-13	1.00
0.01	2	4.75E-07	6.069	5.56E+12	6.21E-14	1.00	2.55E+11	1.56E-13	0.837	4.21E+14	3.72E-13	1.00
0.1	1	4.75E-07	6.069	1.98E+11	2.06E-12	1.00	6.16E+11	1.70E-12	0.568	4.21E+14	4.10E-13	1.00
0.1	2	4.75E-07	6.069	1.52E+13	1.27E-13	1.00	1.57E+12	1.42E-13	0.807	4.21E+14	4.05E-13	1.00
0.5	1	4.75E-07	6.069	1.64E+11	1.77E-13	1.00	4.77E+12	1.67E-13	0.750	4.21E+14	4.50E-13	1.00
0.5	2	4.75E-07	6.069	3.21E+10	1.00E-12	1.00	1.76E+13	2.81E-13	0.707	4.21E+14	4.04E-13	1.00
1	1	4.75E-07	6.069	1.91E+10	1.77E-11	1.00	3.08E+11	5.29E-12	0.482	4.21E+14	4.03E-13	1.00
1	2	4.75E-07	6.069	1.80E+11	4.32E-13	1.00	1.50E+13	1.78E-13	0.892	4.21E+14	4.41E-13	1.00
1.75	1	4.75E-07	6.069	1.05E+03	1.76E-13	1.00	1.10E+02	1.55E-09	0.954			
1.75	2	4.75E-07	6.069	7.02E+02	8.00E-11	1.00	3.39E+03	2.08E-10	0.600			
2.5	1	4.75E-07	6.069	6.74E+03	4.56E-11	1.00	2.76E+04	3.76E-11	0.840			
2.5	2	4.75E-07	6.069	2.23E+03	3.56E-11	1.00	6.37E+03	3.19E-11	0.845			
5	1	NA	191.7									
5	2	NA	267.5									
7.5	1	1.38E-07	6.069	1.76E+01	-2.07E-07	0.494						
7.5	2	1.74E-07	6.069	2.26E+01	-1.46E-07	0.475						
10	1	1.87E-07	6.069	1.01E+01	-1.85E-07	0.614						
10	2	1.77E-07	6.069	3.97E+00	-3.25E-07	0.754						

Comparison of equivalent circuit fits for 2.5 phr SPS samples made using the UA, TT, and GT SPS equipment with a hold temperature of 610°C, a ramp rate of 50°C/min, a hold time of 5 minutes, and an applied pressure of 23.4 MPa showed much larger differences compared to the 680°C samples made on the different SPS equipment. The fitting values, provided in Table 6.8, do show that all three samples fit to the same circuit, but comparison of the individual values, shown in Figure 6.18, reveal the extent of these differences. The UA sample exhibited larger resistances than the others, matching the higher resistivity and the higher porosity of the microstructure in that sample (Figure 5.3). The differences in all four presented circuit values are in line with the similarly large differences in the microstructures and the processing voltage and current data between these samples shown in the previous chapter (Figure 5.3). This leads to a question as to why differences between the equipment were present in the 610°C samples but not in the 680°C samples. However, this can be explained by the fact that the densities of the samples made at 610°C could vary quite a bit and were, therefore, sensitive to changes in the processing parameters, whereas samples made at 680°C showed low porosity regardless of the processing conditions.

Table 6.8. 2.5 phr SPS Equipment Comparison Equivalent Circuit Fitting Values

SPS Equipment	L-ITO (H)	R-ITO (Ω)	$R_{ITO\text{-}Grain1}$ (Ω)	$CPE_{T\text{-}Grain1}$ (F)	$CPE_{P\text{-}Grain1}$	$R_{ITO\text{-}Grain2}$ (Ω)	$CPE_{T\text{-}Grain2}$ (F)	$CPE_{P\text{-}Grain2}$
GT	4.75E-07	6.069	182.4	5.55E-09	0.8	1299	1.04E-12	1
TT	4.75E-07	6.069	110.1	2.87E-05	0.13821	362.9	2.86E-12	1
UA	4.75E-07	6.069	33247	7.25E-11	0.86437	16039	3.14E-12	1

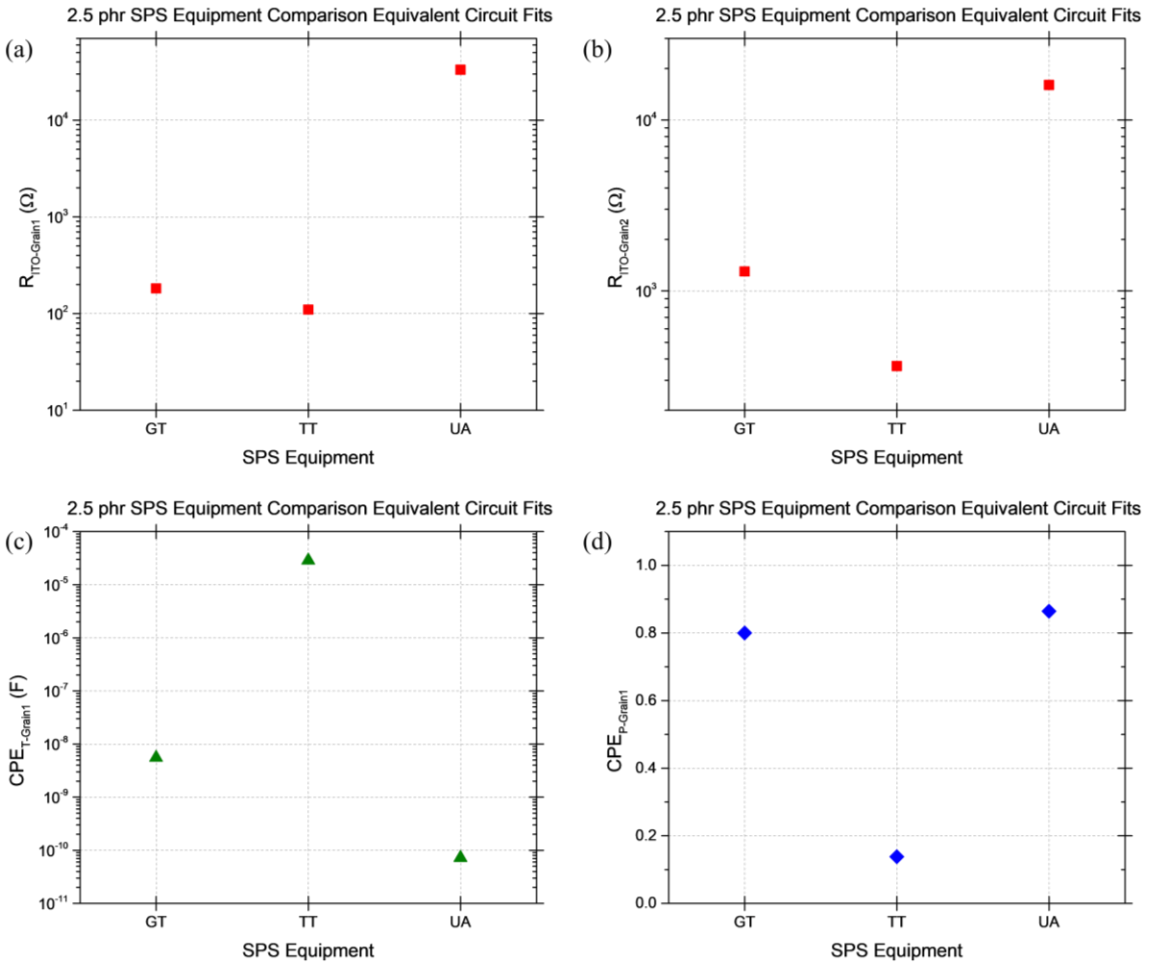

Figure 6.18. Equivalent circuit element value plots for samples made under the same processing conditions of a 610°C hold temperature, 50°C/min ramp rate, 5-minute hold time, 23.4 MPa applied pressure, and 2.5 phr powder composition on the three different SPS equipment. The resistor values for grains (a) 1 and (b) 2, as well as the (c) CPE-T and (d) CPE-P values for grain 1 all show large differences between the three samples.

Based on the presented equivalent circuit fitting results, it can be concluded that such fitting was able to characterize many aspects of the microstructure of the multitude of samples studied, as the results matched those of SEM data, the punch displacement, voltage, and current data from the SPS processing procedure, and the relative density data. Major changes in the sintering behavior corresponded with changes in the equivalent circuit and, through comparison of changes in the circuit values with those seen using other

characterization methods, each circuit element could be attributed to a specific feature of the composite microstructure. In addition to the wide range of features which could be characterized through equivalent circuit fitting, the results also showed a high sensitivity in detecting these changes, thus demonstrating the strength of this characterization method.

CHAPTER 7. CONCLUSIONS

Borosilicate glass matrix-ITO filler composites were successfully fabricated using hot pressing and SPS under processing conditions which formed segregated ITO networks. The formation of the segregated networks resulted in low percolation thresholds between 0.154 and 0.764 vol% ITO and resistivities as low as 29 (Ω·cm) at 2.99 vol% ITO under all of the studied processing conditions. These values showed that the samples possessed a lower percolation threshold and smaller resistivity after percolation compared to the ATO-borosilicate composites made in previous work[13], and thus, that the initial hypothesis was confirmed regarding superior electrical properties when using ITO. However, transparency could not be maintained at the ITO concentrations necessary to achieve percolation, so a conducting network and transparency were not achieved simultaneously in any sample. This issue has not been resolved, but further work could reveal a solution, as discussed in the suggested future work section.

The hot-pressed samples, which were processed at a maximum temperature of 610°C, densified completely, whereas the SPS samples processed to the same maximum temperature possessed lower relative densities. Apart from a smaller impedance at the highest studied ITO concentrations, the UA SPS samples showed worse densification, optical properties, and electrical properties compared to HP samples, thus disproving the hypothesis of superior properties when using SPS. Comparison of punch position data from samples made with maximum temperatures of 610°C, 620°C, 655°C, and 680°C showed a large shift in final density between 620°C and 655°C, indicative of crossing the pressure-dependent ductile-to-brittle transition of the glass during SPS sintering. Only the samples

brought to 680°C showed no observable porosity, indicating that the composite powders had to be subjected to much higher temperatures to achieve complete densification when SPS was used rather than HP. This result contradicts the findings of many reports in the literature, which have reported full densification at lower times and temperatures when using SPS.

While most of the proposed mechanisms to explain the effect of the SPS sintering process would not be able to explain the lower densities seen in the SPS samples, one possible explanation which does support these results is that proposed by Holland et al.[36] involving a synergistic effect between the heating rate and the electric field, which leads to enhanced densification only when the heating rate is above a threshold value but can hinder densification at lower heating rates.

Through the comparison of samples made from the same 2.5 phr powder composition, discussed in the study of the effects of changing SPS processing parameters, it has been shown that differences in the independent processing parameters in SPS, including hold temperature, heating rate, applied pressure, equipment hardware and software, and the tooling material and geometry, all noticeably affect the applied current and voltage experienced by the samples. These variations affect the final electrical properties of the SPS fabricated samples as follows: (a) While keeping the hold temperature and heating rate constant (610°C and 50°C/min), varying the applied pressure shows that higher applied pressures result in nominally more dense samples, and the far more sensitive impedance data showed a difference in their electrical response of about 2 orders of magnitude. (b) While keeping the applied pressure at 23.4 MPa, increasing the temperature to 680°C resulted in much closer values of the electrical resistivity of the samples, with a total

variation of approximately a factor of two. Therefore, the effect of changing the maximum temperature, which is one of the primary variables given attention in the literature, was far less pronounced than that of changing SPS equipment and tooling; the equipment and tooling change resulted in differences in the applied voltage/electric field of up to a factor of 4 and differences in the relative density of the samples of up to about 13%. (c) Changing the heating rates from 2°C/min up to 200°C/min resulted in changes of over 5 orders of magnitude in the electrical response of the final samples. It was found that analysis of the current and voltage data recorded during the SPS process is useful in identifying differences between samples as well as differences between SPS equipment. Since this information is already collected by typical SPS control software, such data is readily available. It was demonstrated that analysis of the trends in the current and voltage can facilitate the identification of such differences, which may be easily missed when analyzing temperature profile data alone. The results also confirmed the hypothesized presence of additional variables, besides the heating rate, hold temperature, hold time, and applied pressure, which can significantly affect sintering when using the SPS method. Furthermore, it was shown that these other variables can more strongly affect the resulting microstructure than those typically reported. Therefore, the value of incomplete reporting of processing conditions associated with published results may be limited, since the repeatability of the results may be severely hampered or rendered impossible.

It was demonstrated that changes in one processing parameter may affect multiple other parameters, making fair comparisons even more difficult and complicating the determination of the effects of any single parameter on overall densification behavior. It was also found that regardless of the values input into the control software, actual heating

rates will vary throughout a sintering procedure, calling into question the significance of the single heating rate often reported in many publications without the accompanying voltage and current trends. All of these issues are made worse when using the highest heating rates because the response times of the SPS control software, and physical factors such as heat dissipation from the chamber all start to introduce significant errors into the programmed SPS procedure. Most of these effects have limited effect on the temperature vs time scans as was demonstrated in the various parameter sets investigated.

Although many of the issues associated with high heating rates may be significantly reduced by optimizing the PID settings for a given SPS machine, this information is seldom if ever reported. Results indicated that using the same PID settings with the same machine on the same types of samples led to large fluctuations as the heating rate was increased and had a concomitant large effect on the final electrical properties of the specimens fabricated. Regarding this point, the findings described in this work show that the potential errors can be massive and, therefore, cannot be ignored.

Based on the presented equivalent circuit fitting results, it can be concluded that such fitting was able to characterize many aspects of the microstructure of the multitude of samples studied, as the results matched those of SEM data and the punch displacement, voltage, and current data from the SPS processing procedure. Appropriate models were derived for the composites by combining the circuits of the constituent phases. In the studied composite samples, it was found that there were three applicable equivalent circuits across samples over the entire ITO concentration range. The equivalent circuit best matching the impedance behavior of the samples changed with increasing ITO concentration, each time becoming simpler, as the conducting network grew and enabled

the applied current to avoid traversing across the more insulating microstructural features. Through comparison of changes in the circuit values with those seen using other characterization methods, each circuit element could be attributed to a specific feature of the composite microstructure, including the bulk ITO and glass phases and the interfaces between them. In addition to the wide range of features which could be characterized through equivalent circuit fitting, the results also showed a high sensitivity in detecting these changes, thus demonstrating the strength of this characterization method. The demonstration of using impedance spectroscopy and equivalent circuit analysis on a variety of powder materials in-situ during compaction and on sintered samples shows the high flexibility of IS testing, and characterization of the composites showed the usefulness of applying this technique to any composite system.

In an effort to more completely characterize microstructural changes in powder beds throughout the process of sintering, a process combining ac impedance spectroscopy and SAS/USAS testing in-situ during powder compaction has been developed and successfully demonstrated. Progressive updates to the experimental procedure, test setup, and scattering technique have improved the quality of the resulting data over the course of multiple experiments, and good agreement between the scattering and impedance data was consistently present. Fitting of the scattering data using the Unified Fit model was able to quantify the microstructural changes and the various levels were able to be attributed to specific expected or observed microstructural features of the powder compacts.

Testing with the incorporation of elevated temperatures, which is the final addition to the in-situ compaction setup that is necessary to conduct the characterization techniques during in-situ sintering, has begun with an initial proof of concept test. Experiments

showed the successful differentiation between powder compositions and changes in behavior as a result of the initiation of densification. Upon the successful development and operation of the combined temperature and pressure test, it is expected that a detailed in-situ characterization throughout the sintering process will be demonstrated. It is expected that the data provided through this test will allow sintering models to be developed from the resulting data, thus achieving the overall goal of this project. This method could then be used by other scientists and in industry to develop process models for hot pressing or pressureless sintering any powder material, and thus this method would have wide applicability. The data for and discussion of the SAS tests are presented in the appendix.

CHAPTER 8. FUTURE WORK

8.1 ITO-glass composites

Further work on the fabrication of ITO-glass composites possessing both high electrical conductivity and high optical transparency may extend in several directions. Preliminary tests have been conducted in which the borosilicate glass is replaced with a barium titanate silicate glass (Cole Safety Products), also known as barium titanate glass, which closely matches the particle size of the borosilicate microspheres and the refractive index of ITO (~1.9). Initial results of SPS fabrication trials on the glass microspheres have been mixed; high relative density and moderate translucency have been achieved, but the samples possess a distinct orange color which seems to be limiting the optical properties. This characteristic may be related to impurities in the glass, as it was identified via EDS that Al, Ca, and Zn were present at concentrations of approximately 1-3 at%. However, it is also possible that the color arises from color center defects in the glass, as the microspheres are sometimes described by manufacturers as having a slightly yellow appearance, which may simply grow darker into the orange color range as the glass thickness increases when consolidated to a bulk sample. Attempts should be made to either remove impurities in the glass or to find a source of cleaner glass. Alternatively, a different glass composition with a similar refractive index could be tested to determine whether superior optical properties could be achieved.

Another possible research direction is optimization of the ITO material. According to percolation theory, a smaller filler particle size will decrease the percolation threshold, so the same conductivity should be achievable while preserving more of the translucency seen in the pure glass sintered samples. Additionally, other manufacturers of ITO may synthesize the nanoparticles in a way which results in less agglomeration, which would enhance densification of the ITO by producing a higher-density green body in the ITO phase region of the composites and facilitate a more even distribution of ITO in these regions thus further reducing the percolation threshold.

Furthermore, the properties of the composites could be improved by applying an optimized post-sintering annealing procedure. Both the electrical conductivity and the color of the ITO nanopowder is sensitive to oxygen concentration; more oxidation results in a yellow color and a decrease in conductivity, whereas a very nonstoichiometric reduced oxide is blue and has a higher conductivity. This darker color appears to be contributing to the loss of translucency, so optimization would necessitate some balance between color and conductivity. The powder used in this work started in a fully oxidized state but was reduced due to the high temperature and vacuum/inert gas conditions used during sintering. It was shown in Figure 6.3 that this can result in a difference in oxidation state between ITO in the center of the sample and ITO at the surface. The effect of an oxidation gradient through the thickness of the sintered samples was not studied but considering the high sensitivity of optical properties to even small concentrations of defects or impurities[32], it is plausible that this lack of consistency has some negative impact. Tests with ITO starting in the reduced state may provide more insight into this issue.

8.2 Investigation of sintering process parameters

In addition to all of the studied SPS processing parameters, a factor which may have influenced the sintering behavior in every sample is the concentration of adsorbed water in the powder before the start of sintering. Reports in the literature have found that humidity can influence the green body density of the powder[89], the driving force for consolidation[88], and the rate of mass transport during sintering, each of which could affect the final degree of densification of the ITO phase within the composites. Investigation into this issue should involve loading powder mixes of identical composition into dies within a humidity control box, each under a different relative humidity and, ideally, at the same temperature. The loaded dies could then be sealed in airtight bags, transported to the SPS equipment, quickly mounted in the chamber and subjected to vacuum, and sintered as soon as possible to minimize the exchange of water molecules between the powder volume and the atmosphere outside the die. Another test series could involve loading the powders at a fixed high humidity and using different sintering ramp rates, since it has been reported that high ramp rates amplify humidity effects by reaching higher temperatures before the water is driven out of the powder[37], thereby allowing its influence to extend into the intermediate sintering stage.

An ultimate goal of this line of investigation would be to develop a method to standardize SPS processing for multiple equipment, which would solve many problems in the field of SPS study.

APPENDIX A. SMALL ANGLE SCATTERING EXPERIMENTS OF POWDER COMPACTS AS A FUNCTION OF PRESSURE AND TEMPERATURE

In this chapter, the results of ac impedance spectroscopy and small angle scattering techniques carried out during in-situ compaction or heating of ceramic nanopowders and powder mixes are detailed.

Since both IS and SAS methods have been established as particularly useful in the characterization of multi-phase materials and the powder beds present during the process of hot-press sintering fall into this category, experiments were conducted to determine the viability of each method and a combination of the two methods in the characterization of powders during in-situ compaction. In doing so, the goal was to determine whether enough information could be gathered through these methods to gain a more complete understanding of how the microstructures change as a result of the compaction process. Portions of the work in this chapter have been presented at the SNS and HFIR User's Group Meeting (2015), the 10th Annual TechConnect World Innovation Conference and Expo (2016), and the SAS 2018 conference, and published as part of a conference proceedings.[97]

Although a lot of work and analysis has been conducted on this project, the point at which the data could be used to develop accurate sintering models has not yet been reached. Since this work cannot directly support the analysis in the body of this thesis until reaching that point, it is presented in this appendix.

A.1 Background

A.1.1 Objective and motivation for the development of a sintering characterization method combining ac impedance spectroscopy and small angle scattering

The objective of this project was to develop an in-situ characterization method for sintering which can provide enough microstructural information to accurately model the process. This model would then allow for the development of process models, so the microstructure and properties of the final part could be predicted for a given set of processing conditions, or processing conditions could be determined to achieve desired properties.[98,99]

A wide range of methods can be used to characterize the porous microstructures present during the various stages of sintering, each with its own advantages and limitations (Table A.).[100,101] However, continuous characterization throughout the sintering process requires a non-destructive method that can be conducted in-situ, which limits the potential candidates considerably. Furthermore, as a result of the limitations of each method, no single characterization method is sufficient to completely characterize these microstructures.[100] Therefore, to achieve the goal of complete microstructural characterization of the powder compacts throughout sintering, a novel technique combining multiple in-situ characterization methods is necessary, ideally requiring as few combined methods as possible to minimize the complexity.

Table A.1. Overview of Characterization Methods for Porous Microstructures, Modified From [4] and [5]

Technique	Main Limitations
OM	Resolution, sample preparation
SEM	Sample preparation
TEM	Very small volume, preparation
3D Tomography	Labor intensive
X-ray microtomography	Limited resolution
X-ray magnified tomography	Small field of view
Mercury intrusion porosimetry	Model-based, large sample volume
Gas Adsorption	Large sample volume
Archimedean porosimetry	Large sample volume
Multiple small-angle scattering	Limited applicability
Anisotropic-specific surface area	
NMR Relaxation	Resolution limited to μm scale
Geometric Density Calculation	No pore characteristics except porosity
Dielectric Constant	Only gives porosity, accuracy deteriorates above 50% porosity
N_2 Sorption	Limited feature size detection range, requires assumption of pore shape
SANS/SAXS	Restricted sample thickness, limited to sub-μm and smaller pores
AC impedance spectroscopy	Data modelling and interpretation can be challenging

Given all the imposed restrictions on and requirements of the available methods, it was proposed that a combination of small angle scattering and ac impedance spectroscopy would be optimal, due to their non-destructive nature and the wide range of complementary microstructural information given by each of these methods.

In the sintering process, the evolution of the microstructure and, therefore, the progressive changes in the properties and performance, are strongly influenced by the shape of the free energy surface because the minimization of surface free energy is the driving force for sintering.[99,102] Therefore, data regarding topological characteristics such as pore sizes, surface areas, and volume and number distributions gives a direct measure of the microstructure which drives the sintering.[102] Small angle scattering (SAS) was chosen as a primary characterization technique to be used for these tests because when

using SAS, all of these characteristics can be measured for both open and closed porosity simultaneously in a non-destructive and in-situ manner.

As detailed in Chapter 1, during the process of sintering, there are a few different types of interfaces that will be present between the powder particles as the particles deform and the microstructure evolves.[102] The different types of interfaces, such as point contact of un-deformed particles in the initial stage of sintering and contact between fully sintered grains in the final stage of sintering, affect the properties of the material. The electrical properties of a material are very sensitive to microstructural changes and especially to interfacial changes, therefore making them very useful as a means of characterizing the evolution of microstructure during sintering.[12] Ac impedance spectroscopy (IS) gives a great deal of information on the electrical properties of a material and can be used to develop equivalent circuit models which can identify the types of interfaces present between the particles.[8] This has been demonstrated for a series of glass composites containing conducting fillers at the interstices between the glass particles[12] as discussed in Chapters 3-6. These studies were conducted ex-situ. Monitoring the changes in the interfacial properties between the particles as sintering progresses provides another avenue for tracking the evolution of the microstructure and, therefore, the combined use of ac impedance spectroscopy with equivalent circuit fitting has been chosen as the second primary means of non-destructive in-situ characterization of the evolution of microstructure during sintering.

Combining the acquisition of SAS and ac impedance spectroscopy data during the sintering of a ceramic powder will allow for the correlation of porosity with electrical properties and provide a complete and detailed picture of the microstructure at any stage

of sintering, thus providing a novel and useful test to anyone producing bulk materials through sintering. The idea is that once the SAS experiments are conducted for a given material, ex-situ ac impedance measurements could be used to track the sintering behavior since a statistically representative response will have been identified via the SAS measurements and matched to the densification mechanisms operating in that given material.

A.1.2 SAS Principles

Small angle x-ray scattering (SAXS) and small angle neutron scattering (SANS) are two SAS methods which operate under the same principles, and the same equations apply to both processes. However, due to the behavioral differences between neutrons and x-rays, these techniques can provide different information, can make one technique more or less useful for a given material, and may require major changes in testing setups and/or procedures when employing both tests to the same material. X-ray sources generally have a far higher flux, which allows for shorter testing times, and can be directed or focused using electromagnetic fields, giving for far more flexibility in test fixture geometries and capabilities, compared to neutron sources. However, x-rays have a far smaller penetration depth than neutrons, requiring smaller sample sizes and imposing harsher limitations on sample holders, in terms of both material and thickness within the beam path, if sufficient transmission for useful data collection is to be maintained.

Small angle scattering techniques are based on the same principle as other diffraction methods, in which an incident beam of particles or electromagnetic radiation contacts the sample under test, scatters off microstructural or atomic features of the material, depending

on the type of incident beam, and is collected by a 2-D detector (Figure A.1).[103] Due to wave-like behavior of the scattering species, coherent and incoherent scattering occur and can be detected at different angles relative to the incident beam, 2θ. The measured angles can then be related to the distances between the features which produced coherent scattering, d, of the incident beam of wavelength λ. The condition for coherent scattering is defined by Bragg's Law, shown in equation (A.).

$$n\lambda = 2dsin(\theta) \tag{A.1}$$

In small angle scattering techniques, the scattering angle is not measured directly. Instead, a planar detector, oriented perpendicular to the incident beam, records the intensity of the scattered beam at each of many points distributed across its plane. The location on the detector at which an intensity measurement is made is related to the location at which the incident beam hits the detector by a scattering vector, q, which is the vector on the detector plane from the incident beam point to the scattered beam point as shown in Figure A.1.

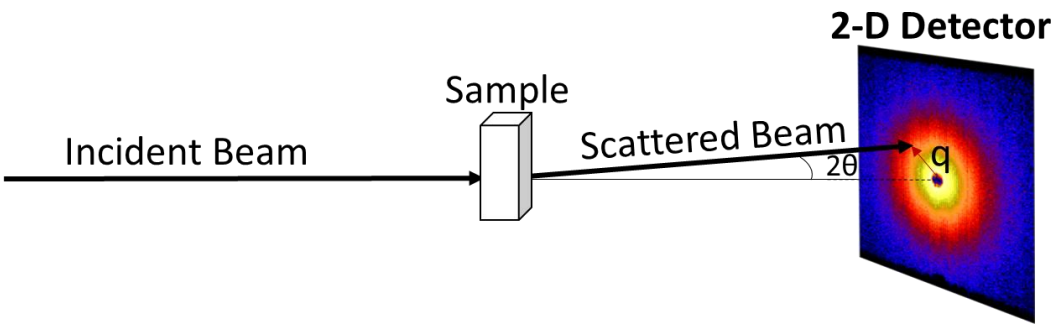

Figure A.1. Schematic of a small angle scattering test, where the detected intensity on the 2-D detector vs the scattering vector at that location, q, is used to characterize microstructural features of the sample. Modelled after reference 9.

The relationship between the scattering vector, q, and the scattering angle, 2θ, in Figure A.1 is shown in equation (A.2) .[103]

$$q = \frac{4\pi}{\lambda} sin\theta \tag{A.2}$$

Using this equation, the scattering vector is shown to be inversely related to the distance between the features, d, through equation (A.).

$$d = \frac{2\pi}{q} \tag{A.3}$$

Therefore, since the typical angles probed in diffraction methods, on the order of degrees, are ideal for measurements on the scale of the distances between crystallographic planes, the far smaller scattering angles measured in SAS methods are necessary to characterize larger microstructural features. The scattering data can be fit to models based on equations for idealized microstructural features and when such fitting has been carried out, it has been shown that SAS methods can provide extensive data on a wide range of features present in

porous microstructures. Such features include the number and volume fractions of pores, the surface areas of both open and closed pores, the pore size distribution, and the topology of the microstructure.[104-106]

The scattering cross section of a material phase is a measure of how strongly the incident species will scatter from the atoms of that phase.[107] In real materials systems, the total scattering cross section will consist of a combination of coherent and incoherent scattering, where incoherent scattering results from distributions of elements present in the phase as well as distributions of the isotopes of those elements present in the sample under test.[107] The macroscopic scattering cross section for a two-phase system can be treated as consisting of a combination of factors known as a contrast factor, a form factor, and a structure factor.[107] The contrast factor is dependent on the properties of the atoms present in each phase and the type of incident particles/waves. For example, the scattering cross section of a phase upon exposure to an incident beam of neutrons will depend on the atomic numbers of the atoms present in that phase, since a larger nucleus increases the probability that a neutron will hit that nucleus, resulting in a scattering event unless the neutron incorporates into the nucleus. The form factor represents the interference due to scattering from different parts of the same object, and is thus dependent on particle geometry, whereas the structure factor represents interference due to scattering from different objects, making this factor dependent on the spatial distribution of particles.[107] Therefore, to extract useful information from the 1-D scattering data for a sample of known composition, the contrast can be directly calculated and the structure and form factors can be fitted to a theoretical model. In the present work, 1-D scattering data is fit to the Unified Fit Model[108], in which regions of the data are fit to a combination of equations describing the scattering response

from one microstructural feature over different length scales. The equations for the individual regions are then added together to fit the entire data curve.

Under an assumption of isotropic particle distribution and geometry, radial averaging of the two-dimensional I(q) vs q SAS data can be carried out, resulting in one dimensional I(q) vs q data. This 1-D data, when plotted on a log-log scale, gives a data curve consisting of the sum of the responses of each distinct microstructural feature of the sample. The general form of the response of a single feature is shown in Figure A.2.[109] In this figure, the curve is divided into three separate linear sections, which are the Guinier region, the fractal region, and the Porod region. The Guinier region encapsulates the average, bulk response of a microstructural feature, such as particle volume and correlation length, but does not include any local description of structure, such as the responses from surfaces or mass fractals.[108] Meanwhile, the Porod region encompasses the response of local structure but fails to describe the larger-scale averaged structure.[108] The equations which describe the Guinier and Porod regions are used in combination in the Unified Fit Model[108] to fit the scattering response of each unique microstructural feature. The Guinier and Porod regions are defined by Guinier's Law and Porod's Law, respectively, which will be described in the following section.

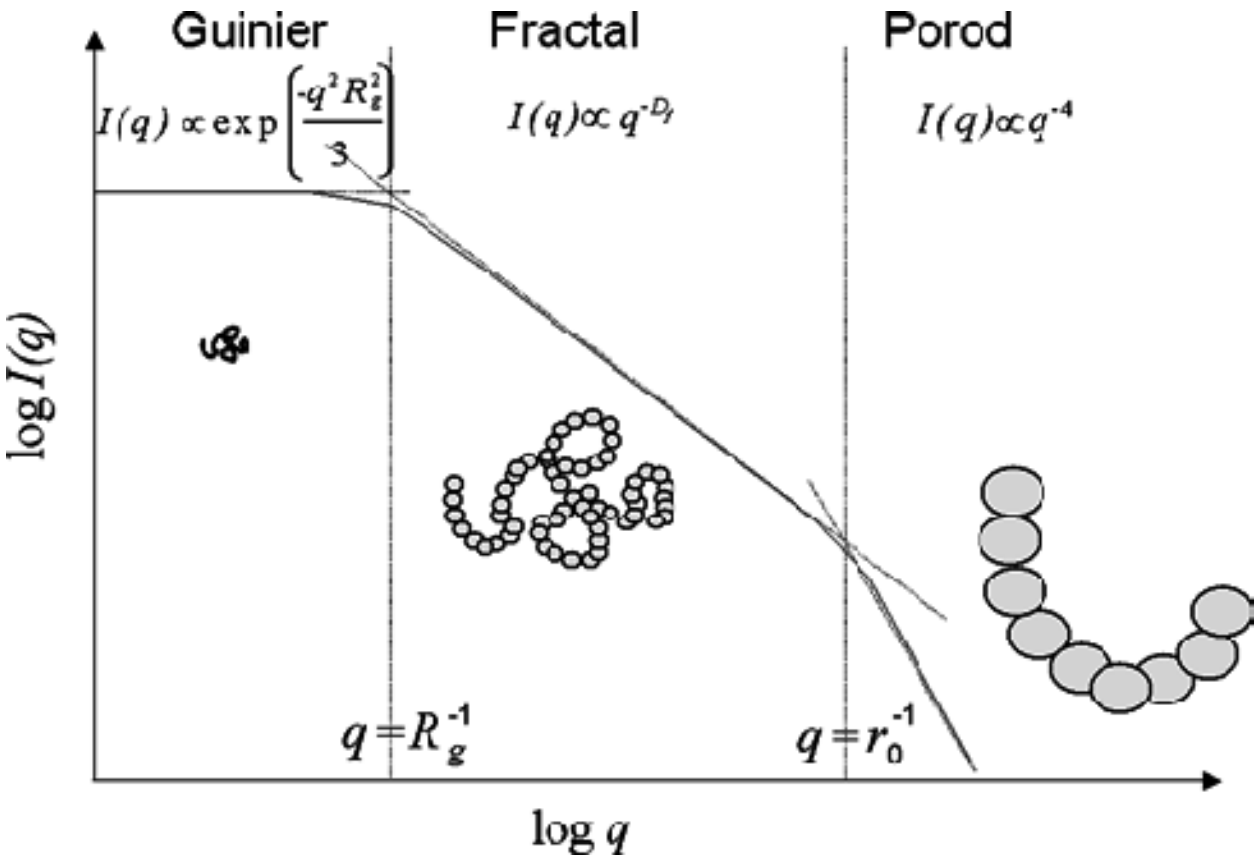

Figure A.2.[109] An example of a log I(q) vs log q plot for one prevalent feature of a tested material. Here, the total response is separated into a Guinier region, a fractal region, and a Porod region, each with the equation defining the curve in its section given at the top of the plot. Since q is a reciprocal distance value, the length scale is increasing as the q value decreases. The drawings in each plot section illustrate this, showing that the Guinier region represents average bulk features of the microstructural feature, whereas the Porod region is the local response including the response from surfaces.[108]

A.1.3 Scattering data analysis

A.1.3.1 Guinier's Law Behavior

To derive Guinier's Law, a correlation function, γ(r), is defined, which represents the probability that a point at a radial distance, r, from a given point in a particle phase will also be in that phase.[108] Under an assumed condition of rotationally averaged,

centrosymmetric particles, this function is related to the particles' form factor through the equation

$$\overline{F^2 q} = V_p \rho_e^2 \int_0^\infty \gamma(r) \left[\frac{\sin(qr)}{qr}\right] 4\pi r^2 dr \qquad \text{(A.4)}$$

where V_p is the volume of a particle, ρ_e is the particle's electron density, q is the scattering vector which was defined in a preceding paragraph, the term sin(qr)/qr is a weighting function, and the $\gamma(r)r^2$ term is called the distance distribution function.[108] The correlation function can only be calculated exactly for very simple structures, so two different approximations are used; one approximation applies at high q values, known as a power law regime, and the other at low q values, known as a Guinier regime.[108] Under a condition of small q values, the weighting function approaches 1 and equation (A.4) simplifies to

$$\overline{F^2 q} = V_p \rho_e^2 \int_0^\infty \gamma(r) 4\pi r^2 dr \qquad \text{(A.5)}$$

where the integral is then equal to the average particle volume, V_p.[108] When q is large, however, the weighting function quickly decays as r increases and proceeds in a dampened oscillation pattern around 0. Therefore, at high q, only values of r less than $(2\pi)/q$ significantly contribute to the high-q intensity. Therefore, in considering both the low-q and high-q extremes, the relationship is established that for small q, only large r values contribute significantly to the intensity, whereas for large q, only small values of r will affect the intensity. This relationship will be important when determining which correlation function approximation will dominate the total intensity for a given range of q.

Guinier's law can be defined as the Fourier transform of the correlation function describing a particle randomly averaged about both its orientation and its position relative to the scattering reference plane (Figure A.3).[108] Under this condition, the odds that a point a distance r from an initial point, randomly placed within the particle ($0 \leq r \leq r_{max}$), is inside the particle is given by a function which is equal to 1 at the location of the initial point, since the initial point had to be placed within the particle. Under this condition, the correlation function for the Guinier regime is

$$\gamma(r)_{Guinier} = e^{\left(\frac{-3r^2}{4R_g^2}\right)} \tag{A.6}$$

where R_g is the radius of gyration of the particle, which functions as a size variable for the particle.[108] A Fourier transformation of this function gives the relationship between the scattering intensity, I(q), and scattering vector, q, which was indicated in Figure A.2:

$$I(q) = I_e \overline{N_p} n^2 e^{\frac{-R_g^2 q^2}{3}} \tag{A.7}$$

where I_e is the scattering factor for one electron, $\overline{N_p}$ is the number of particles in the scattering volume, and n is the number of electrons in a particle.[108]

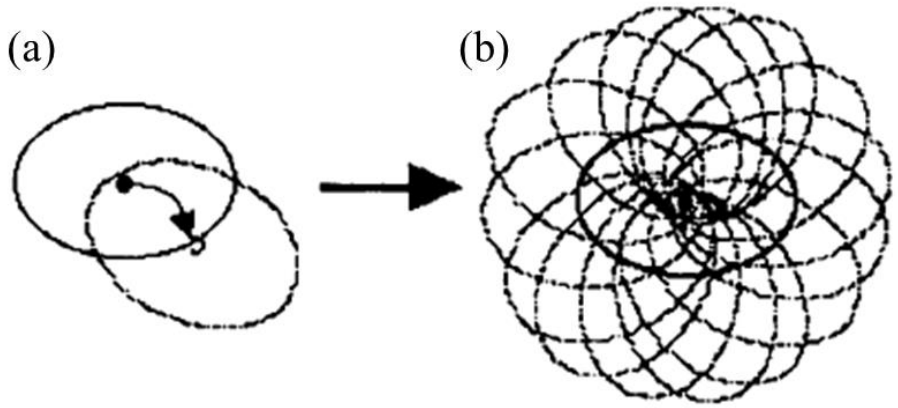

Figure A.3.[108] Illustration of the process of averaging a particle about the origin of the vector r, representing random rotations and translations of the particle about the origin of r. (a) shows a single translation and rotation of the particle. The superposition of many translations and rotations in random directions, shown in (b), results in a Gaussian distribution of the scattering density.

A.1.3.2 Power law behavior

Porod's law is derived from an extreme case of considering a particle at such a small length scale that the arbitrarily-shaped surface of the particle is considered to be locally flat (Figure A.4 (a)).[108,110] In this model, the particle is divided into two regions, the Porod bulk and the Porod surface, and the Porod correlation function is defined as the probability that two points, separated by a distance, r, in an arbitrary direction, will be located within either the Porod bulk or the inner half of the Porod surface. From these conditions, the Porod correlation function is given by

$$\gamma_{Porod}(r) = 1 - \frac{Sr}{4V} \tag{A.8}$$

where S is the particle's surface area and V is the particle's volume.[108] Using this identity, the shape function becomes

$$\overline{F^2 q} \cong 2\pi\rho_e^2 \frac{S}{q^4} \tag{A.9}$$

However, the classical Porod model breaks down under conditions of small q or large |r|, for which the assumption of a locally flat particle surface is no longer valid, and considerations for structural restrictions on the model (Figure A.4 (b)) must be made in these cases.[108] A modified correlation function which accounts for this change in the model can then be derived:

$$p(q, R_g) = [\mathrm{erf}(\frac{qR_g}{6^{0.5}})]^3 \tag{A.10}$$

which can then be used as a correlation function for the structurally-limited power law condition.[108] This gives a modified, structurally limited Porod's law equation

$$\overline{F^2(q)} = 2\pi\rho_e^2 S[\frac{\left(\mathrm{erf}\left(\frac{qR_g}{6^{0.5}}\right)\right)^3}{q}]^4 \tag{A.11}$$

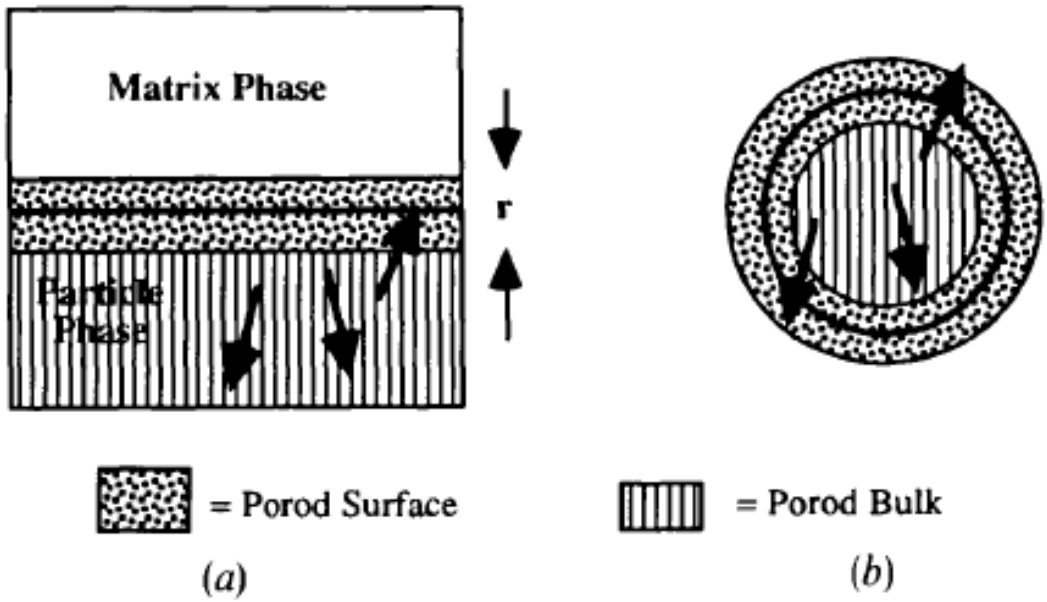

Figure A.4.[108] Schematics which illustrate (a) classical Porod scattering and (b) structurally limited Porod scattering. Classical Porod scattering is based on an idealized structure with a flat surface of infinite area, and the rotational averaging of distance r, represented by the arrows, leads to the derivation of Porod's law. When structural limits are considered, the correlation function changes to account for the errors of the classical model in cases of small q or large |r| values.

where erf represents the error function.[108]

In cases of mass-fractal or surface-fractal behavior (Figure A.2) or of diffuse interfaces, power-law scattering is also seen. Considering these conditions in addition to Porod's law scattering leads to a more general expression which can describe all power-law behavior

$$I(q) \propto [\frac{\left(\mathrm{erf}\left(\frac{qR_g}{6^{0.5}}\right)\right)^3}{q}]^P \qquad \text{(A.12)}$$

where P=4 in the case of Porod scattering and takes other values when describing other power law behavior.[108]

A.1.3.3 Unified Fit model for SAS data

As alluded to previously, the Unified Fit model uses a combination of Guinier's law and power law equations to model the small-angle scattering from the features at a particular microstructural level. Doing so is valid because considering structural limits for the Porod condition leads to the derivation of a low-q limit to the power-law behavior of the Porod region. Combining the exponential forms of the Guinier correlation function and the structurally-limited power law correlation function gives a unified equation[108]

$$I(q) = Ge^{\frac{-q^2R_g^2}{3}} + B[\frac{\text{erf}\left(\frac{qR_g}{6^{0.5}}\right)^3}{q}]^P \quad \text{(A.13)}$$

In the Guinier's law term, the pre-exponential factor is defined as $G=n^2N_pI_e$, where n is the number of electrons in a particle, N_p is the number of particles in the scattering volume, and I_e is the scattering factor for a single electron. In the power-law term, $B=2\pi N_p\frac{n^2}{V_p}S_pI_e$, where S_p is the surface area of the particle. Using this unified equation, any features common throughout a material under SAS tests will produce a response consisting of a lower-q Guinier region and a higher-q Porod region. Therefore, whenever the tested material shows features at different length scales, such as a mixture of powders with a bimodal particle size or a powder with aggregates and agglomerates, each separate feature, designated as a level, will have its own Guinier and Porod region within the total SAS response. It was demonstrated that any SAS data for a material with features on distinctly

different length scales can be approximated by a combination of these levels, and in doing so the complete scattering response of a sample can be modeled.[108]

In order to make use of the results of the fit resulting from use of the Unified Fit model, each level of the fit must be assigned to a scattering species, which has either been confirmed to be present using other characterization methods or can be reasonably expected based on knowledge of the material, in order to verify that each level is physically meaningful. As with the fitting of impedance data, the addition of more terms to any fitting model will eventually allow that model to fit any data, but the model is only useful if all terms can be assigned a physical meaning. When this is accomplished, then the fit indicates the properties of the individual constituent features. Specifically, for each level, a proper fit will give values for G, Rg, B, and P pertaining to that level's contribution to the total I(q) vs q curve.

A.1.3.4 Derivation of porosity from transmittance data

In all the SAS testing, the porosities of the powder compacts were determined from the transmission values included in the 1-D data files, given as the ratio of the beam flux measured by the detector to that of the incident beam at q=0,[111] equivalent to the fraction of the beam which made it through the die and the powder to reach the detector. Since the background removal process should have removed the effects of the die on the resulting data, these transmission values were taken to represent the effect of the powder alone. The equation relating the transmission to sample thickness is the Beer-Lambert law:

$$I = I_0 e^{-\mu\rho x} \tag{A.14}$$

where I is the intensity of the transmitted beam, I_0 is the intensity of the incident beam, μ is the mass absorption coefficient, ρ is the tested material's density, and x is the distance travelled by the beam through the material.[112] Transmission is then equal to $\frac{I}{I_0}$, x is the thickness of the powder, which was a constant 3.175 mm for the in-situ tests, ρ is the theoretical density of the SiC powder, 3.21 g/cm^3, and μ is the material-specific, thickness-independent mass absorption coefficient, which represents the degree to which the incident beam will be scattered and absorbed per gram of material.[102] This value was obtained by importing the powder composition, its theoretical density, and the incident beam energy into the scattering contrast calculator and anomalous scattering contrast calculator found in the Irena tool suite.[113] This gave a value for $\frac{\mu}{\rho}$ and since this value is constant, using this value with the experimental powder thickness gave the actual density of the powder. Solving the Beer-Lambert law for the density gives $-\frac{\ln(transmission)}{\mu x} = \rho$. Multiplying both sides by ρ and taking the square root gives the final equation:

$$\rho = \sqrt{\frac{-\ln(transmission)}{\frac{\mu}{\rho}x}} \tag{A.15}$$

The experimental density derived with this equation, divided by the theoretical density, then gives the relative density, and one minus that value gives the porosity.

A.2 Small angle scattering experimental methods

In-situ impedance testing during powder compaction was carried out as described in the experimental procedure chapter (section 2.5.8). SANS tests were conducted at the

CG-2 beamline (Figure A.5) within the High Flux Isotope Reactor (HFIR) facility at Oak Ridge National Lab (ORNL) in collaboration with Ken Littrell, Jeff Bunn, and Paris Cornwell.[114] These tests covered a q range of 0.00285 $Å^{-1}$ – 0.376 $Å^{-1}$ and were conducted concurrently with IS tests in-situ during powder compaction. IS testing was conducted using a Solartron 1260 impedance analyzer in conjunction with a Solartron 1296 (Solartron Analytical, Farnborough, Hampshire, UK) dielectric interface. Testing was conducted over a frequency range of 10^{7}-10^{-1} Hz and a constant voltage of 500 mV was applied.

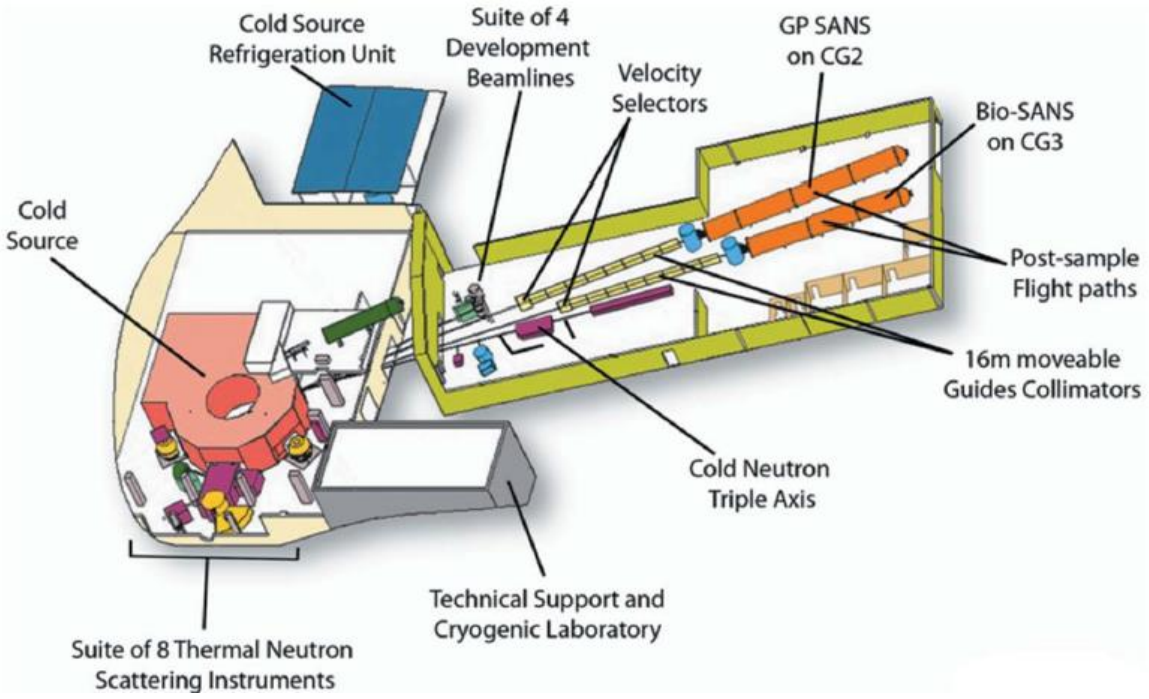

Figure A.5.[114] Layout of the HFIR facility at ORNL, showing the CG-2 beamline at the top right.

USANS tests were conducted at the BL-1A beamline (Figure A.6) at the Spallation Neutron Source facility at ORNL, working with Ken Littrell and Luke Heroux.[115] They were conducted on pre-compacted powders over a q range of 4.23×10^{-5} $Å^{-1}$ – 2.51×10^{-2} $Å^{-1}$.

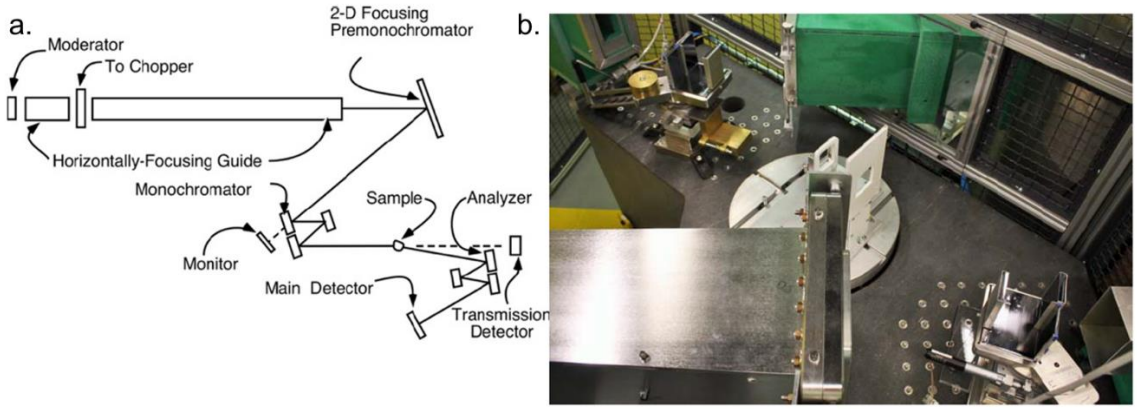

Figure A.6.[115] (a) Schematic and (b) image of the USANS equipment at the BL-1A beamline at the SNS facility at ORNL.

SAXS/USAXS tests were conducted at the 9ID-C beamline (Figure A.7) at the Advanced Photon Source (APS) at Argonne National Lab (ANL) in collaboration with Jan Ilavsky and with assistance from Ivan Kuzmenko.[116,117] The equipment was able to switch between SAXS, USAXS, and WAXS detectors and run all 3 tests in under 5 minutes total. The combined SAXS-USAXS data covered a q range of 1.022×10^{-3} Å^{-1} – 1.615 Å^{-1}. When impedance testing was conducted, a Gamry Reference 3000 Potentiostat/Galvanostat/ZRA was used in the 4-probe configuration using a constant voltage of 100 mV and taking measurements over a frequency range of 10^{6}-10^{-1} Hz.

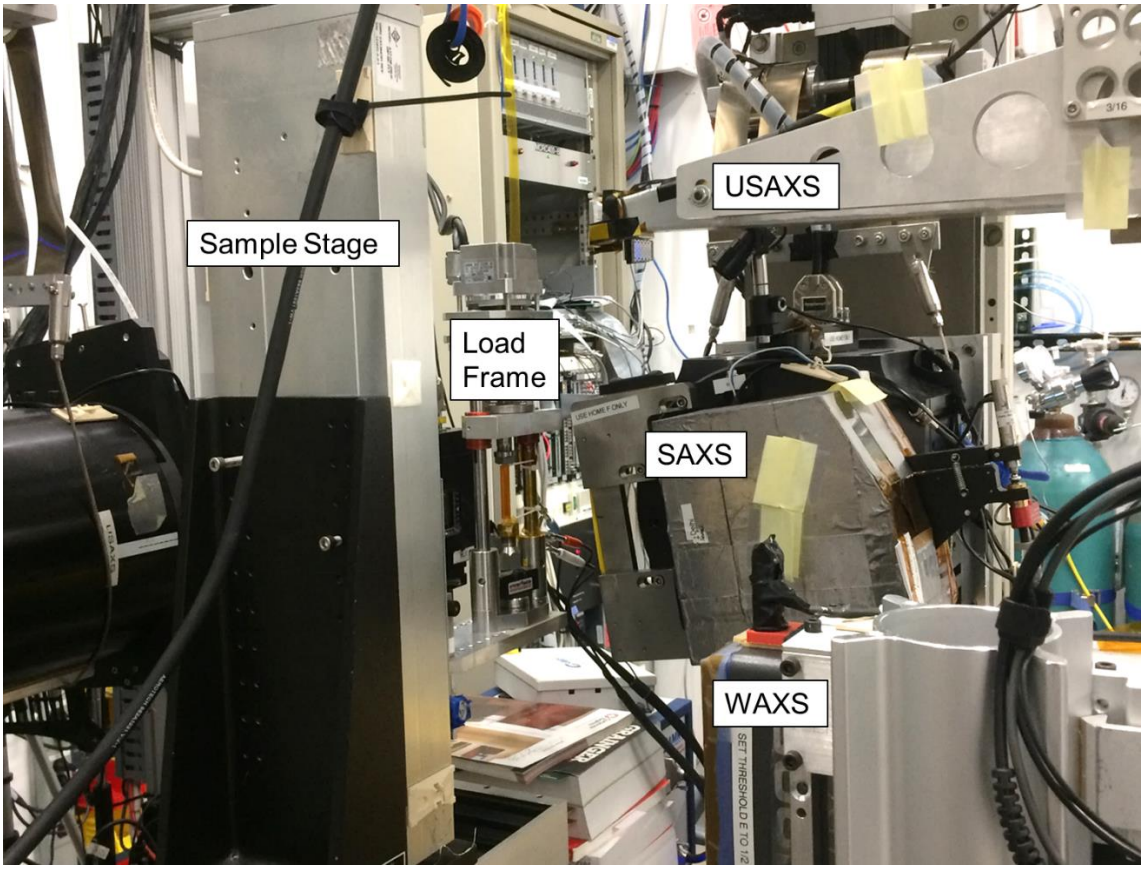

Figure A.7. Image of the equipment at the 9ID-C beamline at the APS facility at ANL.[116,117] Here, the USAXS, SAXS, and WAXS detectors can be seen, as well as the sample stage holder and the load frame used during in-situ SAXS testing.

An overview of the testing conditions used for all SAS tests, as well as the sections in which each test is discussed in detail, are presented in Table A.2.

Table A.2. Materials and Conditions for IS-SAS Testing of Powder Compacts

Section Where Discussed	Test Name	Test Location	Powder Compositions	Applied Pressure Range (MPa)	Test Cell ID (mm)	Test Cell OD (mm)	Test Cell Material	Punch/Spacer Material	IS Equipment	SAS Testing Direction
A.3	In-situ IS + SANS	HFIR CG-2	β-SiC nano, ITO nano, ATO nano	0-300	8.4	15.6	Polycrystalline sapphire	SS/Ti	Solartron 1260 + 1296	Radial
A.4	Ex-Situ USANS	SNS BL-A1	β-SiC nano, ITO nano, ATO nano, β-SiC whisker, β-SiC micron	300	8.4	15.6	Polycrystalline sapphire	SS/Ti	-	Axial
A.5	Ex-situ SAXS + USAXS	APS 9ID-C	β-SiC nano	0-1000	4.75	5	Borosilicate glass	PS	-	Radial, Axial
A.6	In-situ IS + SAXS + USAXS	APS 9ID-C	β-SiC nano	0-300	0.74	2.63	Polycrystalline sapphire	WC	Gamry Reference 3000	Radial
A.7	Pre-compacted Heating SAXS + USAXS	APS 9ID-C	ITO-borosilicate, 0.001 phr, 1.0 phr, 5.0 phr	50, 150	0.74	2.63	Polycrystalline sapphire	WC/Glass wool	-	Radial

A.3 In-situ IS+SANS

In this section, data is presented for tests of three different nanopowders, β-SiC, ITO, and ATO during in-situ compaction over a pressure range from 0 MPa – 300 MPa at 50 MPa increments. In these tests, conducted at the CG-2 beamline at the HFIR facility at ORNL[114], both SANS and IS were conducted simultaneously, making this the first set of tests to do so. The results, shown to be promising yet mixed, paved the way for the SAXS tests presented in the following section.

A.3.1 Testing Procedure

In this procedure, approximately 0.3g of a chosen ceramic powder was measured and placed into a sapphire die which was surrounded by an aluminum shroud as a safety measure in case the die were to fracture. The powders used in this series of tests were an ITO nanopowder (Sigma Aldrich, <50 nm), an ATO nanopowder (Alpha Aesar, 22-44 nm), and a β-SiC nanopowder (10-70 nm, US Research Nanomaterials Inc.). Sapphire and aluminum are "transparent" to neutrons, so they could be used to contain the powder under pressure without contributing much of their own signal and without absorbing much of the incident beam, thereby preserving the strength of the signal reaching the detector. On either end of the sapphire tube, a series of titanium spacers, which are also "transparent" to neutrons, were inserted, followed by a set of custom-made steel punches (Figure A.8). The titanium spacers separated the powder from the punches such that even when the powder was highly compressed, the punches did not enter the path of the neutron beam, which is important since the steel strongly absorbs neutrons. These punches were secured to the

inside of a tension-to-compression (T2C) fixture, between which were insulating phenolic spacers to electrically isolate the punches and steel spacers to adjust the position of the die within the load frame to ensure the powder was in the path of the neutron beam.

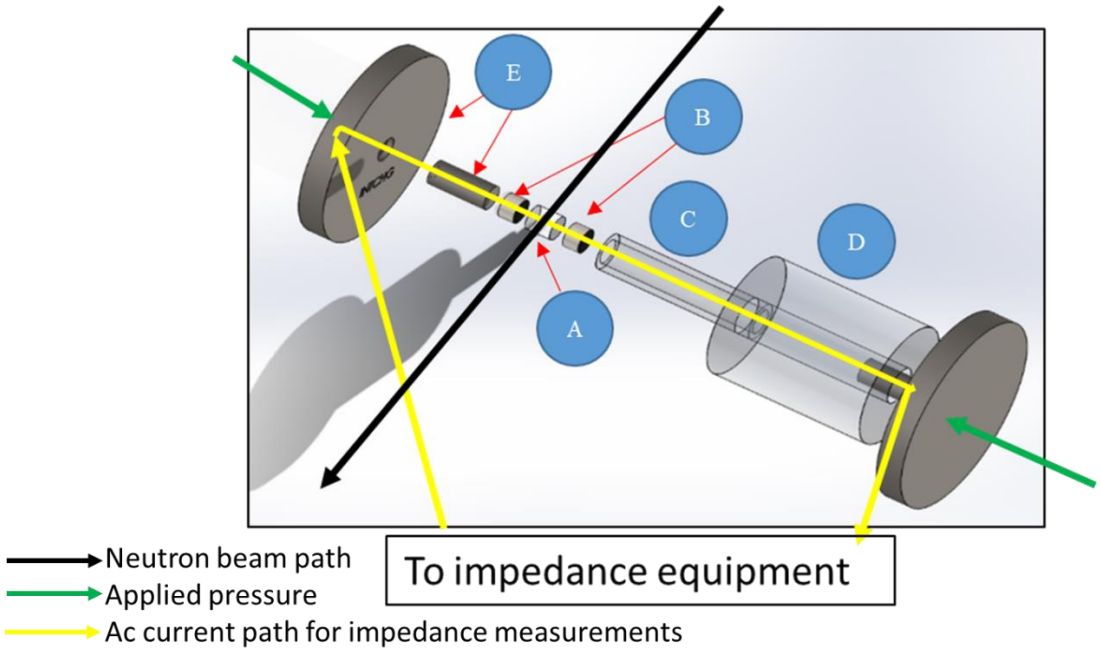

Figure A.8.[97] Schematic of the test cell used in in-situ combined impedance spectroscopy and SANS during powder compaction on the CG-2 beamline at the HFIR facility at Oak Ridge National Lab.[114] The ceramic powder under test (A) is surrounded by Ti spacers (B), which are contained in a cylindrical sapphire cell (C). The cell was housed within an aluminum shroud (D) for safety, although there was never any indication of powder escape or damage to the cell during testing. The Ti, Al, and sapphire components do not scatter or absorb neutrons very much and, therefore, the background signal was easier to deal with. Stainless steel punches (E) fit into the sapphire cell to transfer the load from the load frame to the powder. Electrical leads were fixed to the outer diameter of each punch for connection to the ac impedance spectroscopy equipment. Insulating phenolic spacers on the ends of the punches electrically isolated the test cell from the load frame for the benefit of the impedance tests. SolidWorks schematic courtesy of Paris Cornwell at ORNL.

The T2C fixture consisted of two rigid metal frames which could slide in the directions of the movement of the load frame such that, by applying a tensile force to one of the two T2C frames, it would decrease the space between the two frames, in which the die assembly

was mounted. In doing so, the tensile force of the load frame was effectively converted to a compressive force on the die assembly. The T2C fixture was attached to a computer-controlled load frame which could only apply tensile loads and was mounted within the beam path of the CG-2 beamline (Figure A.9). The load frame was mounted such that there was a 45° angle between the beam direction and the direction of applied pressure to increase the volume of powder in the beam path. Electrical leads were attached on the outsides of the bases of the punches (see E in Figure A.8) and wires from the ac impedance spectroscopy equipment were connected to these leads. During the testing, the current passed from this equipment through the steel punch, the titanium spacer, and the ceramic powder. It then passed through the other steel punch and titanium spacer before returning to the equipment.

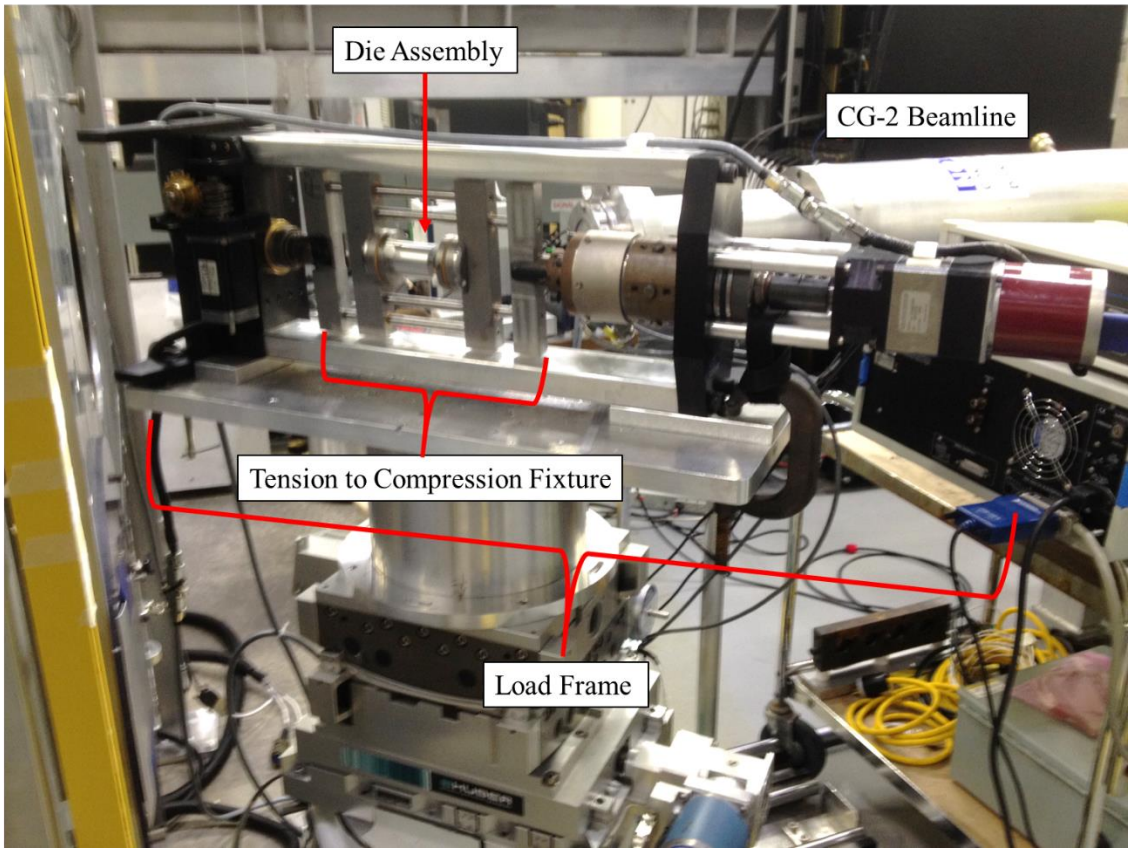

Figure A.9.[97] The die assembly, within the tension to compression fixture, within the load frame, mounted in the path of the CG-2 SANS beamline. The setup was developed through collaboration with Ken Littrell, Jeff Bunn, and Paris Cornwell at ORNL.

After mounting the die assembly within the load frame, the load frame was used to bring the punches close enough to each other that contact was made with the powder from both punches. This condition was designated as 0 MPa. Before the neutron beam was turned on, a looping impedance test with a frequency sweep from 10 MHz to 0.1 Hz was initiated so the electrical properties were measured continuously throughout the test. Each SANS test was composed of a set of three individual SANS scans, where one scan was carried out with the detector at a distance of 2 m from the sample to get larger angle scattering data, one was carried out with the detector at a distance of 18.5 m from the

sample to get smaller angle scattering data, and one was carried out with an 18.5 m sample to detector distance with the beam trap moved away from the center of the detector in order to get the direct beam scattering data. Once the SANS tests had completed, a signal was given to start the load frame moving until the next target pressure was reached, after which the entire process was repeated until the tests were concluded at all desired pressures. For these tests, the pressure on the powders was increased from 0 to 300 MPa in 50 MPa increments.

Each time the powder reached the next set pressure and the load frame was stopped, all impedance tests afterward were essentially identical to each other until the SANS tests were completed and the load frame was started up again to reach the next pressure. To get a single set of electrical data points for each pressure, each data point at each frequency for all ac impedance tests run during the time between movements of the load frame were averaged together.

A.3.2 Reduction and correction of scattering data

After the tests were completed, the 2-D SANS data at each pressure was reduced to 1-D data using the SPICE software package developed at ORNL.[118] This reduction involves adding the trans scan data to both the long and short scan data (Figure A.10(a)), removing the empty cell data, then converting from 2D to 1-D by radial averaging, resulting in two 1-D curves (Figure A.10 (b)). There was a region of overlap in the q values of the two 1-D data sets. Ideally, each pair of data points with the same q should have had the same intensity, and although this was not quite the case, as seen in the example Figure A.10 (b), the overlapping data was close and the discrepancy could be fixed with a simple

procedure; to proceed with data fitting, the two 1-D data sets had to be combined into one continuous data set. This was done using the "merge two data sets" program within the Irena tool suite[113]; first, a region was identified defining the data with overlapping q values between the two detectors in which there were no artifacts or particularly noisy points. The program then multiplied the intensities of the short scan data by a scaling factor such that the intensities of the short scan points in the overlap region were as close as possible to those of the long scan points with the same q values. This procedure had the overall effect of turning the two data curves into a single, continuous curve (Figure A.10 (c)). Finally, data points with high errors or which were determined to be artifacts at the q extrema were removed (Figure A.10 (d), enabling data fitting via the Unified Fit model.

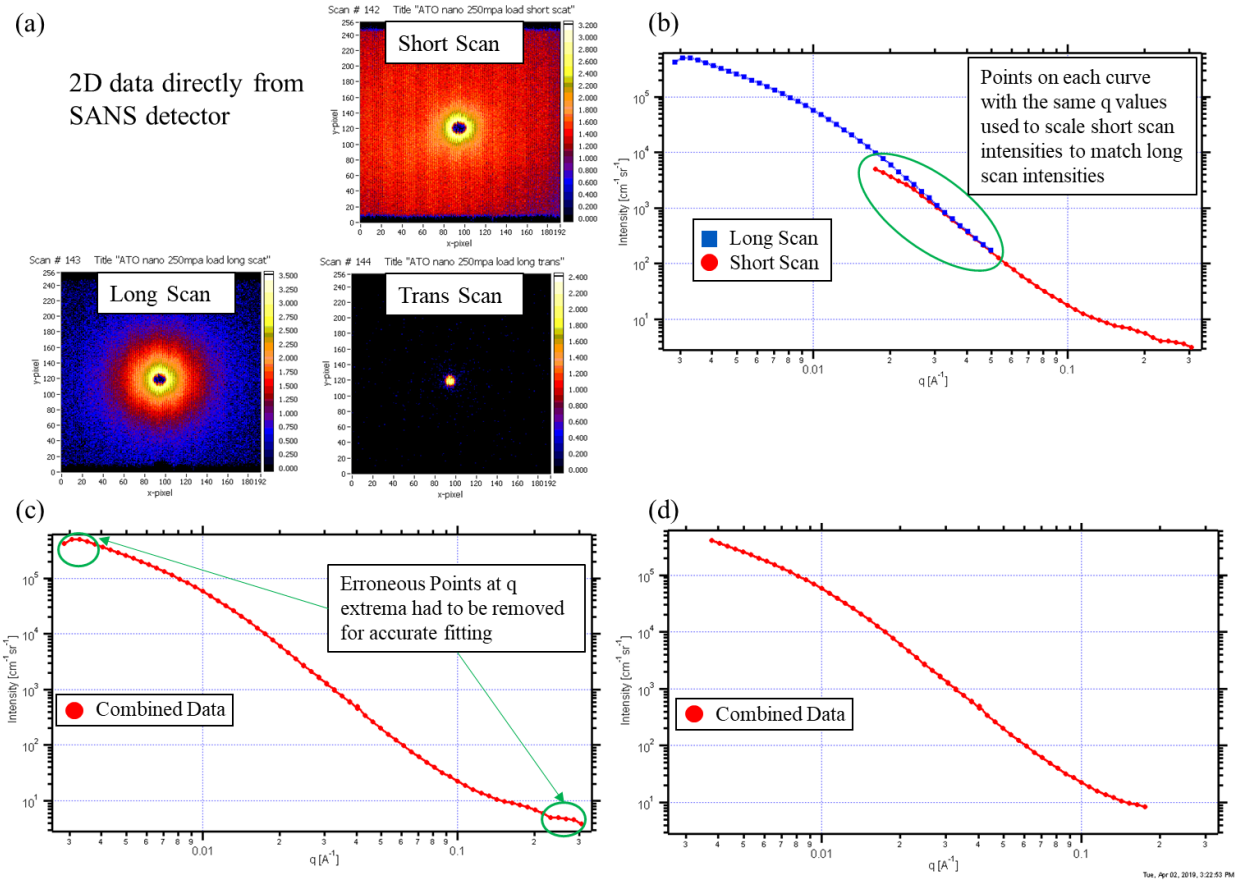

Figure A.10. The conversion of the raw data from the 200 MPa SiC SAS measurements from (a) the three 2-D data sets measured by the SANS detector into a single continuous 1-D curve required (b) the reduction of the three 2-D data sets into two 1-D curves through radial averaging using the SPICE software for Igor Pro developed at ORNL[118], followed by (c) short scan intensities were multiplied by a scaling factor which gave the region of overlapping data the same intensities. Erroneous data points due to experimental artifacts and high errors at the extrema of the combined q range were then removed (d), giving the final curve used in the Unified Fit modelling.

A.3.3 SAS Data fitting and analysis

The reduced, combined data curves for each of the three powders at all studied pressures is presented in Figure A.11. The prevalent trend across this data is decreasing intensity with increasing pressure, and the general shape of the curves is maintained over the entire pressure range for each powder. One notable difference between the data for the

different powders is apparent in the 0 MPa data. For the SiC data, the 0 MPa curve has a significantly different shape and intensity than the curves for the other pressures and violates the decreasing intensity with increasing pressure trend seen in all other curves across all of the powders. Due to the high irregularity of this curve, it seems most likely that some error in the testing process resulted in an incorrect curve for this data. The 0 MPa curve in the ATO data also shows a much different intensity than the others for that powder. However, this curve followed the general trend and maintained a similar shape to the others, so this data was less likely to be erroneous. The ATO data shows that almost all of the compaction of the powder took place between applied pressures of 0 and 50 MPa. The ITO data corroborates this assertion, as again virtually all of the total change in intensity occurs before reaching 89 MPa. The unexpectedly low early applied pressures in this data resulted from an error in the macro controlling the operation of the load frame. However, this ended up being advantageous to some extent, as the progression of the intensity changes can be seen as a result of collecting data at two pressures between 0 and 50 MPa. Interestingly, despite having a particle size on the same order as the other nanopowders, the SiC shows a more gradual decrease in intensity with increasing pressure and visible changes continue to occur even between the largest pressures. A good reason for this difference in behavior has not yet been found.

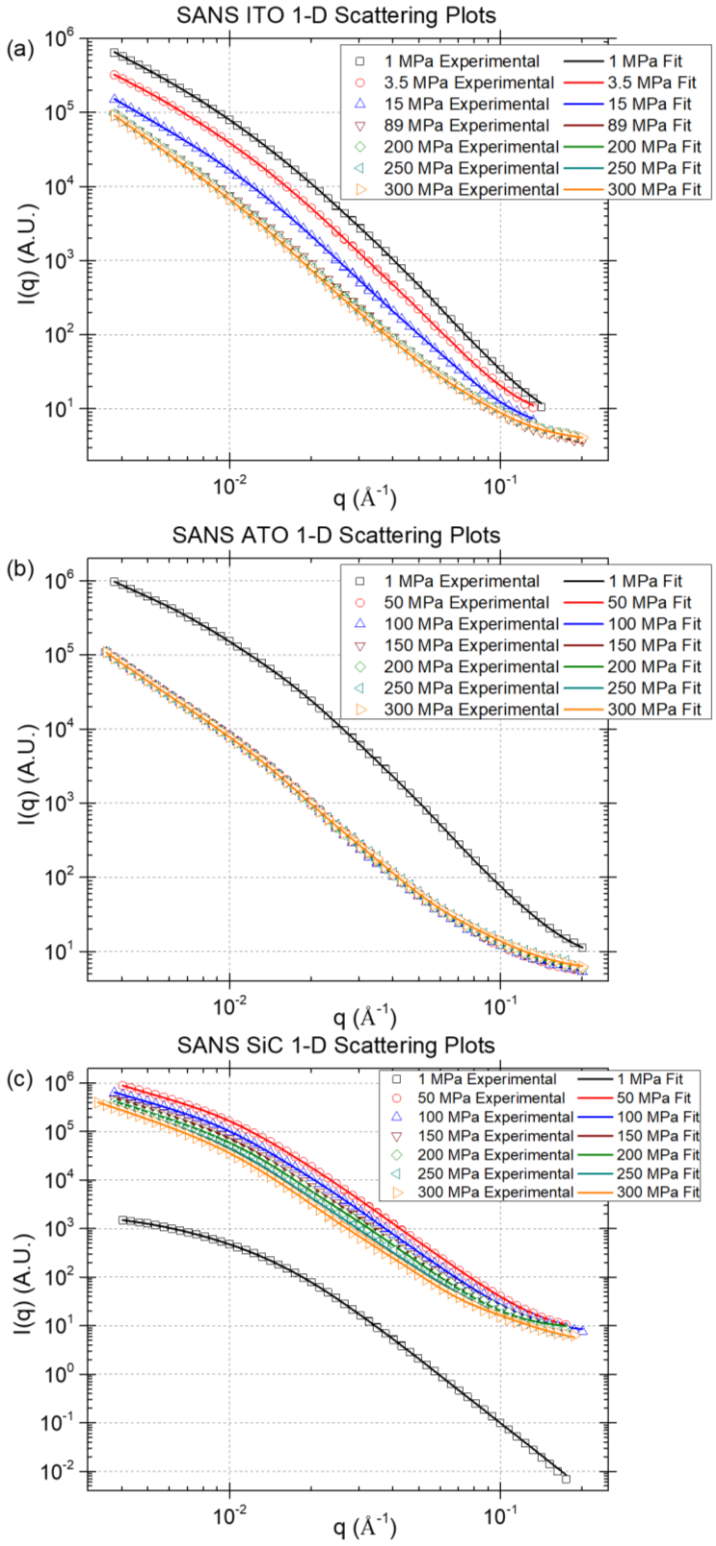
SANS ITO 1-D Scattering Plots
(a)
1 MPa Experimental
3.5 MPa Experimental
15 MPa Experimental
89 MPa Experimental
200 MPa Experimental
250 MPa Experimental
300 MPa Experimental
1 MPa Fit
3.5 MPa Fit
15 MPa Fit
89 MPa Fit
200 MPa Fit
250 MPa Fit
300 MPa Fit
I(q) (A.U.)
q (Å-1)
SANS ATO 1-D Scattering Plots
(b)
1 MPa Experimental
50 MPa Experimental
100 MPa Experimental
150 MPa Experimental
200 MPa Experimental
250 MPa Experimental
300 MPa Experimental
1 MPa Fit
50 MPa Fit
100 MPa Fit
150 MPa Fit
200 MPa Fit
250 MPa Fit
300 MPa Fit
I(q) (A.U.)
q (Å-1)
SANS SiC 1-D Scattering Plots
(c)
1 MPa Experimental
50 MPa Experimental
100 MPa Experimental
150 MPa Experimental
200 MPa Experimental
250 MPa Experimental
300 MPa Experimental
1 MPa Fit
50 MPa Fit
100 MPa Fit
150 MPa Fit
200 MPa Fit
250 MPa Fit
300 MPa Fit
I(q) (A.U.)
q (Å-1)

Figure A.11. q vs I(q) log-log plots for the (a) ITO, (b) ATO, and (c) SiC nanopowders characterized via SANS after combining the long scan and short scan data and removing bad data points. Experimental data and fit data are shown as symbols and lines, respectively.

A.3.3.1 Unified Fit Results

To analyze the reduced, processed, and combined SAXS/USAXS data, the data files were selected in the Unified Fit tool, and fitting was started by fitting the background signal, found at the highest q values, to a horizontal line on the log-log q vs I(q) plot. Levels were then built up from the highest q values to the lowest, with an additional level added whenever a Guinier region contacted a Porod region with a lower q value. The plot was set to automatically update, so any change to a fitting value would immediately change the plot. This feature was used to manually obtain starting values for G, R_g, B, and P for each level by incrementally changing the individual values so the response of the level was "walked" into its appropriate place on the experimental curve. Although a reasonable guess as to the total number of levels needed to fit an experimental curve can be made based on the number of unique linear (Porod) regions apparent in the data, the number of levels in the final model had to be determined based on how close a fit could be made with a given number of levels and whether additional levels could still be assigned a physical meaning.

The final fitting parameters for the ITO, ATO, and SiC powders are presented in Table A., Table A., and Table A., respectively. For the ITO and ATO powders, a 3-level model was found to give the best fit with a minimum number of levels. An example of such a fit is shown in Figure A.12, which presents data for the ATO powder under an applied pressure of 250 MPa. Examination of the R_g values in each level provides clues as to the microstructural feature represented by that level. For the ITO and ATO data, the first level,

representing the smallest features, generally had values of less than 10 nm. The radius of gyration of the particles, which were assumed to be spherical, is related to the particle radius, R, through the equation

$$R_g^2 = \frac{3}{5}R^2 \tag{A.16}$$

and the actual particle size, equal to the diameter, is double the radius.[107] Therefore, the particle sizes represented by R_g values between approximately 2.5 and 10 nm are 6.5 and 25.8 nm, respectively. These are at or below the nominal lower size limit of these particles, so level 1 may represent scattering from a thin shell layer at the particle surfaces. This layer could be a region of depletion or excess of the dopant species, which is Sn in ITO and Sb in ATO, or a region with a higher degree of oxidation compared to the bulk. Differences in dopant concentration could have been induced during the synthesis of the powders, and oxidation could have progressed over time during the storage periods of each powder, so either situation seems possible.

Table A.3. Unified Fit Parameters for ITO Powder Tests

		Level 1					Level 2					Level 3				
Applied Pressure (MPa)	SASBackground	G	Rg (nm)	B	P	RgCO (nm)	G	Rg (nm)	B	P	RgCO (nm)	G	Rg (nm)	B	P	RgCO (nm)
1	4.57	3.70E+04	10.85	0.00	4.00	0.00	2.56E+05	25.26	7.52E-02	3.04	10.85	0.00	1.00E+09	6.84E+00	2.03	25.26
3.5	6.46	9.10E+03	9.18	0.00	4.00	0.00	3.20E+05	32.79	4.31E-02	3.04	9.18	0.00	1.00E+09	3.78E-01	2.36	32.79
15	4.89	1.29E+03	6.62	0.00	4.00	0.00	2.45E+04	17.51	2.82E-03	3.53	6.62	0.00	1.00E+09	7.94E-01	2.18	17.51
89	2.44	1.47E+02	4.42	0.01	2.69	0.00	1.26E+04	17.51	1.94E-03	3.39	4.42	0.00	1.00E+09	6.13E-02	2.56	17.51
200	3.16	3.46E+01	2.63	0.01	2.85	0.00	1.26E+04	17.51	1.83E-03	3.36	2.63	0.00	1.00E+09	2.64E-02	2.71	17.51
250	3.18	3.84E+01	2.75	0.01	2.85	0.00	1.26E+04	17.51	1.71E-03	3.36	2.75	0.00	1.00E+09	1.92E-02	2.77	17.51
300	3.31	2.81E+01	2.47	0.01	2.85	0.00	4.34E+03	13.58	1.32E-03	3.44	2.47	0.00	1.00E+09	6.84E-02	2.53	13.58

Table A.4. Unified Fit Parameters for ATO Powder Tests

		Level 1					Level 2					Level 3				
Applied Pressure (MPa)	SASBackgroundd	G	Rg (nm)	B	P	RgCO (nm)	G	Rg (nm)	B	P	RgCO (nm)	G	Rg (nm)	B	P	RgCO (nm)
1	7.02	2.03E+03	3.9727	5.95E-03	4.10	0.00	7.07E+05	24.674	1.39E-01	3.13	3.97	0.00	1.00E+09	4.22E-01	2.53	24.67
50	4.65	2.99E+02	5.3369	6.14E-03	3.09	0.00	9.34E+03	15.567	6.78E-03	3.08	5.34	0.00	1.00E+09	9.86E-02	2.47	15.57
100	4.40	3.07E+02	5.3369	1.17E-02	2.83	0.00	8.70E+03	15.427	1.30E-03	3.49	5.34	0.00	1.00E+09	8.49E-02	2.49	15.43
150	4.96	3.00E+02	5.3369	8.94E-03	2.96	0.00	9.32E+03	15.794	5.14E-03	3.14	5.34	0.00	1.00E+09	7.90E-02	2.50	15.79
200	5.12	3.04E+02	5.3369	7.93E-03	3.00	0.00	9.00E+03	15.702	4.25E-03	3.18	5.34	0.00	1.00E+09	8.22E-02	2.49	15.70
250	6.19	3.09E+02	5.3369	5.26E-03	3.17	0.00	9.14E+03	15.805	1.49E-02	2.86	5.34	0.00	1.00E+09	7.62E-02	2.51	15.81
300	5.14	2.89E+02	5.3369	1.22E-02	2.86	0.00	8.97E+03	15.745	1.51E-02	2.86	5.34	0.00	1.00E+09	7.70E-02	2.51	15.75

Table A.5. Unified Fit Parameters for SiC Powder Tests

		Level 1					Level 2					Level 3				
Applied Pressure (MPa)	SASBackground	G	Rg (nm)	B	P	RgCO (nm)	G	Rg (nm)	B	P	RgCO (nm)	G	Rg (nm)	B	P	RgCO (nm)
1	0.00	4.13E+02	12.12	3.92E-06	4.40	0.00	1.8E+03	2.99E+01	1.98E-03	2.67	12.12	NA	NA	NA	NA	NA
50	6.92	4.66E+05	19.41	3.30E-03	4.00	0.00	0.00	1.00E+09	3.33E+00	2.20	19.41	NA	NA	NA	NA	NA
100	7.23	3.08E+05	20.17	2.09E-03	3.98	0.00	0.00	1.00E+09	3.60E+00	2.11	20.17	NA	NA	NA	NA	NA
150	8.15	1.32E+05	17.75	1.35E-03	4.00	0.00	0.00	1.00E+09	1.14E+01	1.89	17.75	NA	NA	NA	NA	NA
200	8.59	4.67E+04	15.32	1.19E-03	4.00	0.00	0.00	1.00E+09	3.43E+01	1.69	15.32	NA	NA	NA	NA	NA
250	4.47	1.83E+03	11.49	2.20E-02	2.53	0.00	6.5E+04	1.75E+01	3.72E-04	4.17	0.00	0.00	1.00E+09	10.02	1.87	17.48
300	3.22	7.16E+02	5.29	3.17E-02	2.62	0.00	4.9E+04	1.80E+01	1.25E-03	3.85	5.29	0.00	1.00E+09	11.22	1.83	17.96

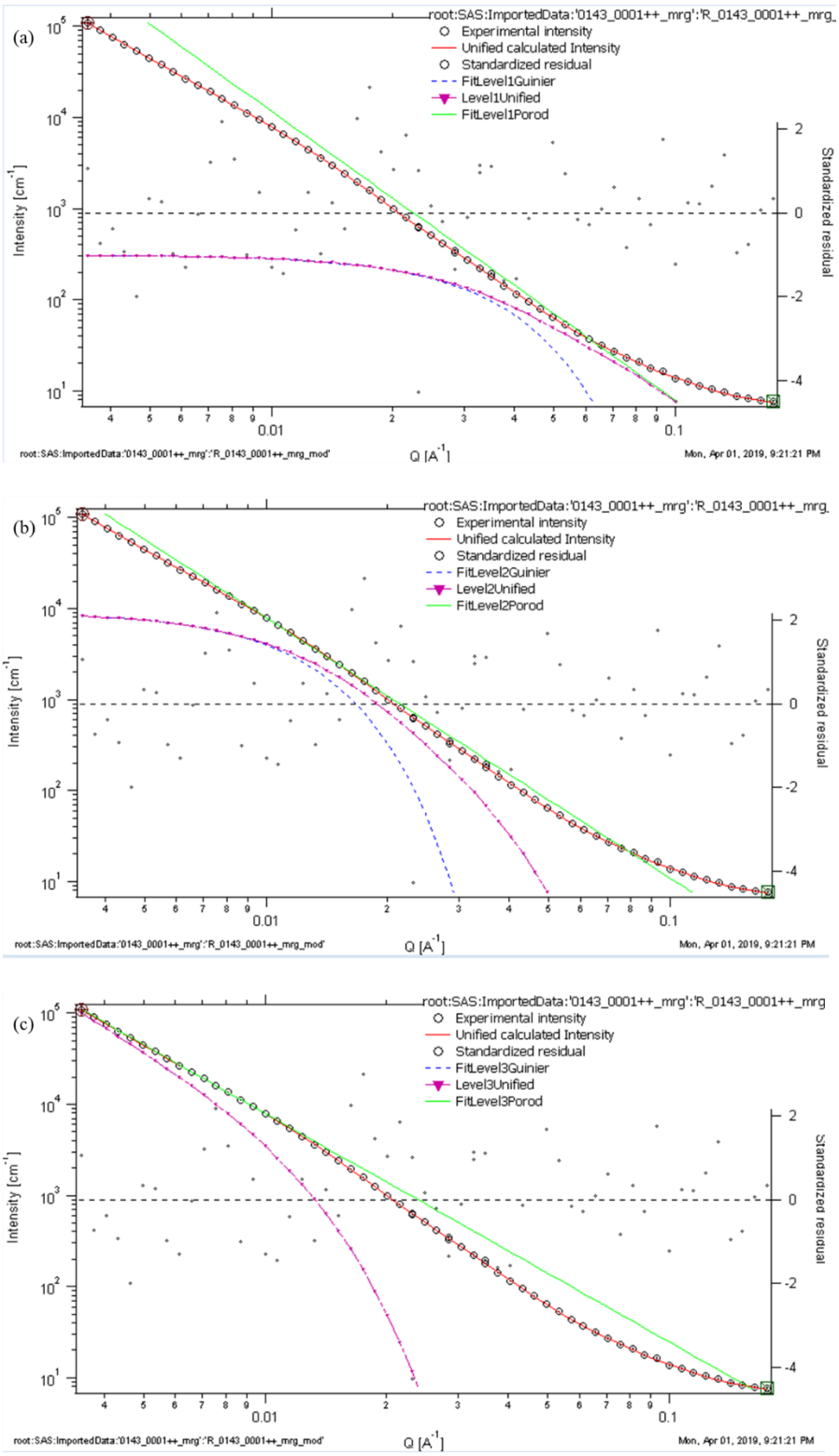

Figure A.12. Unified Fit results for the ATO powder at a pressure of 250 MPa. The fit consisted of three levels, designated as levels 1, 2, and 3 in order from highest to lowest q and shown in (a), (b), and (c), respectively.

One common feature among the three powders was the use of a R_g cutoff in the second and third levels, which is applicable if a higher level is representative of scattering from the same population of particles as the next lowest level but on a larger length scale[119], as in the case of aggregates or agglomerates of the particles represented by the lower level. In practical terms for the fitting of the 1-D data, it was necessary to use a R_g cutoff in situations where the P and B values, which represent the slope and intercept of the linear Porod region, were such that if this region were extended all the way to the largest q values, its intensity would bury the lower levels and thus make these levels impossible to fit. An example of this is seen in Figure A.12 (c), where the level 3 Porod line, shown in green, possesses a higher intensity than the experimental curve throughout the majority of the total q range, which would make fitting impossible without the use of a R_g cutoff. Although such a scenario was not present every time a R_g cutoff was used in the fitting, it was consistently used whenever its use was appropriate for the data at some of the pressures for a given level of each powder since the relationship between scattering from these levels and those of the next lower level would not be expected to change between pressures. In other words, if a R_g cutoff was found to be necessary for a certain level at certain applied pressures for the same powder, possibly representing agglomerates of the particles of the level below it, it would not make physical sense for the same level with similar R_g values would represent scattering from a completely separate species at other applied pressures.

The level 2 R_g values in the ITO and ATO fitting and the level 1 R_g values for the SiC fitting fall within the expected range for the individual nanoparticles of each powder. This, along with the fact that this level corresponded with the most prominent feature of the q-I(q) curve in each case, strongly suggests that these levels represented scattering from

the nanoparticles. It will be shown in a later section that in the analysis of data from SAXS testing that the nanoparticle levels in those tests generally shared a characteristic P value of 4, representing the Porod's Law condition. It is not clear why this is not the case in the present data. However, the curves show evidence of the effects of multiple scattering, in that the different fit levels were far less well-defined in this data compared to the SAXS data and transitions between Guinier and Porod regions were unclear. This issue is discussed further in section 0.

For all three powders, the highest level, representing the largest features within the q range of the detector, has been attributed to agglomerates of the particle species for each respective nanopowder. It has been well established that nanoparticles are subject to a strong driving force to reduce their high surface energies by forming aggregates and agglomerates, and these larger structures can easily attain length scales orders of magnitude larger than those of the constituent particles.[120,121] Furthermore, the P values found in the fitting of these levels were generally between 2 and 3, and therefore well within the fractal region, as shown in Figure A.2. It is in this region of behavior that agglomerates would be present, further supporting the assertion that these levels represent agglomerates of the primary nanoparticles. In general, the highest level found in the fitting is shown as having a G value of 0 and a R_g value of 10^9 nm. These values were necessary for the construction of the model and are not representative of the real values pertaining to the features they represent, but rather are indicative that the feature primarily scattered at q values lower than the lower limit of the detector and, therefore, could not be completely characterized. This was notably not the case in the fitting for the SiC powder at most applied pressures, which featured only 2 levels and had non-zero G values for the highest level. It is believed

that a higher level would be present in these data if lower q values were detectable, but it was difficult to fit these levels in the present data due to only a very small Porod region being present in the available q range.

A.3.3.2 Porosity calculation results

The calculated porosity values for the ATO nanopowder are shown in Figure A.13 (a), which shows that these derived values possessed a similar trend to the powder bed thickness data from the load frame, shown in Figure A.13 (b). This suggests that the scattering and load frame data were behaving as expected, since less powder thickness for the same mass of powder requires an increase in density, which is equivalent to a decrease in porosity. However, the actual porosity values obtained presented a problem, as they were far too low considering the testing was done at room temperature so there was no sintering occurring in the powder bed. These values were compared to porosities calculated from the mass of powder used and the volume of the powder at each pressure. These values, while far closer to expected values, were still suspect so evaluation of possible sources of error was required. This issue is discussed in section 0.

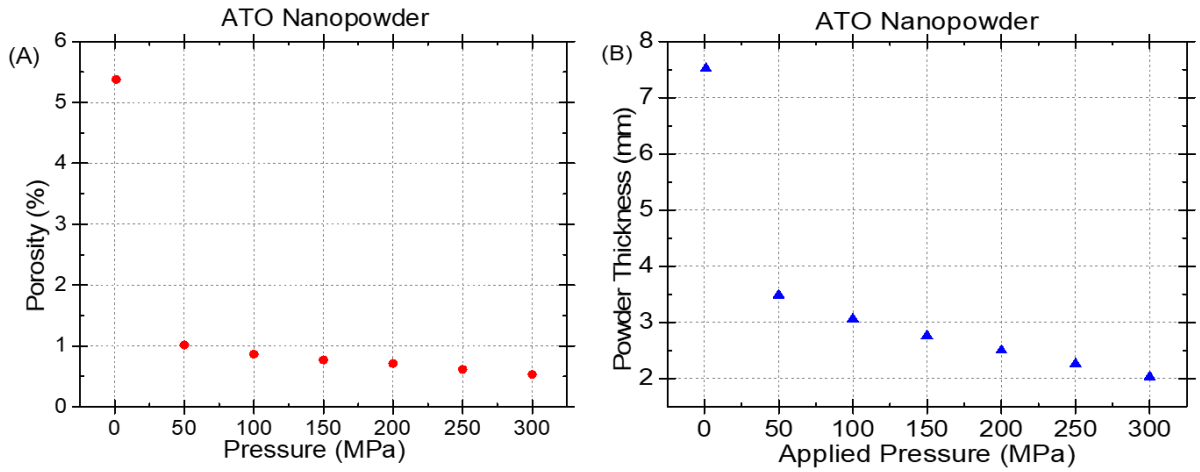

Figure A.13. (a) the porosity values derived from the SANS data and (b) the powder thickness calculated from the load frame data. The trends are similar between these data sets as well as the resistivity data.

A.3.4 IS results

The SANS-IS tests were successful in producing a complete set of electrical and the corresponding SANS data. For the impedance data, this included the real and imaginary impedance, impedance magnitude, impedance phase angle, and derived resistivity for all pressures, Figure A.14 displays the impedance data, which shows a clear, logical progression in the data, with the resistivity of the powder decreasing as the pressure increases, as would be expected since increasing the pressure on the powder should increase the connectedness of the powder particles and therefore increase the conductivity.[50]

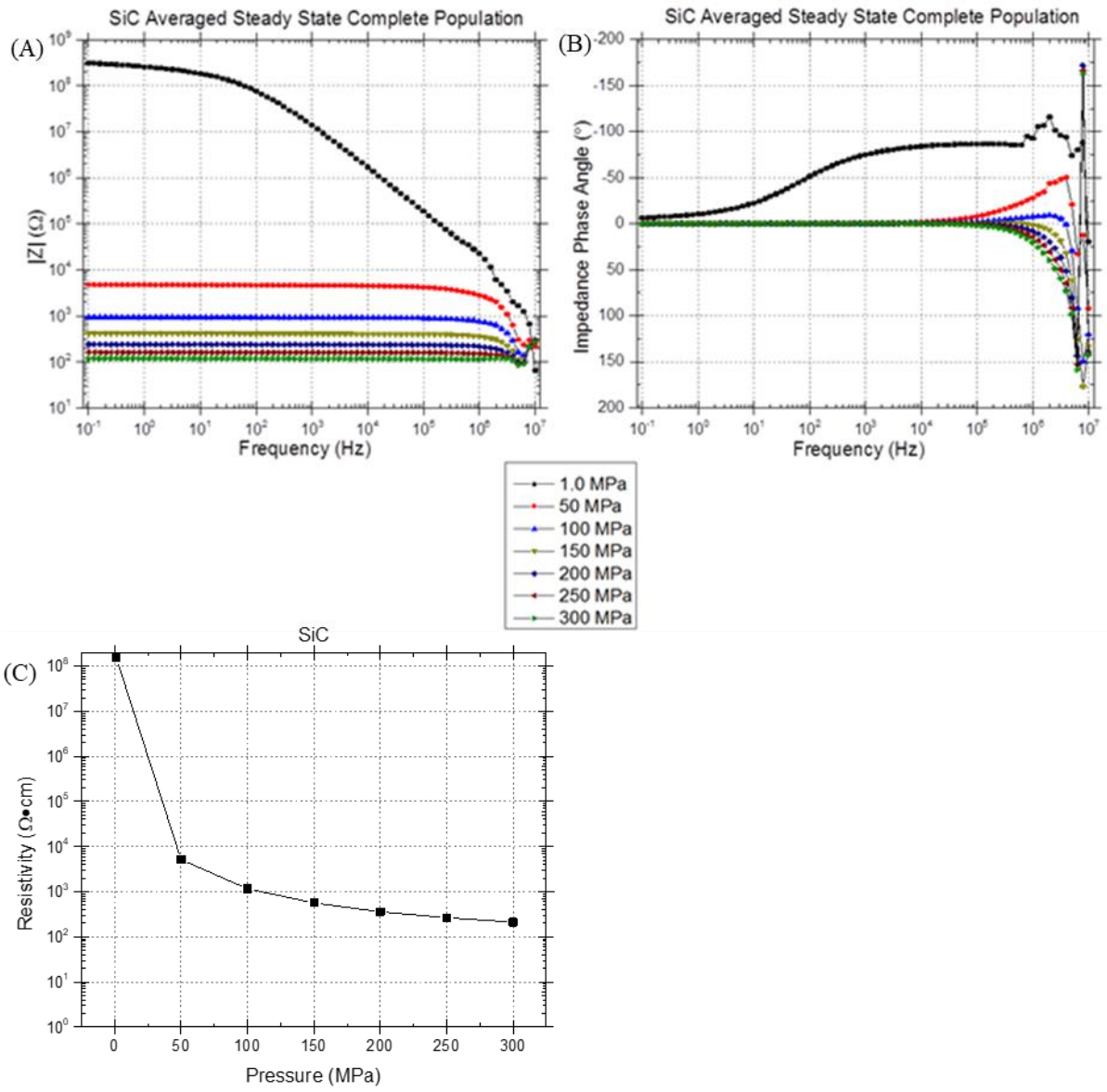

Figure A.14. (a) Frequency explicit impedance magnitude and (b) impedance phase angle plots, and (c) the derived resistivity as a function of applied pressure for data gathered during the compaction testing of a beta-phase silicon carbide nanopowder. The results clearly show the expected progression of the evolution of electrical properties as the pressure on the powder changes.

A.3.5 Challenges related to the collection of useful scattering data using SANS

Despite the promising trends in the IS and SANS data, the porosities derived from the SANS data were far lower than expected (Figure A.13 (a)). Since this test involved compaction rather than sintering, it can be assumed that particle deformation was not significant relative to deformation resulting from sintering, and thus the geometry of the particles was largely constant and roughly spherical. Under the rough assumption that the powder particles are spherical and mono-sized, the lowest possible porosity should be approximately 26%, since the maximum packing density of identical spheres is 74%. The most likely explanation for this discrepancy is that agglomerates of the nanopowders allowed pores to exist in the powder which were larger than the low q limit of the SANS detector and, therefore, a large portion of the total porosity is missed. The 1-D SANS data supports this hypothesis (Figure A.15), since it shows no indication of a horizontal Guinier region[108] at low scattering vectors, thereby guaranteeing that at least some portion of the total scattering behavior could not be characterized.

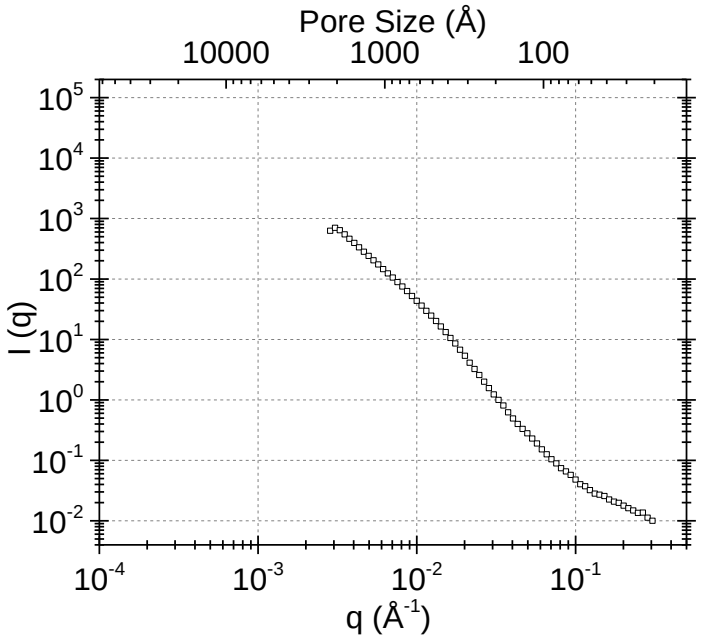

Figure A.15. 1-D I-I(q) log-log SANS data for the ATO nanopowder at 300 MPa applied pressure. This curve shows no low-q Guinier region, which would be expected if all feature sizes had been characterized.

The largest feature size detectible using the CG2 SANS instrument was 0.22 μm based on a minimum scattering vector of 0.0028 $Å^{-1}$. Since all the powders tested in this experiment were nanopowders, no pores should be anywhere near this large if agglomeration were not present. Additionally, a very small number of pores beyond the instrument's detection limit could easily account for a large portion of the total pore volume in the powder compact.

While the porosity discrepancy was the most noticeable issue related to the SANS data, two additional issues were also identified. The first issue is the occurrence of multiple scattering of the incident neutrons due to beam-path powder thicknesses ranging from 2.2 mm to over 10 mm. Multiple scattering occurs when the total scattering cross section of all material in the beam path is large enough that an incident neutron or x-ray can undergo

more than one scattering event before contacting the detector. The effect of multiple scattering on 1-D scattering curves is to smear the actual intensity and, as demonstrated in Figure A.16 and previously seen in the experimental data in Figure A.11, can reduce the definition between the Guinier and Porod regions.[111] The issue of multiple scattering would only be avoidable if the thickness of powder in the beam path could be reduced substantially, but doing so would be difficult due to both the application of pressure, which limits the viable die geometries and thicknesses, and the need to maintain a sufficient quantity of powder within the beam path to ensure sufficient signal reaches the detector, as the incident beam flux is very low for neutrons as compared to x-rays.

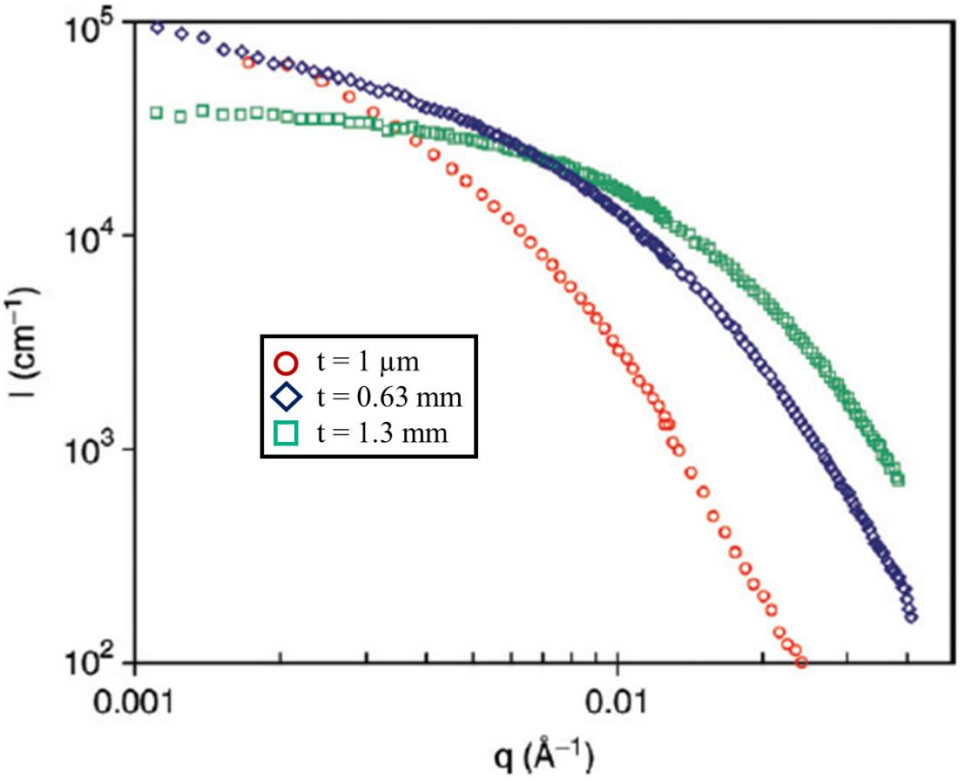

Figure A.16.[111] q-I(q) log-log plots of SANS data collected on the same material with varying sample thickness. Comparison shows the effects of multiple scattering, which is not present in the t = 1 μm data but is present for the thicker samples.

Another issue with the setup used in the SANS-IS testing was settling of the powders during the SANS tests at each pressure. Figure A.17 shows the pressure drop recorded over the course of the SANS tests during testing of the ATO nanopowder at 50 MPa, which is representative of the behavior seen in all the powders. This pressure drop was direct result of the powder settling, and thus shows that the microstructure of the powder compacts changed while the SANS tests were running. Since the load frame maintained its position during the SANS testing rather than maintaining the set pressure, the settling was indicated by the pressure drop, but the settling would also occur if the set pressure was maintained; the powder settling would be indicated by the change in position of the load frame to maintain the target pressure. This issue is expected to be an even bigger

issue when high temperatures are introduced in conjunction with applied pressure, since sintering will progress even if the temperature and pressure are held constant as long as both are high enough.

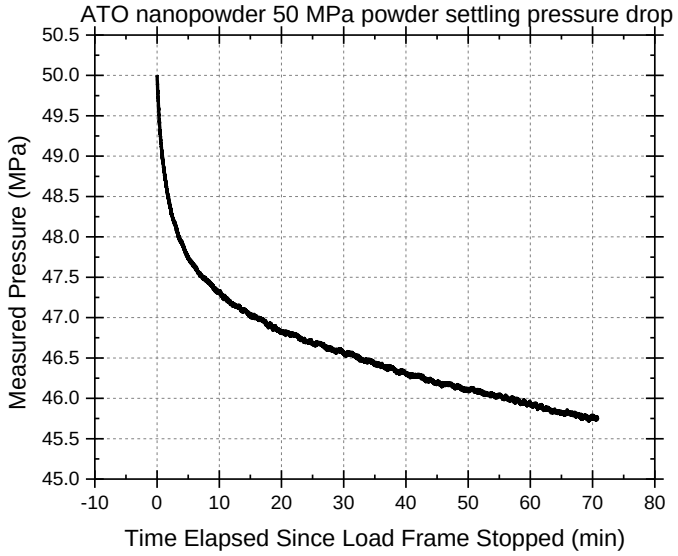

Figure A.17. Plot of the change in pressure measured by the load frame over time starting when the load frame stopped upon achieving a target pressure of 50 MPa and ending when the load frame began travelling again to reach 100 MPa upon completion of all the 50 MPa SANS tests. The decrease in pressure due to settling of the powder was significant, especially over the first few minutes, indicating that the microstructure was changing significantly throughout the SANS tests.

A.4 Ex-situ USANS

Reduced, corrected data from these tests was never made available to us, so no results can be presented, nor any analysis conducted.

A.5 Ex-situ SAXS+USAXS

These tests were conducted on samples of β-SiC nanopowder which were pressed to different pressures using equipment at Georgia Tech and then shipped to the 9ID-C beamline[116,117] at the Advanced Photon Source (APS) facility at Argonne National Lab (ANL) for SAXS and USAXS testing. This served as a preliminary test before in-situ testing on this beamline and the resulting data proved useful for comparisons to other SAS tests.

A.5.1 Sample preparation

For these tests, a series of compressed powder samples were made from 0.0263 g of a SiC nanopowder (10-70 nm, US Research Nanomaterials Inc.). This powder was loaded into a 1/8" internal diameter steel die with a small steel punch at the bottom to hold the powder and a long steel punch inserted into the top of the die to apply a load to the powder within. The assembled die was then placed in the center of a Carver 3851 hydraulic press. Each sample was loaded to a different pressure, given in Table A.6, was kept at that pressure for 2 minutes to allow for powder settling, and was then removed from the die after releasing the pressure. Each of the pressed powder pellets was carefully transferred into a Wilmad Thin Walled High Throughput NMR Tube. Polystyrene rods were used as spacers within the tube to hold the pellet in the center of the tube and to take up all remaining space in the tube, so the pellets would not be able to move within the tube during shipping (Figure A.18 (a)).

Table A.6 Samples Used in Ex-situ SAXS Tests

Sample	Applied Pressure (MPa)	Sample Diameter (mm)
1	0	3.175
2	10	3.175
3	20	3.175
4	30	3.175
5	40	3.175
6	50	3.175
7	100	3.175
8	150	3.175
9	200	3.175
10	250	3.175
11	300	3.175
12	600	3.175
13	1000	3.175

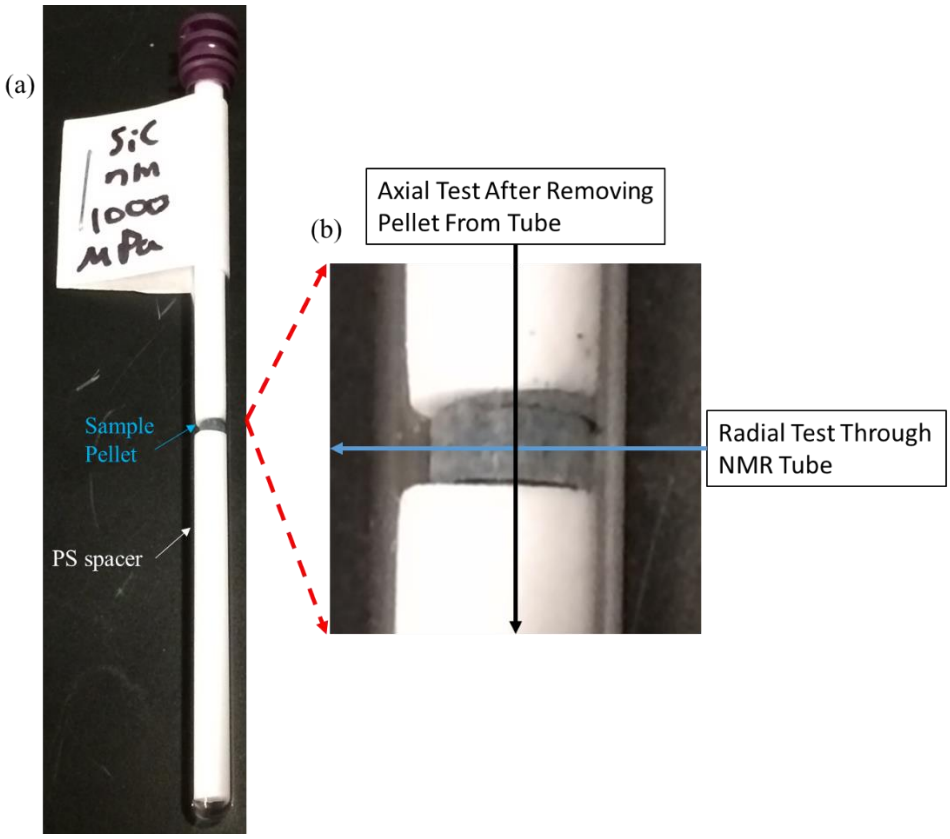

Figure A.18. (a) An NMR tube containing polystyrene spacers and a pressed powder pellet and (b) a magnified image showing the pellet surrounded by the spacers and indicating the SAXS testing directions for the ex-situ tests.

After arriving at the 9ID-C beamline at the Advanced Photon Source at Argonne National Lab[116,117], USAXS, SAXS, and WAXS tests were conducted by Dr. Jan Ilavsky and Dr. Ivan Kuzmenko on each sample in both the radial and axial directions (Figure A.18 (b)). The radial tests were conducted with the beam going through the tube and the sample and a separate test of the tube by itself was used to subtract the signal from the tube. Then, the sample was removed from the tube and suspended in the beam path with translucent tape and the axial tests were performed, again with a separate test of the tape by itself to remove its effect on the data. Not all samples survived both the shipping process and the

handling during these tests, so these samples, which were primarily those at the low pressures (<40 MPa) as they were more fragile, could not be tested.

A.5.2 Radial direction test results

The combined SAXS and USAXS data for the radial-direction tests (Figure A.19) did show changes between the different samples. The most distinct changes are a lower intensity in the 0 MPa data at high q compared to the other samples, and a shift in behavior in the 600 MPa and 1000 MPa samples at low q compared to the other samples. The 0 Mpa sample was just loose powder, and therefore far less dense than any of the compressed samples, so the decreased intensity may be simply due to fewer scattering events occurring since there are fewer opportunities for the beam to interact with any of the particles. The change at the highest pressures must mean that these pressures affected large-scale features of the powder, since these curves begin to deviate approximately $q=10^{-3}$ $Å^{-1}$, or 628 nm, and the difference increases as q continues to decrease, or as feature sizes continue to increase. Since the powder particles were within the size range of 10-70 nm, the change in features on a length scale at least an order of magnitude larger than the powder particles themselves, this seems to be indicative that the high pressures were affecting agglomerates of the powder particles. This seemed to be the most plausible explanation since agglomeration is common in nanopowders due to their high surface area resulting in high surface energy[120], and it has been reported in the literature that high applied pressures can break up agglomerates[120], which would be reflected by a change in the scattering data.

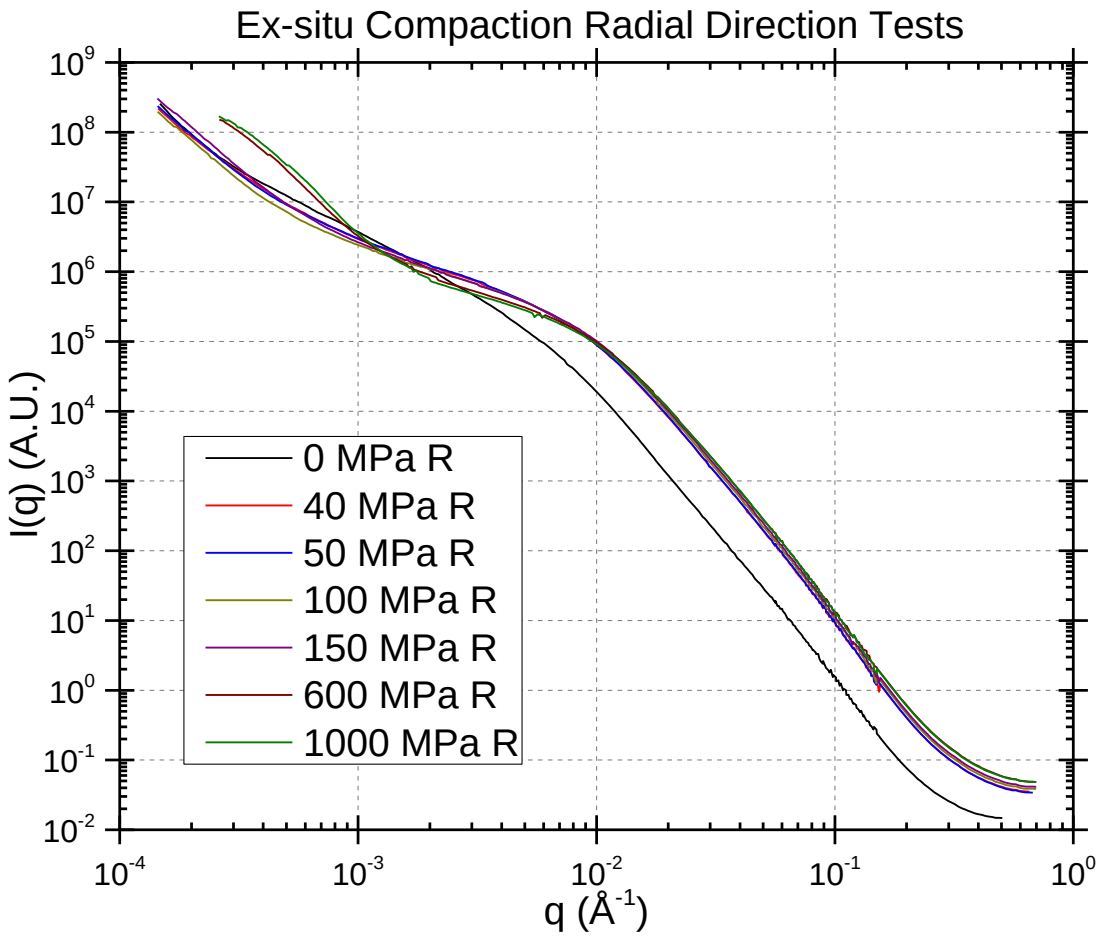

Figure A.19. I(q) vs q data for the radial direction tests.

A.5.3 Axial direction test results

The data for the axial direction (Figure A.20) showed significant differences to the radial direction data. At the low-q end of the curves, the 600 MPa and 1000 MPa curves do not show a change in trend compared to the other pressures, as was seen in the radial tests. Another notable feature of the axial data are the strange breaks and jumps in both the 200 MPa and 250 MPa data at $q=10^{-2}$ Å^{-1}. This may be related to the switching between the USAXS and SAXS detectors, where it is possible that there was either some disturbance

during the testing, or that there were problems with joining the ends of the two curves when testing these samples. However, the actual cause has not been verified.

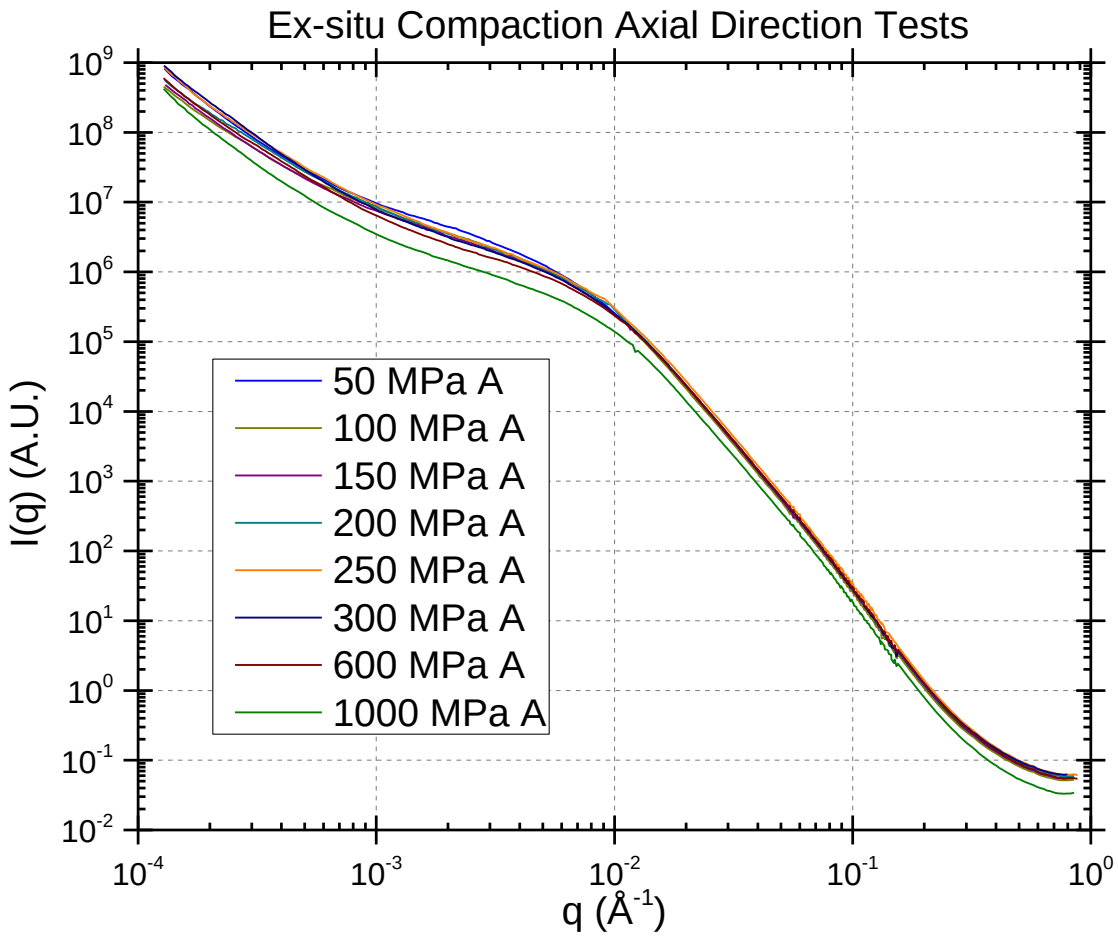

Figure A.20. I(q) vs q data for the axial direction tests.

A.5.4 Porosity calculation with SAXS data

Porosity data for the samples, derived from the transmission data, are shown in Figure A.21. It must be noted that the porosity derivation in the axial direction was subject to more error, as a thickness value of 4 mm was used for all samples since the actual thicknesses were not measured. The radial data shows the expected trend of decreasing porosity with increasing pressure. However, the actual derived values are suspect; the almost 96%

porosity of the 0 MPa sample is unlikely, although not out of the realm of possibility for nanopowders featuring agglomerates.[120] The derived values at the other pressures, although less unlikely, are likely higher than the actual values as well.

The axial data shows the opposite trend to the radial data, and thus directly opposes the expected results. This, along with the even higher derived porosity values, makes the axial results more suspicious than the radial data. An explanation for the derived porosities being too high has not been found.

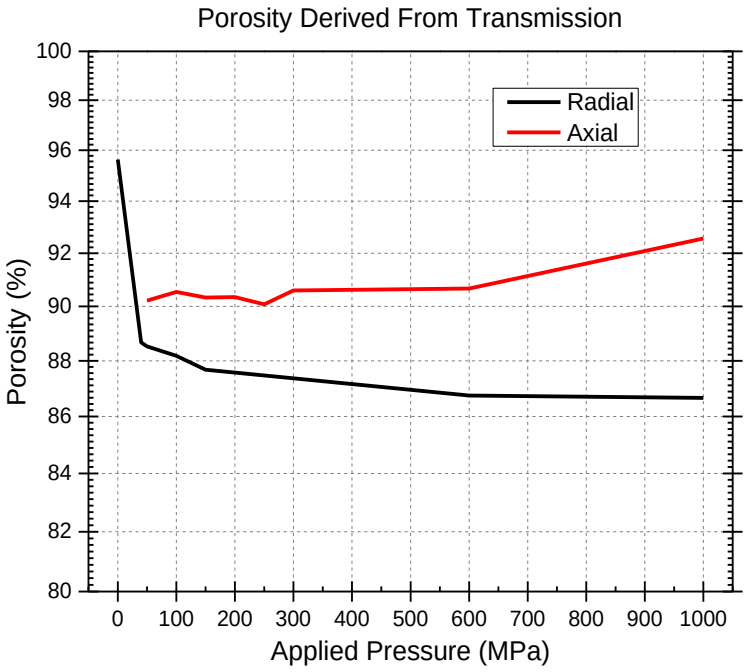

Figure A.21. The porosity data derived from the transmission values recorded by the SAXS detector. The radial test data shows the expected trend, but the values seem unreasonably high. The axial is suspect, with an opposite trend and even larger porosity values.[120]

A.5.5 Unified Fit results

The Unified Fit model which was found to best fit the I(q) vs q data for all samples consisted of 4 levels (Figure A.22), with radius of gyration (R_g) cutoffs applied to all levels except the highest-q level (level 1), indicating multiple feature size ranges. The R_g values for each level in each sample is given in Figure A.23. Level 4 R_g data is not shown because it was lowest-q level and did not show a Guinier region for any sample, so R_g could not be determined for that level. In both sets of tests, as with the fitting of the SANS data in section 0 , it is expected that level 1 is the scattering response of a thin surface layer on the particles. In this case, the layer would most likely be a SiO_2 phase, based on the propensity of the exposed surface atoms to oxidize as well as on reports of low temperature oxidation of SiC

to form a surface layer of SiO_2.[122] There is very little change in the R_g values with pressure for either test set, which was expected because the samples were not under pressure at the time of testing, so there should not be a difference in atomic plane spacing or crystal structure between these samples.

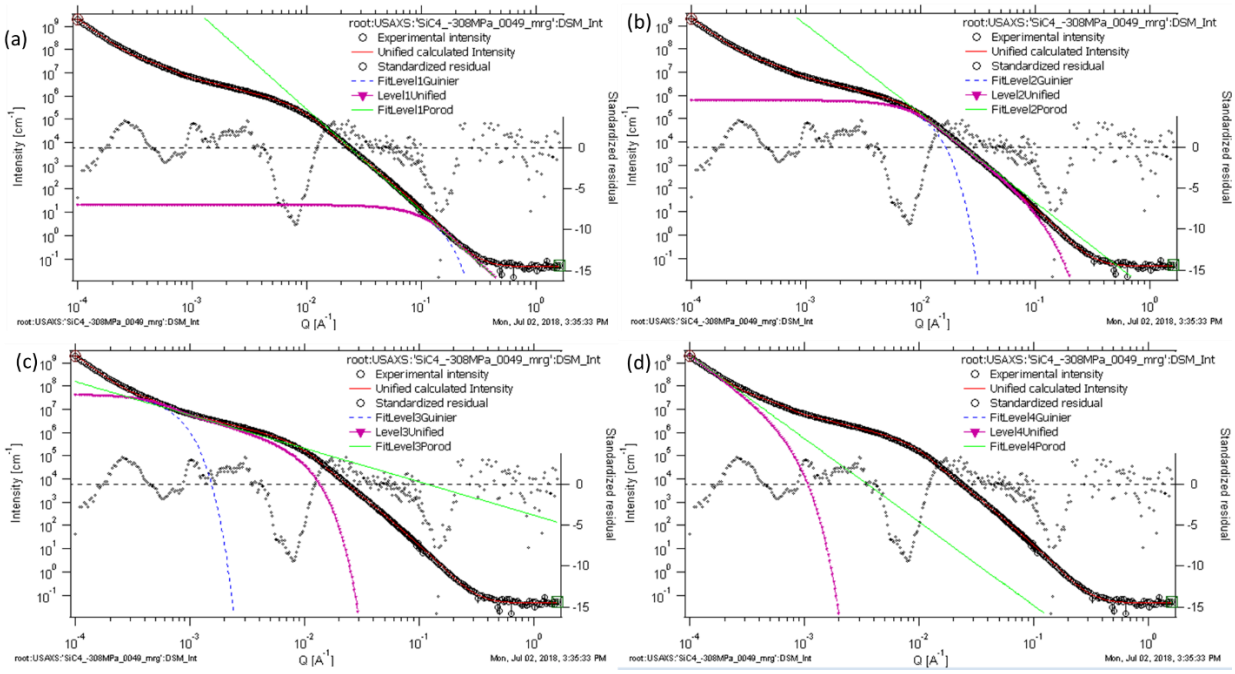

Figure A.22. Example of using the Unified Fit program in the Irena tool suite[113] to fit a 1-D I(q) vs q curve to a combination of individual levels, each with a low-q Guinier region and a high-q Porod region. In this example, the experimental data (black) is fitted to a combination of 4 levels (a-d), where that level's Guinier response is shown in blue, its Porod response in green, and the two responses combined, representing the total response of the level, in purple.

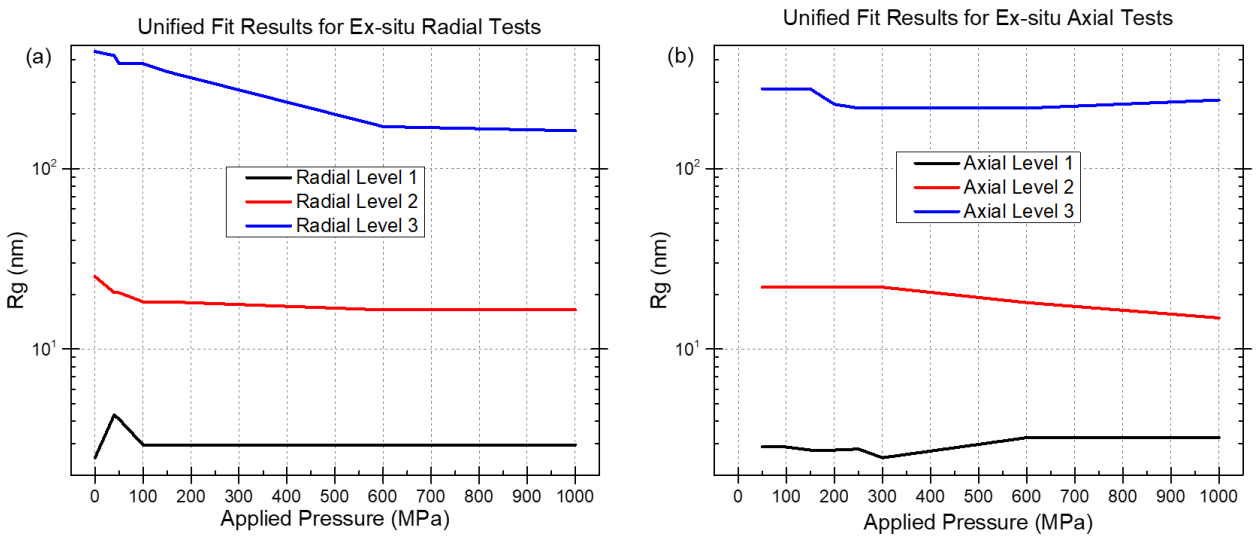

Figure A.23. Radius of gyration vs applied pressure plots for the (a) radial and (b) axial direction ex-situ tests. The values are relatively consistent between the same levels in the two different directions. However, the level 2 and 3 curves have opposing trends. The radial data was assumed to be more trustworthy.

Level 2 gave R_g values in a range of approximately 15-25 nm for all pressures in both sample sets. The size of the powder particles given by the manufacturer was 10-70 nm, so level 2 should be the response from the powder particles and the pores between them. For both sample sets, there is a small decrease in R_g with increasing pressure. This may be a result of small increases in particle packing efficiency driven by the increasing pressure, thereby decreasing the average size of the pores between powder particles. Comparison of the R_g values at each pressure between the two testing directions shows values a few nm larger in the axial direction for most of the tested pressures. Since the pressure was applied uniaxially and in the axial direction, the pressure on the powder in the radial direction should be less than that in the axial direction due to a positive Poisson ratio. However, with less driving force for increasing packing efficiency, it may be expected that, if anything, the average pore sizes between powder particles should be larger in the radial direction, which is opposite to the observed trend. However, since the

difference in the R_g values between the two testing directions is never more than about 3 nm, it seems likely that the differences are within the range of experimental error, so no conclusions can be definitively drawn regarding the differences between the two directions.

Level 3 shows a large range of R_g values, stretching from 162 nm to 444.5 nm. This size range is well beyond that of the powder particles, so it seems most likely that this level represents the response from nanoparticle aggregates and the pores within and between them.[120] Such aggregates were expected since they are very commonly formed by nanoparticles and because their presence supports the finding that the loose powder had a porosity far higher than that of a random close-packed structure of monosize spheres, which is approximately 36%.[123] The level 3 R_g data also shows a clear trend of decreasing R_g with increasing applied pressure, which makes sense since increasing pressure increases the driving force for more efficient packing of the aggregates.

As mentioned before, level 4 R_g values could not be determined since there was no Guinier region at the lowest q values detectable with the USAXS detector, whose low limit was 0.000129 $Å^{-1}$. This indicates that the largest features detected in the USAXS tests were larger than 4.87 μm, which may initially seem improbable since the nanopowder particles themselves had a size range of 10-70 nm. However, it is well known that aggregates can assemble to form agglomerate structures which can have size ranges in the tens to hundreds of μm.[120] Therefore, it is very possible for nanopowders to have features with sizes well above the range of the USAXS tests.

A.6 In-situ IS+USAXS+SAXS

This section presents data from the most recent series of SAS-related tests, in which IS, USAXS, and SAXS were conducted during in-situ compaction of a β-SiC nanopowder. Tests were conducted at the same pressures used for the SANS tests, but with the addition of tests at every 10 MPa between 0 and 50 MPa.

As with the ex-situ IS+SAXS+USAXS tests, this series of tests was also conducted at the 9ID-C beamline at the APS facility at ANL[116,117], in collaboration with beamline scientist Dr. Jan Ilavsky and with assistance from Dr. Ivan Kuzmenko. In this case, to apply pressure to the punches, a custom-configured compact load frame (Interface Force Measurement Solutions, Scottsdale, AZ) was borrowed from the 1-ID beamline at the APS facility at ANL with the support of beamline scientists Dr. Jon Almer and Dr. Jun-Sang Park. A Gamry Reference 3000 potentiostat (Gamry Instruments, Warminster, PA) was used to conduct the impedance tests.

A.6.1 Development of the die assembly

Since these tests included in-situ compaction, sapphire had to again be used for the dies. However, the 8 mm ID dies used in the SANS and USANS tests could not be used, since the amount of sapphire in the beam would absorb all of the x-rays. To accommodate the low penetration of the x-rays, a balance had to be struck between making the die walls thin enough to allow for the necessary x-ray transmission, yet thick enough to withstand the internal pressure. Based on financial restrictions, polycrystalline sapphire tubes from AdValue Technologies LLC (Tuscon, AZ) was chosen as the die material. Using the material's properties given by the manufacturer[124] in conjunction with the physical

properties of the powder material, a range of viable OD and ID combinations was determined using the anomalous scattering calculator included within the Irena software package for Igor Pro.[113] Comparing the OD and ID combinations which the manufacturer could achieve, the optimum dimensions were chosen according to the combination with the highest safety factor and new set of polycrystalline sapphire dies was made, each with a length of 35 mm, ID of 0.74 mm, and OD of 2.63 mm.

Requirements on the punch material were electrical resistivity far lower than that of the powder material and as high a stiffness as possible. The low resistivity was required to enable the IS tests, while the high stiffness was required to avoid buckling stemming from the high aspect ratio of the punches, although the aspect ratio of the free-standing section of the top punch decreases as the powder compacts and/or densifies, somewhat alleviating the issue. Ultimately, tungsten carbide was chosen to be the punch material due to its sufficient conductivity, extremely high elastic modulus, low cost, and the availability of rods with precise diameters. 0.72 mm diameter WC pin gauges were easy to find online, and their use as a measurement tool ensured good tolerance values for their diameters.

Rods of two different lengths were used; a bottom punch totaling 7 mm long and a top punch totaling 40 mm long. Each pair of rods were cut from the same longer rod using an Isomet 1000 precision sectioning saw (Buehler, Lake Bluff, IL) with a model 15LC diamond sectioning blade. The rods had to be fixed within custom made base pieces. The requirements on these base pieces were that they had to be machinable so the rods could be mounted within them and an electrical path could be made from the rods to the impedance equipment, electrically insulating so the electrical circuit for the impedance tests could be isolated from the metal of the load frame, and cylindrical with a diameter of

0.25” in order to be secured with the load frame’s existing collet grips. Macor machinable glass ceramic (Corning Inc., Corning, NY) was chosen as the material for the base pieces since it met all requirements and is relatively inexpensive. From a stock length of 0.25” diameter Macor rod, 10 mm long sections were cut. Then, two holes were drilled into these pieces, the first being 0.72 mm in diameter, located in the center in the axial direction extending 5 mm into the piece (Figure A.24). The second hole, with a diameter of 0.5 mm, was made in the radial direction and intersected the axial hole near its base, as shown in Figure A.24. A small quantity of Electro-Bond G2 silver-infused 1-part heat cured epoxy (ConductiveX, Fort Lauderdale, FL) was placed on one end of the WC rod, then that end was fully inserted into the axial hole. Then, one end of a copper wire, with a small quantity of the same epoxy at the end, was inserted into the radial hole in the punch base until making contact with the WC rod. Finally, the three-piece assembly was placed in an alumina boat, which was inserted into a Carbolite 12/65/550 tube furnace (Carbolite Gero Ltd., Hope Valley, UK). The assembly was heated to 175°C in flowing compressed air and kept at that temperature for 4 hours to cure the epoxy. Afterward, the quality of the epoxy bonds was verified for each punch assembly by applying tension to the WC and copper to ensure they were held fast within the base piece and by running an impedance test with one lead connected to the WC and the other connected to the copper wire to check for good conductivity.

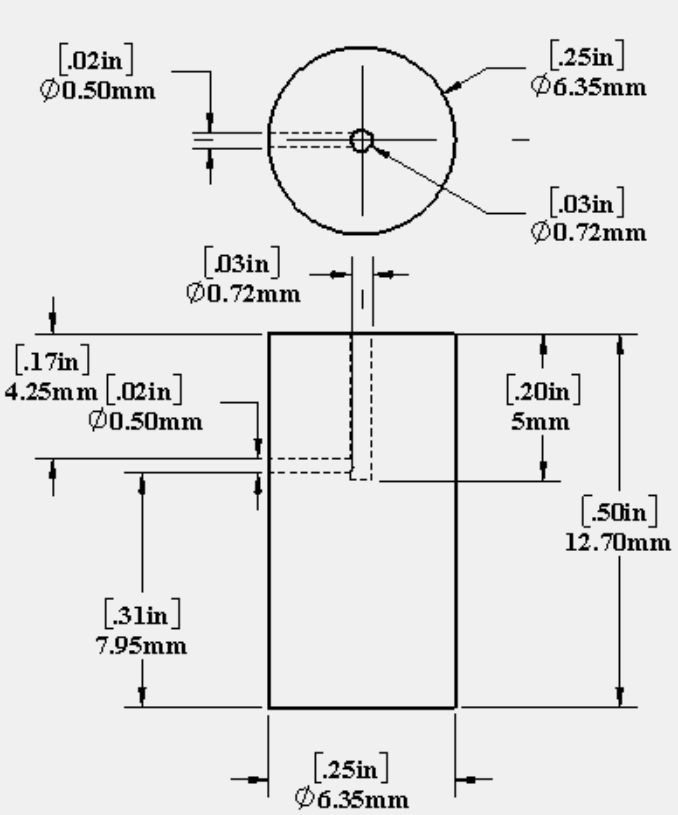

Figure A.24. Schematic of the punch base pieces used for the in-situ SAXS tests. The WC rod was secured to the bottom of the axial hole with silver epoxy and copper wire was inserted into the radial hole and secured to the WC rod with the same epoxy.

Since both the top and bottom rods were inserted 5 mm into the base pieces, the lengths of the exposed rods were 35 mm and 2 mm, respectively. These lengths were chosen to maximize the volume within the 35 mm sapphire die which is available to the powder. Under the assumption that both punches should always begin at least 2 mm into the die before applying pressure, these punch lengths allowed 31 mm of the die's length to be filled with powder. This was important for facilitating the testing of nanopowders since they can shrink to a very small fraction of their starting volume when pressure is applied. The collet grips of the load frame would be secured around the free ends of the punch bases, leaving some space between the grips and the copper wires, and the leads from the impedance

equipment were attached to both copper wires with alligator clips, giving the final complete assembly shown in Figure A.25. Here, in addition to the locations of the various parts of the assembly, the locations of contact with the load frame grips, locations where pressure is applied, connection points for the leads from the impedance testing equipment, and a representation of the path of the incident x-ray beam relative to the assembly are shown. The load frame used in these tests operated by keeping the bottom stationary while changing the position of the top as directed, so the die was mounted in the beam such that the beam passed close to the bottom punch so even if the powder bed became very small it would still be in the beam, so the setup would never have to be repositioned during testing.

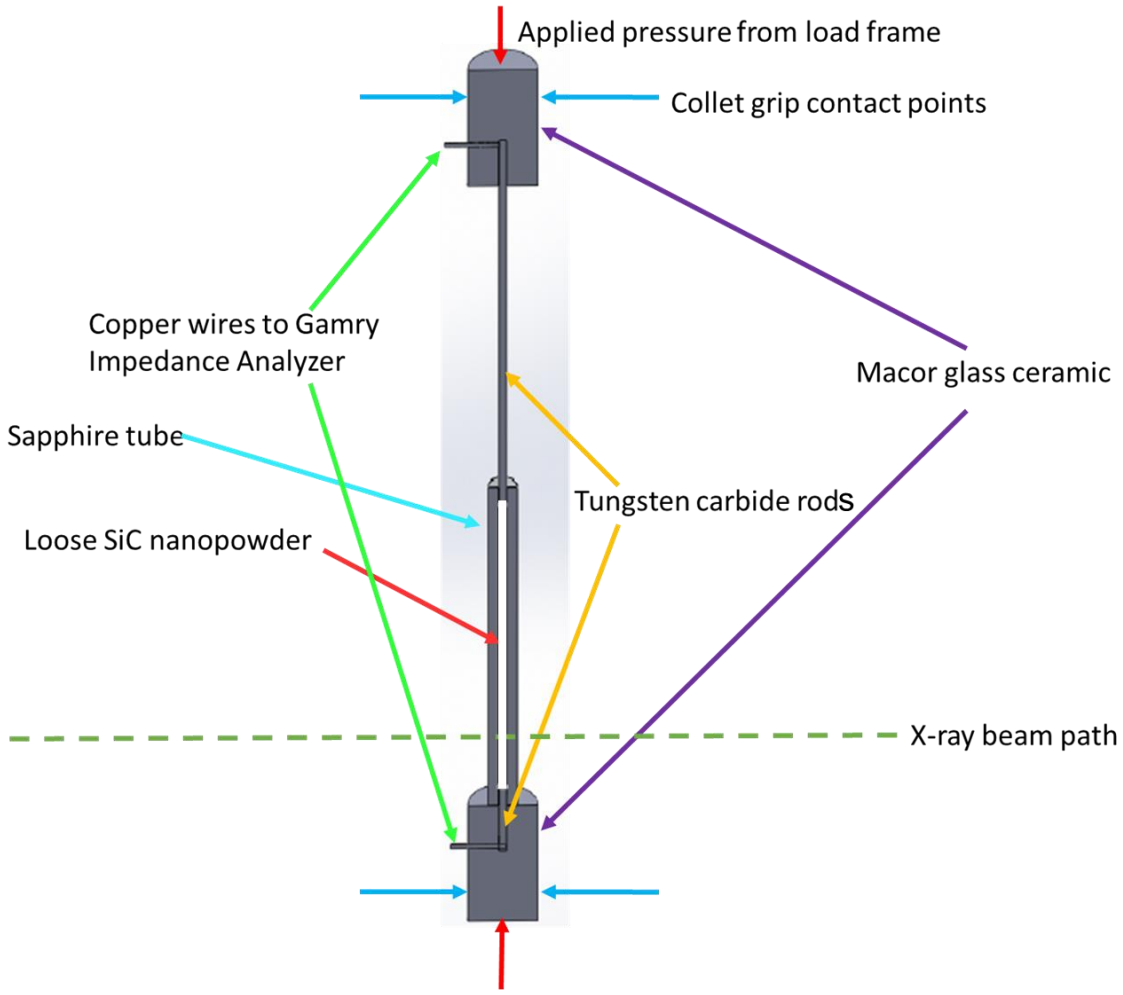

Figure A.25. Cross-sectional view of the complete die assembly, with parts listed by material and with the locations of applied pressure, connections to the impedance equipment, path of the x-ray beam, and regions in contact with the load frame grips indicated. Arrows of the same color indicate the same label applies to each of them.

A.6.2 Setup of the die assembly and measurement of the scattering background signals

The testing procedure began with inserting a bottom punch into a die, then filling the die with the SiC nanopowder until nearly full. This procedure was conducted in a fume hood to minimize the potential of exposure to the nanopowder. The top punch was inserted into the top of the die, then the assembly was placed in a sealed plastic bag and transported to the beamline. Once there, the top and bottom punches were mounted to the load frame,

which was adjusted to a starting position such that there was a small gap between the top punch and the powder. The die was then removed and remounted upside down, such that there was a small gap between the powder and the bottom punch. The powder did not move within the die due to gravity alone, possibly due to the small internal diameter of the die in conjunction with careful handling of the die keeping the powder's energy below the jamming transition.[125] The die was surrounded with a layer of Kapton film (DowDuPont Inc., Wilmington, DE) secured with Kapton tape (DowDuPont Inc., Wilmington, DE) in order to contain the nanopowder if the die were to rupture (Figure A.26). The film material interacts minimally with the x-rays, and thus the beam flux is essentially preserved when passing through the film. The load frame was mounted on a mobile sample stage with three-axis movement capabilities, which was used to properly position the frame, so the beam would pass right through the gap between the powder and the bottom punch. A SAXS test, WAXS test, and USAXS test were then run in order to determine the background response of the die and Kapton film so their effects on the data for the powder tests could be removed. The beam energy used throughout this series of tests was 21 keV, and the three tests together took about 5 minutes to run.

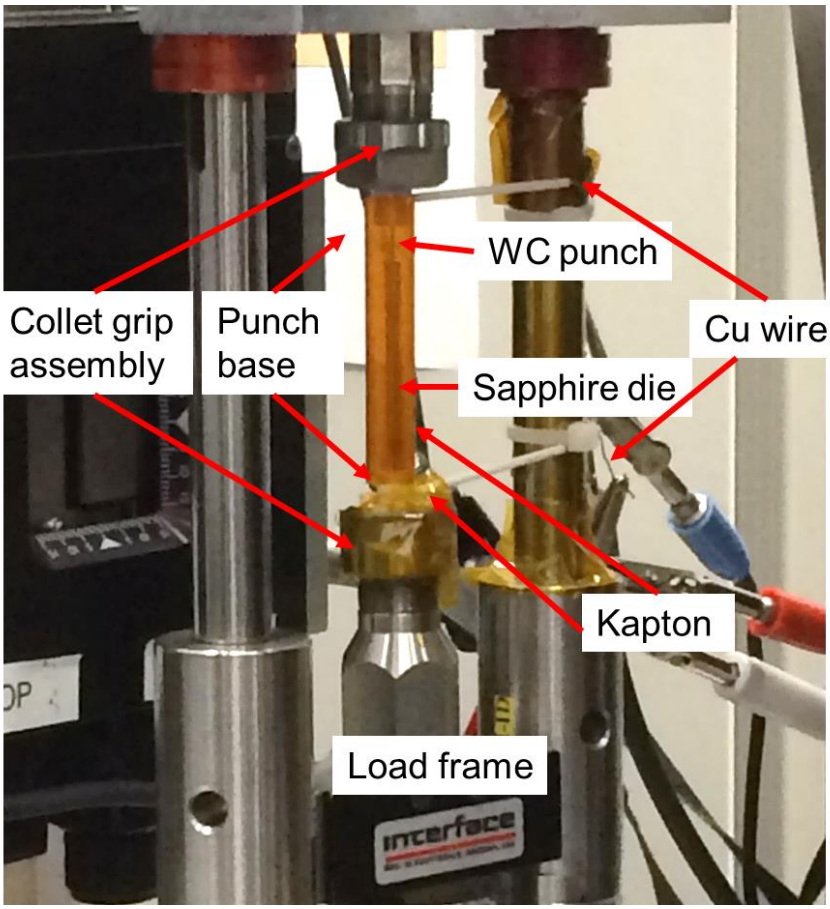

Figure A.26. Image of a die assembly mounted within the compact load frame. The Kapton film is seen as the orange tube surrounding the sapphire die, and the rest of the orange material is Kapton tape. The white tubes coming from the sides of the punch bases are alumina tubes which were used to protect the copper wires and prevent the wires from contacting conducting parts of the load frame. Kapton tape was used to prevent any unintended contacts between conducting parts throughout the setup.

A.6.3 Setup and control of equipment and testing parameters

The load frame and the Gamry impedance equipment were set up to be controlled remotely over the Argonne computer network so both equipment could be controlled from a computer just outside the test chamber. To control the beamline equipment, a computer macro was made by Dr. Ilavsky which would run each of the three scattering tests in sequence. This included automatic changing between the three detectors and generating

data files with automatically generated names which included the pressure measured at the time the scattering tests were started. Neither the USAXS control software, the load frame, nor the impedance equipment was able to communicate with the other two equipment, so each had to be activated manually at the appropriate times. The load frame had no feedback loop to automatically approach target pressures, so manipulation of the load frame to achieve target pressures had to be done by sending commands to the load frame to move up or down by a specified distance, thereby manually approaching the target pressure. Care was taken to minimize overshooting the target pressures since the extra compaction of the powder bed due to pressure overshoot cannot be recovered. For the same reason, any time there was overshoot, the top punch was never raised to reduce the pressure back to the target value, as doing so would only create a gap between the top punch and the powder, rather than returning the system to the state it would be in if exactly at the target pressure.

The program for the impedance tests was a frequency sweep from 10^{6} Hz to 10^{-1} Hz under a constant voltage of 100 mV and no dc bias. The impedance equipment was configured in a two-electrode setup, where the working and working sense are connected to form one electrode and the counter, counter sense, and reference leads are connected together to form the other electrode. The copper wires coming from the punches were each attached to one of the electrodes (Figure A.27). Space limitations of the test setup required the impedance equipment to be relatively far from the load frame, and there was tension on the wires coming from the impedance equipment since the wires were barely long enough to reach the copper wires. Alumina tubes were placed over the copper wires to reduce the potential for damage to the fragile wires, especially at the point where they emerge from the punch base, from any non-axial component of the tension (Figure A.26).

Kapton tape was used to eliminate any instances of unintended contact between exposed parts of the electrical test circuit and other conducting surfaces which were frequent due to the number of wire connections in close proximity for the two-electrode setup with the Gamry equipment (Figure A.27). In this setup, the working current and working sense leads are combined to form one electrode and the counter current, counter sense, and reference leads are combined to form the other electrode.[126]

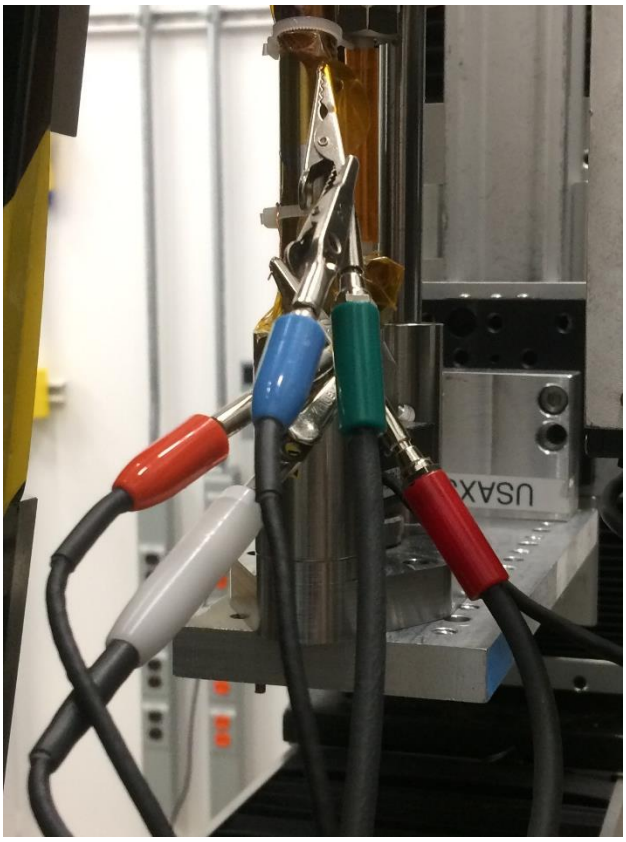

Figure A.27. Two-electrode setup of the Gamry equipment used for the in-situ SAXS tests. Here, the working (green) and working sense (blue) leads are connected together to form one electrode, and the counter (red), counter sense (orange), and reference (white) leads are connected to each other to form the other electrode. One of the alligator clips from each of these electrodes was attached to one of the copper wires coming from the punch bases, while the alligator clips of the other leads comprising that electrode were clipped onto the first alligator clip. Due to the high potential for shorting the electrical circuit via contact between alligator clips belonging to different electrodes, Kapton tape was used extensively to electrically separate the electrodes as well as to separate the copper wires from contact with the load frame.

A.6.4 Testing procedure

After running the background scattering tests through the gap between the powder and the bottom die, the load frame was activated, bringing the top punch down until the powder contacted the bottom punch. The USAXS, SAXS, and WAXS tests were then run concurrently with the impedance test. These data were designated as 0 MPa data. Once

finished, the load frame was engaged until the first target pressure was achieved. The target pressures for this test series is given in Table A.7.After allowing a short time for the powder to settle at the new pressure, the USAXS, SAXS, and WAXS tests were again run simultaneously with the impedance test, followed by increasing the pressure to the next target value. This process was repeated until the scattering and impedance data had been collected at all target pressures.

Table A.7. Target Pressures for All Simultaneous In-situ Scattering and Impedance Tests

Test	Target Pressure (MPa)	Sample Diameter (mm)	Sample Thickness (mm) SiC3/SiC4
1	0	0.74	10.9/7.45
2	10	0.74	7.1/6.67
3	20	0.74	6.3/5.55
4	30	0.74	5.2/5.14
5	40	0.74	4.7/4.65
6	50	0.74	4.43/4.34
7	100	0.74	3.78/3.68
8	150	0.74	3.38/3.45
9	200	0.74	3.13/3.25
10	250	0.74	2.98/3.11
11	300	0.74	2.88/2.97

A.6.5 Data reduction and processing

Data reduction and processing was carried out by Dr. Ilavsky. This included the radial averaging of the 2-D intensity data, converting it to 1-D q vs I(q) data, subtraction of the measured background data from the powder test data, and merging the SAXS and USAXS data into a single continuous curve.

A.6.6 Fitting the combined USAXS/SAXS data using the Unified Fit program

The in-situ combined USAXS and SAXS data was fitted using the Unified Fit tool in the Irena tool suite[113], as was done for the ex-situ tests.

A.6.7 Derivation of resistivity and porosity values

As with the SANS tests, a resistance value for each impedance test was obtained from the impedance magnitude at the lowest tested frequency. For these tests, the A term in equation (2.3) was determined from the internal radius of the die, 0.37 mm, which is equal to the cross-sectional area of the powder. The thickness of the powder bed was determined using both displacement data from the load frame and a high-magnification camera focused on the die, which could see the powder and punches within the die (Figure A.28). The powder thickness was taken as the displacement of the load frame which was required to move the camera from a position where one end of the powder bed was lined up with a mark on the screen to the point where the other end of the powder bed lined up with that same mark.

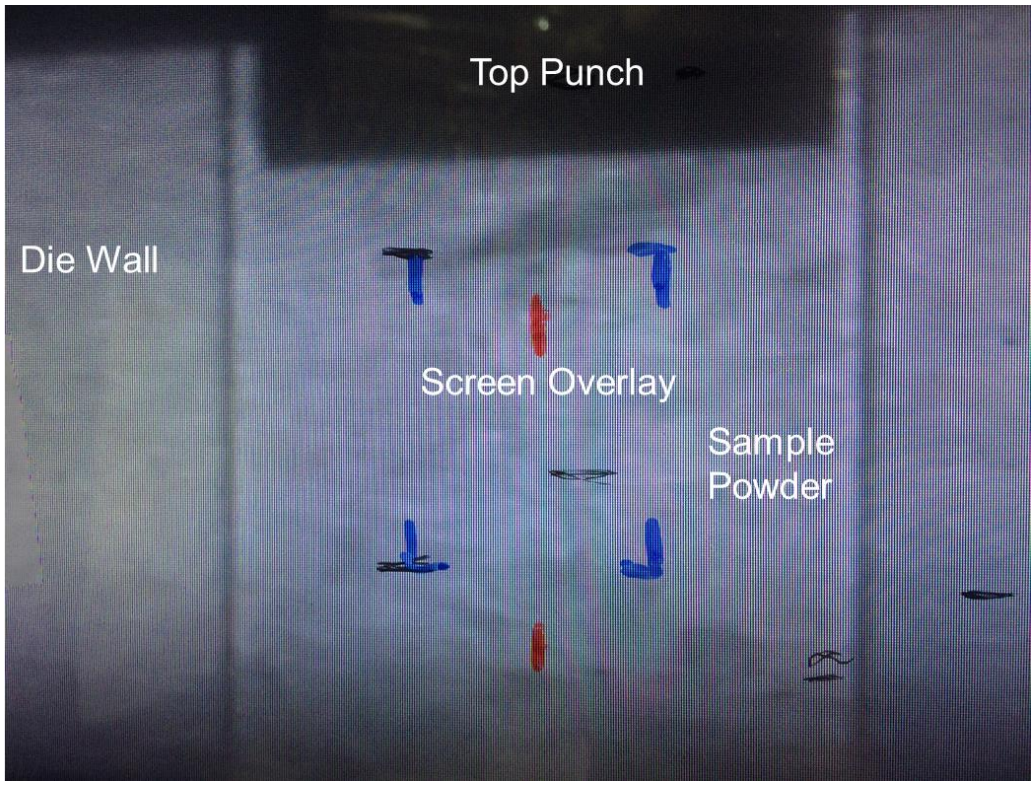

Figure A.28. Image of a monitor showing the live video feed from a high-magnification camera focused on the sapphire die. The vertical lines on either side of the image are the internal wall of the die, and the black rectangle at the top of the image is the end of the top punch. This video feed was used to determine the powder bed thickness, verify when the punches came into contact with the powder, and to help identify problems encountered during the testing process.

Porosity and relative density data were determined in the same way as was detailed for the ex-situ tests using equation (A.15), derived from the Beer-Lambert law (equation (A.14)) and using material-specific data for the SiC powder under test determined using the anomalous scattering contrast calculator in the Irena tool suite.[113]

A.6.8 Impedance results

Impedance spectroscopy data, which started to be collected using the Gamry Reference 3000 equipment during the second test set (SiC2), is shown in Figure A.29. In

general, all of the impedance magnitude data for the SiC2, SiC3, and SiC4 tests show a gradual, sequential decrease with increasing pressure, as was expected since a denser powder bed should have better interparticle contacts. The phase angle data shows a trend of transitioning from -90° to 0° at higher frequencies with increasing pressure, indicating increasing dominance of resistive behavior relative to capacitive behavior. The data for the most insulating test results consistently showed noise at low frequencies, but this is likely due to a combination of the high impedance and the mild applied voltage of 100 mV, which results in very low currents (≈0.2 pA) on the order of the sensitivity of the impedance measurement equipment.

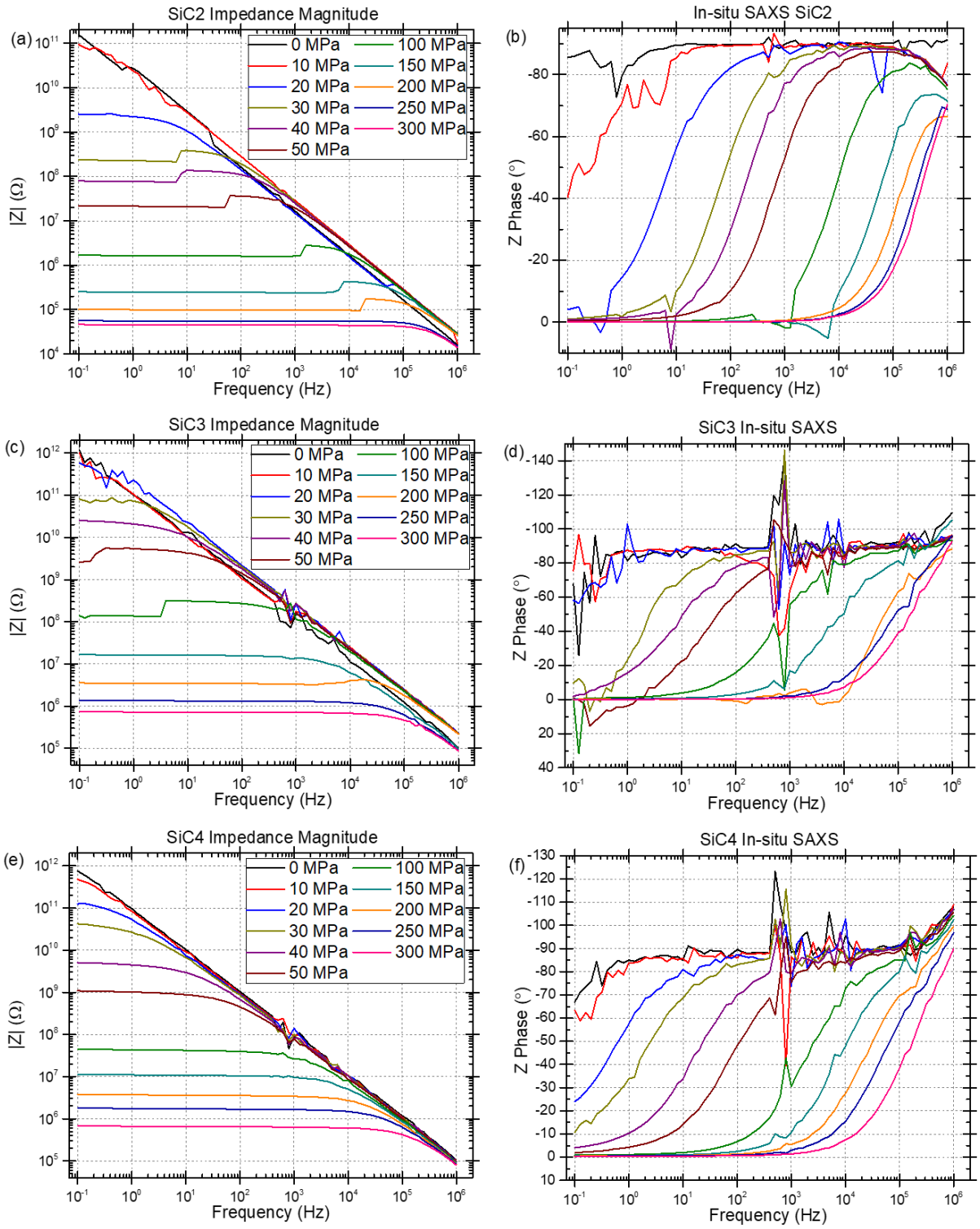

Figure A.29. Impedance magnitude and phase angle data at each pressure for the (a,b) SiC2, (c,d) SiC3, and (e,f) SiC4 test series.

Both the SiC2 and SiC3 impedance magnitude data show a step at intermediate pressures, although they are far more common in the SiC2 data. These may be related to an issue of slipping of the bottom punch base further into the load frame's collet grip as pressure was increased. This issue was first noticed during the SiC2 test, and an initial solution was attempted for the SiC3 test by just adding material into the bottom of the bottom collet grip to take up the remaining space within the grip. However, some slipping, though far less, still occurred. For the SiC4 test, the fit of the material was improved to more closely match the empty space in the grip and, as a result, there was no slipping in the SiC4 test. Looking at the impedance magnitude data, the frequency of the step behavior seems to coincide with the slipping observations, leading to the conclusion that they are likely related.

A final trend, which was especially evident in the phase angle data, is the strong noise at 10^3 Hz for the SiC3 and SiC4 tests but stopped when higher pressures were reached. The noise occurring consistently at the same frequency suggested an equipment-related source of the issue. However, it is not then clear why the SiC2 tests did not show evidence of this same phenomenon. Another factor specific to the SiC3 and SiC4 tests is higher impedance magnitude values at all pressures compared to the SiC2 data. It is also notable that the SiC2 test was run the day before the other two tests. It seems plausible that these three observed trends are somehow related, but no definitive conclusions have been drawn thus far.

A.6.9 SAXS/USAXS Unified Fit data fitting results

The combined USAXS and SAXS data, shown in Figure A.30, showed similar curve shapes, one of which was a region of sequential increases in I(q) with increasing applied pressure extending from between 10^{-3} to 10^{-2} $Å^{-1}$ to the start of the flat background at the largest q values. This trend confirmed the expectation that I(q) should increase with the applied pressure because the higher pressures should increase the density of the powder bed, thereby increasing the total number of powder particles within the beam path, resulting in more scattering events over the same time period. This trend consistently decayed at a q value of approximately 10^{-3} $Å^{-1}$, and at all smaller q values the curves tended to mostly overlap. The deviation of the 40 MPa and 50 MPa curves from the rest of the data seen in the SiC4 test Figure A.30 (c) was unique to that test and cannot presently be explained.

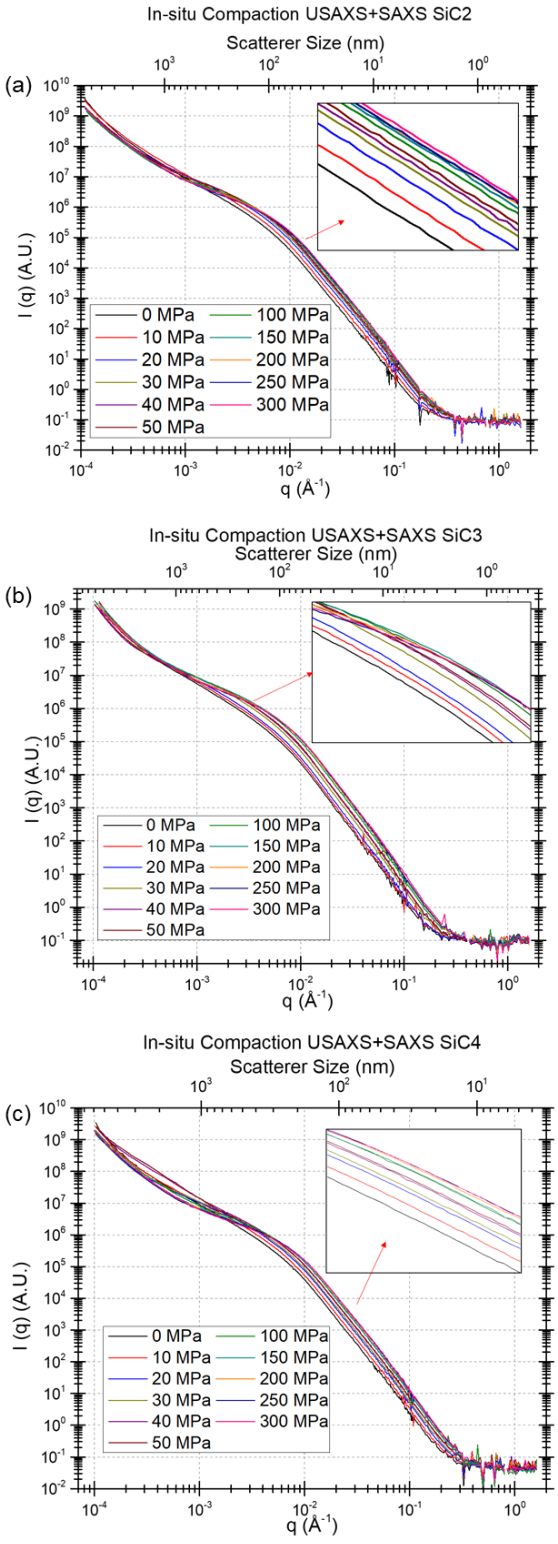
In-situ Compaction USAXS+SAXS SiC2
Scatterer Size (nm)
(a)
I (q) (A.U.)
q (Å^{-1})
0 MPa
10 MPa
20 MPa
30 MPa
40 MPa
50 MPa
100 MPa
150 MPa
200 MPa
250 MPa
300 MPa
In-situ Compaction USAXS+SAXS SiC3
Scatterer Size (nm)
(b)
I (q) (A.U.)
q (Å^{-1})
0 MPa
10 MPa
20 MPa
30 MPa
40 MPa
50 MPa
100 MPa
150 MPa
200 MPa
250 MPa
300 MPa
In-situ Compaction USAXS+SAXS SiC4
Scatterer Size (nm)
(c)
I (q) (A.U.)
q (Å^{-1})
0 MPa
10 MPa
20 MPa
30 MPa
40 MPa
50 MPa
100 MPa
150 MPa
200 MPa
250 MPa
300 MPa

Figure A.30. 1-D I(q) vs q plots at each pressure for the (a) SiC2, (b) SiC3, and (c) SiC4 tests. Close inspection of the 10^{-2} to 10^{-1} $Å^{-1}$ regions (insets) shows a sequential trend of increasing intensity with increasing pressure. However, this relationship did not hold at low q values.

Examination of the change in Unified Fit parameters with pressure (Figure A.31) shows a few consistent trends. The largest changes in all parameters occurred at the lower pressures. This result was expected, since most of the compaction process occurred at the lower pressures. The R_g values for the first 3 levels show relatively consistent values as the pressure changed, although a small, steady increase is observable in the level 3 curve with increasing pressure, whereas the level 2 curve shows small decreases after 50 MPa. The average R_g values for levels 1, 2, and 3 averaged 3.5 nm, 32 nm, and 548 nm, respectively. As with the fitting of the SANS data and the ex-situ SAXS data, it is expected that level 1 is the scattering response of a thin surface layer of SiO_2. As with the previous analyses of Unified Fit results, level 2 represents the response of the powder nanoparticles, and level 3 is the response of aggregates of the nanoparticles. Level 4 which, as with the ex-situ tests, did not show a Guinier region at the lowest measured q, is again taken to represent agglomerates, which can possess characteristic length scales multiple orders of magnitude larger than that of the constituent powder particles.[120]

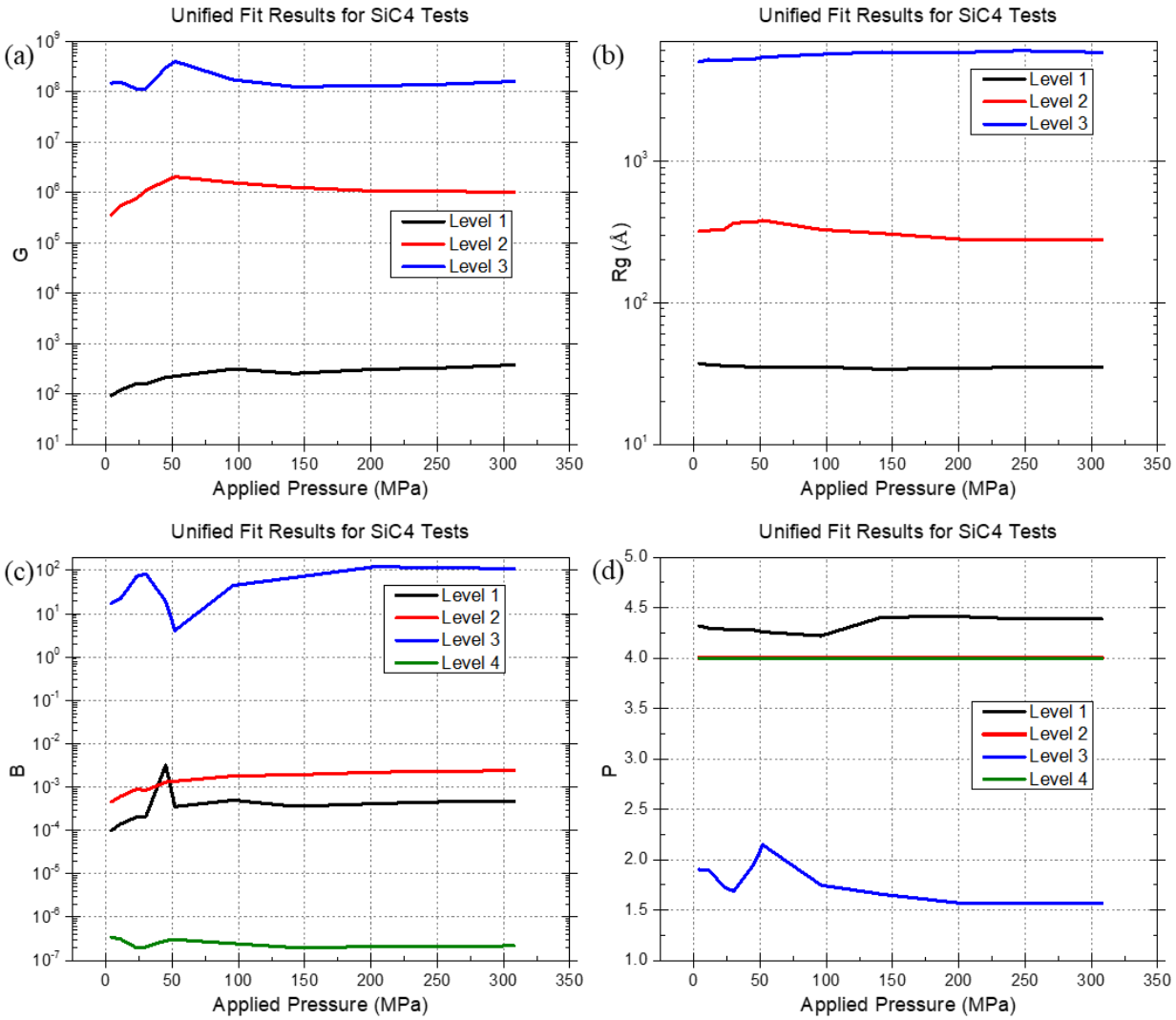

Figure A.31. Values of the four unified fit parameters, (a) G, (b) R_g, (c) B, and (d) P, over the range of pressures in the SiC4 test series.

The fitting parameters for level 3 showed the most change with increasing pressure. Since this level has been attributed to aggregates, which have far lower densities than the particles would have if there were no aggregates, it seems reasonable that, upon applying pressure, the aggregates would tend to be affected before the powder particles themselves. The forces holding the aggregates together are far weaker than those holding the atoms within each individual particle together (covalent or ionic atomic bonds).[120] Also, changes

to the aggregates, whether by rearrangement to increase packing efficiency or some degree of breakdown of the aggregate structures, can increase the overall density of the powder compact far more than rearrangement of the individual particles simply because aggregates fill space so inefficiently.

Level 4 seems to show very little change with pressure, but change would very much be expected for this level, given that agglomerates, to which level 4 was attributed, are larger and pack even more inefficiently than aggregates. However, it needs to be noted that the R_g of level 3, 548 nm, is, on a log scale, near the highest length scale which could be measured in the USAXS tests, which was approximately 6000 nm. If the typical length scale for the agglomerates is significantly larger than that, the large changes expected for level 4 may be present, but just not visible in the data due to the limits of the measurement equipment. Since it has been reported that agglomerates can reach sizes into the 100's of μm[120], this assessment seems quite plausible.

An alternative explanation for the level 4 signal is that it represents scattering from the polycrystalline sapphire die. Since the grain size of this sapphire was 25-100 μm, as per the manufacturer, this explanation is also plausible, despite sapphire's relatively low scattering response. However, since background tests with the empty cell were run and subtracted from the final data, it is not clear why a signal from the sapphire would still show up, although the potentially large portion of the response which was beyond the measurement limit of the USAXS detector may have affected the background subtraction in some way. Additionally, a similar level 4 signal also showed up in the data for the pre-

compacted powders, so even if the sapphire is contributing to the level 4 response, it is expected that large agglomerates are still present.

A.6.10 Porosity and Resistivity results

Between the SiC2, SiC3, and SiC4 tests, the values derived for porosity and resistivity were quite similar at each pressure (Figure A.32 (a,b)), indicating good repeatability. The porosity values were also considerably more reasonable than those for the ex-situ tests, especially for the higher pressures. Both the porosity and resistivity data showed the expected decrease with increasing pressure and, when comparing the porosity and resistivity curves for the individual test sets (Figure A.32 (c,d)), it is clear that their trends were nearly identical at all but the lowest pressures. Together, these observations strongly suggest that the scattering and IS tests were able to be successfully conducted simultaneously along with the compaction, and that both methods were able to produce reasonable, repeatable data. These results, therefore, pave the way for the successful realization of the final step in this combined characterization method, which is the incorporation of elevated temperatures to enable the test to characterize the sintering of the powders rather than just compaction.

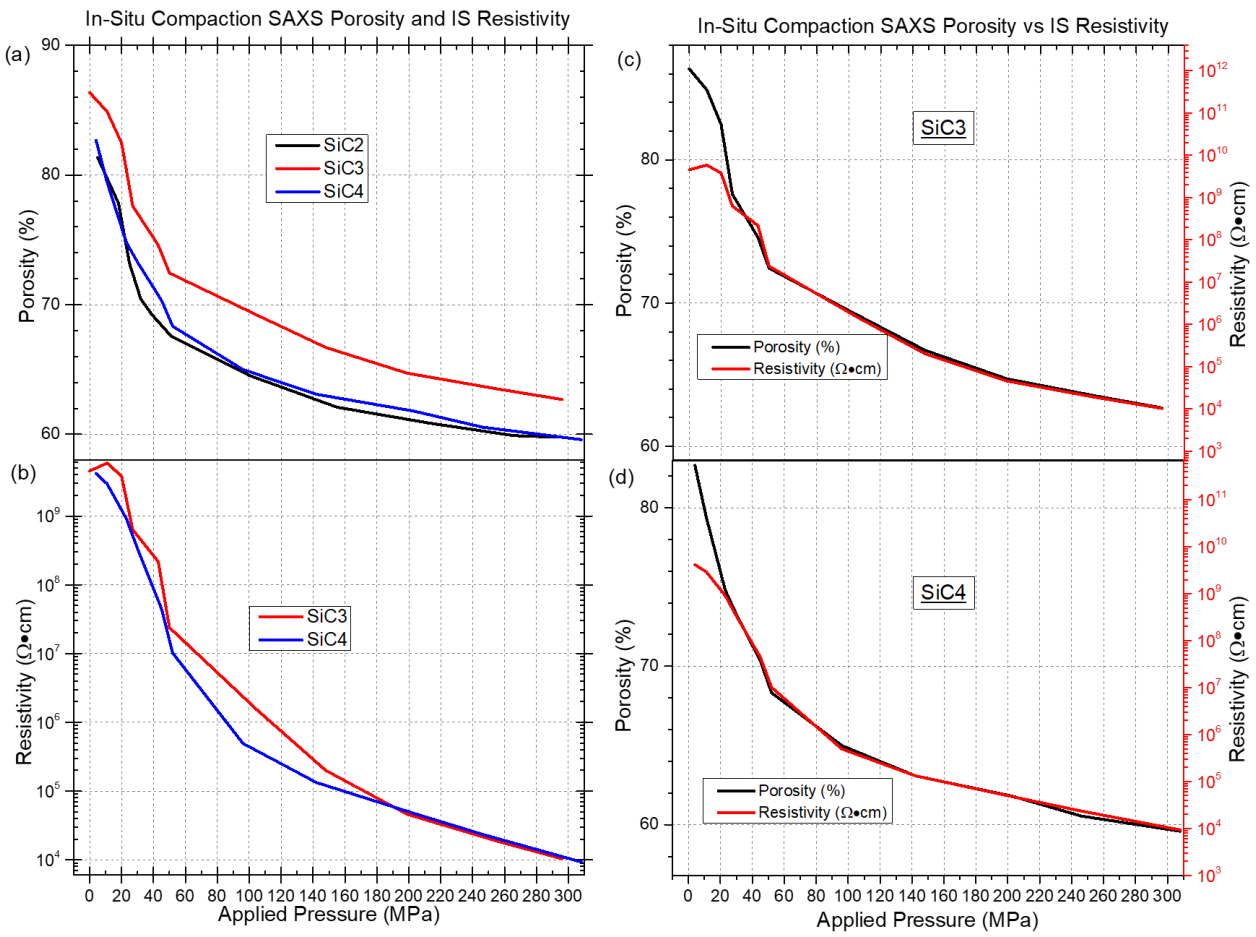

Figure A.32. (a) porosity and (b) resistivity values, derived from the SAXS and IS data, respectively. The data shows similar values between the tests as well as similar patterns, indicating good repeatability. The porosity and resistivity data respective to the (c) SiC3 and (d) SiC4 test series also showed similar patterns, indicating a close, consistent correlation between the SAXS and IS data.

A.7 In-situ SAXS + USAXS during heating of pre-compacted powders

A.7.1 Materials and test setup

These tests were conducted on three different powders, each consisting of a mixture of the borosilicate glass microspheres and ITO nanopowder introduced in Chapter 3, at differing concentrations. The mixes used were the same as those used in making composite samples via sintering which is discussed in Chapter 4. The chosen concentrations were

0.001 phr, 1.0 phr, and 5.0 phr. More detail on the powder mixtures can be found in Table 2.1 and the surrounding text.

For each test, a very small quantity of powder was loaded into a 0.74 mm ID sapphire tube. The same test cell described in Figure A.25 was then assembled and the Macor pieces were again held with collet grips, which were mounted to a manual arbor press (K&M Precision Shooting Products) as shown in Figure A.33. The press was then used to apply an approximately 4.8-pound load to the powder, which applied a resulting pressure of 50 MPa. After doing so, the die and punches were removed from the press, the short punch was removed, and force was applied to the long punch to push the powder compact out of the sapphire tube and into the middle of a 1.3 mm ID 1.5 mm OD glass capillary tube (Friedrich and Dimmock Inc.). Glass wool was inserted into either side of the tube to hold the sample in place, and the capillary was mounted within a capillary heater developed by Dr. Ivan Kusmenko specifically for use in the 9ID-C beamline at the APS facility at Argonne National Lab (Figure A.34). Once mounted in the heater, the two heating coils were moved into position as close as possible to the capillary without making direct contact, and N_2 gas flow was initiated through the capillary.

Figure A.33. Image of the die assembly mounted in a manual arbor press to apply pressure to the powder mixes.

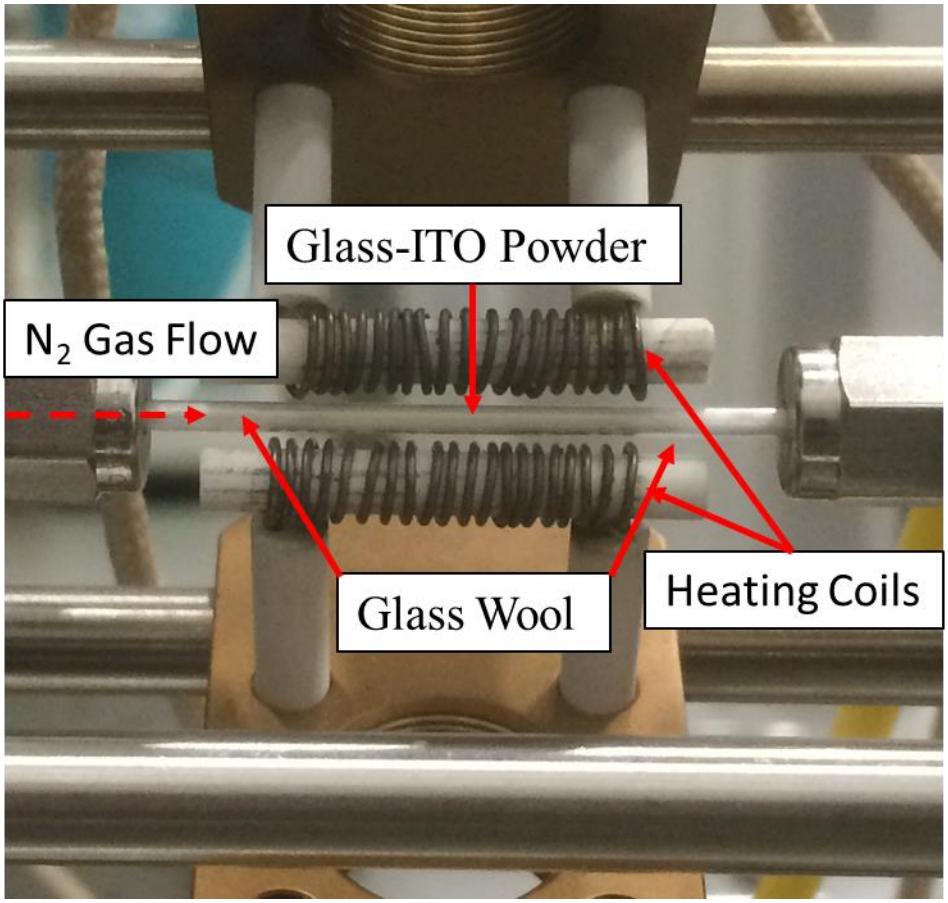

Figure A.34. The capillary heater setup used to conduct in-situ SAS during the heating of borosilicate glass – ITO powder mixes. This view is parallel to the beam path and the relevant parts are labeled.

The testing procedure consisted of increasing the temperature applied to the sample and holding at a series of discreet temperatures to conduct a SAXS, USAXS, and WAXS test. The typical hold temperatures were a baseline at room temperature followed by 150°C, then increasing in increments of 100°C until reaching the target maximum temperature. Upon reaching the maximum temperature, and conducting the three tests, two additional rounds of testing were conducted at that temperature, waiting 5 minutes between test cycles. This was done to determine whether the microstructure was changing over time while at the maximum temperature. Finally, the heating coils were turned off and the

capillary was allowed to cool down to a temperature of 35°C, at which time a final round of tests was conducted.

A.7.2 Data reduction and fitting

The USAXS data was reduced using the Indra macros developed by Dr. Jan Ilavsky for use with the Igor Pro software. SAXS data was reduced using the Nika macros[127], and the USAXS and SAXS curves were merged using the data manipulation tool included in the Irena macros, all of which were also developed by Dr. Jan Ilavsky for use with the Igor Pro software. The merged data sets were fitted using the Unified Fit software also in the Irena package.

After experimenting with different numbers of levels in the model, it was found that a three-level model was able to provide good fits to all the data, regardless of the powder composition or the heating schedule. An example of the three levels is shown in Figure A.35. The R_g values of level 1 were almost exclusively less than 10 nm, as seen in data tables for fits of data for the 0.001 phr, 1.0 phr, and 5.0 phr powder mixes heated to a maximum temperature of 680°C, presented in Table A.8, Table A.9, and Table A.10, respectively. Since the ITO nanopowder present in the powder mixes was claimed to have a particle size range from 20-40 nm by the manufacturer, it would be expected that the level at the highest q values should have R_g values corresponding to particle sizes within that range. Upon conversion of the R_g values to particle diameters, it was found that a R_g greater than 7.5 nm corresponded to a particle size of at least 20 nm, so these were within the expected range. Additionally, as seen in Figure A.35 (a), level 1 is modelling the behavior of the most prominent feature in the data and must then be representing the

primary microstructural feature contributing to the scattering response over the available q range.

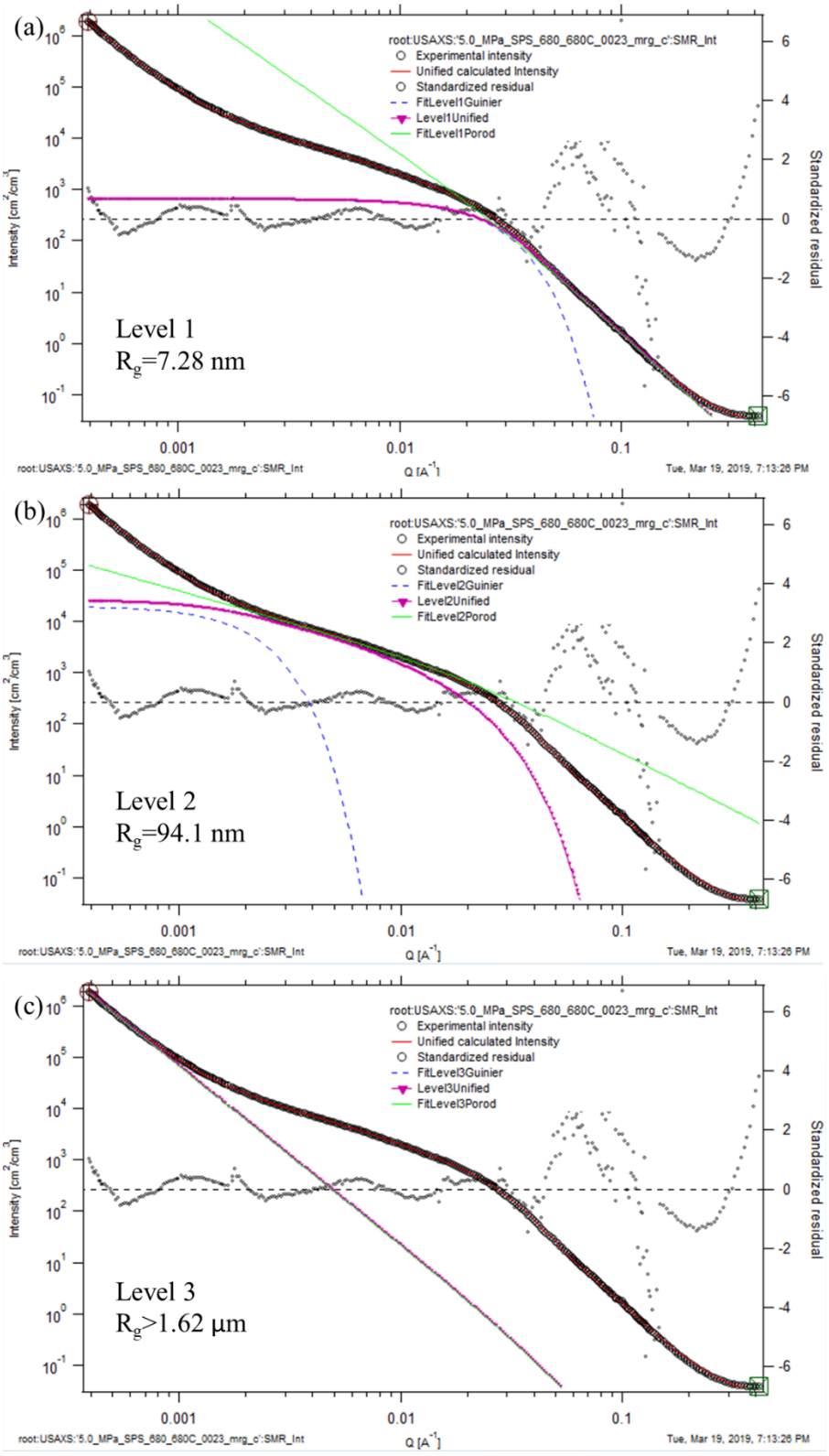

Figure A.35. q vs I(q) log-log plots showing the three levels (a-c) needed for the fitting of the combined USAXS and SAXS data using the Unified Fit method.

Table A.8. 0.001 phr 680°C Unified Fit Parameters

		Level 1			Level 2				Level 3			
Temperature (°C)	SAS Background	G	Rg (nm)	B	P	G	Rg (nm)	B	P	Rg Cutoff	G*	Rg (nm)*	B	P	RD (%)
30	6.96E-02	258.00	17.97	1.58E-05	3.48	7.16E+04	89.27	1.08E-05	3.62	17.97	0	1.00E+09	4.76E-08	4.56	72.05
150	6.03E-02	36.77	8.65	2.10E-05	3.48	1.19E+06	227.76	2.37E-05	3.50	8.65	0	1.00E+09	3.74E-09	4.90	71.54
250	6.61E-02	91.10	11.46	1.75E-05	3.55	7.29E+05	158.65	2.14E-05	3.53	11.24	0	1.00E+09	3.72E-09	4.90	72.85
350	5.33E-02	2.80	4.61	1.48E-05	3.60	4.72E+05	130.98	1.67E-05	3.60	4.61	0	1.00E+09	2.41E-09	4.96	72.57
450	7.25E-02	19.32	8.30	2.74E-05	3.33	5.93E+05	142.28	1.61E-05	3.60	8.30	0	1.00E+09	3.24E-09	4.92	71.12
550	4.76E-02	13.34	7.77	1.49E-05	3.48	7.45E+05	150.23	1.19E-05	3.64	7.77	0	1.00E+09	2.89E-09	4.94	71.89
650	5.50E-02	10.19	7.73	1.27E-05	3.54	8.04E+05	156.87	1.19E-05	3.62	7.73	0	1.00E+09	2.78E-09	4.94	71.46
680	7.55E-02	5.30	6.44	2.96E-05	3.22	7.37E+05	157.12	8.79E-06	3.66	6.44	0	1.00E+09	3.00E-09	4.92	71.51
680	6.48E-02	4.36	6.12	1.19E-05	3.55	7.53E+05	160.52	8.05E-06	3.67	6.12	0	1.00E+09	2.96E-09	4.92	71.11
680	4.25E-02	3.45	5.60	1.02E-05	3.49	1.39E+06	189.62	8.09E-06	3.68	5.60	0	1.00E+09	2.02E-09	4.97	73.57
35	6.77E-02	4.05	5.65	7.23E-05	2.87	7.20E+05	154.37	9.00E-06	3.65	5.65	0	1.00E+09	1.96E-09	4.97	71.19

Table A.9. 1.0 phr 680°C Unified Fit Parameters

		Level 1				Level 2					Level 3			
Temperature (°C)	SAS Background	G	Rg (nm)	B	P	G	Rg (nm)	B	P	Rg Cutoff	G*	Rg (nm)*	B	P	RD (%)
30	5.43E-02	158.97	7.67	5.31E-05	3.78	3.47E+06	209.79	5.82E-04	3.13	7.67	0	1.00E+09	1.84E-09	4.98	72.28
150	7.33E-02	133.17	7.29	9.51E-05	3.58	2.92E+06	225.47	9.03E-04	3.04	7.29	0	1.00E+09	6.25E-09	4.82	72.55
250	7.29E-02	119.07	7.09	1.00E-04	3.56	2.68E+06	223.24	9.91E-04	3.03	7.09	0	1.00E+09	6.75E-09	4.81	72.25
350	6.03E-02	139.27	7.43	6.49E-05	3.72	3.28E+06	202.44	6.44E-04	3.12	7.43	0	1.00E+09	1.72E-09	4.98	72.17
450	7.03E-02	128.82	7.27	9.14E-05	3.60	2.69E+06	195.87	6.18E-04	3.12	8.30	0	1.00E+09	3.28E-09	4.90	72.20
550	7.03E-02	127.28	7.25	9.15E-05	3.60	2.73E+06	197.34	6.25E-04	3.12	7.25	0	1.00E+09	3.28E-09	4.90	72.20
650	5.64E-02	192.45	8.04	3.60E-05	3.89	4.55E+06	243.18	8.32E-04	3.06	8.04	0	1.00E+09	2.12E-09	4.96	71.63
680	6.64E-02	194.65	8.18	4.60E-05	3.78	3.52E+06	227.52	8.49E-04	3.05	8.18	0	1.00E+09	3.32E-09	4.90	71.48
680	5.14E-02	209.02	8.54	2.56E-05	3.96	3.79E+06	228.72	6.91E-04	3.09	8.54	0	1.00E+09	2.59E-09	4.93	71.16
680	7.03E-02	215.00	8.64	4.80E-05	3.75	3.49E+06	219.33	6.18E-04	3.11	8.64	0	1.00E+09	2.49E-09	4.94	71.10
35	7.12E-02	206.70	8.46	5.91E-05	3.69	3.07E+06	220.14	7.16E-04	3.07	8.46	0	1.00E+09	3.97E-09	4.87	71.37

Table A.10. 5.0 phr Unified Fit Parameters

		Level 1				Level 2					Level 3			
Temperature (°C)	SAS Background	G	Rg (nm)	B	P	G	Rg (nm)	B	P	Rg Cutoff	G*	Rg (nm)*	B	P	RD (%)
30	5.29E-02	1144.8	7.76	1.91E-04	4.00	3.93E+05	103.99	1.85E-01	2.20	7.76	0	1.00E+09	2.39E-08	4.51	62.58
150	4.47E-02	1160.8	7.72	1.80E-04	4.00	3.34E+05	96.37	1.33E-01	2.26	7.72	0	1.00E+09	6.11E-08	4.52	62.43
250	4.50E-02	1009.1	7.52	1.68E-04	4.00	3.12E+05	93.44	1.37E-01	2.26	7.52	0	1.00E+09	8.44E-08	4.48	62.58
350	4.14E-02	951.1	7.45	1.64E-04	4.00	3.02E+05	92.56	1.36E-01	2.26	7.45	0	1.00E+09	9.33E-08	4.47	61.91
450	3.73E-02	1113.1	7.71	1.82E-04	4.00	3.26E+05	94.95	1.31E-01	2.27	7.71	0	1.00E+09	8.99E-08	4.47	62.52
550	3.16E-02	1149.8	7.79	1.90E-04	4.00	3.20E+05	94.92	1.27E-01	2.27	7.79	0	1.00E+09	8.75E-08	4.47	62.47
650	3.16E-02	1015.8	7.52	1.70E-04	4.00	2.98E+05	93.49	1.39E-01	2.24	7.52	0	1.00E+09	8.79E-08	4.47	61.56
680	2.69E-02	878.73	7.28	1.58E-04	4.00	3.00E+05	94.14	1.65E-01	2.21	7.28	0	1.00E+09	7.80E-08	4.49	61.46
680	2.88E-02	867.01	7.31	1.58E-04	4.00	3.40E+05	100.33	1.83E-01	2.18	7.31	0	1.00E+09	5.97E-08	4.52	60.32
680	2.91E-02	823.85	7.23	1.54E-04	4.00	3.94E+05	105.75	2.07E-01	2.16	7.23	0	1.00E+09	4.69E-08	4.55	59.25
35	3.54E-02	938.13	7.33	1.73E-04	4.00	4.13E+05	108.31	1.93E-01	2.17	7.33	0	1.00E+09	3.79E-08	4.58	58.74

Potential explanations for the R_g values below 7.5 nm in the fitting relative to the nominal ITO particle size are evident upon inspection of TEM images of the as-received powder, one of which is presented in Figure A.36. In this image, it appears that the ITO particles exhibit features on several distinct length scales, one of which is small, roughly spherical nodules, some of which are shown with red lines on the image. The general size of these features was at around or below 10 nm, and thus may explain the smaller fitted R_g values. There were also larger and more irregularly shaped structures which were more in line with the expected length scales of the nanoparticles, some of which are shown measured in orange in the figure. These features may be aggregates, as both the sizes and shapes vary widely and many of these individual features appear to be fused together.

It has been demonstrated that repeated humidity cycling of ITO at room temperature can induce agglomeration through the creation of bonds between particles, resulting in a microstructural appearance much like that of the ITO in Figure A.36.[92] Therefore, the scattering response of level 1 may represent a combination of the scattering from the small nodules and the aggregates, and the size distribution between these elements may be contributing to broadening of the level 1 Guinier hump in the 1-D curves (Figure A.35 (a)). Finally, the drastic change in the level 1 scattering behavior with changing ITO concentration in the powder mix (Figure A.37) is further proof that this level represents the ITO response.

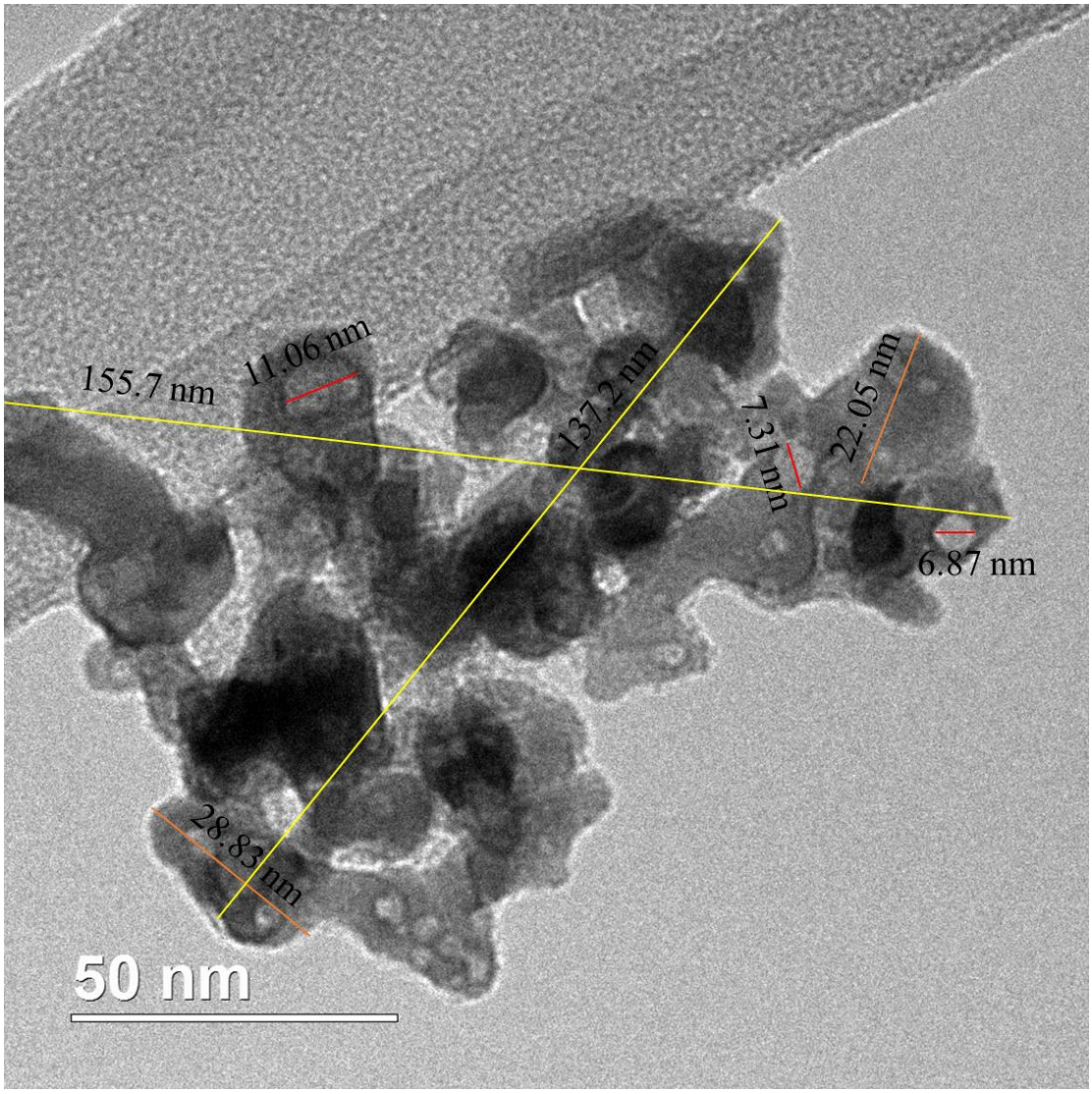

Figure A.36. TEM image of the as-received ITO nanopowder which is claimed to have a particle size range of 20-40 nm.

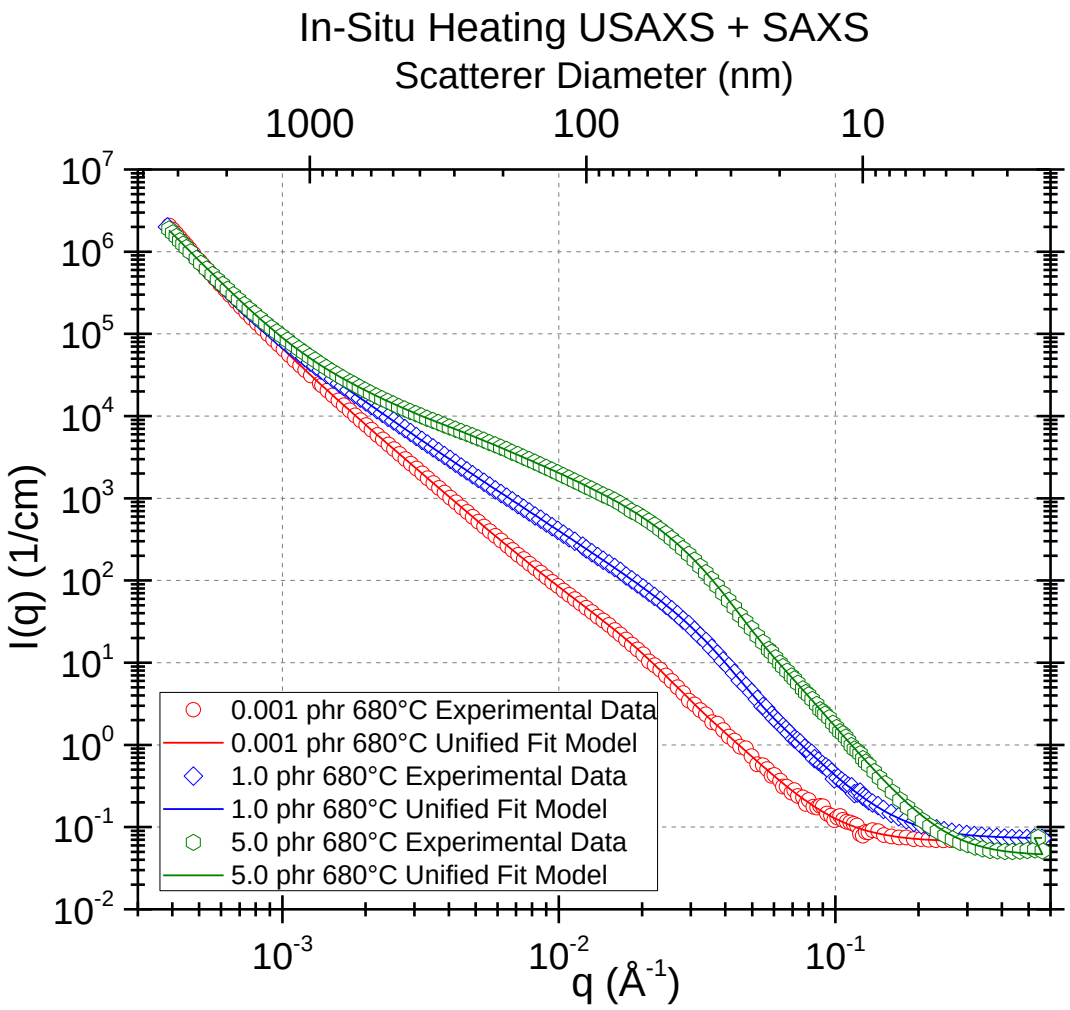

Figure A.37. q vs I(q) log-log plots of the combined SAXS-USAXS data for each of the three powder compositions at a temperature of 250°C, clearly showing increased scattering with increasing ITO concentration around the length scales expected for the ITO nanoparticles.

The level 2 R_g values also varied over a relatively wide range of values. However, these values did not change much between temperatures but changed significantly between powder compositions, with typical values of 150 nm, 200 nm, and 100 nm for the 0.001 phr, 1.0 phr, and 5.0 phr powders, respectively (Table A.8, Table A.9, Table A.10). While that specific characteristic is not currently understood, based on the TEM image, it seems most likely that this level represents agglomerates of the nanoparticles, as indicated with

the yellow lines in Figure A.36., which could easily exhibit a wide range of sizes and shapes. Also based on this reasoning, level 3 likely represents the scattering response from both particularly large ITO agglomerates and the borosilicate glass particles which, at a size range of 45-53 μm, were beyond the measurement range of the USAXS tests.

In the tests of all three powder compositions, very little change was seen in the 1-D data over the entire temperature range from room temperature to 680°C. This was not necessarily unexpected since the powders were not subjected to an applied pressure. Although these same powder compositions achieved densification during HP and SPS sintering to the same or even lower maximum temperatures, the pressures applied during these sintering experiments substantially increased the driving force for densification. Without pressure applied during heating, 680°C was not sufficient to induce any densification in these powders, resulting in a lack of change in the scattering behavior. An additional test series was conducted on the 5.0 phr powder to a maximum temperature of 725°C (Figure A.38) and at the maximum temperature, a significant change can be seen in the scattering data and thus demonstrating the desired characterization of microstructural changes during densification of the powder.

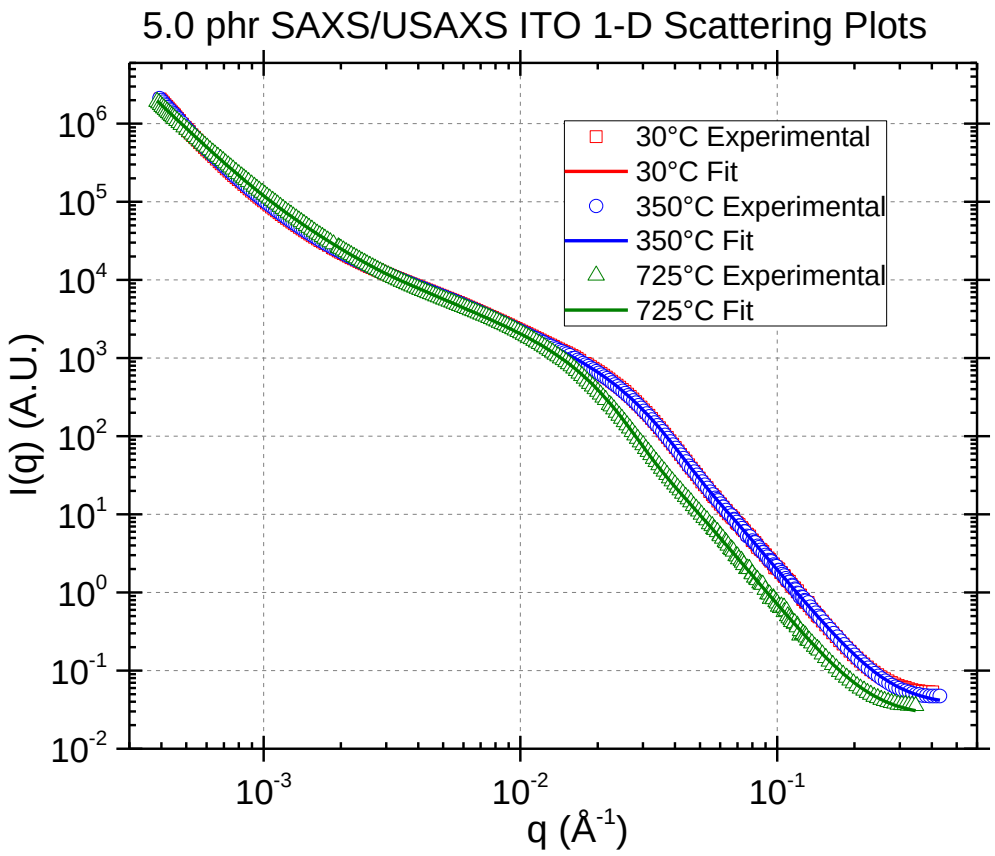

Figure A.38. 1-D log-log plots of scattering data from SAXS and USAXS testing of the 5.0 phr powder at room temperature, an intermediate temperature, and the maximum temperature, showing a change in behavior when reaching 725°C.

A.8 Conclusions

In an effort to more completely characterize microstructural changes in powder beds throughout the process of sintering, a process combining ac impedance spectroscopy and SAS/USAS testing in-situ during powder compaction has been developed and successfully demonstrated. Progressive updates to the experimental procedure, test setup, and scattering technique have improved the quality of the resulting data over the course of multiple experiments, and good agreement between the scattering and impedance data was present

consistently. Fitting of the scattering data using the Unified Fit model was able to quantify the microstructural changes and the various levels were able to be attributed to specific expected or observed microstructural features of the powder compacts.

Testing with the incorporation of elevated temperatures, which is the final addition to the in-situ compaction setup which is necessary to conduct the characterization techniques during in-situ sintering, has begun with an initial proof of concept test, which demonstrated the successful differentiation between powder compositions and changes in behavior as a result of the initiation of densification.

A.9 Future work

The final step of the development of this combined characterization method in-situ during sintering is to incorporate elevated temperatures at the same time as the applied pressure and the SAXS/USAXS and IS testing. Upon the successful development and operation of this test, it is expected that a detailed in-situ characterization throughout the sintering process will be demonstrated and sintering models can be developed from the resulting data, thus achieving the overall goal of this project.

REFERENCES

1. Kang S.L. “Sintering: densification, grain growth and microstructure”. Butterworth-Heinemann, 2004.

2. Munir Z.A., Quach D.V, and Ohyanagi M. "Electric current activation of sintering: a review of the pulsed electric current sintering process." Journal of the American Ceramic Society 94, no. 1 (2011): 1-19.

3. Fang Z.Z.(Ed.). “Sintering of advanced materials”. Woodhead Publishing LTD., Cambridge, UK (2010).

4. Gerhardt R.A., “Impedance and Dielectric Spectroscopy Revisited: Distinguishing dielectric relaxation from long range conductivity,” Journal of the Physics and Chemistry of Solids 55[12], 1491-1506(1994).

5. Pruyn T.L. and Gerhardt R.A., “Percolation in Borosilicate glass matrix composites containing Antimony-doped Tin Oxide segregated networks Part II: Examination of Percolation behavior via Impedance Spectroscopy,” J.Am.Ceram.Soc., 97 [7] 2082-2090 (2014).

6. Cao W., Gerhardt R., and Wachtman, Jr. J.B., “Low Permittivity Porous Silica by a Colloidal Processing Method,” Advances in Ceramics, 26, 409–18 (1989).

7. Gerhardt R.A. and Grossman T.R. “Characterization of porosity in thermal barrier coatings [TBC's]”. Ceramic Transactions 11, 189-199(1990).

8. Gerhardt R.A., “Impedance Spectroscopy and Mobility Spectra”; pp. 350–63 in Encyclopedia of Condensed Matter Physics, Edited by G. Bassani, G. Liedl, and P. Wyder. Elsevier, Oxford, UK, 2005.

9. Mebane D.S. and Gerhardt R.A., “Interpreting Impedance Response of Silicon Carbide Whisker/Alumina Composites through Microstructural Simulation,” J. Am. Ceram. Soc., 89 [2] 538–43 (2006).

10. Gerhardt R.A. and Nowick A.S., “The Grain Boundary Conductivity Effect in Ceria Doped with Various Trivalent Cations. Part I: Electrical Behavior,” J. Amer. Ceram. Soc, 69 [9] 641–6 (1986).

11. Runyan J., Gerhardt R.A., and Ruh R., “Electrical Properties of Boron Nitride Matrix Composites: II, Dielectric Relaxations in Boron Nitride-Silicon Carbide Composites,” J. Am. Ceram. Soc., 84 [7] 1497–503 (2001).

12. Pruyn T.L., and Gerhardt R.A., "Detection of Different Interfaces in Percolated Networks of Antimony Tin Oxide: Borosilicate Glass Composites by Impedance Spectroscopy". Journal of the American Ceramic Society 98, no. 1 (2015): 154-162.

13. Pruyn T.L. and Gerhardt R.A. "Percolation in Borosilicate Glass Matrix Composites Containing Antimony-Doped Tin Oxide Segregated Networks. Part I: Fabrication of Segregated Networks". Journal of the American Ceramic Society 96, no. 11 (2013): 3544-3551.

14. Wang B., Huang W., Chi L, Al-Hashimi M., Marks T.J., and Facchetti A. "High-k gate dielectrics for emerging flexible and stretchable electronics". Chemical reviews. 2018 May 22;118(11):5690-754.

15. Waddell, J., Ou R., Capozzi C.J., Gupta S., Parker C.A., Gerhardt R.A., Seal K., Kalinin S.V., and Baddorf A.P. "Detection of percolating paths in polyhedral segregated network composites using electrostatic force microscopy and conductive atomic force microscopy." Applied Physics Letters 95, no. 23 (2009): 233122.

16. Balberg, I., Anderson C.H., Alexander S., and Wagner N. "Excluded volume and its relation to the onset of percolation." Physical review B 30, no. 7 (1984): 3933.

17. Capozzi C.J., and Gerhardt R.A. "Novel percolation mechanism in PMMA matrix composites containing segregated ITO nanowire networks." Advanced Functional Materials 17, no. 14 (2007): 2515-2521.

18. Deng H., Lin L., Ji M., Zhang S., Yang M., and Fu Q. "Progress on the morphological control of conductive network in conductive polymer composites and the use as electroactive multifunctional materials." Progress in Polymer Science 39, no. 4 (2014): 627-655.

19. Ramond L., Bernard-Granger G., Addad A., and Guizard C. "Sintering of Soda-Lime Glass Microspheres Using Spark Plasma Sintering." Journal of the American Ceramic Society 94, no. 9 (2011): 2926-2932.

20. Risbud S.H., Groza J.R., and Kim M.J. "Clean grain boundaries in aluminium nitride ceramics densified without additives by a plasma-activated sintering process". Philosophical Magazine B 69, no. 3 (1994): 525-533.

21. Shen Z., Peng H., and Nygren M. "Formidable increase in the superplasticity of ceramics in the presence of an electric field". Advanced materials 15, no. 12 (2003): 1006-1009.

22. Chen X.J., Khor K.A., Chan S.H., and Yu L.G. "Overcoming the effect of contaminant in solid oxide fuel cell (SOFC) electrolyte: spark plasma sintering (SPS) of 0.5 wt.% silica-doped yttria-stabilized zirconia (YSZ)". Materials Science and Engineering: A 374, no. 1 (2004): 64-71.

23. Takeuchi T., Betourne E., Tabuchi M., Kageyama H., Kobayashi Y., Coats A., Morrison F., Sinclair D.C., and West A.R. "Dielectric properties of spark-plasma-sintered $BaTiO_3$". Journal of materials science34, no. 5 (1999): 917-924.

24. Ming Y., Zhang J.X., Liu W.Q., and Wang G.P. "Chemical stability and microstructure of Nd-Fe-B magnet prepared by spark plasma sintering". Journal of magnetism and magnetic materials 271, no. 2 (2004): 364-368.

25. Pei P., Song X.P., Liu J., Zhao M., and Chen G.L. "Improving hydrogen storage properties of Laves phase related BCC solid solution alloy by SPS preparation method". international journal of hydrogen energy 34, no. 20 (2009): 8597-8602.

26. Zhao X.B., Yang S. H., Cao Y.Q., Mi J.L., Zhang Q., and Zhu T.J. "Synthesis of nanocomposites with improved thermoelectric properties". Journal of electronic materials 38, no. 7 (2009): 1017-1024.

27. Noudem J.G., Prevel M., Veres A., Chateigner D., and Galy J. "Thermoelectric $Ca_3Co_4O_9$ ceramics consolidated by Spark Plasma sintering". Journal of electroceramics 22, no. 1-3 (2009): 91-97.

28. Ming Y., Zhang J., Xiao Y., Wang G., and Li T. "New kind of NdFeB magnet prepared by spark plasma sintering". IEEE transactions on magnetics 39, no. 6 (2003): 3551-3553.

29. Amezawa K., Nishikawa Y., Tomii Y., and Yamamoto N. "Electrical and mechanical properties of Sr-doped $LaPO_4$ prepared by spark plasma sintering". Journal of the Electrochemical Society 152, no. 6 (2005): A1060-A1067.

30. Kim B., Hiraga K., Morita K., and Yoshida H. "Effects of heating rate on microstructure and transparency of spark-plasma-sintered alumina". Journal of the European Ceramic Society 29, no. 2 (2009): 323-327.

31. Morita, K., Kim B., Hiraga K., and Yoshida H. "Fabrication of transparent $MgAl_2O_4$ spinel polycrystal by spark plasma sintering processing". Scripta Materialia 58, no. 12 (2008): 1114-1117.

32. Krell A., Hutzler T., and Klimke J. "Transmission physics and consequences for materials selection, manufacturing, and applications". Journal of the European Ceramic Society 29, no. 2 (2009): 207-221.

33. Dobedoe, R.S., West G.D., and Lewis M.H. "Spark plasma sintering of ceramics: understanding temperature distribution enables more realistic comparison with conventional processing". Advances in Applied Ceramics104, no. 3 (2005): 110-116.

34. Chakravarty D., and Chokshi A.H. "Direct characterizing of densification mechanisms during spark plasma sintering". Journal of the American Ceramic Society 97, no. 3 (2014): 765-771.

35. Lu K. "Sintering of nanoceramics". International Materials Reviews 53, no. 1 (2008): 21-38.

36. Holland T.B., Tran T.B., Quach D.V., Anselmi-Tamburini U., Groza J.R., and Mukherjee A.K. "Athermal and thermal mechanisms of sintering at high heating rates in the presence and absence of an externally applied field". Journal of the European Ceramic Society 32, no. 14 (2012): 3675-3683.

37. Schwarz S., Thron A.M., Rufner J., Benthem K., and Guillon O. "Low temperature sintering of nanocrystalline zinc oxide: effect of heating rate achieved by field assisted sintering/spark plasma sintering". Journal of the American Ceramic Society 95, no. 8 (2012): 2451-2457.

38. Yang G., Yang Y., Lu D., Huang K., and Wang J. "Effect of heating rate on the densification of NdFeB alloys sintered by an electric field". International Journal of Minerals, Metallurgy, and Materials 19, no. 11 (2012): 1023-1028.

39. Ji W., Parker B., Falco S., Zhang J.Y., Fu Z.Y., and Todd R.I. "Ultra-fast firing: Effect of heating rate on sintering of 3YSZ, with and without an electric field". Journal of the European Ceramic Society 37, no. 6 (2017): 2547-2551.

40. http://www.tainstruments.com/pdf/brochure/sdt.pdf, accessed 6-27-2018. Published in 2010. No author listed.

41. Abudayyeh, H. "Synthesis and Analysis of ZnO Nanowires". PhD thesis (2012).

42. Ii, S. "Nanoscale Chemical Analysis in Various Interfaces with Energy Dispersive X-Ray Spectroscopy and Transmission Electron Microscopy". 10.5772/31645. (2012).

43. Kot, M. (2014). "In-operando hard X-ray photoelectron spectroscopy study on the resistive switching physics of HfO_2-based RRAM". (Thesis)

44. Jones E., Michael S., and Sittampalam G.S. "Basics of assay equipment and instrumentation for high throughput screening". 2016. Eli Lilly & Company and the National Center for Advancing Translational Sciences.

45. Liu T., Henderson C.L., and Samuels R. "Quantitative characterization of the optical properties of absorbing polymer films: Comparative investigation of the internal reflection intensity analysis method". Journal of Polymer Science Part B: Polymer Physics 41, no. 8 (2003): 842-855.

46. Capozzi C.J., Li Z., Samuels R.J., and Gerhardt R.A. "Impedance spectroscopy and optical characterization of polymethyl methacrylate/indium tin oxide nanocomposites with three-dimensional Voronoi microstructures". Journal of Applied Physics 104, no. 11 (2008): 114902.

47. Pruyn T.L. and Gerhardt R.A., "Characterization of Ceramic Powders During Compaction Using Electrical Measurements". Advances in Bioceramics and Porous Ceramics IV: Ceramic Engineering and Science Proceedings, Volume 32, Issue 6, 199-210(2011).

48. Wang C.T., Wu C.L., Chen I.C., and Huang Y.H. "Humidity sensors based on silica nanoparticle aerogel thin films". Sensors and Actuators B: Chemical. May 27;107(1):402-10 (2005).

49. Gerhardt R.A. and Cao W.Q. "Distinguishing bulk water from adsorbed water via dielectric measurements". IEEE 1996 Annual Report – Conference on Electrical Insulation and Dielectric Phenomena.

50. Rudzik T.J. and Gerhardt R.A. "Comparison of hot pressing and spark plasma sintering in the densification behavior of indium tin oxide-borosilicate glass composites". Journal of the American Ceramic Society. 2018 Feb;101(2):577-89.

51. Pruyn T.L. and Gerhardt R.A. "Percolation in borosilicate glass matrix composites containing antimony-doped tin oxide segregated networks. Part I: fabrication of segregated networks". J Am Ceram Soc. 2013;96:3544-3551.

52. Pruyn T.L. and Gerhardt R.A. "Percolation in borosilicate glass matrix composites containing antimony-doped tin oxide segregated networks. Part II: examination of electrical behavior using impedance spectroscopy". J Am Ceram Soc. 2014;97:2082-2090.

53. Bernard-Granger G., Benameur N., Guizard C., and Nygren M. "Influence of graphite contamination on the optical properties of transparent spinel obtained by spark plasma sintering". Scripta materialia. 2009 Feb 1;60(3):164-7.

54. Rudzik T.J. and Gerhardt R.A. "Comparison of hot pressing and spark plasma sintering in the densification behavior of indium tin oxide-borosilicate glass composites". Journal of the American Ceramic Society. 2018 Feb;101(2 Suppl):577-89.

55. Guo W., Wang W.M., Wang H., Wang Y.C., and Fu Z.Y. "Fabrication of Indium Tin Oxide Targets by Spark Plasma Sintering and Hot-Pressing Sintering". Advanced Materials Research 2009 (Vol. 66, pp. 96-99). Trans Tech Publications.

56. Takeuchi T., Ishida T., Ichikawa K., Miyamoto S., Kawahara M., and Kageyama H. “Rapid preparation of indium tin oxide sputtering targets by spark plasma sintering”. Journal of materials science letters. 2002 Jun 1;21(11):855-7.

57. Lee J.S. and Choi S.C. “Solvent effect on synthesis of indium tin oxide nano-powders by a solvothermal process”. Journal of the European Ceramic Society. 2005 Sep 1;25(14):3307-14.

58. Takeuchi T., Takeda Y., Funahashi R., Aihara T., Tabuchi M. and Kageyama H. “Rapid preparation of dense (La0. 9Sr0. 1) CrO3 ceramics by spark-plasma sintering”. Journal of The Electrochemical Society. 2000 Nov 1;147(11):3979-82.

59. Gerhardt R.A., Runyan J., Sana C., McLachlan D.S., and Ruh R. “Electrical properties of boron nitride matrix composites: III, observations near the percolation threshold in BN–B_4C composites”. Journal of the American Ceramic Society. 2001 Oct;84(10):2335-42.

60. Capozzi C.J. and Gerhardt R.A. “Correlation of the ac electrical conductivity and the microstructure of PMMA/ITO nanocomposites that possess phase-segregated microstructures”. J Phys Chem C.2008;112:19372-19382.

61. Schwesig D., Schierning G., Theissmann R., Stein N., Petermann N., Wiggers H., Schmechel R., and Wolf D.E. “From nanoparticles to nanocrystalline bulk: percolation effects in field assisted sintering of silicon nanoparticles”. Nanotechnology. 2011 Feb 22;22(13):135601.

62. McWilliams B. and Zavaliangos A. “Multi-phenomena simulation of electric field assisted sintering”. Journal of Materials Science. 2008 Jul 1;43(14):5031-5.

63. McLaren C., Heffner W., Tessarollo R., Raj R. and Jain H. “Electric field-induced softening of alkali silicate glasses”. Applied Physics Letters. 2015 Nov 2;107(18):184101.

64. Gonzalez-Julian J. and Guillon O. “Effect of electric field/current on liquid phase sintering”. Journal of the American Ceramic Society.2015;98:2018-2027.30.

65. Rudzik T.J. and Gerhardt R.A. “An improved understanding of SPS processing parameters and errors via detailed analysis of the current and voltage data”. [Awaiting Publication].

66. Ramond L., Bernard-Granger G., Addad A., and Guizard C. “Sintering of Soda-Lime Glass Microspheres Using Spark Plasma Sintering”. Journal of the American Ceramic Society. 2011 Sep 1;94(9):2926-32.

67. 7Ohser-Wiedemann R., Martin U., Seifert H.J., and Müller A. “Densification behaviour of pure molybdenum powder by spark plasma sintering”. International Journal of Refractory Metals and Hard Materials. 2010 Jul 1;28(4):550-7.

68. Schwarz S., Thron A.M., Rufner J., van Benthem K., and Guillon O. “Low temperature sintering of nanocrystalline zinc oxide: effect of heating rate achieved by field assisted sintering/spark plasma sintering”. Journal of the American Ceramic Society. 2012 Aug;95(8):2451-7.

69. McLaren C., Roling B., Raj R., and Jain H. “Mechanism of electric field-induced softening (EFIS) of alkali silicate glasses”. Journal of Non-Crystalline Solids. 2017 Sep 1;471:384-95.

70. Holland T.B., Anselmi-Tamburini U., Quach D.V., Tran T.B. and Mukherjee A.K. “Local field strengths during early stage field assisted sintering (FAST) of dielectric materials”. Journal of the European Ceramic Society. 2012 Nov 1;32(14):3659-66.

71. Manière C., Lee G., and Olevsky E.A. “Proportional integral derivative, modeling and ways of stabilization for the spark plasma sintering process”. Results in physics. 2017 Jan 1;7:1494-7.

72. Grasso S. and Sakka Y. “Electric field in SPS: geometry and pulsed current effects”. Journal of the Ceramic Society of Japan. 121 [6] 524-526 (2013).

73. Munoz S. and Anselmi-Tamburini U. “Temperature and stress fields evolution during spark plasma sintering processes”. Journal of materials science. 2010 Dec 1;45(23):6528-39.

74. Allen J.B. and Walter C. “Numerical simulation of the temperature and stress field evolution applied to the field assisted sintering technique”. ISRN Materials Science. 2012 May 9;2012.

75. Schwertz M., Katz A., Sorrel E., Lemonnier S., Barraud E., Carradò A., d’Astorg S., Leriche A., Nardin M., Vallat M.F., and Kosior F. “Coupled electro-thermo-mechanical finite element modeling of the spark plasma sintering technique”. Metallurgical and Materials Transactions B. 2016 Apr 1;47(2):1263-73.

76. Arnaud C., Manière C., Chevallier G., Estournès C., Mainguy R., Lecouturier F., Mesguich D., Weibel A., Durand L., and Laurent C. “Dog-bone copper specimens prepared by one-step spark plasma sintering”. Journal of materials science. 2015 Nov 1;50(22):7364-73.

77. Barrera M. and Sánchez H. “Design of a Die for the Cold Compaction Calibration of Powdered Materials”. Suplemento de la Revista Latinoamericana de Metalurgia y Materiales S. 2009;1:223-34.

78. Grasso S., Sakka Y., and Maizza G. “Pressure effects on temperature distribution during spark plasma sintering with graphite sample”. Materials Transactions. 2009 Aug 1;50(8):2111-4.

79. Anselmi-Tamburini U., Gennari S., Garay J.E., and Munir Z.A. “Fundamental investigations on the spark plasma sintering/synthesis process: II. Modeling of current and temperature distributions”. Materials Science and Engineering: A. 2005 Mar 15;394(1-2):139-48.

80. Thermocouple response time [homepage on the Internet]. No date [cited 2018 Mar 4]. Available from https://www.omega.com/techref/ThermocoupleResponseTime.html

81. Wang S., Tang J., and Younce F. “Temperature measurement”. In: Heldman DR, editor. Encyclopedia of Agricultural, Food, and Biological Engineering (Print). Crc Press; 2003 Aug 29.

82. Bakueva L., Konstantatos G., Musikhin S., Ruda H.E., and Shik A., “Negative Capacitance in Polymer-Nanocrystal Composites”. Appl. Phys. Lett., 85 [16] 3567–9 (2004).

83. Parravicini G.B., Stella A., Ungureanu M.C., and Kofman R. “Low- Frequency Negative Capacitance Effect in Systems of Metallic Nanoparticles Embedded in Dielectric Matrix”. Appl. Phys. Lett., 85 [2] 302–4 (2004).

84. Ershov M., Liu H.C., Li L., Buchanan M., Wasilewski Z.R., and Jonscher A.K., “Negative Capacitance Effect in Semiconductor Devices”. Electron Devices, IEEE Trans., 45 [10] 2196–206 (1998).

85. Doyle B.S., “Anomalous Low-Frequency Resonance-Type Behaviour and Negative Capacitance in Doped Glasses”. J. Phys. D: Appl. Phys., 19 [6] 1129–39 (1986).

86. Joshi S.M. “Effect of heat and plasma treatments on the electrical and optical properties of colloidal indium tin oxide films”. (Doctoral dissertation, Georgia Institute of Technology). 2013.

87. Bertram B.D. and Gerhardt R.A. “Room temperature properties of electrical contacts to alumina composites containing silicon carbide whiskers”. Journal of Applied Physics. 2009 Apr 1;105(7):074902.

88. Guo J., Guo H., Baker A.L., Lanagan M.T., Kupp E.R., Messing G.L., and Randall C.A. “Cold sintering: a paradigm shift for processing and integration of ceramics”. Angewandte Chemie International Edition. 2016 Sep 12;55(38):11457-61.

89. Siedl N., Gügel P., and Diwald O. “Synthesis and aggregation of In_2O_3 nanoparticles: impact of process parameters on stoichiometry changes and optical properties”. Langmuir. 2013 May 6;29(20):6077-83.

90. Joshi S.M. and Gerhardt R.A. “Effect of annealing atmosphere (Ar vs. air) and temperature on the electrical and optical properties of spin-coated colloidal indium tin oxide films. Journal of Materials Science”. 2013 Feb 1;48(4):1465-73.

91. Cao W. and Gerhardt R.A. “Calculation of Various Relaxation Times and Conductivity for a Single Dielectric Relaxation Process”. Solid State Ionics, 42 213–21 (1990).

92. Gerhardt R.A., “Impedance and Dielectric-Spectroscopy Revisited – Distinguishing Localized Relaxation from Long-Range Conductivity”. J. Phys. Chem. Solids, 55 [12] 1491–506 (1994).

93. Gamry Instruments. “Equivalent Circuit Modeling Using the Gamry Electrochemical Impedance Spectroscopy Software” [internet]. [cited 2/26/2019]. Available from: https://www.gamry.com/application-notes/EIS/equivalent-circuit-modeling-using-the-gamry-eis300-electrochemical-impedance-spectroscopy-software/

94. Johnson D. “Equivalent Circuits – Fitting Results”. *ZView 2*. Version 3.5b. Southern Pines, NC: Scribner Associates, Inc.; 2016.

95. Risbud S.H., Groza J.R., and Kim M.J. “Clean grain boundaries in aluminium nitride ceramics densified without additives by a plasma activated sintering process”. Philos Mag B. 1994;69:525-533.

96. Wei G., Weimin W., Xiuhua M., and Tiekun J. “Preparation of Indium Tin Oxide Sputtering Targets by Spark Plasma Sintering”. Rare Metal Materials and Engineering. 2009 Dec 1;38:407-10.

97. Rudzik T.J. and Gerhardt R.A. "In-situ Characterization of Nanopowders during compaction using SANS and AC impedance spectroscopy." In 10th Annual TechConnect World Innovation Conference and Expo, Held Jointly with the 19th Annual Nanotech Conference and Expo, and the 2016 National SBIR/STTR Conference. TechConnect, 2016.

98. Kerch H.M., Burdette H.E., Gerhardt R.A., Krueger S. and Long G.G., “In-Situ Microstructure Characterization of Sintering of Controlled Porosity Materials,” Mat.Res.Soc.Symp.Proc. 346, 177-182 (1994).

99. Long G.G., Krueger S., Gerhardt R.A. and Page R.A., “Small Angle Neutron Scattering Characterization of Processing/Microstructure Relationships in the Sintering of Crystalline and Glassy Ceramics,” J. Mat. Res. 6 [12], 2706-2715 (1991).

100. Ilavsky J. "Characterization of Complex Thermal Barrier Deposits Pore Microstructures by a Combination of Imaging, Scattering, and Intrusion Techniques." Journal of thermal spray technology 19, no. 1-2 (2010): 178-189.

101. Gerhardt R.A. "A Review of Conventional and Non-Conventional Pore Characterization Techniques." MRS Online Proceedings Library Archive 137 (1988).

102. Kingery W.D. and Berg M. "Study of the Initial States of Sintering Solids by Viscous-Flow, Evaporation Condensation and Self-Diffusion," Journal of Applied Physics 26, 1205 (1955).

103. Grillo I. "Small-angle neutron scattering and applications in soft condensed matter." Soft matter characterization. Springer Netherlands, 2008. 723-782.

104. Long G.G., Krueger S., Jemian P.R., Black D.R., Burdette H.E., Cline J.P., and Gerhardt R.A. "Small-angle-scattering determination of the microstructure of porous silica precursor bodies." Journal of applied crystallography 23, no. 6 (1990): 535-544.

105. Ilavsky J., Long G.G., Allen A.J., and Berndt C.C. "Evolution of the void structure in plasma-sprayed YSZ deposits during heating." Materials Science and Engineering: A 272, no. 1 (1999): 215-221.

106. Allen A.J. "Characterization of Ceramics by X-Ray and Neutron Small-Angle Scattering." Journal of the American Ceramic Society 88, no. 6 (2005): 1367-1381.

107. Jackson A.J. "Introduction to small-angle neutron scattering and neutron reflectometry". NIST Center for Neutron Research. 2008 May:1-24.

108. Beaucage G. "Approximations leading to a unified exponential/power-law approach to small-angle scattering." Journal of Applied Crystallography 28, no. 6 (1995): 717-728.

109. Carnal F., Laguecir A., and Stoll S. "Simulations and scattering functions of polyelectrolyte–macroion complexes". Colloid and Polymer Science. 2004 Dec 1;283(3):317-28.

110. Porod G. "Die Röntgenkleinwinkelstreuung von dichtgepackten kolloiden Systemen." Colloid & Polymer Science 124, no. 2 (1951): 83-114.

111. Borsali R., Pecora R., editors. "Soft-matter characterization". Springer Science & Business Media; 2008 Jul 28. Chapter 13: Small Angle Neutron Scattering and Applications in Soft Condensed Matter; p. 707-764.

112. Thomsen V., Schatzlein D., and Mercuro D. "Tutorial: Attenuation of X-rays by matter". Spectroscopy. 2005 Sep 1;20(9):22-5.

113. Ilavsky J. and Jemian P.R. “Irena: tool suite for modeling and analysis of small-angle scattering”. Journal of Applied Crystallography. 2009 Apr 1;42(2):347-53.

114. Wignall G.D., Littrell K.C., Heller W.T., Melnichenko Y.B., Bailey K.M., Lynn G.W., Myles D.A., Urban V.S., Buchanan M.V., Selby D.L. and Butler P.D. “The 40 m general purpose small-angle neutron scattering instrument at Oak Ridge National Laboratory”. Journal of Applied Crystallography. 2012 Oct 1;45(5):990-8.

115. Agamalian M., Heroux L., Littrell K.C., Carpenter J.M. “Progress on The Time-of-Flight Ultra Small Angle Neutron Scattering Instrument at SNS”. In Journal of Physics: Conference Series 2018 May (Vol. 1021, No. 1, p. 012033). IOP Publishing.

116. Ilavsky J., Zhang F., Andrews R.N., Kuzmenko I., Jemian P.R., Levine L.E., Allen A.J. “Development of combined microstructure and structure characterization facility for in situ and operando studies at the Advanced Photon Source”. Journal of Applied Crystallography. 2018 Jun 1;51(3):867-82.

117. Ilavsky J., Zhang F., Allen A.J., Levine L.E., Jemian P.R., and Long G.G. “Ultra-Small-Angle X-ray Scattering Instrument at the Advanced Photon Source: History, Recent Development, and Current Status.” Metallurgical and Materials Transactions a-Physical Metallurgy and Materials Science. 44A(1): 68-76; (2013).

118. Lumsden M.D., Robertson J.L., and Yethiraj M. "SPICE—spectrometer and instrument control environment." Physica B: Condensed Matter 385 (2006): 1336-1339.

119. Ilavsky J. “Irena SAS modeling macros manual”, version 2.59, February 2016.

120. Fabre A., Salameh S., Ciacchi L.C., Kreutzer M.T., and van Ommen J.R. “Contact mechanics of highly porous oxide nanoparticle agglomerates”. Journal of Nanoparticle Research. 2016 Jul 1;18(7):200.

121. Fang Z.Z. and Wang H. "Densification and grain growth during sintering of nanosized particles." International Materials Reviews 53, no. 6 (2008): 326-352.

122. Amy F., Soukiassian P., Hwu Y.K., and Brylinski C. “Si-rich 6 H-and 4 H− SiC (0001) 3× 3 surface oxidation and initial SiO_2/SiC interface formation from 25 to 650° C”. Physical Review B. 2002 Apr 8;65(16):165323.

123. Jaeger H.M. and Nagel S.R. “Physics of the granular state”. Science. 1992 Mar 20;255(5051):1523-31.

124. https://www.advaluetech.com/technical-sapphire-products, accessed 09/12/2018.

125. http://www.physics.upenn.edu/liugroup/jamming.html, accessed 09/12/2018

126. https://www.gamry.com/assets/Uploads/Interface5000-Users-Manual.pdf, accessed 09/12/2018.

127. Ilavsky J. "Nika: software for two-dimensional data reduction." Journal of Applied Crystallography. 45(2): 324-328; (2012).